Hydrino States of Hydrogen[121923]
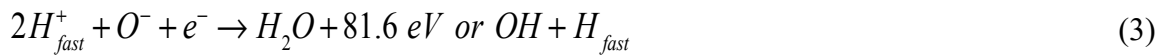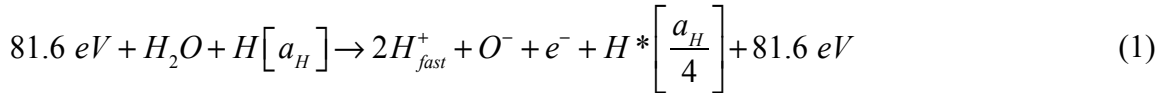
R. Mills[1,2]

[1]Brilliant Light Power, Inc., 493 Old Trenton Road, Cranbury, NJ 08512, USA

[2] Corresponding author

Abstract: In addition to the reciprocal integer squared electronic energy states of atomic hydrogen, hydrogen possesses integer squared electronic energy levels corresponding to 1/p replacing n in the Rydberg formula, corresponding so-called *hydrino state* of hydrogen. Atomic hydrino, hydrino hydride ion, and molecular hydrino have been produced in the laboratory and analyzed by over 23 methodologies and spectroscopies at numerous laboratories. The formation and existence of hydrino resolves many astrophysical mysteries and the identity of the dark matter of the universe. For example, the observed and theoretical molecular hydrino rotational lines match the Diffuse Interstellar Bands (DIBs) and the EUV continuum emission from the formation of hydrino matches that observed from all over the universe, the continuum band of solar corona, and the continuum bands of white dwarf stars as well as providing the source of ionization of the solar corona and interstellar media as an alternative mechanism to thermal ionization.

1 Introduction

Classical physical laws predict that atomic hydrogen may undergo a catalytic reaction with certain species, including itself, that can accept energy in integer multiples of the potential energy of atomic hydrogen, $m \cdot 27.2$ eV, wherein m is an integer. The predicted reaction involves a resonant, nonradiative energy transfer from otherwise stable atomic hydrogen to the catalyst capable of accepting the energy. The product is H(1/p), fractional Rydberg states of atomic hydrogen called "hydrino atoms," wherein $n = 1/2, 1/3, 1/4,…, 1/p$ ($p \leq 137$ is an integer) replaces the well-known parameter n = integer in the Rydberg equation for hydrogen excited states. Each hydrino state also comprises an electron, a proton, and a photon, but the field contribution from the photon increases the binding rather than decreasing it corresponding to energy desorption rather than absorption. Since the potential energy of atomic hydrogen is 27.2 eV, $m\,H$ atoms serve as a catalyst of $m \cdot 27.2\ eV$ for another ($m+1$)th H atom. For example, an H atom can act as a catalyst for another H by accepting 27.2 eV from it via through-space energy transfer such as by magnetic or induced electric dipole-dipole coupling. In addition to atomic H, a molecule that accepts $m \cdot 27.2\ eV$ from atomic H with a decrease in the magnitude of the potential energy of the molecule by the same energy may also serve as a catalyst. The potential energy of H_2O is 81.6 eV [1]. Then, by the same mechanism, the nascent H_2O molecule (not hydrogen bonded in solid, liquid, or gaseous state) may serve as a catalyst. Based on the 10% energy change in the heat of vaporization in going from ice at 0°C to water at 100°C, the average number of H bonds per water molecule in boiling water is 3.6 [1]; thus, H_2O must be formed chemically as isolated molecules with suitable activation energy in order to serve as a catalyst to form hydrinos. The catalysis reaction $(m=3)$ regarding the potential energy of nascent H_2O is

$$81.6\ eV + H_2O + H\left[a_H\right] \rightarrow 2H^+_{fast} + O^- + e^- + H*\left[\frac{a_H}{4}\right] + 81.6\ eV \tag{1}$$

$$H*\left[\frac{a_H}{4}\right] \rightarrow H\left[\frac{a_H}{4}\right] + 122.4\ eV \tag{2}$$

$$2H^+_{fast} + O^- + e^- \rightarrow H_2O + 81.6\ eV\ or\ OH + H_{fast} \tag{3}$$

And, the overall reaction is

$$H\left[a_H\right] \rightarrow H\left[\frac{a_H}{4}\right] + 81.6\ eV + 122.4\ eV \tag{4}$$

After the energy transfer to the catalyst, an intermediate $H*\left[\dfrac{a_H}{m+1}\right]$ is formed having the radius of the H atom and a central field of m +1 times the central field of a proton (e.g. $H*\left[\dfrac{a_H}{4}\right]$ is the

intermediate in Eq. (1) wherein m = 3, and H_{fast}^{+} and H_{fast} refer to these species with excessive kinetic energy). The radius is predicted to decrease as the electron undergoes radial acceleration to a stable state having a radius of 1/(m +1) the radius of the uncatalyzed hydrogen atom, with the release of $m^2 \cdot 13.6$ eV of energy. The extreme-ultraviolet continuum radiation band due to the $H*\left[\dfrac{a_H}{m+1}\right]$ intermediate (e.g. Eq. (2)) is predicted to have a short wavelength cutoff and energy $E_{\left(H \rightarrow H\left[\frac{a_H}{p=m+1}\right]\right)}$ given by

$$E_{\left(H \rightarrow H\left[\frac{a_H}{p=m+1}\right]\right)} = m^2 \cdot 13.6 \ eV; \quad \lambda_{\left(H \rightarrow H\left[\frac{a_H}{p=m+1}\right]\right)} = \frac{91.2}{m^2} \ nm \tag{5}$$

and extending to longer wavelengths than the corresponding cutoff.

The continuum radiation band at 10.1 nm and going to longer wavelengths for theoretically predicted transitions of H to lower-energy, so called "hydrino" states, was observed only arising from pulsed pinched hydrogen discharges first at BlackLight Power, Inc. (BLP) and reproduced at the Harvard Center for Astrophysics (CfA) [2-8]. Similarly, in hydrogen-helium microwave plasma having a high concentration of atomic H, the H undergoing catalysis with H (m=1) as the reactant and catalyst gives rise to fast H^+ and e^- [1] which recombine to emit a broad continuum peak observed at 45.6 nm [9]. H undergoing catalysis in the hydrogen-helium microwave plasma also gives rise to a concerted energy exchange of the total energy of 40.8 eV with the excitation of the He ($1s^2$) to He ($1s^1 2p^1$) transition (58.5 nm, 21.21 eV) yielding an observed [9] broad continuum emission with $\lambda \leq 63.3 \ nm$ (≥ 19.59 eV). In independent replication experiments the broad 63.3 nm emission of this nature and the continuum radiation have been observed in helium-hydrogen microwave plasmas and in hydrogen pinch plasmas, respectively [10]. The 10.1 nm continuum with the 22.8 nm and 91.2 nm continuum observed previously [2-8, 11] gives a spectrum with continua having edges at 10.1, 22.8, and 91.2 nm, a match to the otherwise challenging white dwarf spectrum [8].

Based on the catalyst mechanism, high current was predicted to facilitate a rapid hydrino transition rate (higher kinetics) by recombining charges that cause an inhibiting space charge build up from the ionization of the HOH catalyst. The application of a high current to a conductive matrix having a source of catalyst such as HOH to react with supplied H was shown to form a low-voltage arc current to dissipate space charge from the hydrino reaction to support high kinetics [2,8,12]. It was shown previously that the kinetics of catalysis of H to H(1/4) by HOH catalyst was explosive when a very low voltage, high current such as 35,000 A was flowed through a solid fuel [2,8,12] comprising 80 mg silver shots each comprising a source of H and HOH embedded in a highly conductive matrix. The resulting brilliant light-emitting expanding plasma (Figure 1)

produced a strong shock wave and emitted 20 MW-levels of EUV continuum radiation emission with a short wavelength cutoff of 10.1 nm and a cutoff energy of 122.4 eV (Eq. (5) with p = 4) when it was expanded into a vacuum chamber such that its atmospheric pressure was dissipated sufficiently to overcome the optical thickness. Such characteristic continuum radiation is observed over the entire universe [2,8].

Figure 1. High-speed (6500 frames per second) photography of brilliant light-emitting expanding plasma formed from the low voltage (15 V), high current (35,000 A) detonation of hydrated shot.
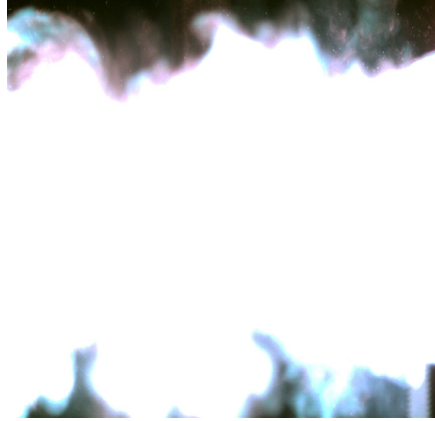
Indeed, there are some serendipitous observations in the scientific literature that comprise evidence of hydrino. In addition to HOH, as predicted, mH atoms acting as a catalyst was previously evidenced by the observation of EUV radiation from a solid fuel comprising a highly conductive material and a source of hydrogen such as a hydrocarbon through which a low voltage, high current was flowed [8]. Ion emission lines were also observed as expected on a continuum radiation background due to continuum absorption and reemission as spectral lines as in the case of HOH catalyst. The same mechanism applies to H pinch plasma emission and to astrophysical H plasma sources [8]. Specifically, mH catalyst was identified to be active in astronomical sources such as the Sun, stars, and interstellar medium wherein the characteristics of hydrino product match those of the dark matter of the universe [8]. The EUV continuum results offer resolution to many otherwise inexplicable celestial observations with (a) the energy and radiation from the hydrino transitions being the source of extraordinary temperatures and power regarding the solar corona problem, the cause of sunspots and other solar activity, and why the Sun emits X-rays [2,8], (b) the hydrino-transition radiation being the radiation source heating the WHIM (warm-hot ionized media) and behind the observation that diffuse $H\alpha$ emission is ubiquitous throughout the Galaxy requiring widespread sources of flux shortward of 912 Å, and (c) the identity of dark matter being hydrinos [8]. The novel energetic light source, decaying dark matter

to UV radiation, has been proposed to address the crisis created by the Hubble Space Telescope's Cosmic Origins Spectrograph results showing that the amount of required ultraviolet light from known quasars is five times lower than what is needed to explain the amount of electrically neutral intergalactic hydrogen observed. EUV continuum radiation from the formation of hydrino resolves this photon underproduction crisis wherein hydrino is the identity of dark matter [13].

Anomalous H Lyman alpha emission is also observed from atmospheric lightning wherein H and HOH are created with an arc current that provides a positive feedback mechanism of hydrino reaction kinetics [14]. The explosive hydrino reaction is also a likely explanation for why lightning produces a shockwave [15]. XPS spectra of shock quartz or fulgurite formed by lightning strike of silica has shown a peak at 496 eV characteristic of molecular hydrino $H_2(1/4)$ that matches the peak shown in Figures 27 and 28 *infra*.

A broad X-ray peak with a 3.48 keV cutoff was observed in the Perseus Cluster by NASA's Chandra X-ray Observatory and by the XMM-Newton [16-18] that has no match to any known atomic transition. The 3.48 keV feature assigned to dark matter of unknown identity by Bulbul et al. [1,16] matches the $H\left[\dfrac{a_H}{4}\right] + H\left[\dfrac{a_H}{1}\right] \rightarrow H\left[\dfrac{a_H}{17}\right]$ transition and further confirms hydrinos as the identity of dark matter.

Physical laws such as those of mechanics (Newton-Lorentz) and those of electrodynamics (Maxwell) require that as matter converts into energy according to $E=mc^2$, spacetime expands according to $c^3/(4PiG)$ wherein G is the Newtonian gravitational constant. The resulting dynamic behavior is a universe that oscillates between matter-filled and energy-filled with a period of one trillion years. In 1995, Mills published the GUTCP prediction [19] that the expansion of the universe was accelerating from the same equations that correctly predicted the present Hubble constant and the mass of the top quark before they were measured as well as those of the other fundamental particles and cosmological parameters. To the astonishment of cosmologists, Mills acceleration prediction was confirmed by 2000. Moreover, Mills GUTCP value for the Hubble constant matches the present observed value which has created another crisis in astrophysics regarding cosmological models that inescapably predict an unacceptable fitted value of Hubble constant from other fitted terms [20]. Mills made another prediction based on GUTCP that the identify of dark matter is Hydrino, a more stable allotrope of molecular hydrogen. The best evidence yet for the existence of dark matter is its direct observation as a source of massive gravitational mass evidenced by gravitational lensing of background galaxies that does not emit or absorb light as shown in Figure 2 [21]. We report herein that the existence of Hydrino is confirmed by 23 spectroscopic methods, and its characteristics fit those of dark matter. Furthermore, the recent unanticipated Webb telescope images confirm additional GUTCP predictions of fully

formed galaxies and old galaxies at the beginning of the expansion of the universe that disprove the long held metaphysical Big Bang and related theories of cosmology.

Figure 2. Dark matter ring in galaxy cluster. This Hubble Space Telescope composite image shows a ghostly "ring" of dark matter in the galaxy cluster Cl 0024+17. The ring is one of the strongest pieces of evidence to date for the existence of dark matter, a prior unknown substance that pervades the universe. Courtesy of NASA/ESA, M.J. Jee and H. Ford (Johns Hopkins University), Nov. 2004.

Bournaud et al. [23, 24] suggest that dark matter is hydrogen in dense molecular form that somehow behaves differently in terms of being unobservable except by its gravitational effects. Theoretical models predict that dwarf galaxies formed from collisional debris of massive galaxies should be free of nonbaryonic dark matter. So, their gravity should tally with the stars and gas within them. By analyzing the observed gas kinematics of such recycled galaxies, Bournaud et al. [22, 23] have measured the gravitational masses of a series of dwarf galaxies lying in a ring around a massive galaxy that has recently experienced a collision. Contrary to the predictions of Cold-Dark-Matter (CDM) theories, their results demonstrate that they contain a massive dark component amounting to about twice the visible matter. This baryonic dark matter is argued to be cold molecular hydrogen, but it is distinguished from ordinary molecular hydrogen in that it is not traced at all by traditional methods. These results match the predictions of the dark matter being molecular hydrino.

Additionally, astronomers Jee at al. [24] using data from NASA's Hubble Telescope have

mapped the distribution of dark matter, galaxies, and hot gas in the core of the merging galaxy cluster Abell 520 formed from a violent collision of massive galaxy clusters and have determined that the dark matter had collected in a dark core containing far fewer galaxies than would be expected if dark matter was collisionless with dark matter and galaxies anchored together. The collisional debris left behind by the galaxies departing the impact zone behaved as hydrogen did, another indication that the identity of dark matter is molecular hydrino.

Moreover, detection of alternative hypothesized identities for dark matter such as super-symmetry particles such as neutralinos has failed at the Large Hadron Collider; nor, has a single event been observed for weakly interacting massive particles or wimps at the Large Underground Xenon (LUX) experiment [25]. The HADES search for dark matter eliminated the leading candidate, "Dark Photon" or U Boson, as a possibility. This failure also undermines the Standard Model of particle physics [26].

Diffuse interstellar bands (DIBs) are absorption features seen in the spectra of astronomical objects in the Milky Way and other galaxies caused by the absorption of light by the interstellar medium. Development of many theories to assign the approximately 500 bands observed to date in ultraviolet, visible, and infrared wavelengths [27] have been futile as the nature of the absorbing material (the 'carrier') became a crucial problem in astrophysics. An essential challenge is that the central wavelengths do not correspond with any known spectral lines of any ion or molecule. It is widely believed by DIBs researchers that the existence of sub-structure is caused by molecules, particularly large molecules such as polycyclic aromatic hydrocarbons and other large carbon-bearing molecules. Specifically, it is held that the substructure results from band heads in the rotational band contour and from isotope substitution in these large molecules. The existence of molecular hydrino presents another possibility especially given that it is the best candidate for the identity of dark matter.

EPR and Raman spectroscopy recorded on $GaOOH:H_2(1/4):H_2O$ formed by a hydrino reaction in our laboratory as well as electron beam emission spectroscopy recorded on gas released by thermal decomposition of $GaOOH:H_2(1/4):H_2O$ dispositively confirmed that the compound comprised $H_2(1/4)$, and the gas was identified as $H_2(1/4)$ gas. The EPR peaks were each assigned to a spin flip transition with spin-orbital splitting and fluxon linkage splitting. Both the Raman and e-beam spectra show the same splitting, except they each involve a rotational principal transition. It is remarkable, that eight-one emission lines recorded by Raman spectroscopy on Ni foils run in the SunCell® and $GaOOH:H_2(1/4):H_2O$ match those of DIBs as shown in Tables 7B and 14A-C *infra*. The assignment of all the 380 DIBs listed by Hobbs [27] to $H_2(1/4)$ rotational transitions with spin-orbital splitting and fluxon sub-splitting are given in the Appendix.

Using a long path length (60 m), multi-reflection absorption cell coupled to a Fourier transform interferometer, Wishnow et al. [28-31] recorded the H_2 spectrum at a spectral resolution

of 0.24 cm^{-1} over the wavenumber, temperature, and pressure ranges of 20–320 cm^{-1}, 21–38 K, and 1-3 atmospheres, respectively. Similar to the case with the 21 cm (1.42 GHz) line of ordinary hydrogen, H(1/4) hydrino atom was identified by its predicted 642 GHz (21.4052 cm^{-1}) spin-nuclear hyperfine transition observed by TeraHz absorption spectroscopy of cryogenically cooled H$_2$ below 35K [32].

Another signature characteristic of the HOH catalyst mechanism is the observation of extraordinarily fast H. Plasmas from sources such as glow, RF, and microwave discharges that are ubiquitous in diverse applications ranging from light sources to material processing are now increasingly becoming the focus of a debate over the explanation of the results of ion-energy-characterization studies on specific hydrogen "mixed gas" plasmas. In mixtures of argon and hydrogen, the hydrogen emission lines are significantly broader than any argon line. Historically, Kuraica and Konjevic [33-34], Videnovic et al. [35], and others [36-50] have characterized mixed hydrogen-argon plasmas by determining the excited hydrogen atom energies from measurements of the line broadening of one or more of the Balmer α, β, and H_α lines of atomic hydrogen at 656.28, 486.13, and 434.05 α, respectively. They found that the Balmer lines were extremely broadened and explained the phenomenon in terms of Doppler broadening due to the various models involving acceleration of charges such as H^+, H_2^+, and H_3^+ in the high fields (e. g. over 10 kV/cm.) present in the cathode fall region herein called field-acceleration models (FAM). The field-acceleration mechanism, which is directional, position dependent, and is not selective of any particular ion cannot explain the Gaussian Doppler distribution, position independence of the fast H energy, absence of the broadening of the molecular hydrogen and argon lines, gas composition dependence of the hydrogen mixed plasma, and is often not internally consistent or consistent with measured densities and cross sections. The energetic hydrino chemical reaction of hydrogen as the source of broadening explains all the aspects of the atomic H line broadening such as lack of an applied-field dependence, the observation that only particular hydrogen-mixed plasmas show the extraordinary broadening. Specifically, HOH and mH can serve as catalysts to form fast protons and electrons from ionization to conserve the m27.2 eV energy transfer for H (e.g. Eq. (1)). These fast ionized protons recombine with free electrons in excited states to emit broadened H lines [51-59]. Of the noble gases, HOH is uniquely present in argon-H$_2$ plasmas because oxygen is co-condensed with argon during purification from air, and H catalyst is present in hydrogen plasmas from dissociation of H$_2$. Water vapor plasmas also show extreme selective broadening of over 150 eV [53,54, 57] and further show atomic hydrogen population inversion [60-62] also due to free electron-hot-proton recombination following resonant energy transfer from atomic hydrino to HOH catalyst according to Eq. (1).

Argon gas is cryo-distilled from the atmosphere. Due to the likeness of boiling points, oxygen co-condenses. Oxygen is removed by adding hydrogen and recombining O_2 on a recombination catalyst. An exemplary recombination catalyst is Pt or Pd on an alumina support. The reaction is $H_2 + O_2$ to H_2O. Recombination catalysts work by creating H atoms and they produce water. Argon greatly increases the concentration of H and HOH (versus water dimers) by interfering with interactions between H atoms and HOH molecules. Commercial argon gas uniquely contains trace H_2 and O_2 that remains after recombination process, and it contains $H_2(1/4)$ as a product of the H and HOH catalyst reaction. The ro-vibration band of $H_2(1/4)$ was shown by electron beam excitation spectroscopy. Specifically, irradiation of argon comprising $H_2(1/4)$ with high energy electrons of an electron beam showed equal, 0.25 eV spaced line emission in the ultraviolet (150-180 nm) region with a cutoff at that matched the $H_2(1/4)$ $\nu = 1$ to $\nu = 0$ vibrational transition with a series of rotational transitions corresponding to the $H_2(1/4)$ P-branch. The spectral fit was a good match to $4^2 0.515 eV - 4^2 (J+1) 0.01509; J = 0,1,2,3....$ wherein 0.515 eV and 0.01509 eV are the vibrational and rotational energies of ordinary molecular hydrogen, respectively. The same series was previous reported by Murnick et al. as shown in Figure 6 of Ref. [63] and could not be unambiguously assigned by the authors. The series was observed with the same type of e-beam argon plasma with a "contaminant gas" and not observed in krypton and xenon plasmas. The band assigned to $H_2(1/4)$ was confirmed through the observation of a spectral match with purified $H_2(1/4)$ gas as reported previously [64] and *infra*.

In this paper we present a very extensive array of spectroscopic and energetic signature measurements that confirm the existence of the hydrino state of hydrogen. The hydrino signals cannot be assigned to any known species since they have one or more extraordinary features such as (i) the signals are outside of an energy range of those of known species, (ii) the signals have a physical characteristic unique to hydrino, there is an absence of other signatures that are required for the alternative assignment, or hydrino has an alternative combination of signatures absent that of known species, (iii) the signature is totally novel, and (iv) in the exemplary case of energetics, the energy or power-related signature is much greater than that of a known species, an alternative explanation does not exist, or an alternative is eliminated upon further investigation.

2 Classical Theory

In the atom such as the simplest one, hydrogen, the electron is constantly accelerating around the proton in an atomic orbit. Yet, classical physics requires that accelerating charges radiate energy, which would cause the electron to spiral into the nucleus in a fraction of a second. This seminal problem of the stability of the atom was one of the key obstacles that physicists faced early in the 20th century, and their inability to solve it led to the construction of quantum theory.

Mills solved the structure of the electron using classical physical laws, such that electron orbits were stable to radiation. This allowed Mills to construct a new theory of atoms and molecules that was based entirely on classical physics that provides exact solutions for core phenomena and observables of chemistry and physics over the scale of quarks to cosmos, 85 orders of magnitude.

According to Mills GUT-CP, nature is classical [1]. Electrons, when bound in an atom, are considered to be discrete two-dimensional spherical membranes of charge and current that completely surround the nucleus as a bubble that can be viewed in a medium such as superfluid helium [65]. These shells, called electron atomic orbitals, each have an organized pattern of super-current filaments on the surface that gives rise to electron spin. The current may be modulated with a time and spherical harmonic pattern that gives rise to orbital angular momentum. Electrons obey classical physics such that the intrinsic electron angular momentum that arises from the pattern of motion is quantized, and invoking this property predicts that bound electrons are stable to emitting radiation according to Maxwellian electrodynamics. This solves the problem that has plagued atomic physics since the Bohr model of the atom: how an electron, continuously accelerating in the Coulombic field of the proton, is able to remain in a stable orbit [65].

This approach is extended to exactly solve multi-electron atoms and molecules of boundless extent and complexity [1,67-70]. In multi-electron atoms, bound electrons group into a series of concentric shells, each of which is an atomic orbital and may contain several electrons. In molecules, the electrons stretch over two nuclei of each bond of the molecule to form a prolate spheroidal membrane with the nuclei at the foci of the corresponding molecular orbital (MO) which linearly superimposes other such MOs of the molecule. Each MO reaches an equipotential, minimum energy configuration for the system, governed by Maxwellian and Newtonian laws.

From within this frame of reference, GUT-CP unwinds the mysteries of quantum theory. GUT-CP is not a "hidden variables" interpretation of the formalism of quantum theory, rather, it is a new classical theory based on Maxwell's Equations and Newton's Laws with relativistic considerations. It explains canonical experiments of quantum mechanics such as the double-slit experiments and the Aspect experiments classically, and provides exact solutions for all the basic phenomena and observables of chemistry and physics over the scale of quarks to cosmos, 85 orders of magnitude [1]. The GUT-CP has been extensively peer reviewed [71].

3 Parameters and Magnetic Energies Due to the Spin Magnetic Moment of $H_2(1/4)$

This new model of the atom predicted the theoretical existence of the hydrino, or energy states of the hydrogen atom that exist below the $-13.6\ eV$ energy state of atomic hydrogen. Akin to the case of molecular hydrogen, two hydrino atoms may react to form molecular hydrino.

Molecular hydrino $H_2(1/p)$ comprises (i) two electrons bound in a minimum energy, equipotential, prolate spheroidal, two-dimensional current membrane comprising a molecular orbital (MO), (ii) two $Z=1$ nuclei such as two protons at the foci of the prolate spheroid, and (iii) a photon wherein the photon equation of each state is different from that of an excited H₂ state given in the Excited States of the Hydrogen Molecule section of Mills [1], in that the photon increases the central field by an integer rather than decreasing the central prolate spheroidal field to that of a reciprocal integer of the fundamental charge at each nucleus centered on the foci of the spheroid, and the electrons of $H_2(1/p)$ are superimposed in the same shell at the same position ξ versus being in separate ξ positions. The interaction of the integer hydrino state photon electric field with each electron of the MO, electron 1 and electron 2, gives rise to a nonradiative radial monopole such that the state is stable. To meet the boundary conditions that each corresponding photon is matched in direction with each electron current and that the electron angular momentum is $\hbar$ are satisfied, one half of electron 1 and one half of electron 2 may be spin up and matched with the two photons of the two electrons on the MO, and the other half of electron 1 may be spin up and the other half of electron 2 may be spin down such that one half of the currents are paired and one half of the currents are unpaired. Thus, the spin of the MO is $\frac{1}{2}(\uparrow\uparrow + \downarrow\uparrow)$ where each arrow designates the spin vector of one electron. The two photons that bind the two electrons in the molecular hydrino state are phase-locked to the electron currents and circulate in opposite directions. Given the indivisibility of each electron and the condition that the MO comprises two identical electrons, the force of the two photons is transferred to the totality of the electron MO comprising a linear combination of the two identical electrons to satisfy the central force balance given by Mills Eq. (11.200) [1]. The resulting angular momentum and magnetic moment of the unpaired current density are $\hbar$ and a Bohr magneton μ_B, respectively.

Due to its unpaired electron, molecular hydrino is electron paramagnetic resonance (EPR) spectroscopy active. Moreover, due to the unpaired electron in a common molecular orbital with a paired electron, the EPR spectrum is uniquely characteristic of and identifies molecular hydrino as shown *infra*. The spin flip transition energy is

$$\Delta E^{spin}_{mag\ g} = g_{H_2(1/4)}\mu_B B \tag{6}$$

Given that flux is linked by an unpaired electron in quantized units of the fluxon or magnetic flux quantum $\frac{h}{2e}$ the corresponding g factor given by Mills Eq. (16.218) [1] is

$$g_{H_2(1/p)} = 2\left(1+2\left(\frac{\alpha}{2\pi}+\frac{2}{3}\alpha^2\left(\frac{\alpha}{2\pi}\right)-\frac{4}{3}\left(\frac{\alpha}{2\pi}\right)^2\right)\right) = 2.0046386 \tag{7}$$

wherein α is the fine structure constant. The unpaired-paired coupling or spin-orbital coupling energy is given as the diamagnetic moment times the magnetic flux of the unpaired electron. Since flux is linked by an unpaired electron in units of the magnetic flux quantum, the spin-orbital coupling energy $E_{S/O}$ between two magnetic moments of $H_2(1/4)$ given by Mills Eqs. (2.194) and (16.225) [1] can be expressed as:

$$ E_{S/O} = \chi_m m \left[\frac{1}{\left(4\sqrt{2}\right)^{-3}} \alpha^5 \left(2\pi\right)^2 m_e c^2 \sqrt{\frac{3}{4}} \right] \tag{8} $$

wherein the semiminor radius of the $H_2(1/4)$ MO is given by Mills Eq. (11.205) [1] with $p = 4$ and χ_m is the magnitude of the diamagnetic susceptibility of the paired electron given by Mills Eqs. (11.416) and (16.226) [1]:

$$ \chi_m = \alpha \frac{\Delta B_T}{B} \sqrt{\frac{3}{4}} = \alpha \mu_0 \left(4 - \sqrt{2} \ln \frac{\sqrt{2}+1}{\sqrt{2}-1} \right) \frac{pe^2}{36 a_0 m_e} \left(1 + p\alpha^2\right) \sqrt{\frac{3}{4}} = 7.0821 \ X \ 10^{-7} \tag{9} $$

The unpaired-paired coupling energy given by Mills Eq. (16.227) [1] is

$$ E_{s/o} = m7.0821 X 10^{-7} \left(64(2)^{1.5} \alpha^5 \left(2\pi\right)^2 \right) m_e c^2 \sqrt{\frac{3}{4}} = m7.426 \ X \ 10^{-27} \ J \tag{10} $$

wherein m is a positive integer.

Consider the case that the EPR frequency is 9.820295 GHz, the resonance magnetic flux B for the principal peak given by Eqs. (6-7) is

$$ B = \frac{h9.820295 GHz}{2.0046386 \mu_B} = 0.35001 \ T \tag{11} $$

where h is Planck's constant and μ_B is the Bohr magneton. The resonance magnetic flux shift ΔB_C of a principal peak at position B_1 due to a splitting energy E_C is given by

$$ \Delta B_C = B_1 \frac{E_C}{h9.820295 GHz} \tag{12} $$

Using Eqs. (10-12), the downfield and upfield shifts $\Delta B_{S/O}$ with quantized spin-orbital splitting energies $E_{S/O}$ (Eq. (10) and electron spin-orbital coupling quantum numbers $m = 0.5, 1, 2, 3, 5....$ are given in units of Gauss by

$$ \Delta B_{S/O} = m0.35001 \left[\frac{7.426 \ X \ 10^{-27} \ J}{h9.820295 GHz} \right] T = m3.99427 \ G \tag{13} $$

The spin-orbital splitting shift of $m7.426 \ X \ 10^{-27} J$ (Eq. (10)) is independent of the applied EPR field/frequency combination for both downfield and upfield shifted peaks.

The free electron of $H_2(1/4)$ must link the magnetic flux component corresponding to spin-orbital coupling. This flux contribution increases the magnetic energy and the energy of the combined spin flip (Eq. (11)) and spin-orbital coupling (Eq. (13)) transition energy for a given

spin-orbital quantum number m. Based on the potential energy of a superconducting quantum interference device (SQUID), the magnetic energies $U_{S/OMag}$ arising from the absorption of the corresponding spin-orbital coupling transitional flux given by Mills Eq. (16.231) [1] are

$$U_{S/OMag} = (0.5)\frac{0.5\Delta E^{spin}_{mag\ 2.0046}}{g_{H_2(1/p)}\mu_B}\left(\frac{2\pi(\Delta B_{S/O})}{\frac{0.5\Delta E^{spin}_{mag\ 2.0046}}{g_{H_2(1/p)}\mu_B}}\right)^2 \tag{14}$$

$$= (0.5)\frac{\left(2\pi m3.99427\,X\ 10^{-4}\right)^2}{0.1750}\,X\ 10^4\,G$$

The downfield magnetic energy shifts $U_{S/OMag}$ given by Eq. (14) are added to the quantized spin-orbital splitting energies $E_{S/O}$ (Eq. (13)) to give combined quantized spin-orbital downfield shift energies $\Delta B^{downfield}_{S/Ocombined}$ in units of Gauss:

$$\Delta B^{downfield}_{S/Ocombined} = -\left(m3.99427\,X\ 10^{-4} + (0.5)\frac{\left(2\pi m3.99427\,X\ 10^{-4}\right)^2}{0.1750}\right)X\ 10^4\,G \tag{15}$$

The downfield peak positions $B^{downfield}_{S/Ocombined}$ due to the combined shifts due to the magnetic energy and the spin-orbital coupling energy given by Eqs. (11) and (15) are:

$$B^{downfield}_{S/Ocombined} = \left(0.35001 - m3.99427\,X\ 10^{-4} - (0.5)\frac{\left(2\pi m3.99427\,X\ 10^{-4}\right)^2}{0.1750}\right)T \tag{16}$$

Using Eq. (11) and Eqs. (10) and (12-13), the upfield peak positions $B^{upfield}_{S/O}$ with quantized spin-orbital splitting energies $E_{S/O}$ (Eq. (10)) and electron spin-orbital coupling quantum numbers $m = 0.5, 1, 2, 3, 5....$ are given by

$$B^{upfield}_{S/O} = 0.35001\left(1 + m\left[\frac{7.426\,X\ 10^{-27}\,J}{h9.820295GHz}\right]\right)T = \left(0.35001 + m3.99427\,X\ 10^{-4}\right)T \tag{17}$$

The downfield shifts due to the magnetic energies in units of Gauss (Eq. (14)), the downfield shifts due to spin-orbital coupling energies in units Gauss (Eq. (13)) for spin-orbital coupling quantum numbers $m = 0.5, 1, 2, 3, 5....$ are given in Table 1

Table 1. The frequency independent $H_2(1/4)$ EPR downfield shifts due to the magnetic energies and the downfield shifts due to spin-orbital coupling energies for spin-orbital coupling quantum numbers $m = 0.5, 1, 2, 3, 5$.

m	Downfield Magnetic Energy Shift (G)	Spin-Orbital Shift (G)
0.5	0.04499	1.99714
1	0.17995	3.99427
2	0.71981	7.98854
3	1.61957	11.98281
4	2.87924	15.97708
5	4.49881	19.97135

The combined downfield shifts due to the magnetic and spin-orbital coupling energies in units of Gauss (Eq. (15)), the resulting downfield peak positions (Eq. (16), and the upfield peak positions (Eq. (17)) shifted only by the spin-orbital coupling energies (Eq. (13)), for spin-orbital coupling quantum numbers $m = 0.5, 1, 2, 3, 5....$ wherein the principal peak with the g-factor of 2.0046386 (Eq. (7)) is observed at 0.35001 T (Eq. (11) are given in Table 2.

Table 2. The 9.820295 GHz $H_2(1/4)$ EPR combined downfield shifts due to the magnetic and spin-orbital coupling, the resulting downfield peak positions, and the upfield peak positions shifted only by the spin-orbital coupling energies for spin-orbital coupling quantum numbers $m = 0.5, 1, 2, 3, 5$.

m	Combined Downfield Magnetic Energy Shift (G)	Downfield Peak Position (T)	Upfield Peak Position (T)
0.5	2.04212	0.34980	0.35021
1	4.17422	0.34959	0.35041
2	8.70835	0.34914	0.35081
3	13.60238	0.34865	0.35121
4	18.85632	0.34812	0.35160
5	24.47016	0.34756	0.35200

During a spin flip transition, magnetic flux is linked by an unpaired electron in quantized units of the fluxon $\Phi_0 = \dfrac{h}{2e}$ or the magnetic flux quantum $\dfrac{h}{2e}$. The fluxon linkage energies E_Φ by molecular hydrino $H_2(1/4)$ during a spin transition given by Mills Eqs. (16.237-16.240) [1] are

$$E_\Phi = m_\Phi 4\left(\frac{\alpha}{2\pi} + \frac{2}{3}\alpha^2\left(\frac{\alpha}{2\pi}\right) - \frac{4}{3}\left(\frac{\alpha}{2\pi}\right)^2\right)\chi_{m\Phi}\frac{\mu_B}{\sqrt{s(s+1)}}\left(\frac{j\Phi_0}{A}\right)$$

$$= m_\Phi\left(j0.0046386\frac{\chi_{m\Phi}\mu_B}{\sqrt{s(s+1)}}\frac{\mu_0}{r^3}\left(\frac{e\hbar}{2m_e}\right)\right) \tag{18}$$

$$= m_\Phi\left(j5.7830\ X\ 10^{-28}\ J\right)$$

wherein $m_\Phi = 1,2,3$ based on the quantized angular momentum components involved in the transition. Using Eq. (12) with the E_Φ, the fluxon linkage energy of $H_2(1/4)$ (Eq. (18)), and the spin-orbital peak positions (Eqs. (16) and (17)), the separation ΔB_Φ of the integer series of peaks at each spin-orbital peak position (Table 2) for an EPR frequency of 9.820295 GHz is given by

$$\Delta B_\Phi^{downfield} = \left(\begin{array}{c}0.35001 - m3.99427\ X\ 10^{-4}\\ -(0.5)\dfrac{(2\pi m3.99427\ X\ 10^{-4})^2}{0.1750}\end{array}\right)\left[\frac{m_\Phi 5.7830\ X\ 10^{-28}\ J}{h9.820295GHz}\right]X\ 10^4 G \tag{19}$$

and

$$\Delta B_\Phi^{upfield} = \left(0.35001 + m3.99427\ X\ 10^{-4}\right)\left[\frac{m_\Phi 5.7830\ X\ 10^{-28}\ J}{h9.820295GHz}\right]X\ 10^4 G \tag{20}$$

for electron fluxon quantum numbers $m_\Phi = 1,2,3$. The 9.820295 GHz $H_2(1/4)$ EPR spectral separations ΔB_Φ (Eqs. (19) and (20)) of each integer series of the peaks comprising sub-splitting of the downfield and upfield peaks of Table 2 corresponding to the principal peak having a g-factor of 2.0046386 (Eq. (7)) split by quantized spin-orbital coupling energies $\Delta B_{S/O}$ (Eq. (13)) and magnetic energies $U_{S/OMag}$ (Eq. (14)) for electron spin-orbital coupling quantum numbers $m = 0.5,1,2,3,4,5$ and electron fluxon quantum numbers $m_\Phi = 1,2,3$ (Eq. (18)) are given in Table 3.

Table 3. The 9.820295 GHz $H_2(1/4)$ EPR spectral separation ΔB_Φ of each integer series of the peaks comprising sub-splitting of the downfield and upfield peaks of Table 2 for electron spin-orbital coupling quantum numbers $m = 0.5, 1, 2, 3, 4, 5$ and electron fluxon quantum numbers $m_\Phi = 1, 2, 3.$

m	m_Φ	Downfield Peak Position (T)	ΔB_Φ (G)	Upfield Peak Position (T)	ΔB_Φ (G)
0.5	1	0.34980	0.3109	0.35021	0.3112
1	2	0.34959	0.6214	0.35041	0.6228
2	3	0.34914	0.9309	0.35081	0.9353
3	3	0.34865	0.9296	0.35121	0.9364
4	3	0.34812	0.9282	0.35160	0.9375
5	3	0.34756	0.9267	0.35200	0.9385

     The predicted EPR spectrum was confirmed experimentally [72]. The 9.820295 GHz EPR spectrum was performed on a white polymeric compound identified by X-ray diffraction (XRD), energy-dispersive X-ray spectroscopy (EDS), transmission electron spectroscopy (TEM), scanning electron microscopy (SEM), time-of-flight secondary ionization mass spectroscopy (ToF-SIMs), Rutherford backscattering spectroscopy (RBS), and X-ray photoelectron spectroscopy (XPS) as GaOOH:H_2(1/4). The GaOOH:H_2(1/4) was formed by dissolving Ga_2O_3 and gallium-stainless steel metal (~0.1-5%) alloy collected from a hydrino reaction run in a SunCell® in 4M aqueous KOH, allowing fibers to grow, and float to the surface where they were collected by filtration. The white fibers were not soluble in concentrated acid or base, whereas control GaOOH is. No white fibers formed in control solutions. Control GaOOH showed no EPR spectrum. The experimental EPR shown in Table 4 was acquired by Professor Fred Hagen, TU Delft, with a high sensitivity resonator at a microwave power of -28 dB and a modulation amplitude of 0.02 G, that can be changed to 0.1 G since Dr. Hagen rigorously determined that the minimum line width is 0.15 to 0.2 G. The average error between EPR spectrum and theory for peak positions given in Table 4 was 0.097 G. The EPR spectrum was replicated by Bruker (Bruker Scientific LLC, Billerica, MA) using two instruments on two samples as shown in Figures 3A-C.
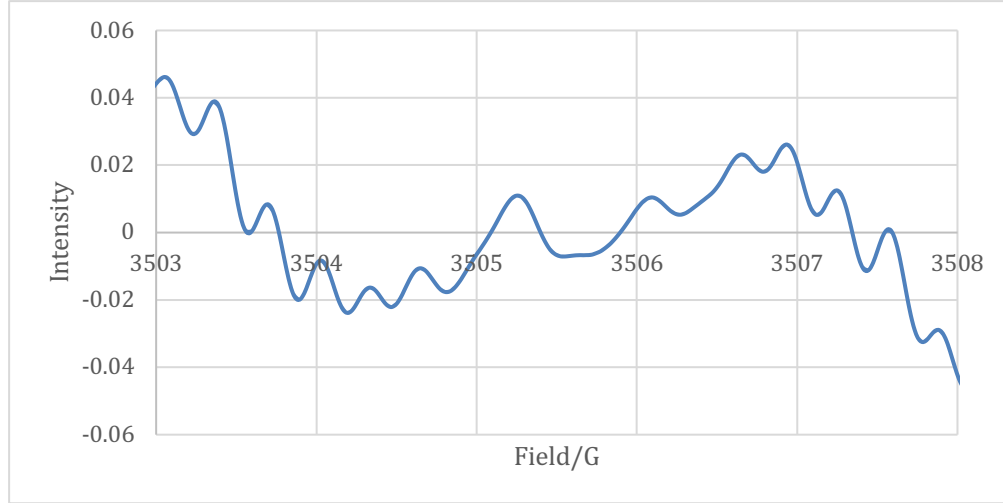
Figures 3A-C. EPR spectra of GaOOH:H$_2$(1/4) replicated by Bruker using two instruments on two samples. (A) EMXnano data. (B) EMXplus data. (C) Expansion of EMXplus data, 3503 G - 3508 G region.
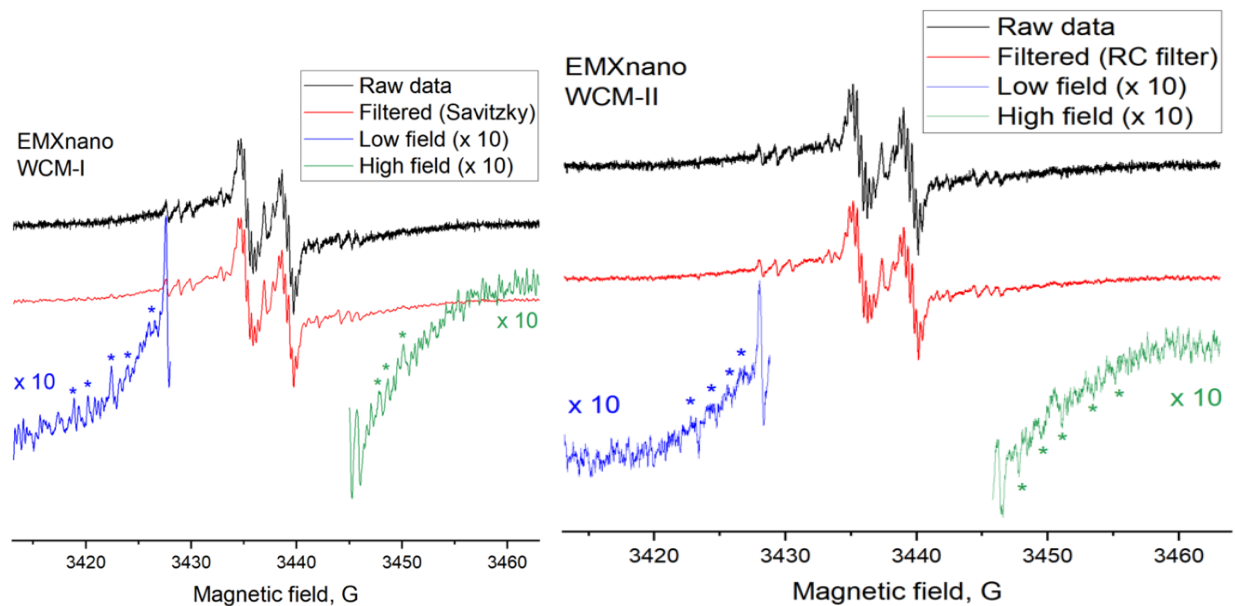
(A)
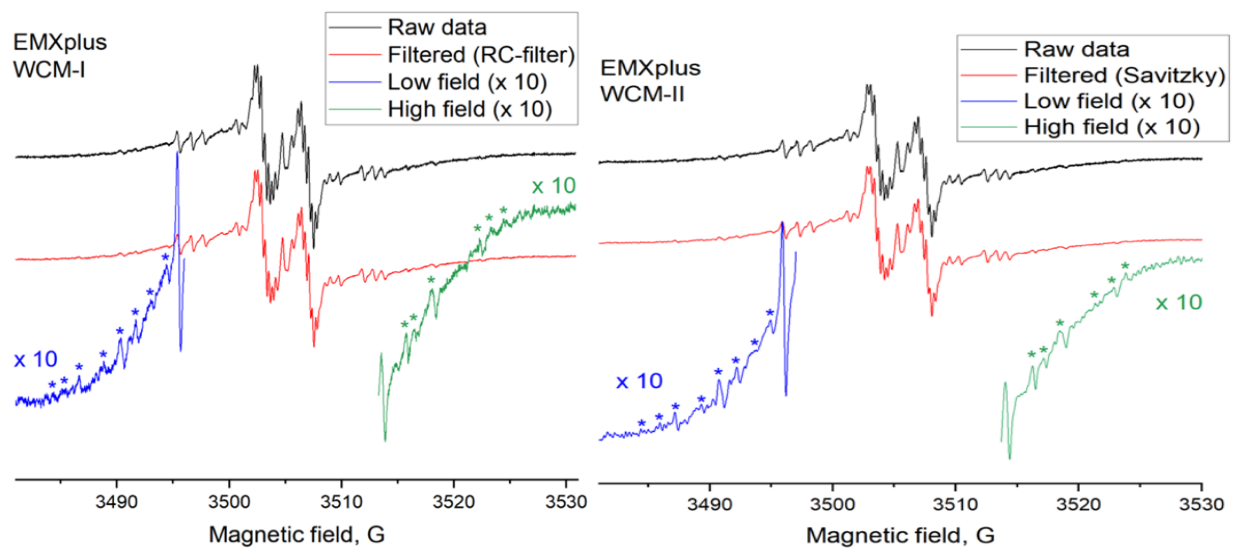
(B)

(C)

Table 4. The Hagen EPR data at 9.820295 GHz, the theoretical peak positions due to the electron spin-orbital coupling splitting energies for downfield and upfield spin-orbital coupling quantum numbers $m = 0, 0.5, 1, 2, 3, 4$, and the difference between theory and experiment.

m	Experimental EPR Peak (T)	Theoretical EPR Peak (T)	Difference (G)
4	0.34805	0.34812	-0.67
3	0.34868	0.34865	0.32
2	0.34917	0.34914	0.33
1	0.34957	0.34959	-0.19
0.5	0.34985	0.34980	0.45
0	0.35004	0.35001	0.33
0.5	0.35023	0.35021	0.25
1	0.35040	0.35041	-0.04
2	0.35078	0.35081	-0.22
3	0.35115	0.35121	-0.57
4	0.35173	0.34812	1.26
		Average	**0.097**

Specifically, the observed principal peak at g = 2.0045(5)) was assigned to the theoretical peak having a g-factor of 2.0046386 (Eq. (7)). This principal peak was split into a series of pairs of peaks with members separated by energies matching $E_{S/O}$ (Eqs. (10) and (13)) corresponding to each electron spin-orbital coupling quantum number m. The results confirmed the spin-orbital coupling between the spin magnetic moment of the unpaired electron and an orbital diamagnetic moment induced in the paired electron alone or in combination with rotational current motion about the semimajor molecular axis that shifted the flip energy of the spin magnetic moment. The

data further matched the theoretically predicted one-sided tilt of the spin-orbital splitting energies wherein the downfield shift was observed to increase with quantum number m due to the magnetic energies $U_{S/OMag}$ (Eq. (14)) of the corresponding magnetic flux linked during a spin-orbital transition. Each spin-orbital splitting peak was further sub-split into a series of equally spaced peaks that matched the integer fluxon energies ΔB_Φ (Eqs. (19) and (20)) dependent on electron fluxon quantum number m_Φ corresponding to the number of angular momentum components involved in the transition. The evenly spaced series of sub-splitting peaks was assigned to flux linkage during the coupling between the paired and unpaired magnetic moments in units of the magnetic flux quantum $\dfrac{h}{2e}$ while a spin flip transition occurs. The EPR spectrum recorded at different frequencies showed that the peak assigned the g factor of 2.0046386 (Eq. (7)) remained at constant g factor. Moreover, the peaks, shifted by the fixed spin-orbital splitting energies relative to this true g-factor peak, exactly maintained the separation of the spin-orbital splitting energies independent of frequency as predicted. The GaOOH:H_2(1/4) EPR spectrum recorded at Delft University showed remarkably narrow line widths due to the dilute presence of H_2(1/4) molecules trapped in GaOOH cages that comprised a diamagnetic matrix. The structure of GaOOH:H_2(1/4) and electronic state of H_2(1/4) permitted the observations of unprecedented low splitting energies that are between 1000 and 10,000 times smaller than the H Lamb shift.

As given in the Hydrino Hydride Ion Hyperfine Lines section of Mills [1], the pattern of integer-spaced peaks predicted for the EPR spectrum of $H_2\left(1/4\right)$ is very similar to that experimentally observed on the hydrino hydride ion shown in Figure 4 that also comprises a paired and unpaired electron in a common orbital, except that the orbital is an atomic orbital [11, 73-76].

Figure 4. A wavelength-calibrated spectrum (3900-4090 Å) of a hydrino-reaction-plasma formed by heating KNO_3 and dissociating H_2 using a tungsten filament overlaid with a hydrogen microwave plasma. Due to the requirement that flux is linked by $H(1/2)$ in integer units of the magnetic flux quantum, the energy is quantized, and the observed emission due to $H^-(1/2)$ formation comprises a series of hyperfine lines in the corresponding bound-free band with energies given by the sum of the fluxon energy E_Φ, the spin-spin energy E_{ss}, and the observed binding energy peak E_B^*.
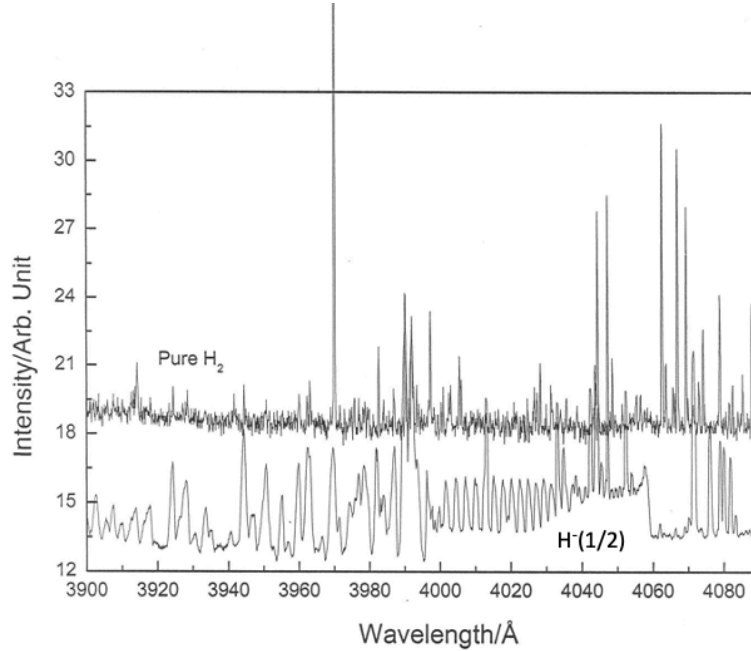
In addition to the peaks in Tables 2 and 3, several very weak peaks assigned to continuations and possible overlaps of series of fluxons of contiguous spin orbital splitting peaks were observed wherein the series intensity decreased significantly due to interference between the competing transitions. This assignment was confirmed by the observation that the very weak peaks shifted with the principal peak and its fine structure peaks with variation in the EPR microwave frequency. Only the principal peak assigned to a g-factor of 2.0046386 (Eq. (7)) at the center of the spectrum is a real g value with a field value that moves linearly with the frequency. All other features including the very weak lines are at a constant distance in field value from the spectral center, implying that they represent an interaction independent of the microwave frequency.

The EPR spectrum showing the principal peak with an assigned g-factor of 2.0046386 and fine structure comprising spin-orbital and spin-orbital magnetic energy splitting with fluxon sub-splitting was observed superimposed on a broad background feature with a center at about the position of the principal peak. It was observed that the fine structure features broadened into a continuum that overlaid the broad background feature as the temperature was lowered into a

cryogenic range with the peak assigned to the downfield member corresponding to the electron spin-orbital coupling quantum number $m = 0.5$ being less sensitive to a decrease in temperature than the corresponding upfield peak. The same trend was also observed with increasing microwave power wherein the higher energy transition saturated at a higher power. Thus, the peak assigned to downfield member corresponding to the electron spin-orbital coupling quantum number $m = 0.5$ was selectively observed over the corresponding upfield peak. The higher sensitivity of the upfield peak to low temperature and microwave power is excepted since it corresponds to de-excitation of a spin-orbital energy level during the spin flip transition wherein the spin-orbital energy level requires thermal excitation to be populated. Thus, the population decreases with temperature due to a decreased source of thermal excitation, and the population is smaller than the unexcited population so that it is more easily depleted with microwave power.

The GaOOH:H_2(1/4) sample was observed by TEM to comprise two different morphological and crystalline forms of GaOOH. Observed morphologically polymeric crystals comprising hexagonal crystalline structure were very sensitive to the TEM electron beam, whereas rods having orthorhombic crystalline structure were not electron beam sensitive. The latter crystals' morphology and crystalline structure matches those of the literature for control GaOOH that lacks molecular hydrino inclusion. The hexagonal phase is likely the source of the fine structure EPR spectrum and the orthorhombic phase is likely the source of the broad background EPR feature. Cooling may selectively eliminate, e.g., by microwave power saturation, the observed near free-gas-like EPR spectral behavior of $H_2(1/4)$ trapped in the hexagonal crystalline matrix. Any deviations from theory could be due to the influence of the proton of GaOOH and those of water. Also, matrix orientation in the magnetic field, matrix interactions and interactions between one or more $H_2(1/4)$ could cause some shifts.

Deuterium substitution was performed to eliminate an alternative assignment of any EPR spectral lines as being nuclear split lines. The power released when H_2 was replaced by D_2 was decrease by at least 1/3. The deuterated analog of GaOOH:H_2(1/4), GaOOH:HD(1/4), was confirmed by Raman spectroscopy as shown in Figures 13A-C and Table 9B wherein GaOOH:HD(1/4) was also formed by using D_2O. The deuterated analog required a month to form from 4 M potassium hydroxide versus under three days for GaOOH:H_2(1/4). The EPR spectrum of the deuterated analog shown in Figure 5 only showed a singlet with no fine structure; thus, eliminating any possible nuclear splitting assignment to the lines given in Table 4.

**Figure 5.** EPR spectrum of GaOOH:HD(1/4) (3464.65 G - 3564.65 G) region.
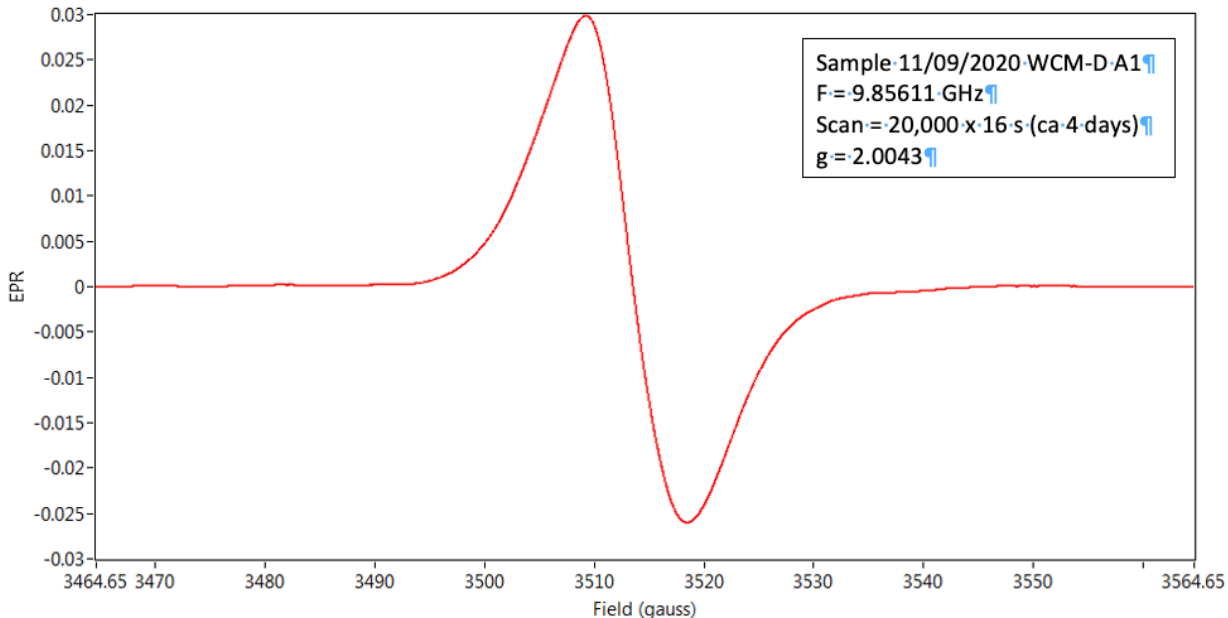
The g factor and profile matched that of the singlet of GaOOH:H_2(1/4) wherein the singlet in both cases was assigned to the orthorhombic phase. The XRD of the deuterated analog matched that of the hydrogen analog, both comprising gallium oxyhydroxide. TEM confirmed that the deuterated analog comprised 100% orthorhombic phase. The phase preference of the deuterated analog may be due to a different hydrino concentration and kinetic isotope effect which could have also reduced the concentration.

The unpaired electron of molecular hydrino may give rise to non-zero or finite bulk magnetism such as paramagnetism, superparamagnetism and even ferromagnetism when the magnetic moments of a plurality of hydrino molecules interact cooperatively. Matrix magnetism manifest as an upfield shifted matrix peak due to the magnetism of molecular hydrino was observed by ^{1}H MAS nuclear magnetic resonance spectroscopy (NMR) [77], and superparamagnetism was observed using a vibrating sample magnetometer to measure the magnetic susceptibility of compounds comprising molecular hydrino. Specifically, the magnetic characteristic of molecular hydrino is demonstrated by proton magic angle spinning nuclear magnetic resonance spectroscopy (^{1}H MAS NMR) as shown by Mills et al. in the case of electrochemical cells that produce hydrinos called CIHT cells [78]. The presence of molecular hydrino in a solid matrix such as an alkali hydroxide-alkali halide matrix that may further comprise some waters of hydration gives rise to an upfield ^{1}H MAS NMR peak, typically at -4 to -5 ppm due to the molecular hydrinos' paramagnetic matrix effect whereas the initial matrix devoid of hydrino shows the known down-field shifted matrix peak at +4.41 ppm. Ga_2O_3:H_2(1/4) collected from a stainless steel SunCell® was dissolved in NaOH, filtered, and the filtrate comprising

stainless steel oxide and GaOOH was heated to 900 °C in a pressure vessel and the decomposition gas was flowed through hydrated KCl getter packed in a tube connected to the pressure vessel. The ^{1}H MAS NMR spectrum relative to external TMS of the KCl getter exposed to hydrino gas shows an upfield shifted matrix peak at -4.6 ppm due to the magnetism of molecular hydrino (Figure 6). ^{1}H MAS NMR was performed on solid samples using a 500 MHz Bruker instrument with spin speeds of 5 kHz, 10 kHz, and 17.5 kHz to eliminate spinning side bands that shifted with a change in spin speed.

Figure 6. ^{1}H MAS NMR spectrum relative to external TMS of KCl getter exposed to hydrino gas that shows upfield shifted matrix peak at -4.6 ppm due to the magnetism of molecular hydrino.
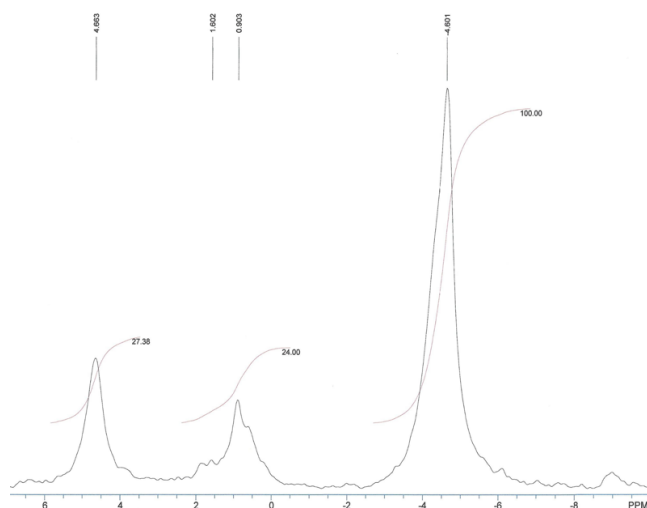
A convenient method to produce molecular hydrinos is by wire detonation such as Fe wire detonation in the presence of H_2O to serve as the hydrino catalyst and source of H to form $H_2(1/4)$ trapped in iron oxides. A self-assembly mechanism is magnetic ordering in addition to van der Waals forces. It is well known that the application of an external magnetic field causes colloidal magnetic nanoparticles such as magnetite (Fe_2O_3) suspended in a solvent such as toluene to assemble into linear structures. Due to the small mass and high magnetic moment, molecular hydrino magnetically self assembles even in the absence of a magnetic field. Wire detonations in an atmosphere comprising water vapor produced magnetic linear chains of $FeOOH/Fe_2O_3{:}H_2(1/4)$ that aggregated in air to forms webs. The web did not form without the presence of water vapor. The Fe web was akin to the structure of $GaOOH{:}H_2(1/4)$, confirming the ability of molecular hydrino to form web like complexes in different media. Remarkably, the web fibers were observed to form macroscopically in real time in air and on the micron scale by observation with a scanning electron microscope.

Paramagnetic material responds linearly with the induced magnetism, whereas an observed "S" shape is characteristic of superparamagnetism, a hybrid of ferromagnetism and para magnetism. A web of non-magnetic MoO_2 complexed to $H_2(1/4)$ was formed by detonation of an ultra-high purity Mo wire in an air-water vapor atmosphere. The polymeric $MoO_2:H_2(1/4)$ web compound was observed to exhibit superparamagnetism. The vibrating sample magnetosusceptometer recording showed an S-shaped curve (Figure 7). It is exception that the induced magnetism peaks at 2-3 kOe and declines with higher applied field.

Figure 7. Vibrating sample magnetometer recording of the hydrino reaction product comprising $MoO_2:H_2(1/4)$ formed by the detonation of Mo wire in an atmosphere comprising water vapor in air.
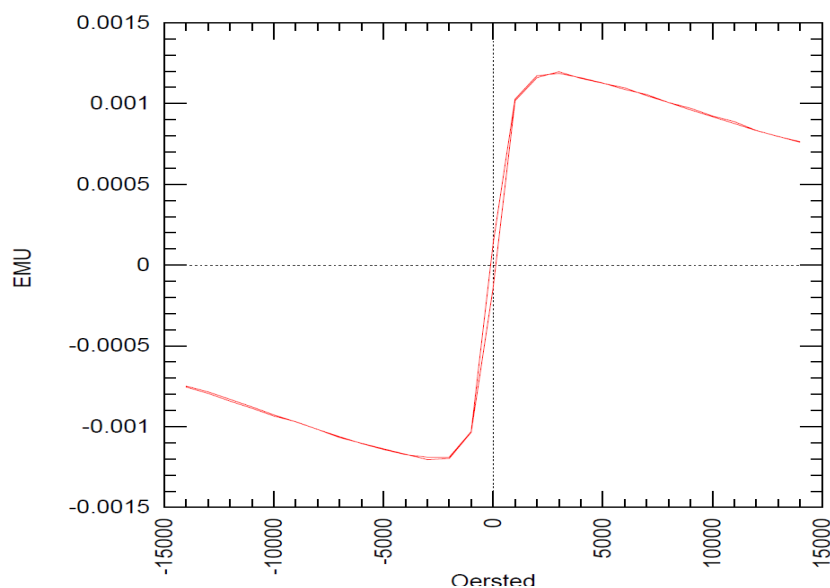
4 Rotational Energies Due to the Spin Magnetic Moment of $H_2(1/4)$

Molecular hydrino $H_2(1/p)$ possesses no electric dipole moment, but it does possess an unpaired electron that effects selection rules for rotational transitions. The forbidden selection rule barrier to observing infrared spectra may be circumvented by application of an external magnetic field. Raman selection rules are also altered from those of a symmetrical diatomic molecule due to the unpaired electron wherein the electron and consequently the rotational selection rules may be influenced by the application of an external magnetic field. Due to the potential magnetic field effect, both the infrared and Raman spectra may be influenced by recording each spectrum on a compound or material with intrinsic magnetization such as one being ferromagnetic or paramagnetic. An example of the former is molecular hydrino bonded or absorbed on the surface of a nickel or iron foil. An example of the latter is a paramagnetic compound that cages the

molecular hydrino such as FeOOH, Fe_2O_3, or a compound that may be diamagnetic but possess paramagnetic ions in proximity to $H_2(1/p)$ such as KCl crystals with trapped $H_2(1/p)$ molecules close to paramagnetic impurity ions. Another potential strong agent to particularly enhance the Raman spectrum is a conductive surface that amplifies the laser field locally for absorbed $H_2(1/p)$ molecules.

The presence of molecular hydrino in strong matrix magnetic field may result in the alignment of the free electron angular moment of $\dfrac{\hbar}{2}$ along the magnetic field vector direction in either the z-axis or the y-axis direction of the coordinates of $H_2(1/p)$ shown in Figure 11.4 of Mills [1]. The external alignment may enhance the permitted excitation of a concerted transition of a rotational molecular hydrino transition coupling to the spin-orbital splitting and fluxon linkage sub-splitting of the free electron energy levels. The spin flip energy given by Eqs. (6-7) with an exemplary intrinsic field of 1 T is

$$\Delta E^{spin}_{mag\ 2.0046} = g_{H_2(1/p)}\mu_B B = 2.0046386\mu_B B = 1.85910\ X\ 10^{-23} J\ (0.93588\ cm^{-1}) \tag{21}$$

To conserve the photon's angular momentum of $\hbar$, rotational excitation requires $\hbar$ of angular momentum along the axis of molecular rotation, a semiminor axis being either the z-axis or y-axis. The $\hbar$ of angular momentum gives rise to a corresponding magnet moment of a Bohr magneton along this rotational angular momentum axis. Typically, the unpaired electron of $H_2(1/p)$ gives rise to a Bohr magneton of magnetic moment along the internuclear axis when a magnetic field is applied. However, the molecular rotation of the hydrino molecule about one of the semiminor axes causes the excitation of the semimajor-axis Bohr magneton of magnetic moment to be forbidden. The rotational transition energy may be split by the spin-orbital energy given by Eq. (8), except that the orbital component of spin-orbital splitting is not diamagnetically induced such that $\chi_m = 1$ and the spin-orbital energy $E_{S/O,rot}$ due to rotational excitation is:

$$E_{S/O,rot} = m\left[\frac{1}{\left(4\sqrt{2}\right)^{-3}}\alpha^5\left(2\pi\right)^2 m_e c^2 \sqrt{\frac{3}{4}}\right] \tag{22}$$

$$= m1.04853 X\ 10^{-20}\ J\ \ (m6.54434 X\ 10^{-2}\,eV,\ m527.83\ cm^{-1})$$

wherein $m = 0.5, 1, 2, 3, ...$. The spin-orbital splitting energies due to rotation are given in Table 5.

The energies of the concerted excitation of the rotational and spin-orbital coupling transitions are sub-split by the energy corresponding to flux linkage in units of the magnetic flux quantum $\dfrac{h}{2e}$. The free electron angular momentum of $\dfrac{\hbar}{2}$ and the rotational angular momentum of $\hbar$ add when the corresponding vectors are aligned along a common z-axis to give a resultant

angular momentum of $L = \dfrac{3}{2}\hbar$. The energy contribution of the flux linkage of a fluxon by molecular hydrino is given by Eq. (18) with $\chi_{m\Phi} = 1$ since the orbital component of spin-orbital coupling is not diamagnetically induced. In the case of $L = \dfrac{3}{2}\hbar$, the $H_2(1/4)$ fluxon linkage energies $E_{\Phi,rot,concerted}$ for fluxon sub-splitting quantum numbers $m_{\Phi3/2} = 0.5,1,2,3...$ due to spin-orbital coupling to a molecular rotational transition are

$$E_{\Phi,rot,concerted} = m_{\Phi3/2} 4 \left(\frac{\alpha}{2\pi} + \frac{2}{3}\alpha^2 \left(\frac{\alpha}{2\pi} \right) - \frac{4}{3} \left(\frac{\alpha}{2\pi} \right)^2 \right) \frac{3}{2} \mu_B B$$

$$= m_{\Phi3/2} \frac{3}{2} \left(j0.0046386 \frac{\mu_0 \mu_B}{r^3} \left(\frac{e\hbar}{2m_e} \right) \right) \tag{23}$$

$$= m_{\Phi3/2} j46.24 \ cm^{-1}$$

wherein j is an integer corresponding to the number of fluxons linked having fluxon linkage quantum number $m_{\Phi3/2}$ and the semiminor radius of the $H_2(1/4)$ MO is given by Mills Eq. (11.205) [1] with $p = 4$ ($r = \dfrac{a_0}{4\sqrt{2}}$). As in the case with spin flip transitions observable by EPR spectroscopy, the fluxon sub-splitting quantum number is determined by the number of angular momentum components active during the transition. Due to the nature of the rotation transition wherein the rotational quantum number J may be arbitrarily large, the upper range of the fluxon sub-splitting quantum number is not bounded.

Alternatively, the spin component of $\dfrac{\hbar}{2}$ may align perpendicular to the rotational angular momentum of $\hbar$ to give a resultant z-axis angular momentum of $L = \hbar$ wherein the spin component averages to zero since it rotates about the z-axis due to molecular rotation. In the case of $L = \hbar$, the $H_2(1/4)$ fluxon linkage energies $E_{\Phi,rot}$ for fluxon sub-splitting quantum numbers $m_\Phi = 0.5,1,2,3,...$ due to spin-orbital coupling to a molecular rotational transition are

$$E_{\Phi,rot} = m_\Phi \left(j0.0046386 \frac{\mu_B^2 \mu_0}{r^3} \right)$$

$$= m_\Phi j30.83 \ cm^{-1} \tag{24}$$

wherein j is an integer corresponding to the number of fluxons linked having fluxon linkage quantum number m_Φ and the semiminor radius of the $H_2(1/4)$ MO is given by Mills Eq. (11.205) [1] with $p = 4$ ($r = \dfrac{a_0}{4\sqrt{2}}$). The fluxon linkage energies $E_{\Phi,rot}$ due to spin-orbital coupling to molecular rotation transition are given in Table 5.

The absorption of fluxons increases the magnetic energy of $H_2(1/p)$. Using Eq. (14), the Josephson coupling energies due to fluxon linkage during concerted rotational-spin rotational and spin-orbital transitions are given by Eq. (23), and the magnetic energies $U_{S/OMag,concerted}$ arising from the absorption of the integer number of fluxons j having fluxon linkage quantum number $m_{\Phi3/2} = 2$ are given by

$$U_{S/OMag,concerted} = \frac{1}{2}U_0\left(\frac{2\pi(\Delta\Phi)}{\Phi_0}\right)^2$$

$$= 46.24 \ cm^{-1}(0.5)\left(\frac{j(2)46.24 \ cm^{-1}}{1950 \ cm^{-1}}\right)^2 \qquad (25)$$

$$= 0.0520\,j^2 \ cm^{-1}$$

wherein $U_0 = 46.24 \ cm^{-1}; \Delta\Phi = E_{\Phi,rot,concerted} = (2)46.24 \ cm^{-1}$ (Eq. (23)), and the energy between rotational transitions corresponds to the term Φ_0 (Eq. (32, $p = 4$)). The fluxon peak spacing increases as the energy of the concerted rotation-fluxon absorption transition increases and decreases in the case of emission.

Using Eq. (14), the magnetic energies $U_{S/OMag}$ arising from the absorption of the integer number of fluxons j having fluxon linkage quantum number $m_\Phi = 2$ during concerted rotational and spin-orbital transitions are given by

$$U_{S/OMag} = \frac{1}{2}U_0\left(\frac{2\pi(\Delta\Phi)}{\Phi_0}\right)^2$$

$$= 30.83 \ cm^{-1}(0.5)\left(\frac{j(2)30.83 \ cm^{-1}}{1950 \ cm^{-1}}\right)^2 \qquad (26)$$

$$= 0.0154\,j^2 \ cm^{-1}$$

wherein $U_0 = 30.83 \ cm^{-1}; \Delta\Phi = E_{\Phi,rot} = (2)30.83 \ cm^{-1}$ (Eq. (24)), and the energy between rotational transitions corresponds to the term Φ_0 (Eq. (32, $p = 4$)). The fluxon peak spacing increases as the energy of the concerted rotation-fluxon absorption transition increases and decreases in the case of emission.

27

Table 5. The electron spin-orbital coupling splitting energies and fluxon sub-splitting energies of molecular rotational transitions for spin-orbital coupling quantum numbers $m = 0.5, 1, 2, 3, ..., 10$ and for electron fluxon quantum numbers $m_\Phi = 1, 2, 3, ..., 10$ and $m_{\Phi 3/2} = 1, 2, 3, ..., 10$.

m	Spin-Orbital Splitting Energy (cm^{-1})	m_Φ	Fluxon Sub-Splitting Energy (cm^{-1})	$m_{\Phi 3/2}$	Fluxon Sub-Splitting Energy (cm^{-1})
0.5	264	0.5	15.4	0.5	23.1
1	528	1	30.8	1	46.2
2	1056	2	61.7	2	92.5
3	1583	3	92.5	3	138.7
4	2111	4	123.3	4	185.0
5	2639	5	154.1	5	231.2
6	3167	6	185.0	6	277.5
7	3695	7	215.8	7	323.7
8	4223	8	246.6	8	370.0
9	4750	9	277.5	9	416.2
10	5278	10	308.3	10	462.4

The observation of spin-orbital transitions by Raman spectroscopy may be greatly enhanced by the deposition or absorption of molecular hydrinos on a metal surface to enhance the Raman spectrum. Surface enhanced Raman (SER) is very sensitive because of the surface plasmon waves set up by the stimulating wavelength. The surface plasmon field may extend about 40-60 nm below the surface, providing some depth sensitivity in the material.

The moment of inertia may be measured using rotational energy spectroscopy such as Raman spectroscopy, and using the known nuclear masses, the moment of inertia gives the nuclear separation which is characteristic of and identifies molecular hydrino of a given p quantum state. Specifically, for a diatomic molecule having atoms of masses m_1 and m_2, the moment of inertia is (Mills Eq. (12.66)) [1]:

$$I = \mu r^2 \tag{27}$$

where μ is the reduced mass given by (Mills Eq. (12.67)) [1]:

$$\mu = \frac{m_1 m_2}{m_1 + m_2} \tag{28}$$

and where r is the distance between the centers of the atoms, the internuclear distance. The rotational energy levels follow from Mills Eq. (1.71) [1] and are given by (Mills Eq. (12.68)) [1]:

$$E_{rotational} = \frac{\hbar^2}{2I} J(J+1) \tag{29}$$

where J is an integer. The pure rotational energies of hydrogen type molecules for transition

from the J to the quantized J' rotational state are given by (Mills Eq. (12.77)) [1]:

$$\Delta E_{J \to J'} = E_{J'} - E_J$$

$$= \frac{p^2 \hbar^2}{2 \left(0.5 m_p \left(7.411 X 10^{-11} m \right)^2 \right)} \left(J'(J'+1) - J(J+1) \right) \qquad (30)$$

$$= \frac{\left(J'(J'+1) - J(J+1) \right)}{2} p^2 121.89 \ cm^{-1}$$

wherein m_P is the mass of the proton, the moment of inertia $I = 0.5 m_p \left(\dfrac{7.411 X 10^{-11} m}{p} \right)^2$, and the

integer-squared dependence is due to the reciprocal integer dependence of the internuclear distance given by (Mills Eq. (12.76)) [1]:

$$2c' = \frac{0.7411}{p} \ \mathring{A} \qquad (31)$$

For example, the predicted rotational energy of $H_2(1/4)$ is four squared or 16 times that of H_2 due to the internuclear distance being one fourth that of H_2 (Eq. (31)). At ambient laboratory temperature, molecules overwhelmingly populate the rotational state $J = 0$. Then, Eq. (30) becomes

$$\Delta E_{J=0 \to J'} = \frac{J'(J'+1)}{2} p^2 121.89 \ cm^{-1} \qquad (32)$$

Molecular hydrino $H_2(1/p)$ is a diatomic molecule comprising two protons and two electrons, except that it is unique from molecular hydrogen in that it has an unpaired electron having an intrinsic angular momentum of $\dfrac{\hbar}{2}$. This electron spin angular momentum may align along the same axis as the rotational angular of $\hbar$ or transverse to it. Consider that the rotational energy $E_{rotational}$ of $H_2(1/p)$ about z-axis which is the common axis of the intrinsic electron angular momentum of $\dfrac{\hbar}{2}$ and rotational angular momentum of $\hbar$. The rotational energy due to the concerted double excitation of rotation due to spin and diatomic rotation is given by the sum of the diatomic molecular rotational energy given by Eq. (30) and the spin rotational energy also given by Eq. (30) with the exception that the rotational quantum number J can only change by ± 1:

$$E_{rotational+spin} = \frac{\hbar^2}{2I} \left(J'(J'+1) - J(J+1) \right) + \frac{\hbar^2}{I} (J+1)$$

$$= \left(\frac{J'^2 + J' - J^2 + J + 2}{2} \right) p^2 121.89 \ cm^{-1} \qquad (33)$$

In the case that the initial rotational state is $J = 0$, Eq. (33) becomes

$$E_{rotational+spin} = \frac{\hbar^2}{2I}\left(J'(J'+1) - J(J+1)\right) + \frac{\hbar^2}{I}(J+1)$$

$$= \left(\frac{J'^2 + J' + 2}{2}\right) p^2 121.89 \ cm^{-1} \tag{34}$$

Consider that the diatomic molecular rotation is about the z-axis such that the corresponding rotational angular momentum of $\hbar$ is aligned along the z-axis. In the case that the axis of the intrinsic electron spin angular momentum of $\frac{\hbar}{2}$ is along the orthogonal semiminor axis, the y-axis, the rotation energy $E_{rotational}$ of $H_2(1/p)$ is given by Eq. (32).

The radiation of a multipole of order (ℓ, m_ℓ) carries $m\hbar$ units of the z component of angular momentum per photon of energy $\hbar\omega$. Thus, the z component of the angular momentum of the corresponding excited rotational state is (Mills Eq. (12.69)) [1]:

$$L_z = m\hbar \tag{35}$$

Thus, the selection rule for dipole and quadrupole rotational transitions are (Mills Eq. (12.70)) [1]:

$$\Delta J = \pm 1 \tag{36}$$

and

$$\Delta J = \pm 2 \tag{37}$$

Not only are the lowest energy Raman transitions for pure rotational transitions (Eq.(32)) and for concerted rotational-spin transition (Eq. (34)) allowed by each of the selection rules given by Eqs. (36) and (37) but coupling of allowed dipole and quadrupole transitions permit excitation of higher rotational energy levels. Isotopic substitution and ortho-para state occupancy also determines the section rules of Raman transitions. Exemplary transitions are given in Table 6.

Due to the equivalence of the two semiminor axes, a double rotational excitation comprising the superposition of the independent rotations about each may occur. The energy of the double excitation of these two rotational modes is the sum of the individual pure and concerted rotational transitions. Using Eqs. (32) and (34), the energies $E_{double \ rotation}$ of the combined rotational excitations are

$$E_{double \ rotational} = \left(\frac{J'^2_c + J'^2_c + 2}{2}\right) + \frac{J'_p\left(J'_p + 1\right)}{2} p^2 121.89 \ cm^{-1} \tag{38}$$

Exemplary transitions are given in Table 6.

Table 6. $H_2(1/4)$ Raman energies for (i) pure $J=0$ to $J'=1,2,3,...$ rotational transitions, (ii) concerted $J=0$ to $J'=0,1,2,3,...$ molecular rotational transition involving a spin rotation transition having the spin rotational state quantum number change from $J=0$ to $J=1$, and double transition having energies given by the sum of the independent transitions.

J'	Pure Rotational Transition (cm⁻¹)	Concerted Molecular Rotational-Spin Rotation Transition (cm⁻¹)	J'_p / J'_c	Double Rotational Transition (cm⁻¹)
0	0	1950	1/0	3900
1	1950	3900	2/0	7801
2	5851	7801	2/1	9751
3	11701	13652	3/0	13652
4	19502	21453	3/1	15602
5	29254	31204	3/2	19502
6	40955	42905	4/0	21453
7	54607	56557	4/1	23403
8	70209	72159	4/2	27303
9	87761	89711	4/3	33154
10	107263	109213	5/0	31204

The Raman excitation of the pure $H_2(1/4)$ molecular rotation is allowed for a $\Delta J = 2$ rotational transition (Eq. (37)) wherein the spin angular momentum vector is aligned along the y-axis perpendicular to the rotational axis along the $H_2(1/4)$ z-axis. The transition energy is given by Eq. (32). Another allowed transition is the coupled excitation of both the rotational transition and an intrinsic spin transition wherein the rotational and intrinsic spin angular momentum are aligned on the common z-axis. The coupled or concerted transition energy is given by the sum of the $\Delta J = 2$ rotational and the $J=0$ to $J=1$ spin rotational components given by Eq. (34). In addition, the excitation of the spin and rotational transitions results in spin-orbital splitting and fluxon linkage sub-splitting energy shifts of the summation energy given by Eqs. (22-24). These transitions were observed by Raman spectroscopy.

Raman samples of $H_2(1/4)$ absorbed on metallic surfaces and in metallic and ionic lattices by magnetic dipole and van der Waals forces were produced by (i) high voltage electrical detonation or Fe wires in an atmosphere comprising water vapor, (ii) low voltage, high current electrical detonation of hydrated silver shots, (iii) ball milling or heating FeOOH and hydrated alkali halide-hydroxide mixtures, and (iv) maintaining a plasma reaction of H and HOH in a so-called SunCell® comprising a molten gallium injector that electrically shorts two plasma electrodes with the molten gallium to maintain an arc current plasma state. Excess power of over 300 kW was measured by water and molten metal bath calorimetry [79]. Raman spectra were recorded on

these materials using the Horiba Jobin Yvon LabRAM Aramis Raman spectrometer with (i) a 785 nm laser and (ii) a HeCd 325 nm laser in microscope mode with a magnification of 40X.

Figures 8A-B. Schematics of a SunCell® hydrino power generator comprising a single electromagnetic pump injector and electrode in an injector reservoir electrode, a vertically aligned counter electrode, and a glow discharge cell connected through a top flange of the SunCell® to form HOH catalyst and atomic H. A. Exterior view. B. Cross sectional view. 1. Electromagnetic pump assembly. 2. Molten gallium reservoir. 3. Ignition injector electrode. 4. Ignition counter electrode. 5. Reaction cell chamber. 6. Vacuum line. 7. Glow discharge cell. 8. Glow discharge chamber. 9. Discharge cell flange and top plate. 10. Discharge cell high voltage feedthrough. 11. Discharge electrode. 12. Discharge gas inlet. 13. Discharge gas outlet. 14. Auxiliary gas inlet line. 15. Ignition counter electrode water cooling inlet line. 16. Ignition counter electrode water cooling outlet line.
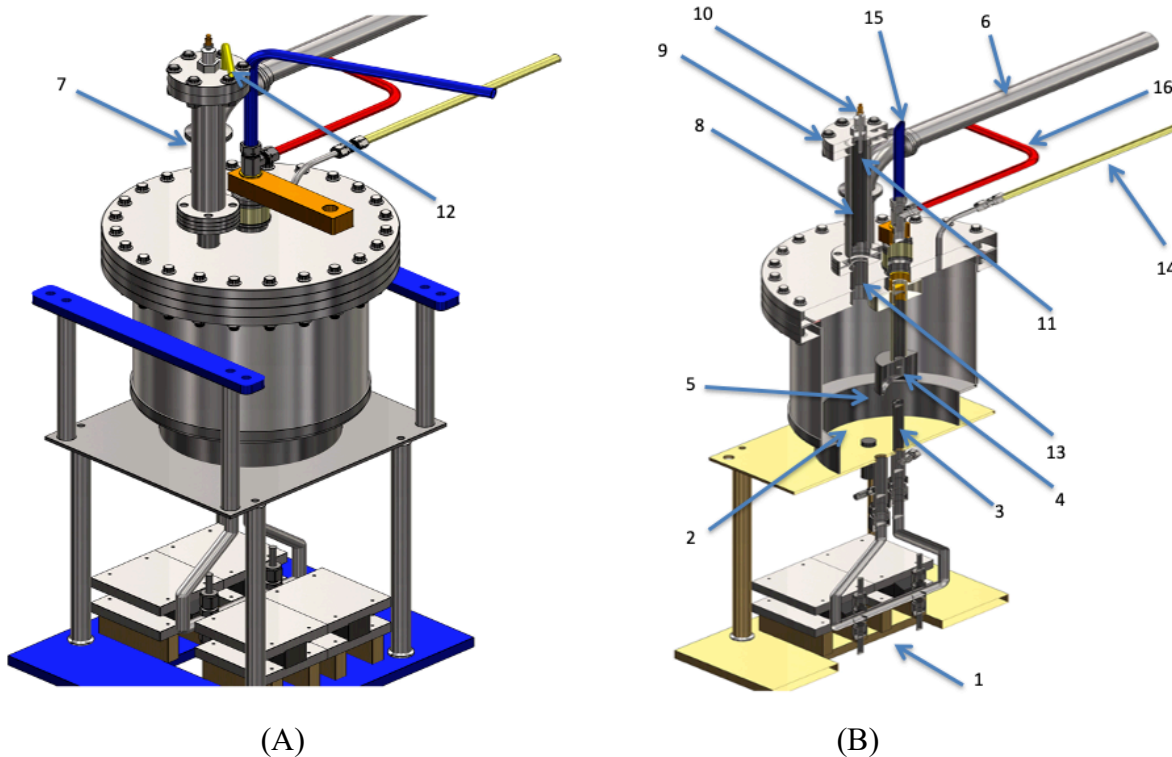
(A)   (B)

Nickel foil Raman samples were prepared by flowing a hydrino reaction mixture comprising 2000 standard cubic centimeters per minute (sccm) H_2 and 1 sccm O_2 into a one-liter reaction volume SunCell® shown in Figure 8. The SunCell® comprised an 8-inch diameter 4130 Cr-Mo steel cell with a Mo liner along the reaction cell chamber wall. The SunCell® further

comprised molten gallium in a reservoir, an electromagnet pump that served as an electrode and pumped the gallium vertically against a W counter electrode, a low-voltage-high-current ignition power source that maintained a hydrino reaction plasma by maintaining a high current between the electrodes, and a glow discharge hydrogen dissociator and recombiner connected directly to the top flange of the SunCell® reaction cell chamber by a 0.75-inch OD set of Conflat flanges. The glow discharge voltage was 260 V. The glow discharge current was 2 A. The operating pressure was 5.9 Torr. The gallium temperature was maintained at 400°C with water bath cooling. Arc plasma was maintained by an ignition current of 1300A at a voltage of 26-27 V. The electromagnetic pump rate was 100 g/s, and the output power was over 300 kW for an input ignition power of 29 kW corresponding to a gain of 10 times. The Ni foils (1 X 1 X 0.1 cm) to make the Raman samples were placed in the molten gallium. The hydrino reaction was run for 10 minutes, and the cloth-wipe-cleaned surfaces of the foils were analyzed by Raman spectroscopy using a Horiba Jobin Yvon LabRAM Aramis Raman spectrometer with (i) a 785 nm laser with a 300 line/mm grating and (ii) a 325 nm laser, and a Horiba Jobin-Yvon Si CCD detector (Model number DU420A-OE-324) and a 300 or 600 line/mm grating.

The Raman spectrum (2500 cm^{-1} to 11,000 cm^{-1}) obtained using a Horiba Jobin Yvon LabRam ARAMIS spectrometer with a 11 mW, 785 nm laser on a Ni foil prepared by immersion in the molten gallium of a SunCell® that maintained a hydrino plasma reaction for 10 minutes is shown in Figures 9A-C. The emission energies $E_{Emission}$ of all the novel lines matched the double transition for final rotational quantum numbers (Eq. (38)) $J_p^{'} = 3$ and $J_c^{'} = 0,1,2$ with spin-orbital coupling (Eq. (22)) and fluxon coupling (Eqs. (23-24)). The energies are given by the sum of the independent transitions:

$$E_{Emission} = \Delta E_{J=0 \to J_p^{'}=3} + \Delta E_{J=0 \to J_c^{'}=0,1,2} + E_{S/O,rot} + E_{\Phi,rot}$$
$$= 13,652\left(15,602\right)\left(19,502\right) \ cm^{-1} + m528 \ cm^{-1} + m_{\Phi}31 \ cm^{-1} + m_{\Phi3/2}46 \ cm^{-1} \quad (41)$$

wherein two-photon absorption plus the laser heating energy is capable of exciting rotational emission of greater energy than the 785 nm laser energy for which the Si CCD has a high detection sensitivity. In addition, the laser multi-order lines given by Eq. (42), are observed in 2nd, 3rd, 4th, 5th, and 6th order at energies $E_{Raman,order \ m}$ of 6371, 8495, 9557, 10,193, 10,618 cm^{-1}, respectively (Figures 9A-C) wherein all the 785 nm laser multi-order lines have a photon energy of 12,742 cm^{-1} (1.58 eV).

$$E_{Raman,order \ m} = 12,742\left(1 - \frac{1}{m}\right)cm^{-1}; \quad m = 2,3,4,5,6,... \quad (42)$$

No lines were observed from a control comprising Ni-gallium alloy Ni$_3$Ga that was formed as a byproduct from the Raman sample nickel foils suspended on the gallium surface during the

SunCell® run (Figure 9D). The novel lines shown in Figures 9A-C were eliminated by a Semrock long-pass edge filter (BLP01-785R-25) having an edge wavelength of 805 nm and $T_{avg} > 93\%$ 812.1 – 1200 nm placed between the sample and the detector confirming the assignment to high energy emission rather than low energy Raman transitions. Only the 4th order laser line was observed at 3133 nm in the filtered emission spectrum shown in Figure 9E.

Figures 9A-D. Raman spectra obtained using a Horiba Jobin Yvon LabRam ARAMIS spectrometer with a 11mW, 785 nm laser on a Ni foil prepared by immersion in the molten gallium of a SunCell® that maintained a hydrino plasma reaction for 10 minutes and control Ni_3Ga byproduct. A. Ni foil 2500 cm^{-1} to 11,000 cm^{-1} region. B. Ni foil 8500 cm^{-1} to 11,000 cm^{-1} region. C. Ni foil 6000 cm^{-1} to 11,000 cm^{-1} region. D. Ni_3Ga byproduct 2500 cm^{-1} to 11,000 cm^{-1} region. E. Ni foil 0 nm to 6000 nm emission region with Semrock long-pass edge filter. All the novel Ni foil emission lines in Figures 9A-C matched those given by Eq. (41).
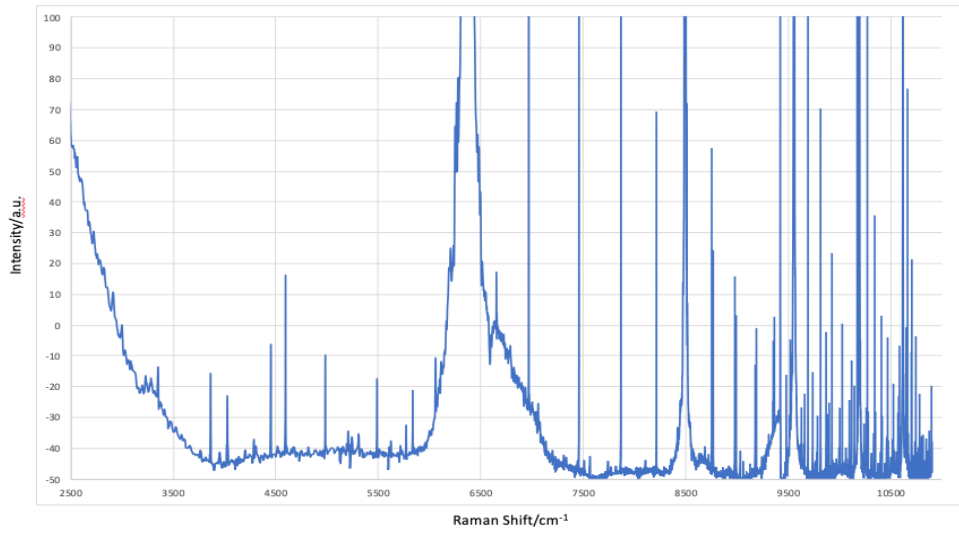
(A)
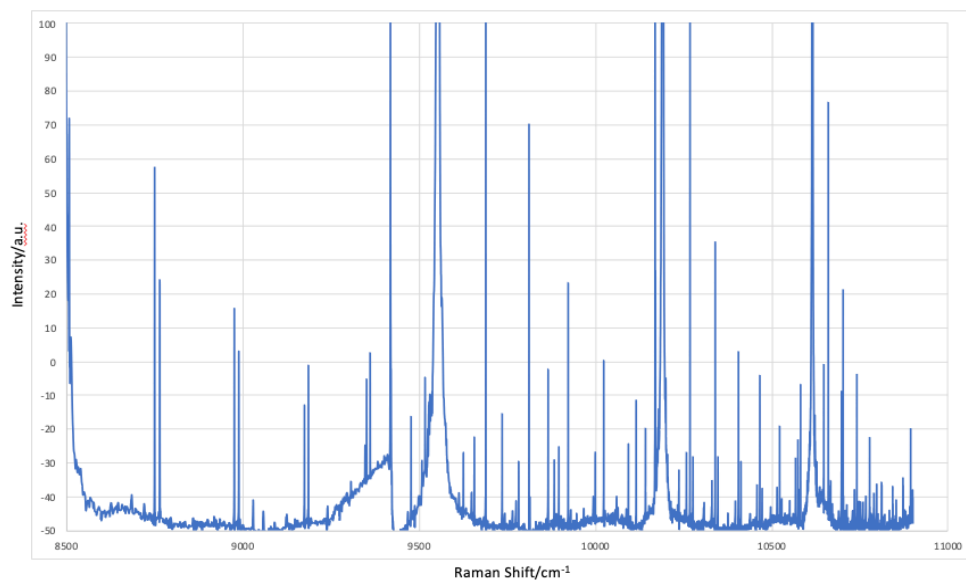
(B)
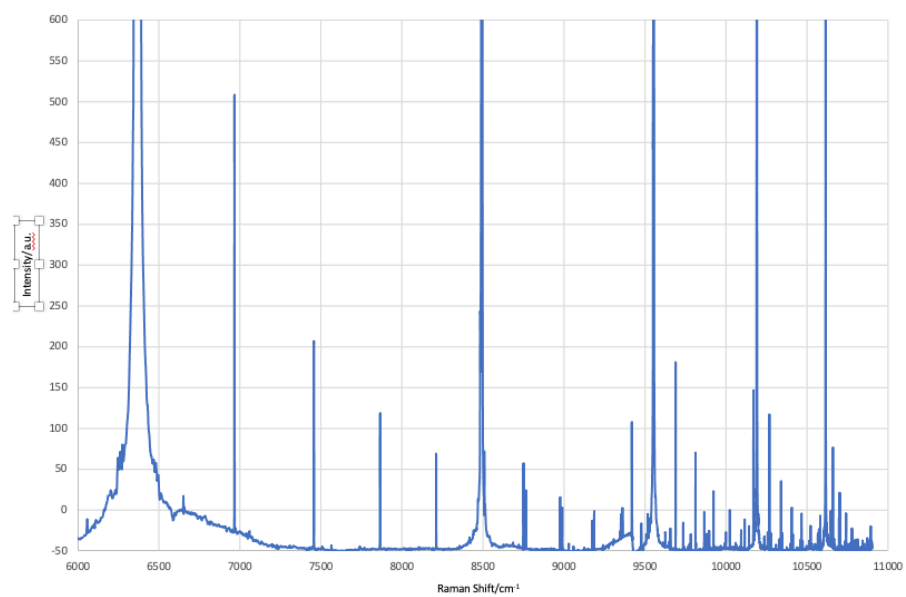
(C)
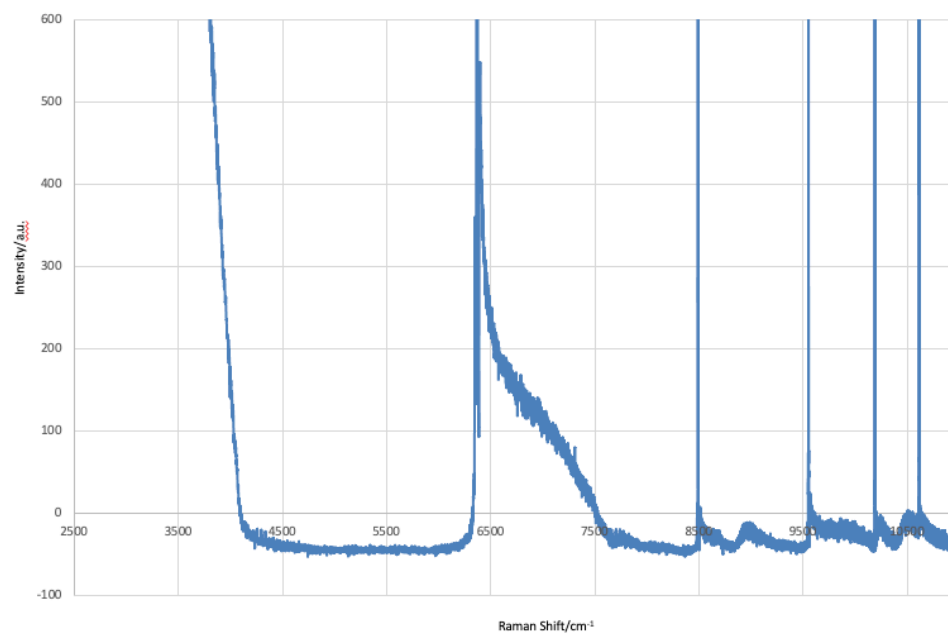
(D)
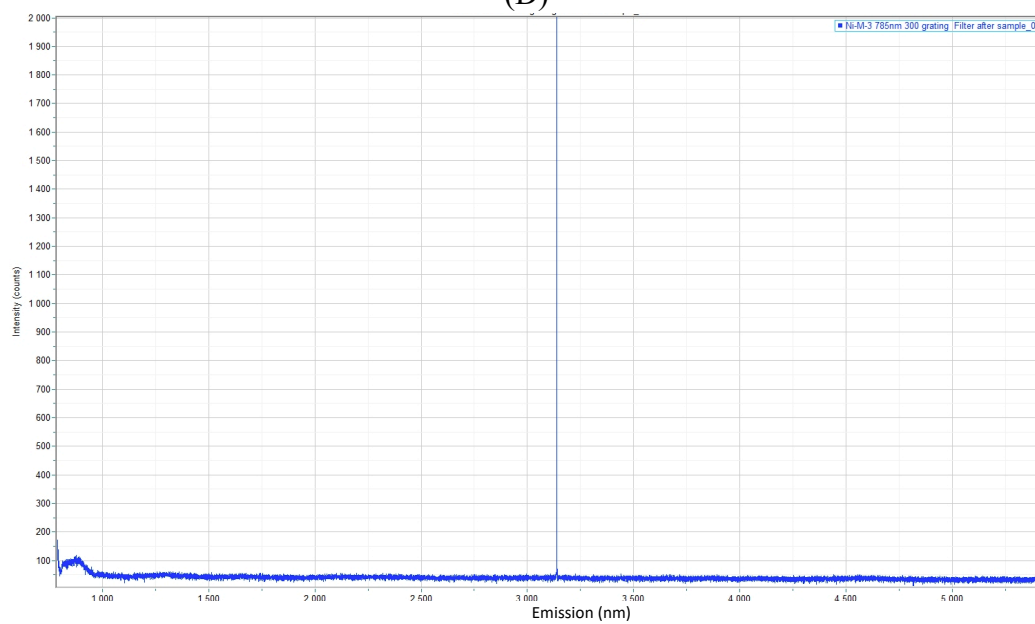
(E)

Table 7A. $H_2(1/4)$ Raman lines and the corresponding multi-order emission lines for the 785 nm Raman spectrum (2500-11,000 cm^{-1}) of a Ni foil exposed to the hydrino reaction (Figures 9A-C). The parent (1st order) emission line of each observed Raman line is the wavenumber of the farthest right-handed column wherein the order of the observed line is given in the corresponding column header. Next, the list of parent lines and the parent lines sorted by energy are given.

| Observed Lines (cm^{-1})	Emission Line (cm^{-1})	2°	3°	4°	5°	6°	7°	Parent Line (cm^{-1})	Sorted Lines (cm^{-1})
3354	9388	18776						18776	12181
3862	8880	17760						17760	12756
4027	8715	17430						17430	12784
4452	8290	16580						16580	12924
4594	8148	16296						16296	12936
4983	7759	15518						15518	13135
5487	7255	14510						14510	13288
5770	6972	13944						13944	13320
5835	6907	13814						13812	13365
6059	6683	13366						13365	13524
6280	6462	12924						12924	13584
6350	6392	12784						12784	13590
6652	6090	12180						12181	13593
6965	5777	11554	17331					17331	13656
7457	5285	10570	15855					15855	13755
7865	4877	9754	14631					14631	13812
8211	4531	9062	13593					13593	13944
8490	4252	8504	12756					12756	14007
8750	3992	7984	11976	15968				15968	14095
8765	3977	7954	11931	15908				15908	14224
8976	3766	7532	11298	15064				15064	14268
8989	3753	7506	11259	15012				15012	14280
9175	3567	7134	10701	14268				14268	14418
9186	3556	7112	10668	14224				14224	14510
9346	3396	6792	10188	13584				13584	14574
9361	3381	6762	10143	13524				13524	14631
9420	3322	6644	9966	13288				13288	14650

9689	3053	6106	9159	12212	15265			15265	14844
9812	2930	5860	8790	11720	14650			14650	15012
9923	2819	5638	8457	11276	14095			14095	15064
10024	2718	5436	8154	10872	13590			13590	15265
10115	2627	5254	7881	10508	13135			13135	15324
10188	2554	5108	7662	10216	12770	15324		15324	15518
10268	2474	4948	7422	9896	12370	14844		14844	15855
10339	2403	4806	7209	9612	12015	14418		14418	15908
10466	2276	4552	6828	9104	11380	13656		13656	15968
10522	2220	4440	6660	8880	11100	13320		13320	16296
10660	2082	4164	6246	8328	10410	12492	14574	14574	16580
10702	2040	4080	6120	8160	10200	12240	14280	14280	17331
10741	2001	4002	6003	8004	10005	12006	14007	14007	17430
10777	1965	3930	5895	7860	9825	11790	13755	13755	17760
10894	1848	3696	5544	7392	9240	11088	12936	12936	18776

Table 7B. $H_2(1/4)$ Raman lines and corresponding hydrino assignments for the 785 nm Raman spectrum (2500-11,000 cm^{-1}) of a Ni foil exposed to the hydrino reaction (Figures 9A-C). The theoretical rotational energy assignments (Eq. 41) are according to the energies given in Table 6. The quantum numbers corresponding to spin-orbital splitting and fluxon sub-splitting of the assigned parent (1st order) emission peaks are m and m_Φ, and $m_{\Phi 3/2}$ respectively, having energies given in Table 5. Delta is the difference between the observed and theoretical lines.

Parent Emission Lines (cm-1)	Rotational Energy (cm-1)	m	m_Φ	$m_{\Phi 3/2}$	Theoretical (cm-1)	Delta (cm-1)	Observed Raman Lines (Å)	DIB (Å)
12181	13652	-3		2.5	12184	-3	8210	
12756	13652	-2	2	2	12750	6	7839	7832.89
12784	13652	-2	1.5	3	12781	3	7822	7822.8
12924	13652	-1.5	0.5	1	12922	2	7738	
12936	13652	-1.5	1	1	12937	-1	7730	
13135	13652	-1	0.5		13139	-4	7613	
13288	13652	-0.5	-0.5	-2	13280	8	7526	7520.6
13320	13652	-0.5		-1.5	13318	2	7508	
13365	13652	-0.5		-0.5	13365	1	7482	7482.91
13524	13652			-3	13513	11	7394	
13584	13652			-1.5	13582	2	7362	7367.13
13590	13652		-2		13590	0	7358	

|								
13593	13652		-2		13590	3	7357	7357.56
13656	13652				13652	4	7323	
13755	13652		1	1.5	13752	3	7270	
13812	13652	0.5	-1	-1.5	13815	-3	7240	
13944	13652	0.5	1		13946	-2	7172	
14007	13652	0.5		2	14008	-1	7139	
14095	13652	1	-2	-0.5	14095	0	7095	7092.67
14224	13652	1		1	14226	-2	7030	7030.29
14268	13652	1		2	14272	-4	7009	
14280	13652	1		2	14272	8	7003	
14418	13652	1.5		-0.5	14420	-2	6936	6944.72
14510	13652	1.5	2		14505	5	6892	
14574	13652	1.5		3	14582	-8	6862	6852.53
14631	13652	2	-2.5		14630	1	6835	6837.71
14650	13652	2	-2		14646	4	6826	6825.8
14844	13652	2		3	14846	-2	6737	6737.28
15012	15602	-1	-2		15012	0	6661	6660.71
15064	15602	-1	-0.5		15059	5	6638	6635.74
15265	15602	-0.5	-2.5		15261	4	6551	6553.92
15324	15602	-0.5	-0.5		15323	1	6526	6523.28
15518	15602		-1	-1	15525	-7	6444	6445.28
15855	15602	0.5	-0.5		15850	5	6307	6308.8
15908	15602	0.5		1	15912	-4	6286	6287.59
15968	15602	0.5	0.5	2	15974	-6	6263	6259.85
16296	15602	1.5		-2	16301	-5	6136	6136.08
16580	15602	2	-1	-1	16581	-1	6031	6030.49
17331	15602	3		3	17324	7	5770	5772.61
17430	15602	3.5	-0.5		17434	-4	5737	5735.89
17760	19502	-3.5	3.5		17763	-3	5631	5634.98
18776	19502	-1.5	2		18772	4	5326	

Twenty-six of the observed emission lines match those of unassignable astronomical lines associated with the interstellar medium called diffuse interstellar bands (DIBs). The assignment of all the 380 DIBs listed by Hobbs [27] to $H_2(1/4)$ rotational transitions with spin-orbital splitting and fluxon sub-splitting are given in the Appendix.

The Raman peaks assigned to $H_2(1/4)$ rotational transitions in Table 7B were also observed on hydrated silver shots that were detonated with a current of about 35,000 A [2] as well as SunCell® gallium and Cr, Fe, and stainless-steel foils immersed in the gallium wherein the Raman spectra were run post a SunCell® hydrino plasma reaction as in the case of the Ni foils. The Ni foils showed the greatest peak intensities. The peaks recorded on carbon witness plates

were very weak to absent. Raman spectra on pure gallium samples as a function of depth showed that the Raman peaks decreased in intensity with depth and were only found in trace on the negatively polarized W electrode which confirmed previous observations that the hydrino reaction occurs in the plasma at the surface and proximal space above the positive electrode, the positively polarized molten gallium in this case. This is consistent with the rate-increasing mechanism of recombining ions and electrons to decrease the space charge caused by the energy transfer to the catalyst and its consequent ionization.

$H_2(1/4)$ was also observed as a product of the SunCell® hydrino reaction by collection and purification of a hydrino product from the molten gallium of the SunCell® following a hydrino reaction. Specifically, a 10-minute-duration hydrino reaction plasma run was maintained in the SunCell®, and a white polymeric compound (GaOOH:H$_2$(1/4)) was formed by dissolving Ga$_2$O$_3$ and gallium-stainless steel metal alloy (~0.1-5%) collected from the SunCell® gallium post run in aqueous 4M KOH, allowing fibers to grow, and float to the surface where they were collected by filtration. The Raman spectrum (2200 cm^{-1} to 11,000 cm^{-1}) shown in Figure 10 was obtained using a Horiba Jobin Yvon LabRam ARAMIS spectrometer with a 785 nm laser on the GaOOH:H$_2$(1/4). All the novel lines matched those of shown in Figures 9A-C with assignment given by Eq. (41) and reported in Table 7B, except that a second set of peaks was additionally observed, shifted 150 cm^{-1} relative to the set observed on Ni foil (Figures 9A-C). This is likely due to the presence of two phases of GaOOH:H$_2$(1/4) that was confirmed by XRD and TEM and was the source of two distinct spectra in the EPR as discussed in the Parameters and Magnetic Energies Due to the Spin Magnetic Moment of H$_2$(1/4) section.

Figure 10. Raman spectrum (2200 cm^{-1} to 11,000 cm^{-1}) obtained using a Horiba Jobin Yvon LabRam ARAMIS spectrometer with a 785 nm laser on GaOOH:H$_2$(1/4) showing H$_2$(1/4) rotational transitions with spin-orbital coupling and fluxon linkage shifts.
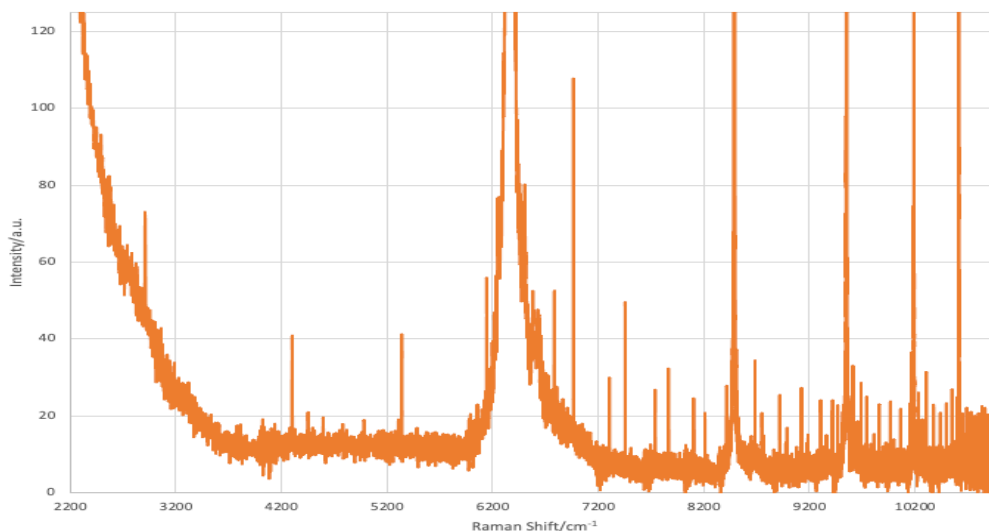

Hydrinos were identified by characteristic extreme ultraviolet (EUV) continuum radiation due to the H to H(1/4) transition that was observed at an average power of 4.6 MW and having a predicted 10.1 nm cutoff. Specifically, HOH catalyst was further shown to give continuum EUV radiation by igniting hydrated silver shots comprising a source of H and HOH catalyst by passing a low voltage, high current through the shot to produce explosive plasma that emitted brilliant light predominantly in the short-wavelength 10 to 300 nm region. The power and energy of the light released from the shot ignition event were determined using absolute spectroscopy over the 22.8-647 nm region using a grazing incidence EUV spectrometer (GIS), normal incidence EUV spectrometer (NIS), and an ultraviolet-visible (UV-Vis) spectrometer wherein the UV-Vis spectrometer was absolutely calibrated using a NIST traceable tungsten lamp and a NIST traceable deuterium lamp. The intensity calibration was extended to the EUV wavelengths by spectral overlap with calibrated regions and the spectral responses of the spectrometers.

A typical 80 mg, 10 microliter silver shot was subjected to a short burst of low voltage, high current electrical energy. The applied 60 Hz AC voltage was less than 15 V peak, and the peak current was about 30,000–35,000 A. The high current caused the shot to explosively ignite as brilliant light-emitting expanding plasma that produced a strong shockwave in air detonations. Based on Stark broadening, the initially optically thick essentially 100% ionized plasma expanded in vacuum and thinned to emit EUV and UV light. The peak power of 20 MW and time-average power of 4.6 MW was measured using absolute spectroscopy over the 22.8-647 nm region (Figure 11A) wherein the optical emission energy was 250 times the applied energy. Synchronized high-

41

speed video and spectroscopic recording of the plasma emission and the measurement of the applied ignition power over time showed that plasma persisted even after the ignition power decayed to zero.

The wavelength calibrated and absolute intensity calibrated spectrum (10-45 nm) of the emission of hydrated silver shots recorded on the GIS with a Zr filter showed the EUV continuum cutoff at 10.1 nm that matches dark matter emission as shown in Figure 11B [2]. The calorimetrically measured power of a typical 80 mg, 10 microliter silver shot ignition released by the nascent HOH catalyzed transition of H to hydrino state $H_2(1/4)$ in a Parr 1341 water bath bomb calorimeter cell was 400,000 W. The optical power and calorimetrically measured thermal power were independently validated [79].

Figures 11A-B. Absolute spectra in the 5 nm to 450 nm region of the ignition of a 80 mg shot of silver comprising absorbed H_2 and H_2O from gas treatment of silver melt before dripping into a water reservoir showing an average NIST calibrated optical power of 1.3 MW, essentially all in the ultraviolet and extreme ultraviolet spectral region. A. 0-700 nm region. B. 0-45 nm region.
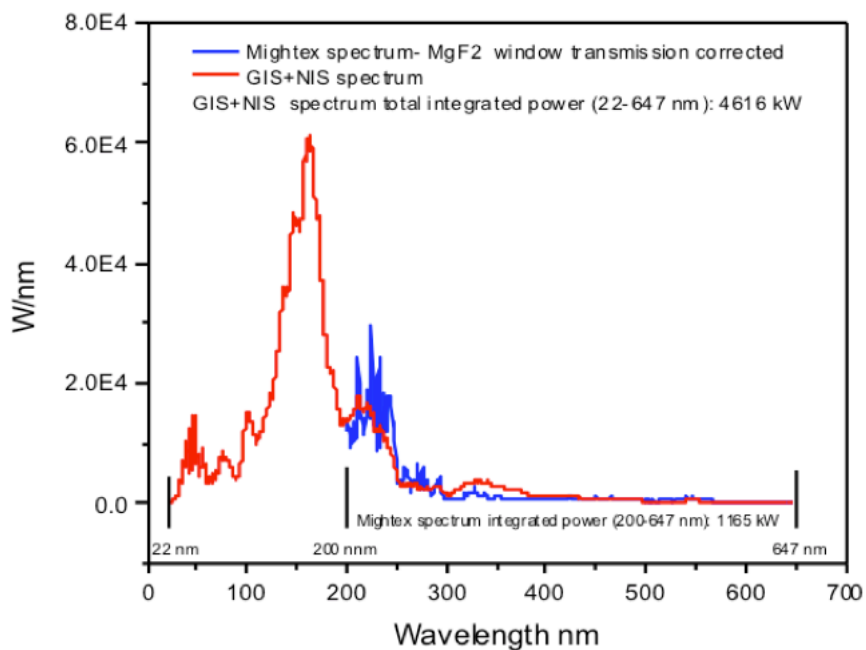

(A)
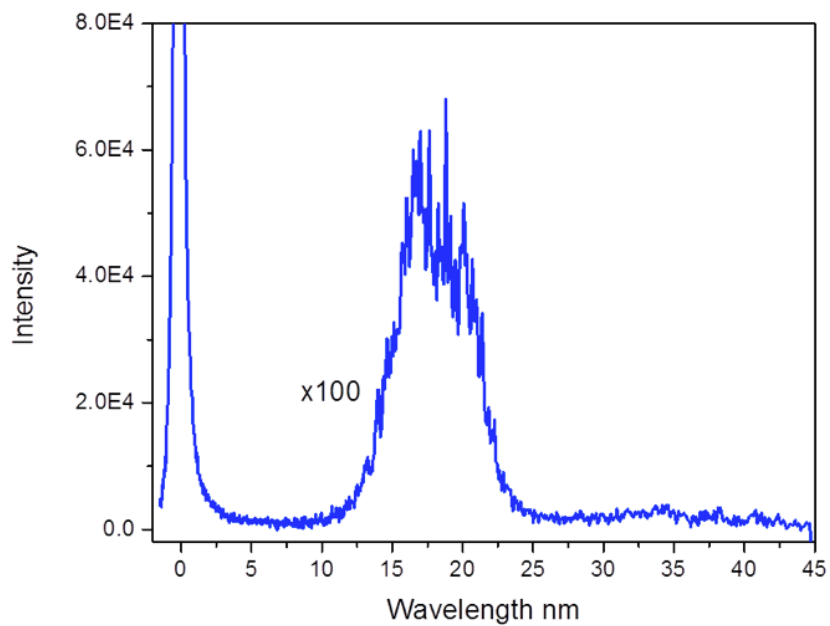
(B)

Using a Horiba Jobin Yvon LabRam ARAMIS with a 785 nm laser, the Raman spectrum was recorded on copper electrodes post ignition of an 80 mg silver shot comprising 1 mole% H_2O wherein the detonation was achieved by applying a 12 V 35,000 A current with a spot welder. A peak optical power of extreme ultraviolet emission was 20 MW [2]. The Raman spectrum (2200 cm^{-1} to 11,000 cm^{-1}) is shown in Figure 12. The silver shot Raman peaks also matched the peaks given in Table 7B.

Figure 12. Raman spectrum (2500 cm^{-1} to 11,000 cm^{-1}) obtained using a Horiba Jobin Yvon LabRam ARAMIS spectrometer with a 785 nm laser on a silver shot electrode post detonation showing $H_2(1/4)$ rotational transitions with spin-orbital coupling and fluxon linkage shifts.
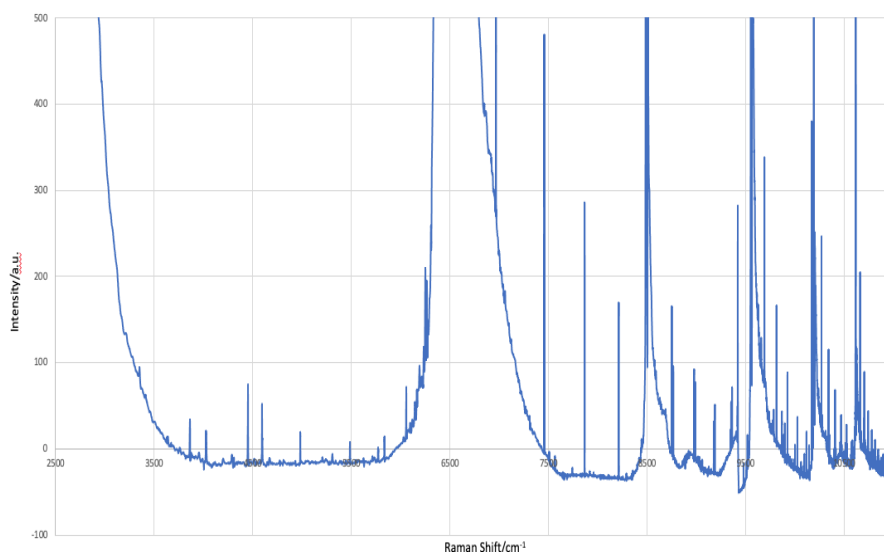
The $H_2(1/4)$ rotational Raman spectral assignments were confirmed by deuterium isotopic substitution. The $HD(1/4)$ rotational energies given by Eqs. (27-34) are shown in Table 8 wherein the reduced mass of $HD(1/4)$ of $\frac{2}{3}m_P$ was used.

Table 8. HD(1/4) Raman energies for (i) pure $J=0$ to $J'=1,2,3,...$ rotational transitions, (ii) concerted $J=0$ to $J'=0,1,2,3,...$ molecular rotational transition involving a spin rotation transition having the spin rotational state quantum number change from $J=0$ to $J=1$, and double transition having energies given by the sum of the independent transitions.

| J'	Pure Rotational Transition (cm⁻¹)	Concerted Molecular Rotational-Spin Rotation Transition (cm⁻¹)	J'_p/J'_c	Double Rotational Transition (cm⁻¹)
0	0	1463	1/0	2925
1	1463	2925	2/0	5851
2	4388	5851	2/1	7313
3	8776	10239	3/0	10239
4	14627	16089	3/1	11701
5	21940	23403	3/2	14627
6	30716	32179	4/0	16089
7	40955	42418	4/1	17552
8	52656	54119	4/2	20478
9	65821	67283	4/3	24866
10	80447	81910	5/0	23403

HD(1/4) product of the SunCell® was formed by propagating a hydrino reaction in the SunCell® with 250 μl of D$_2$O injected into the reaction cell chamber every 30 seconds replacing the H$_2$ and O$_2$ gas mixture as the source of atomic hydrogen and HOH catalyst. A 10-minute-duration hydrino reaction plasma run was maintained in the SunCell®, and a white polymeric compound (GaOOH:HD(1/4)) was formed by dissolving Ga$_2$O$_3$ and gallium-stainless steel metal alloy (~0.1-5%) collected from the SunCell® gallium post run in aqueous 4M KOH, allowing fibers to grow, and float to the surface where they were collected by filtration.

The Raman spectrum (2500 cm⁻¹ to 11,000 cm⁻¹) was obtained using a Horiba Jobin Yvon LabRam ARAMIS spectrometer with a 785 nm laser GaOOH:HD(1/4) (Figures 13A-C). The Raman peaks clearly shifted with deuterium substitution as evident by comparison of the spectrum of pure hydrogen molecular hydrino (Figures 9A-C) and the spectrum of the deuterated molecular hydrino shown in Figures 13A-C. In the latter case, the emission energies $E_{Emission}$ of all the novel lines matched the double transition for final rotational quantum numbers (Table 8) $J'_p=2(3)$ and $J'_c=1(0,1,2)$ with spin-orbital coupling (Eq. (22)) and fluxon coupling (Eqs. (23-24)). The energies are given by the sum of the independent transitions:

$$E_{Emission} = \Delta E_{J=0 \to J'_p=2(3)} + \Delta E_{J=0 \to J'_c=1(0,1,2)} + E_{S/O,rot} + E_{\Phi,rot}$$

$$= 7313(10,239)(11,701)(14,627) \ cm^{-1} + m528 \ cm^{-1} + m_\Phi 31 \ cm^{-1} + m_{\Phi 3/2} 46 \ cm^{-1}$$

(43)

wherein two-photon absorption plus the laser heating energy is capable of exciting rotational emission of greater energy than the 785 nm laser energy for which the Si CCD has a high detection sensitivity. The position and assignment of novel lines assigned to $HD(1/4)$ transitions are given in Tables 9A-B. The comparison of the $H_2(1/4)$ peaks of Table 7B and HD(1/4) peaks are also shown in Table 9B.

Figures 13A-C. Raman spectra obtained using a Horiba Jobin Yvon LabRam ARAMIS spectrometer with a 785 nm laser on GaOOH:HD(1/4). A. 2500 cm^{-1} to 11,000 cm^{-1} region. B. 6000 cm^{-1} to 11,000 cm^{-1} region. C. 8000 cm^{-1} to 11,000 cm^{-1} region. All the novel emission lines matched those of given by Eq. (43).
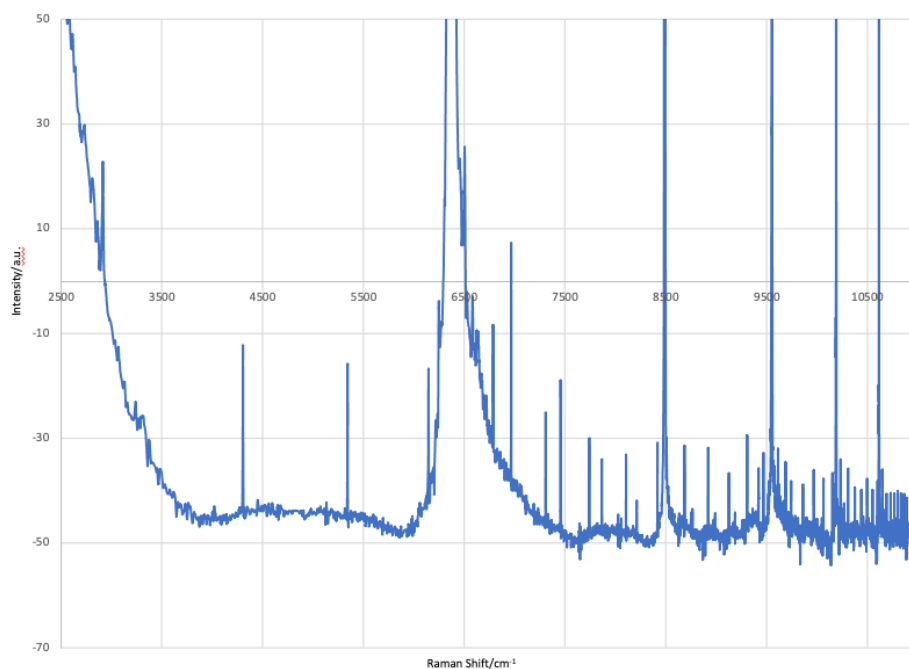
(A)
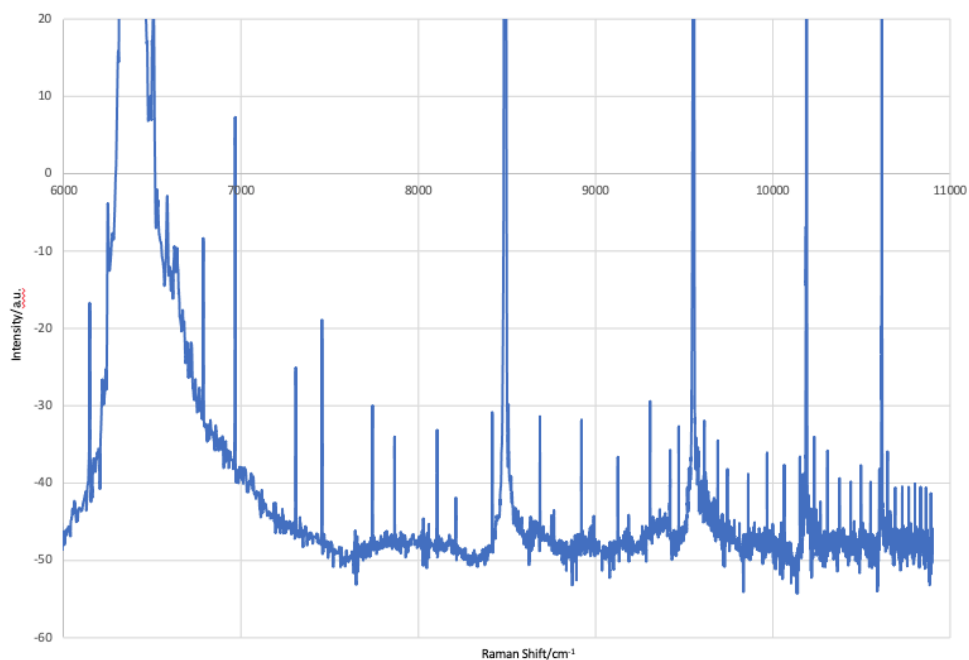
(B)

(C)

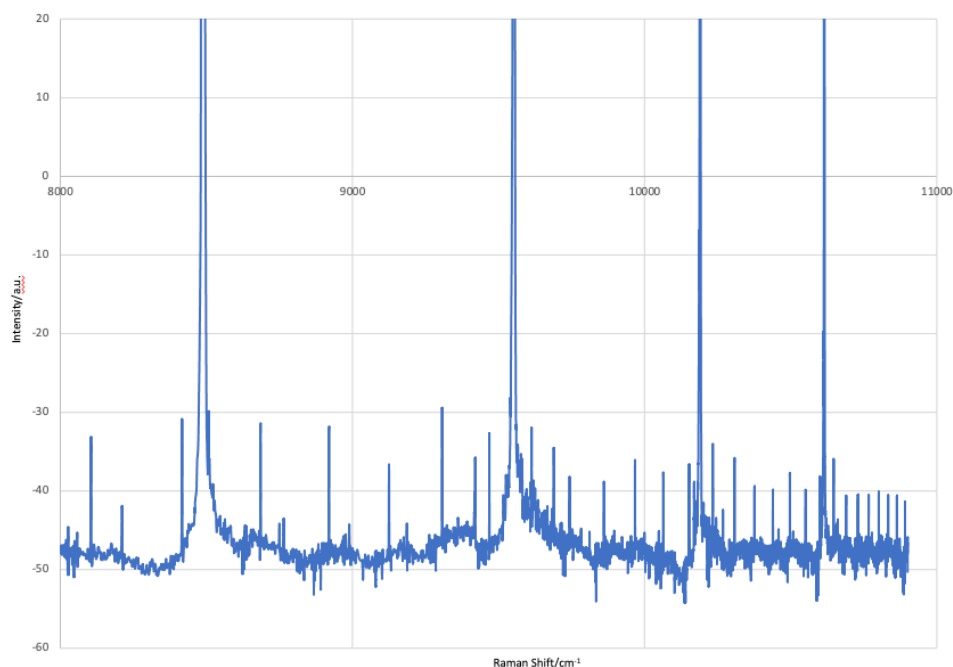Table 9A. HD(1/4) Raman lines and the corresponding multi-order emission lines for the 785 nm Raman spectrum (2500-11,000 cm^{-1}) of GaOOH:HD(1/4) (Figures 13A-C). The parent (1st order) emission line of each observed Raman line is the wavenumber of the farthest right-handed column wherein the order of the observed line is given in the corresponding column header. Next, the list of parent lines and the parent lines sorted by energy are given.

Observed Lines (cm^{-1})	Emission Line (cm^{-1})	2°	3°	4°	5°	6°	Parent Line (cm^{-1})	Sorted Lines (cm^{-1})
2919	9823						9823	7397
4306	8436						8436	8436
5345	7397						7397	9058
6148	6594	13188					13188	9274
6285	6457	12914					12914	9754
6419	6323	12646					12646	9823
6503	6239	12478					12478	9966
6586	6156	12312					12312	10002
6640	6102	12204					12204	10260
6786	5956	11912					11912	10308
6967	5775	11550					11550	10360
7308	5434	10868					10868	10475
7457	5285	10570					10570	10570
7741	5001	10002					10002	10660
7865	4877	9754					9754	10668

8105	4637	9274					9274	10712
8213	4529	9058					9058	10848
8473	4269	8538	12807				12807	10868
8685	4057	8114	12171				12171	10955
8920	3822	7644	11466				11466	11100
9126	3616	7232	10848				10848	11106
9186	3556	7112	10668				10668	11225
9306	3436	6872	10308				10308	11274
9420	3322	6644	9966				9966	11454
9468	3274	6548	9822	13096			13096	11466
9614	3128	6256	9384	12512			12512	11515
9689	3053	6106	9159	12212			12212	11524
9743	2999	5998	8997	11996			11996	11550
9861	2881	5762	8643	11524			11524	11646
9967	2775	5550	8325	11100			11100	11830
10064	2678	5356	8034	10712			10712	11850
10152	2590	5180	7770	10360			10360	11912
10233	2509	5018	7527	10036	12545		12545	11996
10268	2474	4948	7422	9896	12370		12370	12072
10308	2434	4868	7302	9736	12170		12170	12170
10376	2366	4732	7098	9464	11830		11830	12171
10439	2303	4606	6909	9212	11515		11515	12204
10497	2245	4490	6735	8980	11225		11225	12212
10551	2191	4382	6573	8764	10955		10955	12312
10610	2132	4264	6396	8528	10660		10660	12370
10647	2095	4190	6285	8380	10475		10475	12478
10690	2052	4104	6156	8208	10260		10260	12512
10730	2012	4024	6036	8048	10060	12072	12072	12545
10767	1975	3950	5925	7900	9875	11850	11850	12646
10801	1941	3882	5823	7764	9705	11646	11646	12807
10833	1909	3818	5727	7636	9545	11454	11454	12914
10863	1879	3758	5637	7516	9395	11274	11274	13096
10891	1851	3702	5553	7404	9255	11106	11106	13188

Table 9B. HD(1/4) Raman lines and corresponding hydrino assignments for the 785 nm Raman spectrum (2500-11,000 cm⁻¹) of GaOOH:HD(1/4) (Figures 13A-C). The theoretical rotational energy assignments (Eq. (43) are according to the energies given in Table 8. The quantum numbers corresponding to spin-orbital splitting and fluxon sub-splitting of the assigned parent (1st order) emission peaks are m and m_Φ, and $m_{\Phi3/2}$ respectively, having energies given in Table 5. Delta is the difference between the observed and theoretical lines.

HD(1/4)Parent Emission Lines (cm⁻¹)	Rotational Energy (cm⁻¹)	m	m_Φ	$m_{\Phi3/2}$	Theoretical (cm⁻¹)	Delta (cm⁻¹)
7397	7313			2	7405	-8
8436	7313	2	2		8430	6
9058	10239	-2	-1	-2	9060	-2
9274	10239	-2		2	9276	-2
9754	10239	-1		1	9757	-3
9823	10239	-1	0.5	2	9819	4
9966	10239	-0.5			9975	-9
10002	10239	-0.5	1		10006	-4
10260	10239			0.5	10262	-2
10308	10239		2		10301	7
10360	10239		1	2	10362	-2
10475	10239	0.5	-1		10472	3
10570	10239	0.5	2		10565	5
10660	10239	1	-2	-1	10659	1
10668	10239	1		-2	10674	-6
10712	10239	1	-0.5	-1	10705	7
10848	10239	1	1	1	10844	4
10868	10239	1	1	1.5	10867	1
10955	10239	1.5		-1.5	10961	-6
11100	11701	-1		-1.5	11104	-4
11106	11701	-1		-1.5	11104	2
11225	11701	-1	1	0.5	11228	-3
11274	11701	-1		2	11266	8
11454	11701	-0.5	0.5		11453	1
11466	11701	-0.5		0.5	11461	5
11515	11701	-0.5	1	1	11515	0
11524	11701	-0.5		2	11530	-6
11550	11701	-0.5	2	1	11545	5
11646	11701		-1	-0.5	11647	-1
11830	11701		1	2	11825	5
11850	11701	0.5	-1	-2	11842	8
11912	11701	0.5	-1	-0.5	11911	1
11996	11701	0.5	1		11996	0

12072	11701	0.5	2	1	12073	-1
12170	11701	1	-0.5	-1	12168	2
12171	11701	1	-0.5	-1	12168	3
12204	11701	1		-0.5	12206	-2
12212	11701	1	-0.5		12214	-2
12312	11701	1	1	1	12306	6
12370	11701	1		3	12368	2
12478	11701	1.5	-0.5		12478	0
12512	11701	1.5	0.5		12509	3
12545	11701	1.5		1	12539	6
12646	11701	2	-0.5	-2	12649	-3
12807	11701	2	1.5		12803	4
12914	11701	2	2	2	12911	3
13096	11701	2.5	1	1	13098	-2
13188	14627	-3		3	13182	6

Infrared spectroscopic rotational transitions are forbidden for symmetrical diatomic molecules with no electric dipole moment. However, since molecular hydrino uniquely possesses an unpaired electron, the application of a magnetic field to align the magnetic dipole of molecular hydrino is a means to break the selection rules to permit a novel transition in $H_2(1/4)$, in addition to the effect of an intrinsic magnetic field of a sample. Concerted rotation and spin-orbital coupling is another mechanism for permitting otherwise forbidden transitions. Using the absorbance mode of a Thermo Scientific Nicolet iN10 MX spectrometer equipped with a cooled MCT detector, FTIR analysis was performed on solid-sample pellets of $GaOOH:H_2(1/4)$ with the presence and absence of an applied magnetic field using a Co-Sm magnet having a field strength of about 2000 G. The spectrum shown in Figure 14A shows that the application of the magnetic field gave rise to an FTIR peak at 4164 cm^{-1} which is a match to the concerted rotational and spin-orbital transition $J = 0$ to $J' = 1$, $m = 0.5$. Other than H_2 which is not present in the sample, there is no known assignment due to the high energy of the peak. In addition, a substantial increased intensity of a sharp peak at 1801 cm^{-1} was observed. This peak was not observed in the FTIR of control GaOOH. The peak matched the concerted rotational and spin-orbital transition $J = 0$ to $J' = 0$, $m = -0.5$, $m_{\Phi 3/2} = 2.5$. A higher sensitivity scale of the 4000-8500 cm^{-1} region (Figure 14B) shows additional peaks at (i) 4899 cm^{-1} that matched the concerted rotational and spin-orbital transition $J = 0$ to $J' = 1$, $m = 2$, $m_{\Phi 3/2} = -1$; (ii) 5318 cm^{-1} that matched the pure rotational and spin-orbital transition $J = 0$ to $J' = 2$, $m = -1$, and (iii) 6690 cm^{-1} that matched the pure rotational and spin-orbital transition $J = 0$ to $J' = 2$, $m = 1.5$, $m_{\Phi} = 1.5$.

Figure 14A. FTIR spectra (200-8200 cm^{-1}) showing the effect of the application of a magnetic field on the FTIR spectrum (200 cm^{-1} to 8000 cm^{-1}) recorded on GaOOH:H$_2$(1/4). The application of a magnetic field gave rise to an FTIR peak at 4164 cm^{-1} which is an exact match to the concerted rotational and spin-orbital transition $J = 0$ to $J' = 1$, $m = 0.5$. An intensity increase of a peak at 1801 cm^{-1} was observed that matched the concerted rotational and spin-orbital transition $J = 0$ to $J' = 0$, $m = -0.5$, $m_{\Phi 3/2} = 2.5$.
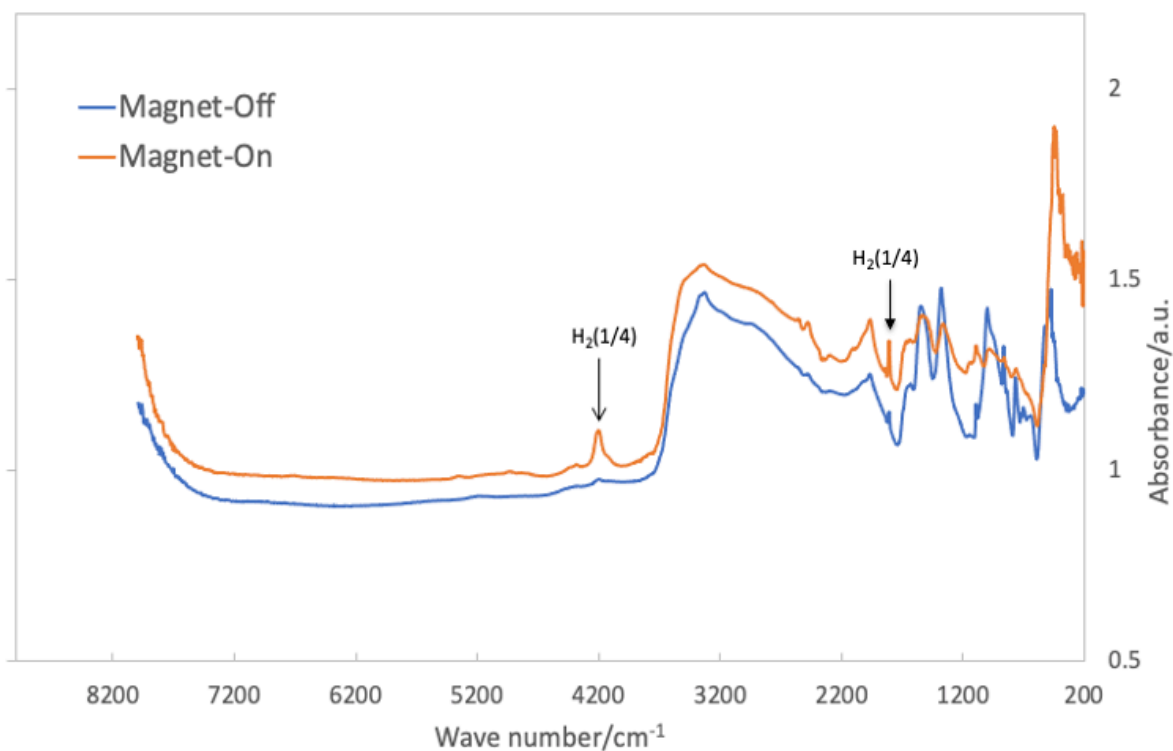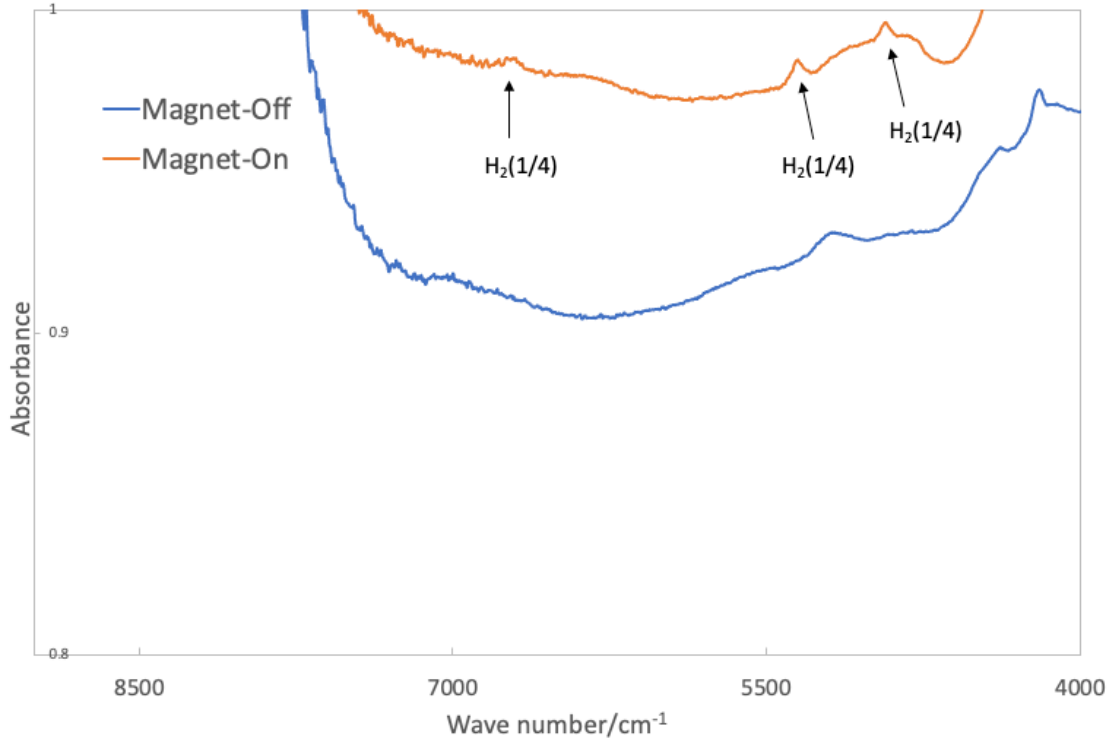
Figure 14B. FTIR spectra (4000-8500 cm^{-1}) recorded on GaOOH:H$_2$(1/4) showing addition peaks having the very high energies of 4899 cm^{-1}, 5318 cm^{-1}, and 6690 cm^{-1} matching H$_2$(1/4) rotational and spin-orbital transitions.

Given that interstitial H$_2$ in silicon and GaAs is nearly a free rotator, and H$_2$ is FTIR active as well as Raman active due to the induced dipole from interactions with the crystalline site [80], FTIR analysis was performed on KI:H$_2$(1/4), H$_2$(1/4) trapped in a KI matrix. The samples were prepared by reaction of atomic hydrogen, adventitious oxygen and H$_2$O, and K metal with high purity KI as described previously [81]. While handling the samples under an inert atmosphere, KBr pellets of KI:H$_2$(1/4) were prepared. As shown in Figure 14C major sharp peaks were observed at 1943 and 2012 cm^{-1} in the FTIR spectrum recorded using the transmittance mode using a Nicolet 730 FTIR spectrometer with DTGS detector at resolution of 0.5 cm^{-1}. Additional less intense sharp peaks observed in the FTIR spectrum are given in Table 10. No additional peaks other than those easily assignable to KI were observed. From Eq. (32), the peak at 1943 cm^{-1} (0.2409 eV) matched the theoretical prediction of 1950 cm^{-1} for the $J = 0$ to $J' = 1$ H$_2$(1/4) rotational transition wherein the unprecedented rotational energy of 4^2 times that of ordinary hydrogen establishes the internuclear distance of H$_2$(1/4) as 1/4 that of H$_2$ (Eq. (31)). The 2012 cm^{-1} peak and three peaks in the 3000 cm^{-1} region match the $J = 0$ to $J' = 1$ H$_2$(1/4) rotational transition with spin-orbital and fluxon linkage splitting, and the two peaks at 588 cm^{-1} match spin-orbital and fluxon linkage splitting of the excited $J' = 1$ H$_2$(1/4) rotational state. Additional small

satellite peaks may be due to phonon coupling, different lattice environments, and additional fluxon splittings with the anticipation that these peaks are temperature sensitive. The assignments are given in Table 10.

The selection rule for infrared absorption corresponding to a dipole transition is given by Eq. (36). The change is quantum numbers between the pure rotational transition having a peak at 1943 cm^{-1} and the one at 2012 cm^{-1} (Table 10) corresponds to a spin angular momentum change of $\frac{\hbar}{2}$ on the y-axis and a spin angular momentum change of $-\frac{\hbar}{2}$ on the z-axis with a resultant total angular momentum change of $\hbar$. The simultaneous transitions along two axes have a transition probability involving the product of the angular projections of the angular momentum vectors over two solids angles ranges for the z-axis and the y-axis. The transition probability and corresponding intensity ratio of the 2012 cm^{-1} peak relative to the 1943 cm^{-1} peak is proportional to the squared amplitude of the dot products of the vectors over the angular range given by $I \propto \int \cos^2 \theta_z \cos^2 \theta_y \, d\theta_z d\theta_y = 0.25$. Similarly, considering the quantum numbers in Table 10, the same changes in angular momentum occur with the excitation of the 588 cm^{-1} transition such that the 588 cm^{-1} peak is about 0.25 the intensity of the 1943 cm^{-1} peak. Also, the change is quantum numbers between the peak at 605 cm^{-1} and the one at 588 cm^{-1} (Table 10) corresponds to the spin angular momentum change of $\frac{\hbar}{2}$ on the y-axis and a spin angular momentum change of $-\frac{\hbar}{2}$ on the z-axis with a resultant total angular momentum change of $\hbar$ such that the 605 cm^{-1} peak is about 0.25 the intensity of the 588 cm^{-1} peak. The peaks at 3023 cm^{-1}, 3097 cm^{-1}, and 3140 cm^{-1} are very weak due to the simultaneous excitation of the rotational, spin orbital, and fluxon linkage transitions wherein the angular momentum change corresponds to a forbidden quadrupole transition (Eq. (37)). The intensities of the peaks shown in Figure 14C match theoretical predictions. $H_2(1/4)$ transitions are allowed due to dipole inducing lattice interactions which are assumed to be homogeneous and isotropic. However, the lattice interactions may change with crystal phase changes and temperature wherein the former depends on composition, temperature, quenching, and other historic and real-time ambient conditions. These effects have been reported previously in the metaborate monomer research literature [82-85].

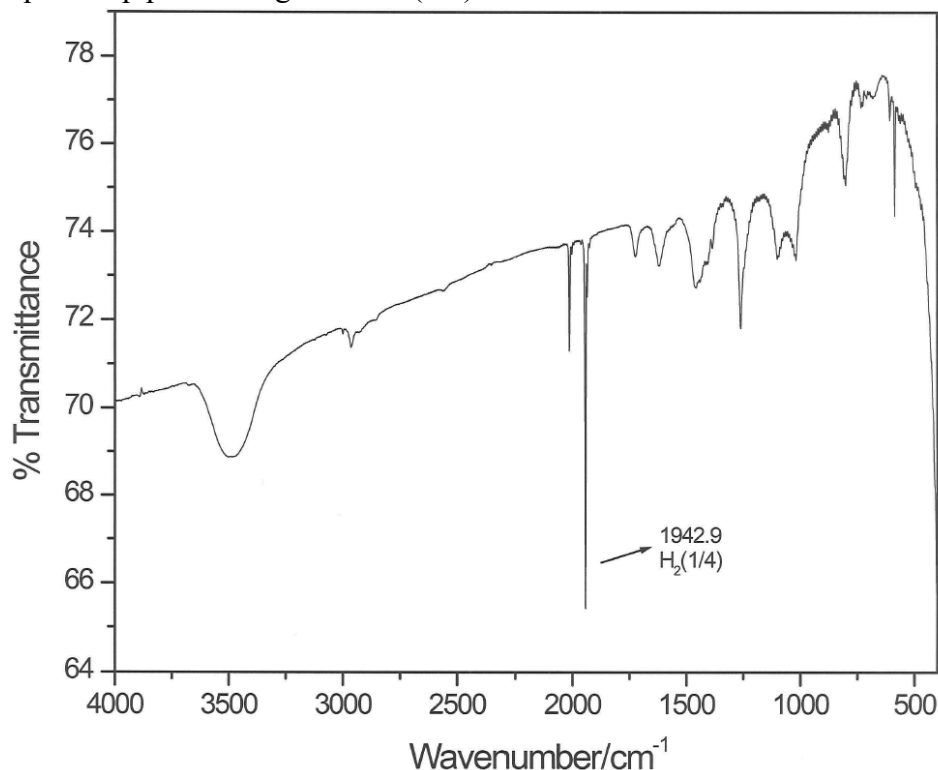Figure 14C. The high resolution (0.5 cm^{-1}) FTIR spectrum (490–4000 cm^{-1}) of KI:H$_2$(1/4) showing unique sharp peaks assigned to H$_2$(1/4).

Table 10. H$_2$(1/4) absorption lines and corresponding hydrino assignments for the FTIR spectrum (490-4000 cm^{-1}) of KI:H$_2$(1/4) (Figure 14C). The assigned theoretical rotational energy and the quantum numbers corresponding to spin-orbital splitting and fluxon sub-splitting of the FTIR peaks are m and m_Φ, and $m_{\Phi3/2}$ respectively, having energies given in Table 5. Delta is the difference between the observed and theoretical lines.

Absorption Lines (cm^{-1})	Rotational Energy (cm^{-1})	m	m_Φ	$m_{\Phi3/2}$	Theoretical (cm^{-1})	Delta (cm^{-1})
588	0	1	0.5	1	589	-1
605	0	1	1	1	605	0
1943	1950	0	0	0	1950	-7
2012	1950	0	0.5	1	2012	0
3023	1950	2	0.5	0	3021	2
3097	1950	2	0	2	3098	-1
3140	1950	2	1.5	2	3144	-4

Sharp peaks such as those shown in Figure 14C have been reported previously regarding FTIR spectra on samples prepared using reactions that dope alkali halides and solid argon with boron oxide compounds [82-85]. Prior assignment to metaborate monomer (BO_2^-) is rejected since the peak designations are based on an erroneous linear symmetrical molecular model whereas metaborate monomer has been determined to be bent [86] and the oxygen atoms in BO_2^- are not equivalent [87]. The sodium metaborate monomer spectrum [86] shows no absorption in the region of the 1950 cm^{-1} and 2012 cm^{-1} peaks, and the features are very broad as expected for an inorganic compound wherein ions bound in a crystalline lattice are not free rotors capable as in the case of some neutral small molecules such as hydrogen. Therefore, FTIR transitions involve vibrational modes that are always coupled with lattice phonons. In addition to different energies, strong symmetrical vibrational transition peaks in the region of 1943 cm^{-1} and 2012 cm^{-1} are required for the metaborate monomer assignment, and they are not observed in the FTIR spectra of Figure 14C or reported in the literature [82-86]. Also, boron was not a reactant of the KI:H$_2$(1/4) sample. KI:H$_2$(1/4) was prepared in a stainless-steel vessel which eliminated glass as a source of boron, and boron was less than 2 ppm by elemental analysis whereas typically 50 to 100 times this amount is the minimum present when so called metaborate monomer peaks are observed [85]. Aging, hydrolysis, and annealing decreased the "monomer" peaks, and reheating regenerated the peaks consistent with KI:H$_2$(1/4) [83-85]. ^{10}B isotope substitution showed variation in peak intensity ratios from those anticipated for natural abundance, but at constant isotope composition, (i) the intensity ratios were inconsistent between ^{10}B and ^{11}B isotope pairs of peaks attributed to the "monomer" including so-called "hot bands", (ii) the peak ratios varied very significantly with temperature, composition, and sample history, (iii) peak ratios were inconsistent with isotope ratios of the isotopes present in the sample, and (iv) in instances, the peak intensities did not match ones physically possible [82, 84-85]. For example, ^{10}B enriched "hot bands" and the corresponding fundamental peaks were observed to be close in intensity depending on the sample temperature and history [84].

However, the isotope substitution results are consistent with the temperature, thermal cycling, composition, storage, magnetization, and FTIR recording-condition dependence of KI:H$_2$(1/4) spin-orbital and fluxon splitting peaks. For example, the intensity ratio of the pair at 588 cm^{-1} has been observed to be temperature dependent upon cooling the sample to liquid nitrogen temperature. The same is true of other small satellite peak pairs. An explanation of the unusual sharp peaks in the so-called metaborate monomer samples is that the reactions used to prepare the "monomer" produce H$_2$(1/4) as the product. Specifically, the samples were prepared by hydrino solid fuel reactions comprising a high-temperature MX melt as matrix for the oxidation

of MBH$_4$ or dehydration of MB(OH)$_4$, or reaction of M metal and hydrated borate wherein M is an alkali metal and X is a halide ion [77, 82].

The influence of magnetic materials on the selection rules to observe molecular hydrino rotational transitions involving interaction with the free electron was further investigated. Raman samples comprising solid web-like fibers were prepared by wire detonation of an ultrahigh purity Fe wire in a rectangular cuboid Plexiglas chamber having a length of 46 cm and a width and height of 12.7 cm. A 10.2 cm long, 0.25 mm diameter Fe metal wire (99.995%, Alfa Aesar #10937-G1) was mounted between two Mo poles with Mo nuts at a distance of 9 cm from the chamber floor, a 15 kV capacitor (Westinghouse model 5PH349001AAA, 55 μF) was charged to about 4.5 kV corresponding to 557 J by a 35 kV DC power supply, and a 12 V switch with a triggered spark gap switch (Information Unlimited, model-Trigatron10, 3 kJ) was used to close the circuit from the capacitor to the metal wire inside of the chamber to detonate the wire. The detonation chamber contained air comprising 20 Torr of water vapor controlled by a humidifier and a water vapor sensor. The water vapor served as a source of HOH catalyst and atomic H to form molecular hydrino $H_2(1/4)$. The high voltage DC power supply was turned off before closing the trigger switch. The peak voltage of about 4.5 kV was discharged as a damped harmonic oscillator over about 300 μs at a peak current of 5 kA. Web-like fibers formed in about 3-10 minutes after the wire detonation. Analytical samples were collected from the chamber floor and walls, as well as on a Si wafer placed in the chamber. Raman spectra were recorded on the web material using the Horiba Jobin Yvon LabRAM Aramis Raman spectrometer with a HeCd 325 nm laser in microscope mode with a magnification of 40X or with a 785 nm laser.

The Raman spectra obtained using a Horiba Jobin Yvon LabRam ARAMIS spectrometer with a 300 mW, 785 nm laser on solid web-like fibers prepared by wire detonation of an ultrahigh purity Fe wire in air maintained with 20 Torr of water vapor are shown in Figure 15 and 16. As shown in the 3420 cm^{-1} to 4850 cm^{-1} Raman spectral region (Figure 15), a periodic series of peaks was observed. The series of peaks was confirmed to originate from the sample by treating the Fe-web:H$_2$(1/4) sample with HCl. As shown in Figure 16, all the Raman peaks were eliminated by the acid treatment of the Fe-web sample by reaction of iron oxides, iron oxyhydroxide, and iron hydroxide species of the sample to form FeCl$_3$ and H$_2$O. Similarly, KCl also showed no peaks over this spectral range further demonstrating that the periodic peaks were not due to an etalon or other artifact of the optics. It was confirmed by the manufacturer, Horiba Instruments, Inc., that the infrared CCD detector (Horiba Aramis Raman spectrometer with a Synapse CCD camera Model: 354308, S/N: MCD-1393BR-2612, 1024x256CCD Front Illuminated Open Electrode) is front illuminated which also precludes the possibility of an etalon artifact. Due to the extraordinary high energies, the transitions cannot be assigned to any prior known compound. No periodic

features were observed in the 0 cm^{-1} to 3420 cm^{-1} Raman region. The periodic features were absent in the 0 cm^{-1} to 8000 cm^{-1} Raman region of FeOOH, Al$_2$O$_3$, Ga$_2$O$_3$, and GaOOH controls.

Figure 15. Raman spectrum (3420 cm^{-1} to 4850 cm^{-1}) obtained using a Horiba Jobin Yvon LabRam ARAMIS spectrometer with a 300 mW, 785 nm laser on solid web-like fibers (Fe web) prepared by wire detonation of an ultrahigh purity Fe wire in air maintained with 20 Torr of water vapor showing a periodic series of peaks.
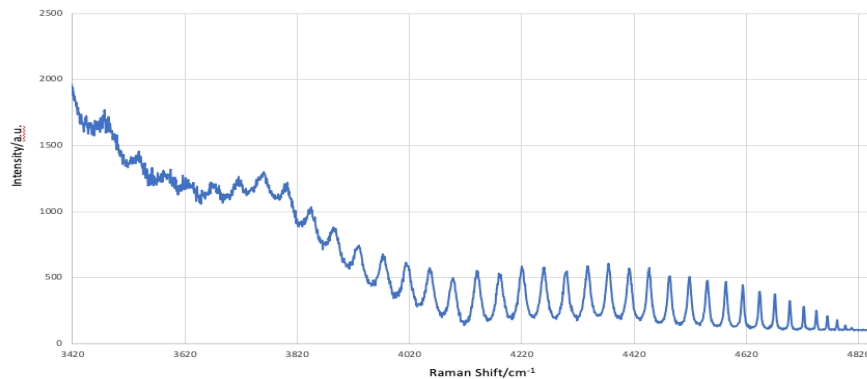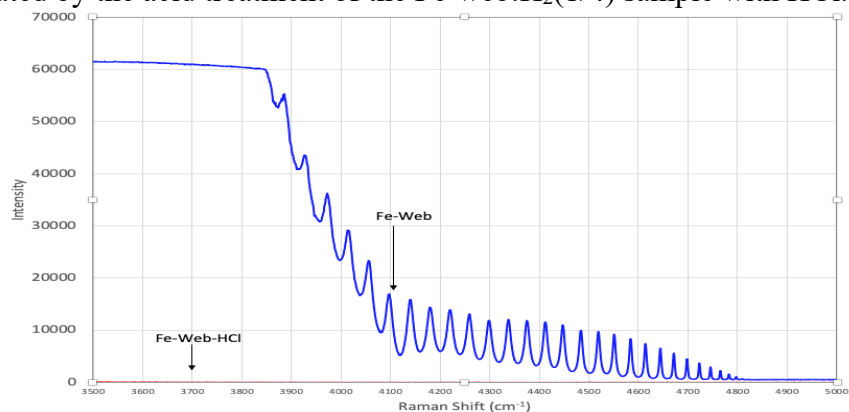

Figure 16. The Raman spectrum (3500 cm^{-1} to 5000 cm^{-1}) obtained using a Horiba Jobin Yvon LabRam ARAMIS spectrometer with a 785 nm laser showing that all the Raman peaks of Figure 15 were eliminated by the acid treatment of the Fe-web:H$_2$(1/4) sample with HCl.

The peak positions of the series of peaks shown in Figure 15 are given in Table 11 with the corresponding peak positions upon conversion from Raman to emission spectral peaks. The series matches and is assigned to the second order emission of fluxon linkages during the $H_2(1/4)$ double rotational and spin-orbital transition for final rotational, spin-orbital, and fluxon quantum numbers $J'_p = 3$ and $J'_c = 2$, $m = -1.5$, and $m_{\Phi3/2} = 2$, respectively, with energies given by Eqs. (22), (23), and (38), respectively. The fluxon separation energies $\Delta E_{\Phi, rot, concerted}$ given in Table 11

are calculated by the sum of the components $E_{\Phi,rot,concerted}$ and $E_{S/O-\Phi3/2}$ (Eqs. (23) and (25), respectively):

$$\Delta E_{\Phi,rot,concerted} = E_{\Phi,rot,concerted} - U_{S/OMag,concerted}$$
$$= (2)46.24 \ cm^{-1} - 0.0520 \, j^2 \ cm^{-1}$$

(44)

Table 11. The observed Raman energies in the 3420 cm^{-1} to 4850 cm^{-1} region shown in Figure 15. The corresponding emission energies assigned to second order emission, parents (1st order) of the second order emission energies, j quantum number of Eq. (44), and observed and theoretical energy separations of the 785 nm Raman spectral peaks demonstrate that the periodic peaks match the second order emission of fluxon linkages during the $H_2(1/4)$ double rotational and spin-orbital transition for final rotational, spin-orbital, and fluxon quantum numbers $J_p' = 3$ and $J_c' = 2$, $m = -1.5$, and $m_{\Phi3/2} = 2$, respectively.

Raman Energy (cm^{-1})	2° Emission Energy (cm^{-1})	Parent of 2° Emission Energy (cm^{-1})	j	Δ Energy Observed (cm^{-1})	Δ Energy Theoretical (cm^{-1})
3432	9307	18614	0	96	92.5
3480	9259	18518	1	94	92.4
3527	9212	18424	2	94	92.3
3574	9165	18330	3	88	92.0
3618	9121	18242	4	92	91.6
3664	9075	18150	5	92	91.2
3710	9029	18058	6	90	90.6
3755	8984	17968	7	90	89.9
3800	8939	17878	8	88	89.2
3844	8895	17790	9	84	88.3
3886	8853	17706	10	84	87.3
3928	8811	17622	11	88	86.2
3972	8767	17534	12	84	85.0
4014	8725	17450	13	84	83.7
4056	8683	17366	14	82	82.3
4097	8642	17284	15	86	80.8
4140	8599	17198	16	80	79.2
4180	8559	17118	17	82	77.5
4221	8518	17036	18	78	75.6
4260	8479	16958	19	78	73.7
4299	8440	16880	20	80	71.7
4339	8400	16800	21	74	69.5
4376	8363	16726	22	74	67.3

4413	8326	16652	23	70	65.0
4448	8291	16582	24	72	62.5
4484	8255	16510	25	72	60.0
4520	8219	16438	26	62	57.3
4551	8188	16376	27	66	54.6
4584	8155	16310	28	60	51.7
4614	8125	16250	29	60	48.7
4644	8095	16190	30	56	45.7
4672	8067	16134	31	52	42.5
4698	8041	16082	32	48	39.2
4722	8017	16034	33	46	35.9
4745	7994	15988	34	40	32.4
4765	7974	15948	35	36	28.8
4783	7956	15912	36	28	25.1
4797	7942	15884	37	24	21.3
4809	7930	15860	38		

In addition, FeOOH (99+%, Alfa Aesar#A1626730) was used as a hydrino solid fuel to form solid Raman samples. FeOOH can form HOH catalyst and atomic hydrogen upon chemical decomposition by heating and was confirmed to produce excess heat. Similar hydrino solid fuels showed analytical signatures of the predicted hydrino product $H_2(1/4)$ [77]. The 785 nm Raman run on FeOOH heated to 600°C to form Fe_2O_3:$H_2(1/4)$ is shown in Figure 17.

Figure 17. Raman spectrum (200 cm^{-1} to 11,000 cm^{-1}) obtained using a Horiba Jobin Yvon LabRam ARAMIS spectrometer with a 785 nm laser on solid fuel FeOOH powder heated to 600 °C showing a peak at 6263 cm^{-1} assigned to the $H_2(1/4)$ pure rotational transition $J = 0$ to $J' = 2$, $m = 1$, and $m_\Phi = -3$. The peak at 1062 cm^{-1} is due to silicate of the Raman slide and the other lines are multi-order 785 nm laser lines.
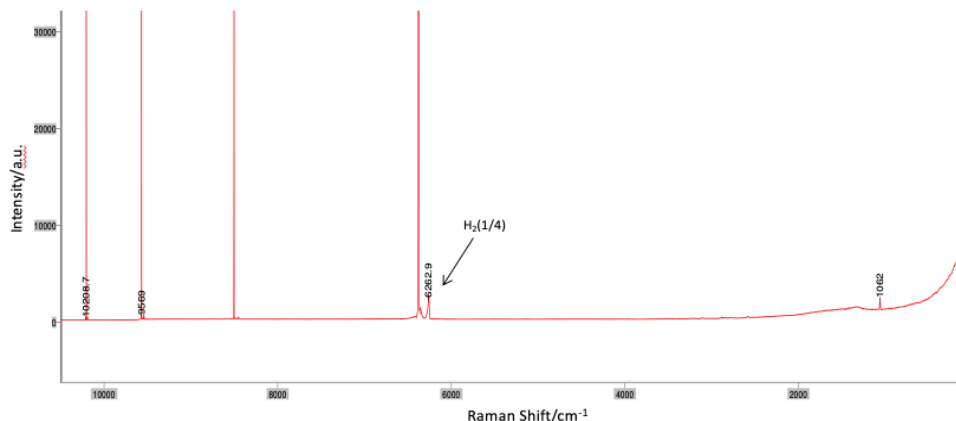
Given that $H_2(1/4)$ was observed by a hydrino solid fuel reaction of FeOOH, and ball milling has an effect equivalent to heating to drive chemical reactions [88], FeOOH was ball milled in a stainless-steel chamber using stainless steel balls for 10 hours to form the hydrino product FeOOH:H$_2$(1/4). Raman spectra were recorded on the solid product using the 785 nm and 325 nm lasers. The Raman spectra obtained using a Horiba Jobin Yvon LabRam ARAMIS spectrometer with a 300 mW, 785 nm laser on solid FeOOH:H$_2$(1/4) are shown in Figures 18-19. As shown in the 3500 cm^{-1} to 8000 cm^{-1} Raman spectral region (Figure 18), the series of emission peaks assigned to fluxon linkages were also observed in the FeOOH:H$_2$(1/4) product of FeOOH ball milling. The 3500 cm^{-1} to 5100 cm^{-1} Raman spectral region (Figure 19) shows the details of the series of peaks assigned to the second order emission of fluxon linkages during the $H_2(1/4)$ double rotational and spin-orbital transition for final rotational, spin-orbital, and fluxon quantum numbers $J'_p = 3$ and $J'_c = 2$, $m = -1.5$, and $m_{\Phi 3/2} = 2$, respectively. And, the 6500 cm^{-1} to 8100 cm^{-1} Raman spectral region (Figure 20) shows the details of another series assigned to the third order emission of the parent (1st order) emission of the corresponding second order emission shown in Figures 15 and 19. The peak positions and energies are shown in Table 12. The observation of both the second and third order emission series of 39 spectral lines over a very wide spectral range further eliminates any possibility of an instrument artifact.

Figure 18. Raman spectrum (3500 cm^{-1} to 8000 cm^{-1}) obtained using a Horiba Jobin Yvon LabRam ARAMIS spectrometer with a 300 mW, 785 nm laser on solid FeOOH powder prepared by ball milling for 10 hours showing two series of peaks assigned to the second and third order emission of fluxon linkages during the $H_2(1/4)$ double rotational and spin-orbital transition for final rotational, spin-orbital, and fluxon quantum numbers $J_p' = 3$ and $J_c' = 2$, $m = -1.5$, and $m_{\Phi 3/2} = 2$, respectively.
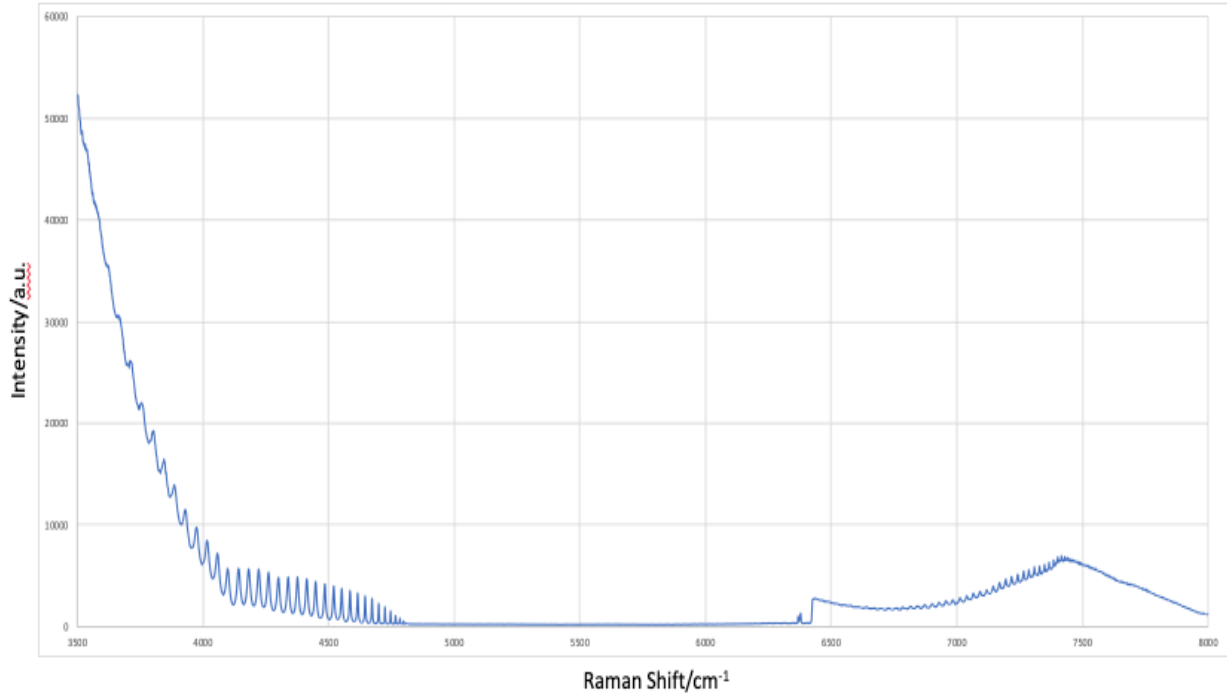
Figure 19. Raman spectrum (3500 cm^{-1} to 5100 cm^{-1}) obtained on solid FeOOH:H$_2$(1/4) showing the details of the series assigned to the second order emission of fluxon linkages during the $H_2(1/4)$ double rotational and spin-orbital transition for final rotational, spin-orbital, and fluxon quantum numbers $J_p' = 3$ and $J_c' = 2$, $m = -1.5$, and $m_{\Phi3/2} = 2$, respectively.
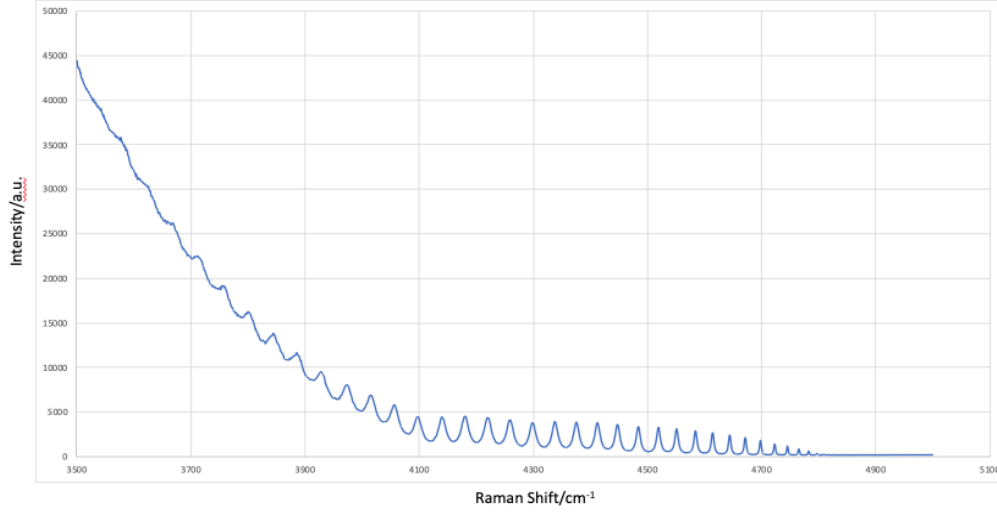

The peak positions of the series of peaks shown in Figure 20 are given in Table 13 with the corresponding peak positions upon conversion from Raman to emission spectral peaks. The series is assigned to the third order emission of fluxon linkages during the $H_2(1/4)$ double rotational and spin-orbital transition for final rotational, spin-orbital, and fluxon quantum numbers $J_p' = 3$ and $J_c' = 2$, $m = -1.5$, and $m_{\Phi3/2} = 2$, respectively with energies given by Eqs. (38), (22), and (23), respectively. The parent (1st order) emission energies are indicative of a two-laser-photon excitation involving excitation to a first and then a second higher-energy state which may be facilitated by the extraordinarily high rotational energies of $H_2(1/4)$. The high energy in turn precludes efficient coupling with lattice phonons, and thereby increases the rotational state lifetime and cross section for two-photon excitation. A corresponding application of material comprising molecular hydrino is a laser frequency doubling or increasing medium.

Figure 20. Raman spectrum (6500 cm^{-1} to 8100 cm^{-1}) obtained on solid FeOOH:H$_2$(1/4) showing the details of the series assigned to the third order emission of fluxon linkages during the $H_2(1/4)$ double rotational and spin-orbital transition for final rotational, spin-orbital, and fluxon quantum numbers $J'_p = 3$ and $J'_c = 2$, $m = -1.5$, and $m_{\Phi 3/2} = 2$, respectively.
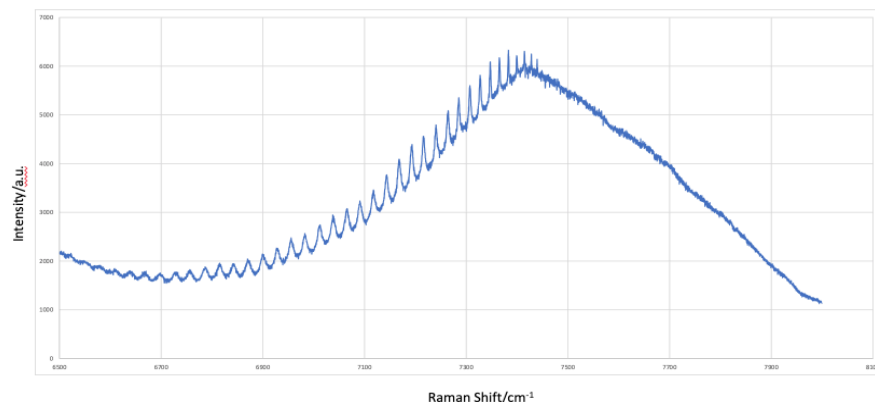
Table 12. The observed Raman energies of the 785 nm Raman spectral peaks in the 6500 cm^{-1} to 8100 cm^{-1} region shown in Figure 20. The corresponding observed Raman energies, parent (1st order) emission energies of second order emission energies from Table 11, corresponding third order emission and Raman energies of the parent emission from Table 11, and difference between the observed and calculated third order Raman lines demonstrate that the periodic peaks are third order emission of fluxon linkages during the $H_2(1/4)$ double rotational and spin-orbital transition for final rotational, spin-orbital, and fluxon quantum numbers $J'_p = 3$ and $J'_c = 2$, $m = -1.5$, and $m_{\Phi 3/2} = 2$, respectively.

Raman Energy (cm^{-1})	Emission Energy (cm^{-1})	Parent Peak of 2° (cm^{-1})	3° Emission (cm^{-1})	3° Raman (cm^{-1})	Δ Energy (Observed – 3°) (cm^{-1})
6532	6207	18614	6205	6534	-2
6565	6174	18518	6173	6566	-1
6595	6144	18424	6141	6598	-3
6630	6109	18330	6110	6629	1
6655	6084	18242	6081	6658	-3
6687	6052	18150	6050	6689	-2
6719	6020	18058	6019	6720	-1
6752	5987	17968	5989	6750	2
6781	5958	17878	5959	6780	1
6811	5928	17790	5930	6809	2
6835	5904	17706	5902	6837	-2
6867	5872	17622	5874	6865	2

6892	5847	17534	5845	6894	-2
6925	5814	17450	5817	6922	3
6953	5786	17366	5789	6950	3
6975	5764	17284	5761	6978	-3
7010	5729	17198	5733	7006	4
7032	5707	17118	5706	7033	-1
7059	5680	17036	5679	7060	-1
7085	5654	16958	5653	7086	-1
7114	5625	16880	5627	7112	2
7140	5599	16800	5600	7139	1
7165	5574	16726	5575	7164	1
7190	5549	16652	5551	7188	2
7214	5525	16582	5527	7212	2
7239	5500	16510	5503	7236	3
7261	5478	16438	5479	7260	1
7279	5460	16376	5459	7280	-1
7300	5439	16310	5437	7302	-2
7321	5418	16250	5417	7322	-1
7340	5399	16190	5397	7342	-2
7360	5379	16134	5378	7361	-1
7375	5364	16082	5361	7378	-3
7392	5347	16034	5345	7394	-2
7410	5329	15988	5329	7410	0
7425	5314	15948	5316	7423	2
7435	5304	15912	5304	7435	0
7445	5294	15884	5295	7444	1
7450	5289	15860	5287	7452	-2

$H_2(1/4)$ lines were observed on Ni foil exposed to the plasma of a hydrino reaction (Figure 9A-9C) using the 11 mW 785 nm laser and 300 line/mm grating, and the $H_2(1/4)$ series of fluxon linkage peaks were recorded on ball milled FeOOH (Figure 18) using the 300 mW 785 nm laser and 600 line/mm grating. Considering that the Ni foil was run at a higher temperature than the Ni Curie temperature and fluxon linkage is more favorable with a sample having a high internal magnetization such as FeOOH, a 1 T neodymium magnet was applied to the Ni foil sample, and the Raman spectrum was reacquired on the Horiba Jobin Yvon LabRam ARAMIS spectrometer as an experiment to cause emission of the series of fluxon linkage peaks on the Ni foil. As shown in the 0 cm^{-1} to 11,000 cm^{-1} Raman spectral region (Figures 21A-C), the series of peaks assigned to the second order emission of fluxon linkages during the $H_2(1/4)$ double rotational and spin-

orbital transition for final rotational, spin-orbital, and fluxon quantum numbers $J'_p = 3$ and $J'_c = 2$, $m = -1.5$, and $m_{\Phi 3/2} = 2$, respectively, were observed. The lower intensity of the series was atributed to the much weaker laser power, 11 mW versus 300 mW. As in the case of the $H_2(1/4)$ emission lines shown in Figure 9A-C, the series of fluxon linkage peaks were eliminated by a Semrock long-pass edge filter (BLP01-785R-25) having an edge wavelength of 805 nm and T_{avg} > 93% 812.1 – 1200 nm placed between the sample and the detector. The blocking of high energy photons confirmed the assignment to high energy emission rather than low energy Raman transitions (Figure 21C). Comparison of the filtered Ni foil spectrum shown in Figure 9A to that with a strong magnet applied (Figure 21A), demonstrates that the magnetic field also increased the high energy broad band emission in the 0-3000 cm^{-1} Raman spectral region (12,700-12,400 cm^{-1} emission spectral region) very significantly (e.g. intensity of 33,000 counts versus 97 at 2000 cm^{-1}).

Figure 21A. Raman spectrum (0 cm^{-1} to 11,000 cm^{-1}) recorded with a 11mW, 785 nm laser on a Ni foil prepared by immersion in the molten gallium of a SunCell® that maintained a hydrino plasma reaction for 10 minutes and magnetized with a 1 T neodymium magnet showing the details of the series assigned to the second order emission of fluxon linkages during the $H_2(1/4)$ double rotational and spin-orbital transition for final rotational, spin-orbital, and fluxon quantum numbers $J'_p = 3$ and $J'_c = 2$, $m = -1.5$, and $m_{\Phi 3/2} = 2$, respectively.
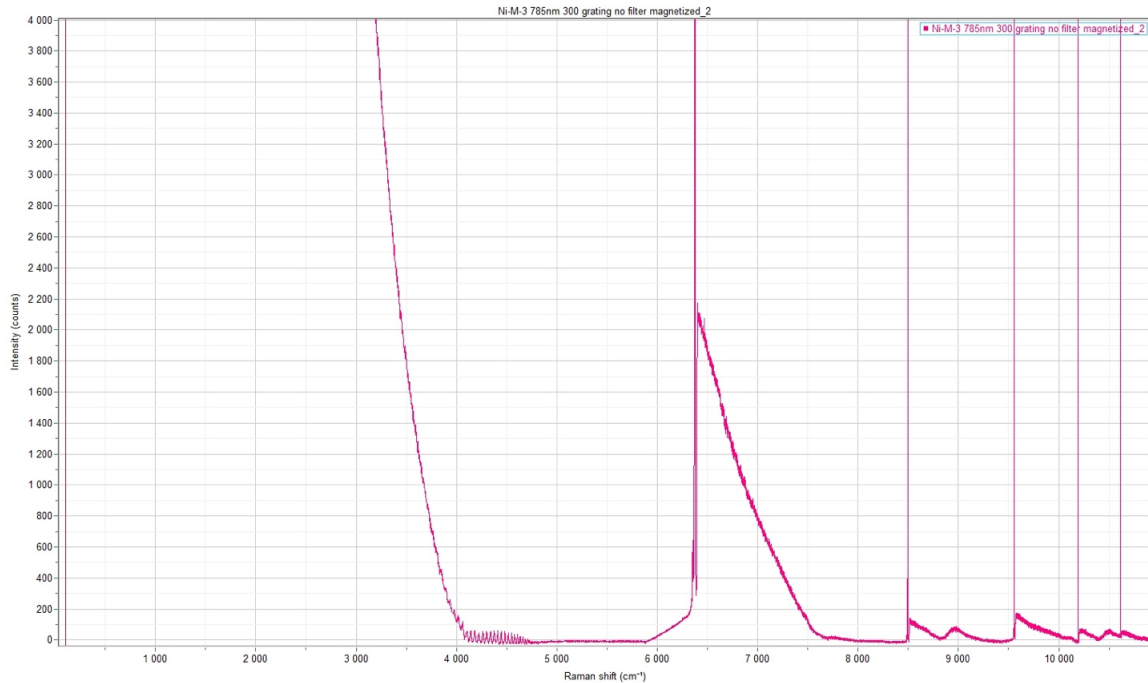

(A)

Figure 21B. Raman spectrum (3700 cm^{-1} to 5500 cm^{-1}) recorded with a 11mW, 785 nm laser on a Ni foil prepared by immersion in the molten gallium of a SunCell® that maintained a hydrino plasma reaction for 10 minutes and magnetized with a 1 T neodymium magnet.
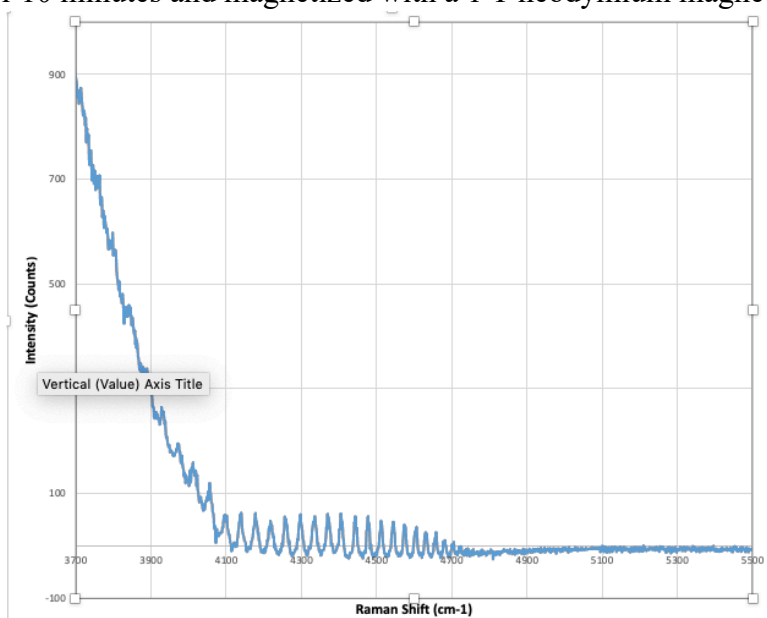
(B)

Figure 21C. Raman spectrum (0 cm^{-1} to 11,000 cm^{-1}) recorded with a 11mW, 785 nm laser on a Ni foil prepared by immersion in the molten gallium of a SunCell® that maintained a hydrino plasma reaction for 10 minutes. The sample was magnetized with a 1 T neodymium magnet and a Semrock long-pass edge filter was applied between the sample and the detector. The series assigned to the second order emission of fluxon linkages during the H$_2$(1/4) were eliminated confirming the assignment to high energy emission.
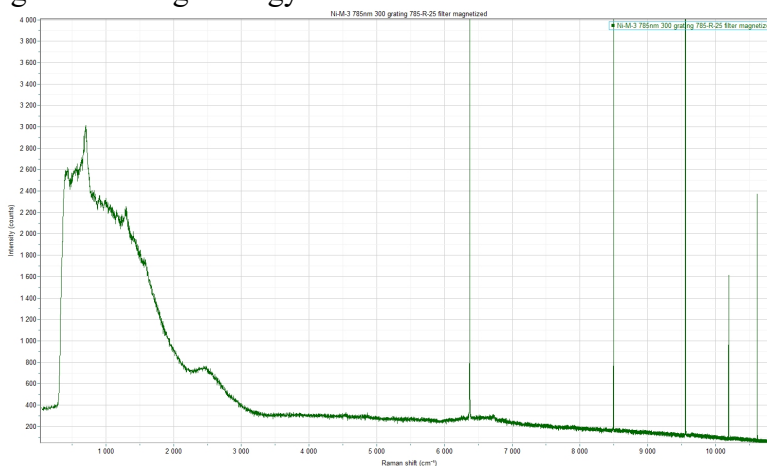
(C)

FeOOH was ball milled at 350 RPM for 3 hours using a Retsch PH 100 ball mill. Raman spectra were recorded to confirm the first order emission assignments of the observed second and third order emission peaks of the Stokes spectra shown in Figures 15-16, 18-21 having the assignments given in Tables 11-12. As well as repeating the Stokes spectra, the anti-Stokes spectra were recorded with the Horiba Jobin Yvon LabRAM Aramis Raman spectrometer using the 300 mW 785 nm laser and 600 line/mm grating. To further test the two-photon excitation mechanism, the spectra were obtained at 100X objective with the power varied from 25% to 50%. The anti-Stokes spectrum and corresponding Stokes spectrum are shown juxtaposed in Figure 21D. The anti-Stokes and Stokes spectra are shown separately in Figures 21E and 21F, respectively. The Stokes lines matches those given in Tables 11-12. The Raman spectral lines corresponding to the first order emission peak assignments of Tables 11-12 matched the observed anti-Stokes peaks within the limits of measurement. The results confirm that the series of periodic peaks observed in the anti-Stokes and Stokes Raman spectra are the emission lines of Tables 11-12 with the first order peaks observed in the anti-Stokes spectrum (Figures 21D and 21E) and the corresponding second and third order peaks observed in the Stokes spectrum (Figures 21D and 21F; Figures 15-16, 18-21). The two two-photon absorption excitation mechanism was also confirmed by the power threshold nature of the emission. The series of peaks was not observed at 25% laser power but was observed at 50% laser power.

The anti-Stokes and Stokes spectra are remarkable in that the energy ranges are higher than any prior recorded, there is a threshold laser intensity to observe the emission lines, and the first, second, and third order peaks are observed that match the rotational transitions of $H_2(1/4)$ and not any known source. The Raman results provide strong confirmation of $H_2(1/4)$ and the two-photon excitation mechanism of the rotational energy levels of $H_2(1/4)$. The fine structure comprising the series of periodic peaks was only observed in magnetic and magnetized samples further confirming the assignment to fluxon linkage during rotational transitions.

Figure 21D.   Raman anti-Stokes (-50 cm^{-1} to -8000 cm^{-1}) and Stokes (100 cm^{-1} to 8000 cm^{-1}) of the ball milled FeOOH sample recorded with 25% and 50% 300 mW 785 nm laser power and 100X objective. The anti-Stokes emission is the source of the Stokes-spectral lines assigned to second and third order high-energy emission.
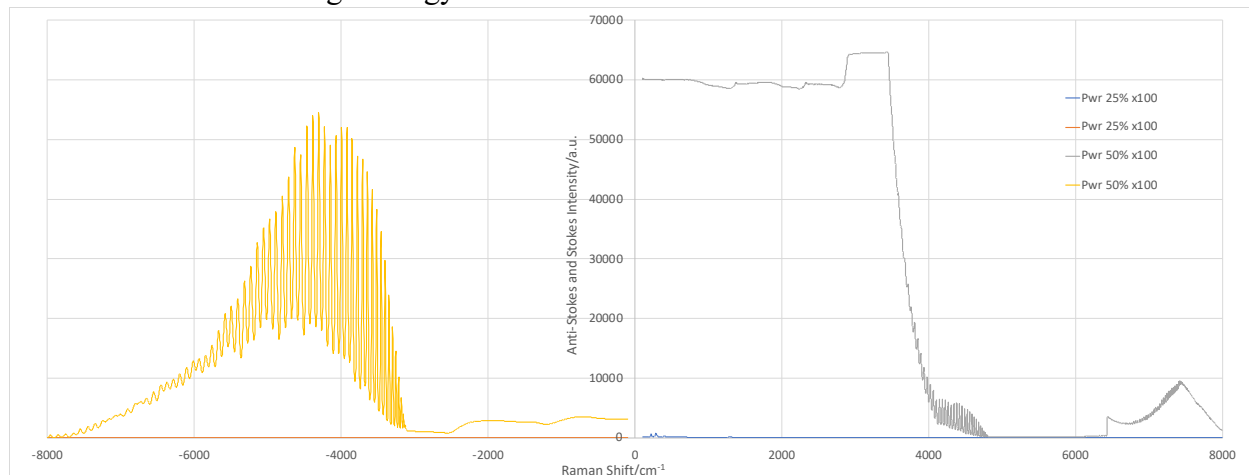

Figure 21E.   Raman anti-Stokes (-50 cm^{-1} to -8000 cm^{-1}) of the ball milled FeOOH sample recorded with 25% and 50% 300 mW 785 nm laser power and 100X objective.
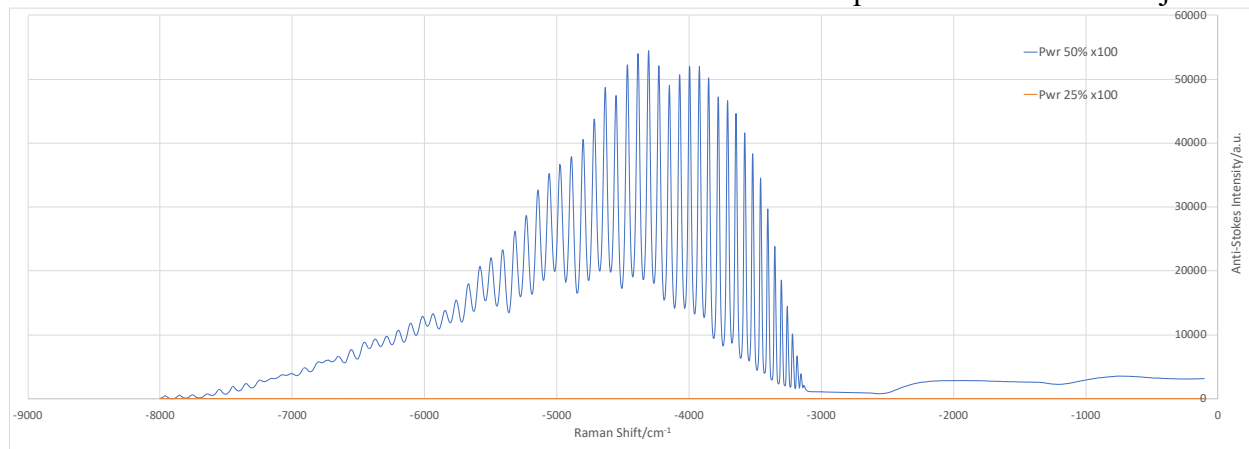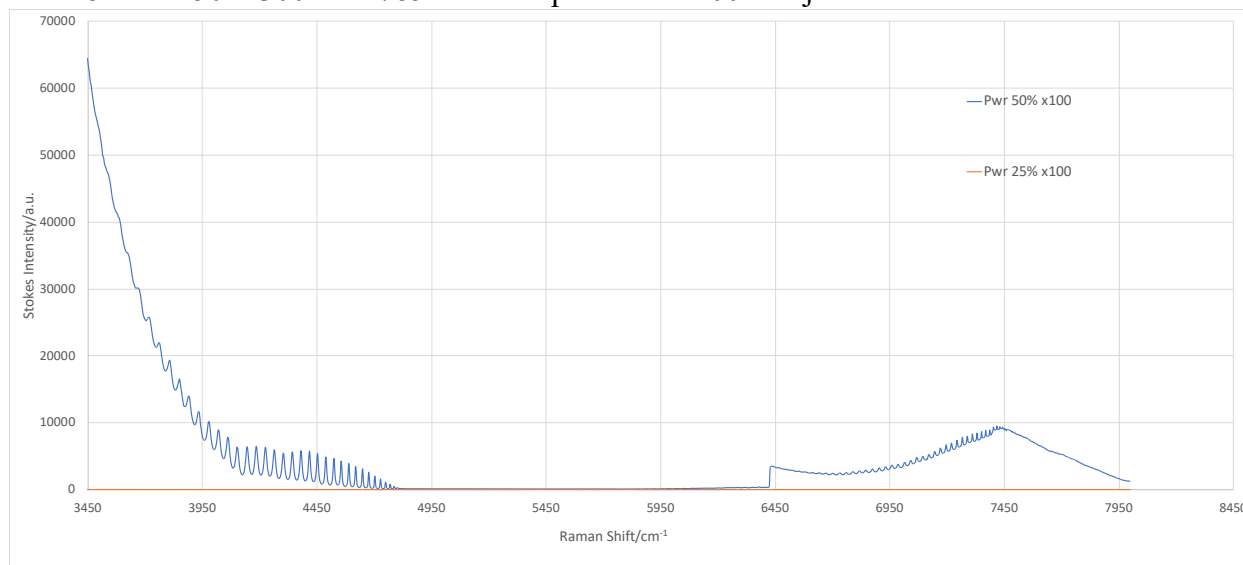
Figure 21F.   Raman Stokes (100 cm^{-1} to 8000 cm^{-1}) of the ball milled FeOOH sample recorded with 25% and 50% 300 mW 785 nm laser power and 100X objective.

Using the Across PQ-N2 Planetary ball mill, transition metal analog CoOOH was ball milled for 5 hours at 250 RPM, and KI-NH$_4$NO$_3$ 90/10 wt%, a non-magnetic chemical mixture comprising a source of H and HOH catalyst was ball milled under identical conditions. Raman Stokes and anti-Stokes spectra were recorded under the same conditions as those used to record spectra on FeOOH. As shown in Figures 21G and 21H, the anti-Stokes first order and the Stokes second order and third order emission peaks of the CoOOH matched those of FeOOH. No anti-Stokes peaks were recorded on KI-NH$_4$NO$_3$ which demonstrates the dependence of the H$_2$(1/4) rotational transitions with fluxon linkage on the magnetic nature of the matrix.

Figure 21G.   Raman anti-Stokes (-50 cm^{-1} to -8000 cm^{-1}) of ball milled CoOOH and ball milled non-magnetic chemical mixture KI-NH$_4$NO$_3$ recorded with 50% of 300 mW 785 nm laser power and 100X objective. The anti-Stokes emission that was only observed on the CoOOH product with a magnetic matrix is the source of the Stokes-spectral lines assigned to second and third order high-energy emission.
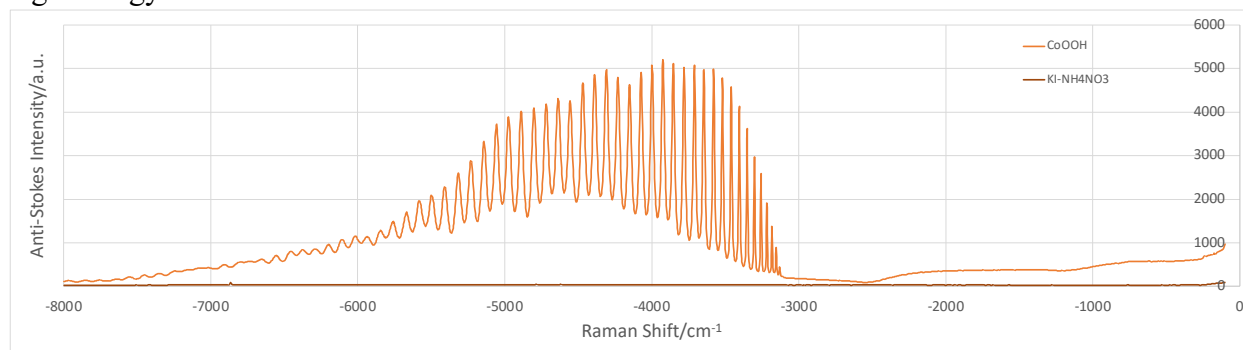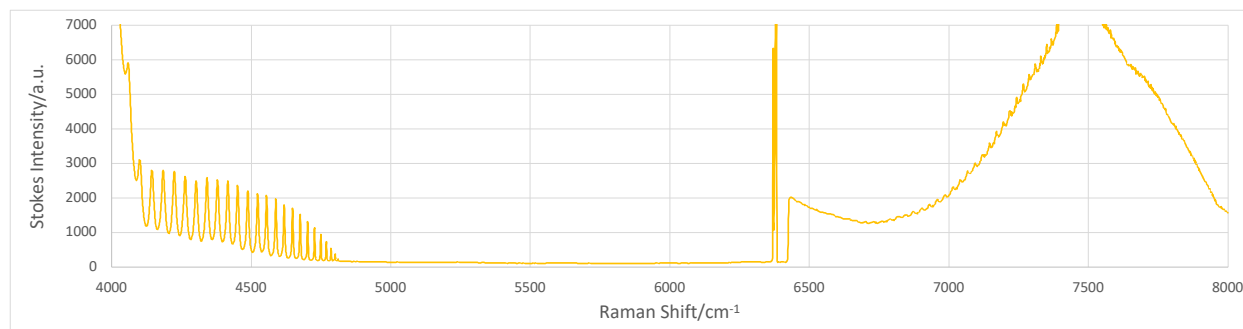

70

Figure 21H.   Raman Stokes (4000 cm^{-1} to 8000 cm^{-1}) of ball milled CoOOH recorded with 50% of 300 mW 785 nm laser power and 100X objective. The peaks match the corresponding second and third order lines of the anti-Stokes lines.

The anti-Stokes spectrum of the FeOOH sample was also recorded with second Raman spectrometer, a Horiba XploRA PLUS Confocal Microscope, over a 1s acquisition time using a 785nm laser with a power of 28.5mW, 50x objective, 600 line/mm grating, and a CCD detector. The spectrum shown in Figure 21I showed the series of periodic peaks in the energy region of 3150 cm^{-1} to 6000 cm^{-1} having corresponding second and third order lines observed in the Stokes spectra (Figure 15-16, 18-21 and Tables 11-12). Controls such as silicon wafer showed zero intensity. In addition, a lower intensity band was observed in the 6000 cm^{-1} to 8000 cm^{-1} region. The corresponding Stokes spectrum was saturated for wavenumbers less than about 3500 cm^{-1} so the corresponding second order emission in the 2370 cm^{-1} to 3370 cm^{-1} region was not recorded. However, the corresponding third order periodic emission peaks in the 5800 cm^{-1} to 6500 cm^{-1} region were observed in Stokes spectrum as shown in Figure 21J. Again, the anti-Stokes emission spectrum is remarkable in that the energy range is higher than any prior recorded with the only possible assignment being the rotational energy levels of $H_2(1/4)$.

Figure 21I. Raman anti-Stokes spectra (-50 cm^{-1} to -9500 cm^{-1}) of the ball milled FeOOH sample (top curve) and control Si wafer (bottom curve) recorded with a 28.5 mW 785 nm laser on ball milled FeOOH. The anti-Stokes emission is the source of the Stokes-spectral lines assigned to second and third order high-energy emission.
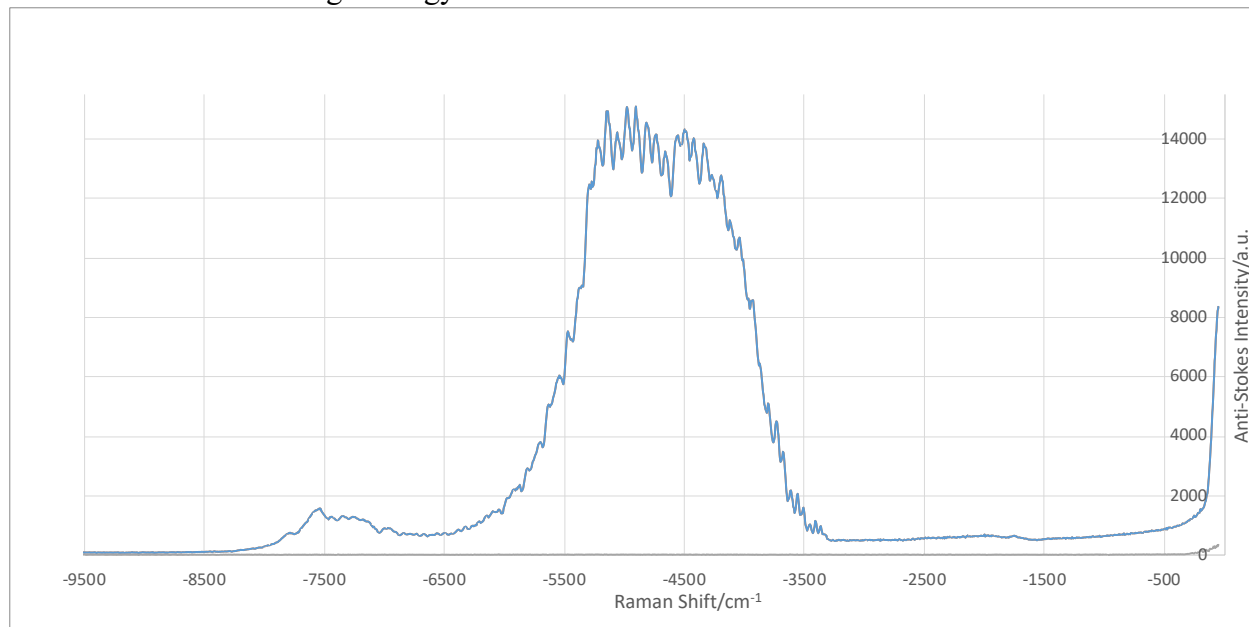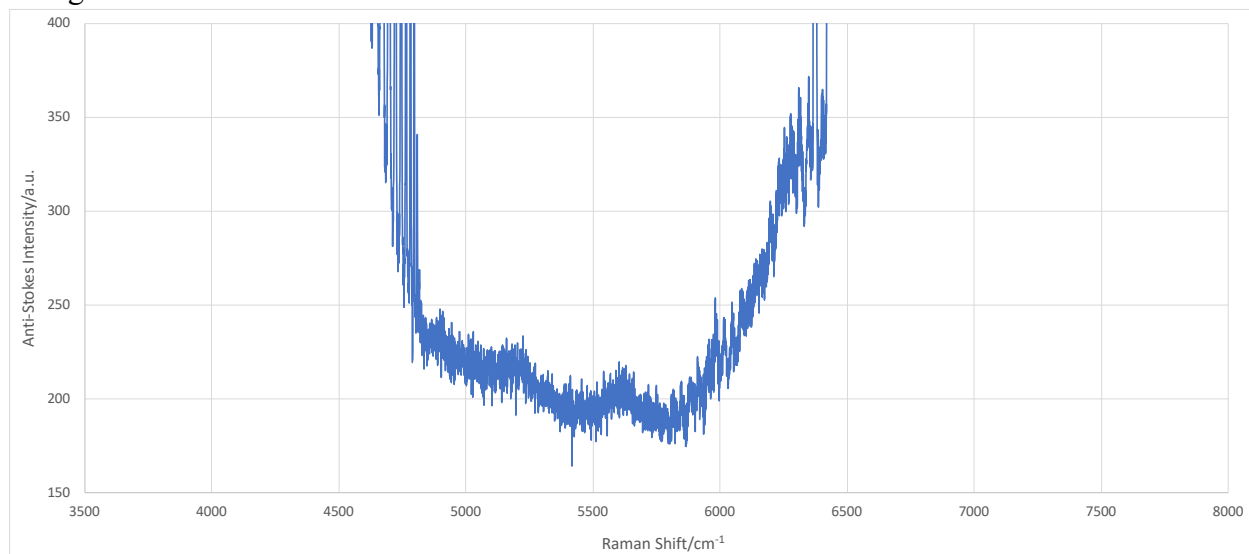

Figure 21J. Spectral expansion of Figure 18 comprising the Raman Stokes spectrum (3500 cm^{-1} to 8000 cm^{-1}) recorded on solid FeOOH powder prepared by ball milling for 10 hours showing the third order emission of the 6000 cm^{-1} to 8000 cm^{-1} lower intensity anti-Stokes band of Figure 21I.

The Stokes and anti-Stokes spectra of the FeOOH sample were further recorded over a 1s anti-Stokes/0.25s Stokes acquisition time with the Horiba XploRA PLUS Confocal Microscope using a 532nm laser at a power of 60 mW anti-Stokes/30 mW Stokes, 50x objective, 600 line/mm grating, and CCD detector. The anti-Stokes spectrum shown in Figure 21L shows a broad strong continuum emission over the energy region of -50 cm^{-1} to -8000 cm^{-1}. Controls such as silicon wafer showed no emission over the entire spectral range. The anti-Stokes spectrum as the first order emission matches the Stokes spectrum (Figure 21K) over the ranges recorded. Although the resolution was not as high as that with the 785 nm laser, 532 nm anti-Stokes and Stokes spectra are remarkable in that again the energy range is higher than any prior recorded with the only matching assignment being the rotational energy levels of $H_2(1/4)$.

Figure 21K. Raman Stokes spectrum (50 cm^{-1} to 9000 cm^{-1}) of the FeOOH sample recorded with the 532 nm laser at 30 mW.
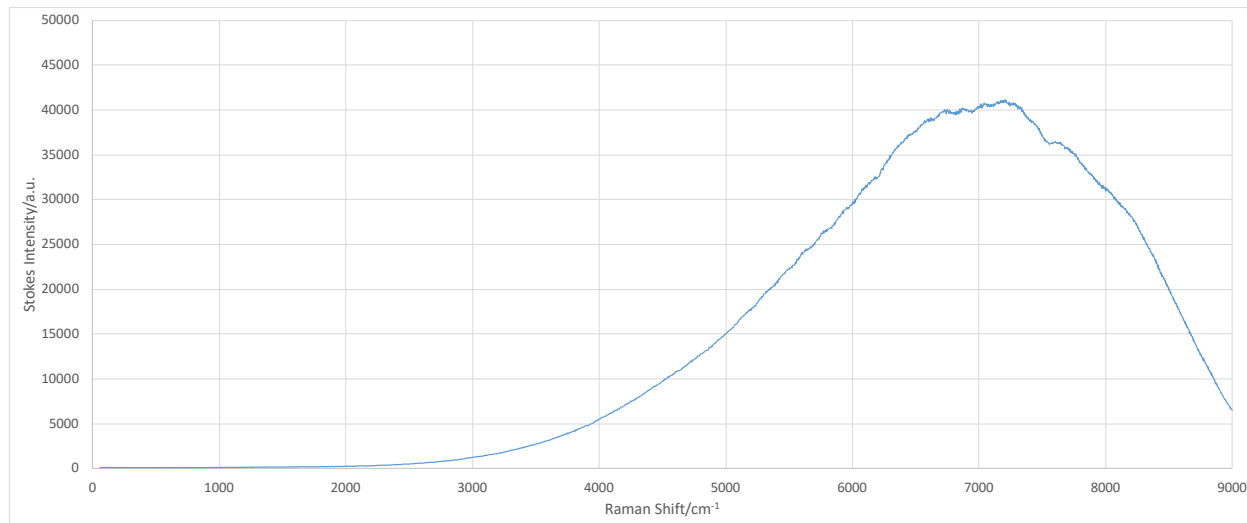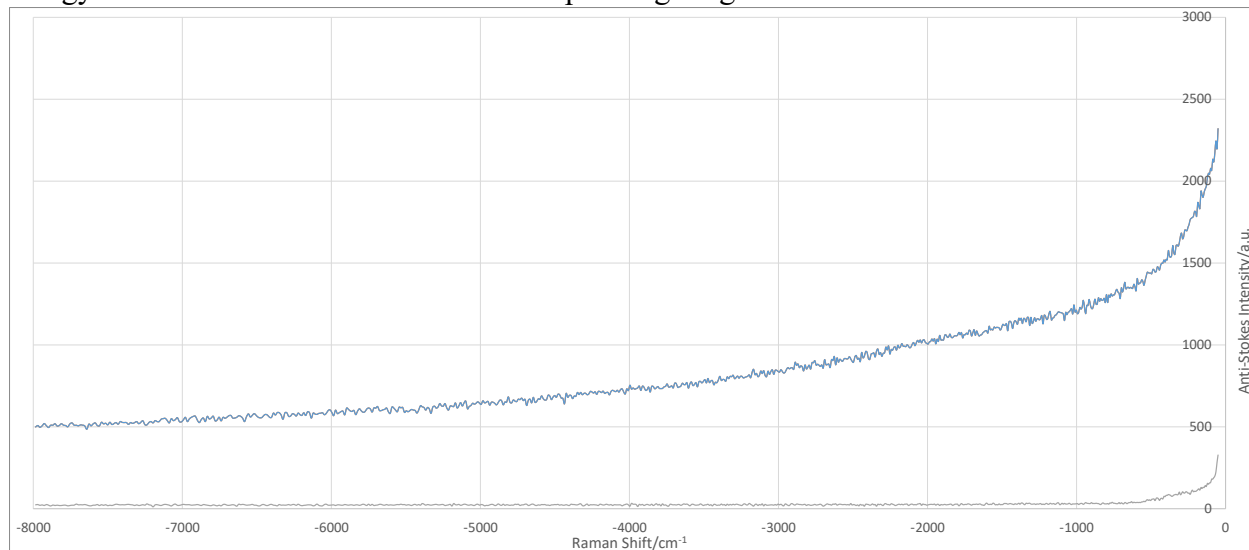
Figure 21L. Raman anti-Stokes spectrum (-50 cm^{-1} to -8000 cm^{-1}) of the FeOOH sample (top curve) and Si control (bottom curve). A strong broad continuum was observed over the entire spectral range. The FeOOH Stokes spectrum shown in Figure 21K matches the second order high-energy anti-Stokes emission over the corresponding ranges recorded.

Nickel foil Raman samples were prepared by flowing a hydrino reaction mixture comprising 1500 standard cubic centimeters per minute (sccm) H_2 and 1 sccm O_2 into a one-liter reaction volume SunCell® comprising a quartz dome for optical power transfer, two molten tin injectors electrodes each having a reservoir and an electromagnet pump that injected a molten metal stream wherein the intersection of the streams maintained an electrical connection for a low-voltage-high-current ignition power source that maintained a hydrino reaction plasma by maintaining the high current. The operating pressure was 5.9 Torr. Plasma was maintained by an ignition current of 200A at a voltage of 15 V. The electromagnetic pump rate was 100 g/s, and the optical output power recorded with a Thor 322C Power Meter was over 30 kW for an input ignition power of 3 kW corresponding to a gain of 10 times. The Ni foils (1 X 1 X 0.1 cm) to make the Raman samples were placed under a quartz reflector in the SunCell® reaction cell chamber. The hydrino reaction was run for 10 minutes, and Ni and tin-coated surfaces of the foils were analyzed by Raman spectroscopy using the Horiba Jobin Yvon LabRAM Aramis Raman spectrometer using the 300 mW 785 nm laser and 600 line/mm grating at 100X objective and 50% power. In addition, the 785 nm Raman spectrum was recorded under identical conditions on a control Ni foil sample run in the SunCell® and stored for six months to allow hydrino to dissipate by diffusion. The anti-Stokes spectrum and corresponding Stokes spectrum are shown in Figures 21M and 21N, respectively. The Stokes lines on the hydrino samples match those given in Tables 11-12 corresponding to the first order emission peaks observed in the anti-Stokes spectrum, and

the peaks were absent in the control. The results demonstrate that the reaction of H_2 to $H_2(1/4)$ is the source of SunCell® power gain.

Figure 21M. Raman anti-Stokes (-50 cm^{-1} to -8000 cm^{-1}) of the Ni and tin-coated Ni foil samples run in the SunCell® and control Ni foil recorded with 50% of 300 mW 785 nm laser power and 100X objective. The anti-Stokes emission is the source of the Stokes-spectral lines assigned to second and third order high-energy emission.
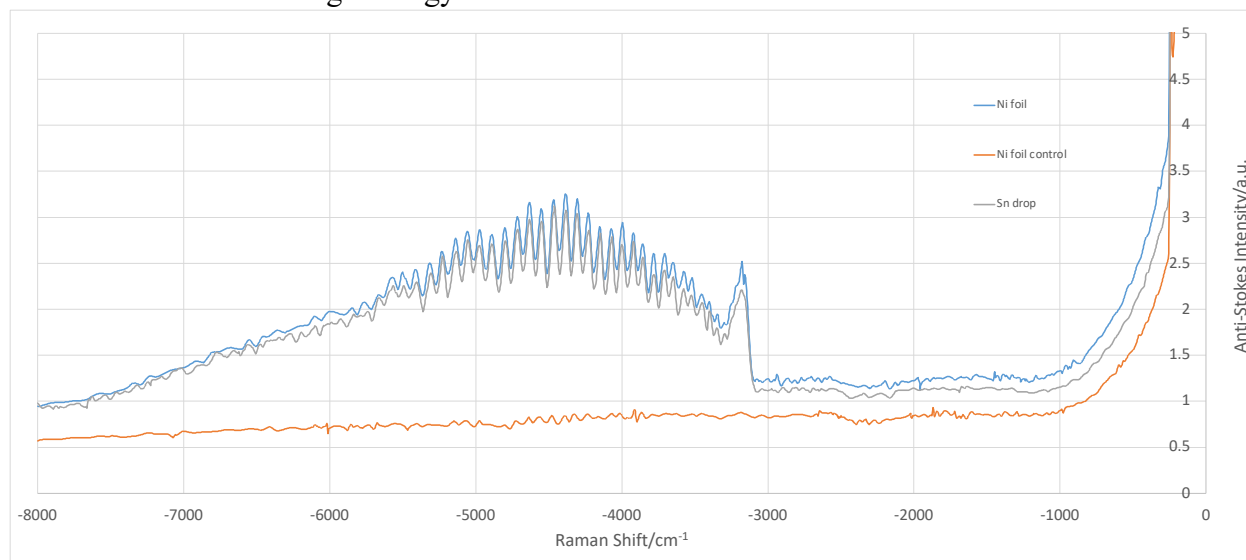
Figure 21N. Raman Stokes (3000 cm^{-1} to 8000 cm^{-1}) of the Ni and tin-coated Ni foil samples run in the SunCell® and control Ni foil recorded with 50% of 300 mW 785 nm laser power and 100X objective. The peaks match the corresponding second and third order lines of the anti-Stokes lines.
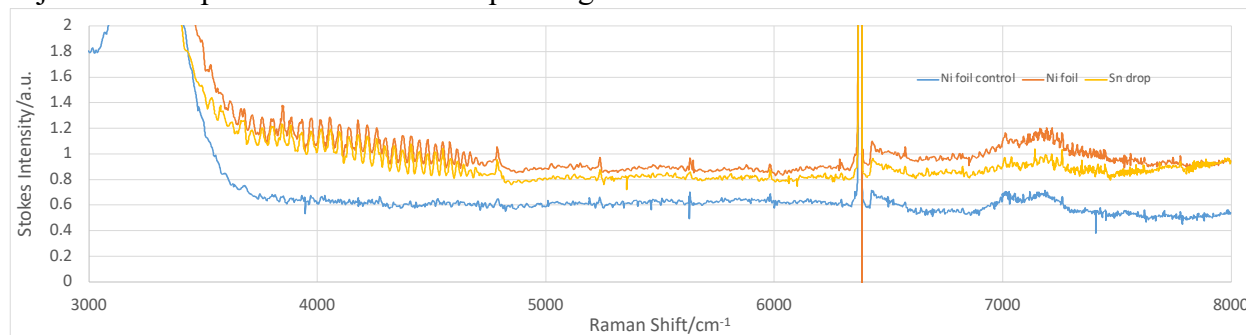
Materials comprising molecular hydrino were further investigated by Raman spectroscopy using a higher energy UV laser. The presence of $H_2(1/4)$ in the GaOOH:H$_2$(1/4) SunCell® product, Fe-web detonation product, and FeOOH:H$_2$(1/4) ball-mill product samples was confirmed using 325 nm Raman spectroscopy by the observation of a characteristic spectral pattern observed previously on hydrino reaction product materials. Specifically, Raman spectra were obtained

using a Horiba Jobin Yvon LabRam ARAMIS spectrometer with a 325 nm laser on (i) GaOOH:H₂(1/4), (ii) NaOH:KCl (1:1 wt%) getter of the $H_2(1/4)$ product gas from high current detonation of hydrated silver shots, (iii) solid web-like fibers prepared by wire detonation of an ultrahigh purity Fe wire in 20 Torr water vapor-air atmosphere, and (iv) FeOOH powder prepared by ball milling for 10 hours. In all four cases, a series of 1000 cm^{-1} separated peaks were observed in the 17,000 to 22,000 cm^{-1} region. The peaks exactly matched the ro-vibration of $H_2(1/4)$ previously observed in the ultraviolet as a 260 nm e-beam band shown in Figures 22A-B [78,81], but at one half the ro-vibration energies. Due to the unique electronic structure of $H_2(1/4)$, the corresponding energy levels matched theoretical predictions of ro-vibration states of molecular hydrino with excitation and decay involving two-photons, each of ½ the energy of the ro-vibrational state.

Figures 22A-B. Ultraviolet electron-beam excitation emission spectrum recorded on KCl getter impregnated with hydrino reaction product gas $H_2(1/4)$ showing the 260 nm band comprising $H_2(1/4)$ ro-vibrational P branch in the crystalline lattice. Q (0), R(0), R(1), R(2), P(1), P(2), P(3), and P(4) ro-vibrational transitions of $H_2(1/4)$ were observed. A. Solid fuels reaction of a source of H, catalyst, and KCl [82]. B. $H_2(1/4)$ gas from a sealed reactor of the gun powder reaction, KNO₃ with softwood charcoal having the formulation C₇H₄O [78].

(A)

Getter from KNO$_3$ + softwood charcoal
e beam 6kV 4.4 uA, slit 500 x 500, 3 s
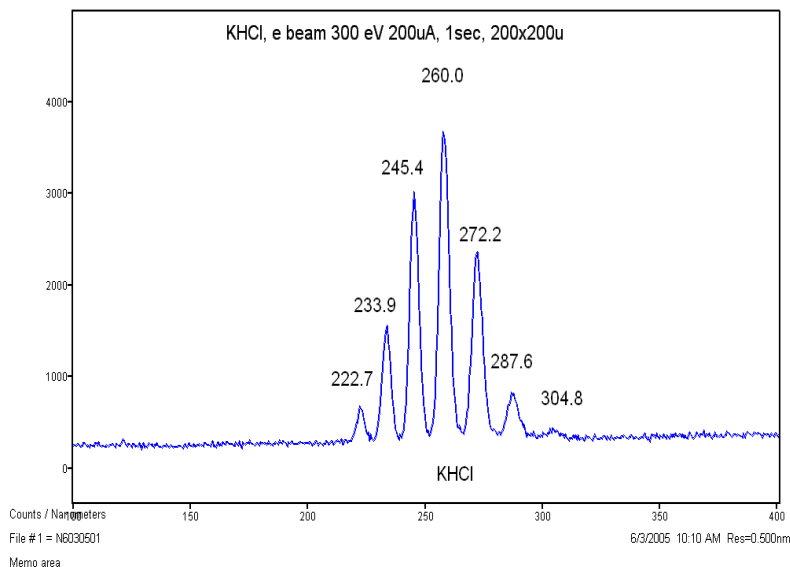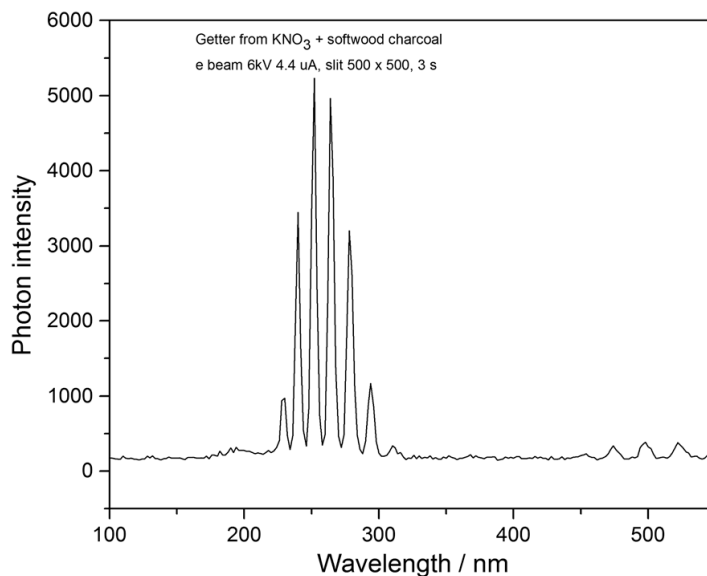
(B)

The 260nm, e-beam band showed no structure other than the broad peaks at 1.4Å resolution when observed using a Jobin Yvon Horiba 1250M spectrometer. Additionally, structure was found to be absent at an enhanced 0.25Å resolution as well as at 1.65 cm^{-1} resolution in the photoluminescence spectra eliminating the possibility of the series comprising unresolved ro-vibrational bands of a common molecule [78]. The corresponding energy spectrum in the ultraviolet comprised a series of 0.24 eV evenly spaced peaks centered at 260 nm called the 260 nm e-beam band (Figure 22) recorded with a EUV spectrometer on emission from high-energy electron beam bombardment of solid getter materials that trapped $H_2(1/4)$ [78]. The intense fluorescence spectra in all cases comprised the ro-vibration band from the $H_2(1/4)$ $v=1$ to $v=0$ vibrational transition shifted by the higher effective mass of $H_2(1/4)$ in a solid matrix and the 1950 cm^{-1} spaced lines of the free rotor P-branch of $H_2(1/4)$.

The series of ro-vibrational level emission lines assigned to H$_2$(1/4) was also observed by trapping H$_2$(1/4) gas released from SunCell® products in a KCl getter that is transparent to UV emission with the extraordinary exception that the 325 nm-laser-photon-excited spectrum comprised the identical ro-vibrational lines but at ½ the energies of the collisional excited spectrum, and the spectrum further comprised a broad emission background of the same intensity profile as the superimposed lines. H$_2$(1/4) formed in a stainless steel SunCell® was released as a gas for analysis by two methods: (i) 900 °C heating of the oxide mixture formed by trace water addition to the SunCell® to maintain a hydrino plasma reaction wherein the heating caused decomposition of Ga$_2$O$_3$:H$_2$(1/4) of the mixture and (ii) 900 °C heating of the filtrate of the oxide mixture dissolved in NaOH. Specifically, KCl was packed in a tube connected to a pressure vessel containing Ga$_2$O$_3$/GaOOH:H$_2$(1/4) collected from the SunCell®, and the decomposition gas from

heating the $Ga_2O_3/GaOOH:H_2(1/4)$ to 900 °C was flowed through the KCl getter. The Raman spectrum of a KCl getter comprising trapped $H_2(1/4)$ gas was recorded using the Horiba Jobin Yvon LabRAM Aramis Raman spectrometer with a HeCd 325 nm laser in microscope mode with a magnification of 40X. The Raman spectrum on KCl starting material was unremarkable, whereas the KCl getter Raman comprised a series of 1000 cm^{-1} (0.1234 eV) equal-energy spaced Raman peaks observed in the 8000 cm^{-1} to 18,000 cm^{-1} region. The conversion of the Raman spectrum into the fluorescence or photoluminescence spectrum revealed a match as the ½ energy ro-vibrational spectrum of $H_2(1/4)$ corresponding to the 260 nm band first observed by e-beam excitation [78]. Assigning Q(0) to the most intense peak, the peak assignments given in Table 13 to the Q, R, and P branches for the spectra shown in Figure 23A are Q(0), R(0), R(1), R(2), R(3), R(4), P(1), P(2), P(3), P(4), and P(5) observed at 13,188, 12,174, 11,172, 10,159, 9097, 8090, 14,157, 15,106, 16,055, 16,975, and 17,873 cm^{-1}, respectively. The theoretical transition energies with peak assignments compared with the observed emission spectrum are shown in Table 13.

Figure 23A. Raman-mode photoluminescence spectrum of KCl getter exposed to gas from the thermal decomposition of $Ga_2O_3:H_2(1/4)$ collected from the SunCell® wherein the spectrum was recorded with a Horiba Jobin Yvon LabRam ARAMIS spectrometer with a 325nm laser and a 300 line/mm grating over a range of 8000-19,000 cm^{-1} Raman shift.
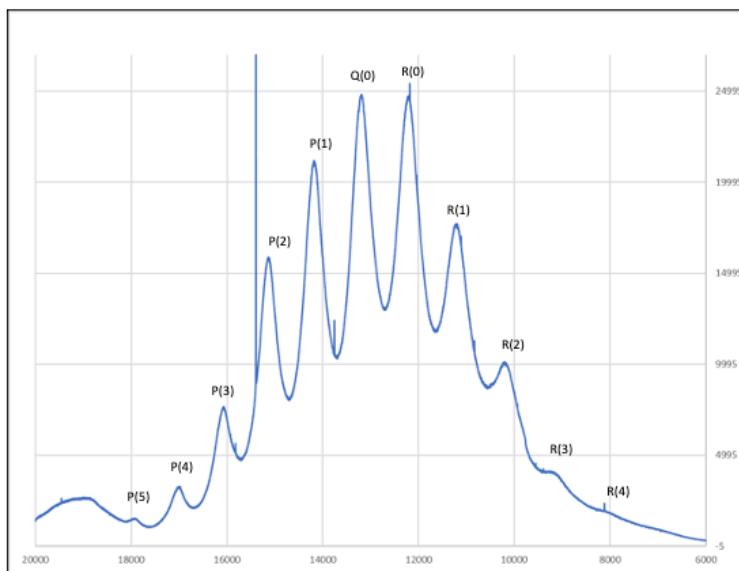
Table 13. Comparison of the theoretical emission energies and assignments, corresponding Raman transition energies, and observed Raman peaks.

Assignment	Emission Calculated (cm^{-1})	Calculated Raman (cm^{-1})	Raman Experimental (cm^{-1})	Difference (%)
P(5)	12,721	18,056	17,873	-1.0
P(4)	13,695	17,082	16,975	-0.6
P(3)	14,668	16,109	16,055	-0.3
P(2)	15,642	15,135	15,106	-0.2
P(1)	16,615	14,162	14,157	0
Q(0)	17,589	13,188	13,188	0
R(0)	18,563	12,214	12,174	-0.3
R(1)	19,536	11,241	11,172	-0.6
R(2)	20,510	10,267	10,159	-1.1
R(3)	21,483	9,294	9,097	-2.1
R(4)	22,457	8,320	8,090	-2.8

The 325 nm Raman spectrum recorded with a Semrock long-pass edge filter (BLP01-325R-25) having an edge wavelength of 331 nm and Tavg > 93% 334.1 – 900 nm is shown in Figure 23B. The first, second, third, and fourth order of the 1000 cm^{-1} spaced series of lines was observed confirming the assignment of ½ energy ro-vibrational spectrum of $H_2(1/4)$ rather than Raman transitions or high energy matrix fluorescence emission due to 325 nm laser excitation.

Figure 23B. Raman-mode photoluminescence spectrum of ball milled KOH-KCl recorded with a Horiba Jobin Yvon LabRam ARAMIS spectrometer with a 325nm laser and a 300 line/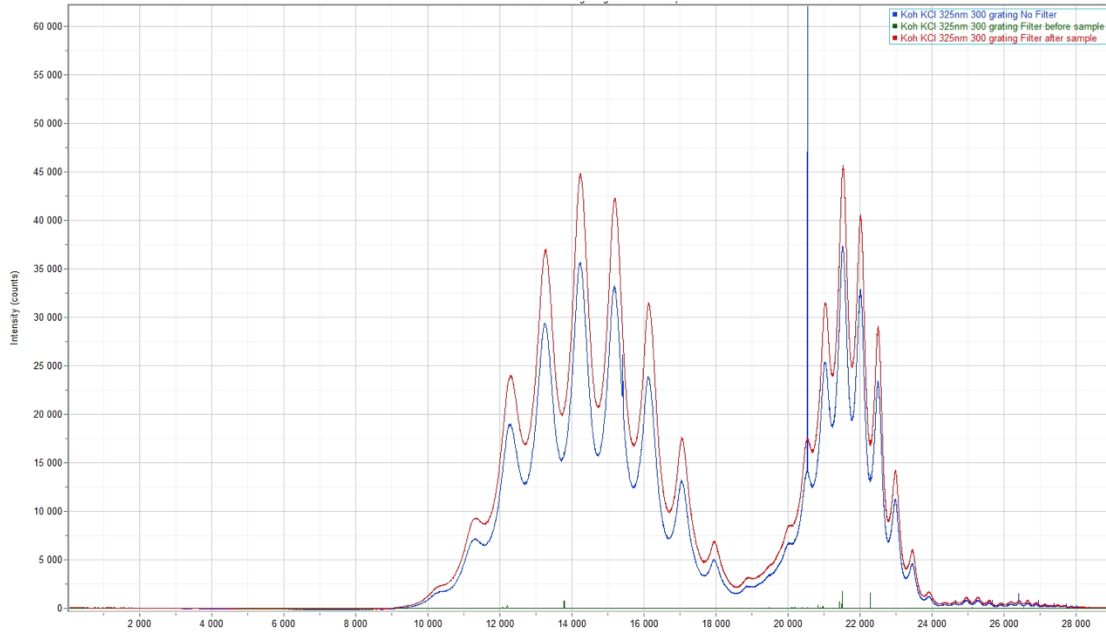mm grating over a range of 8000-19,000 cm^{-1} Raman shift using a Semrock long-pass edge filter (BLP01-325R-25). The two-photon first order $H_2(1/4)$ ro-vibrational emission lines were observed with the corresponding second, third, and fourth order lines.

Regarding the nature of the ½ energy spectral emission, consider the formation of a nonradiative state H_2 molecule from two non-radiative $n=1$ state H atoms requiring the bond energy to be removed by a third body collision:

$$H + H + M \rightarrow H_2 + M* \tag{45}$$

Wherein $M*$ denotes the third body in an energetic state. The hydrino molecule comprises two hydrogen isotope nuclei and two electrons in a single molecular orbital (MO). Uniquely the MO comprises a paired and unpaired electron. To conserve spin angular momentum during the formation of a bond between two hydrino atoms, the bond energy must be released as a neutrino such as an electron neutrino of spin ½ that serves the function of the third body of $M*$ in Eq. (45):

$$H(1/p) + H(1/p) \rightarrow H_2(1/p) + v_e \tag{46}$$

Specifically, a neutrino comprises a photon having $\dfrac{\hbar}{2}$ angular momentum in its electric and magnetic fields (Neutrinos section of Ref. [1]). During the reaction of Eq. (46), the angular momentum of the reactants is conserved in the products wherein each of the two reacting hydrino

atoms are electron spin ½, and the product molecular hydrino and electron neutrino are also each spin ½.

H$_2$(1/p) rotational and vibrational transitions may be excited by particle collision of sufficient energy of at least that of the excitation energies. Pure ro-vibrational excitation of H$_2$(1/4) was achieved with a high energy electron beam wherein molecular hydrino behaved as a pure rotor, but constrained vibrator as shown by comparison of the ro-vibrational emission of the free gas shown in Figure 33 with the emission of H$_2$(1/4) trapped in a KCl matrix (Figures 22A-B). KCl has essentially no absorption or fluorescence over the spectral region UV to infrared [89]. However, very intense green fluorescence and a series of 1000 cm^{-1} evenly spaced peaks were observed from crystalline KCl having trapped H$_2$(1/4) when irradiated by the 325 nm Raman laser. The identical spectrum was observed for KOH matrix as well.

The selection rules for photon mediated excitation of ro-vibrational transitions must obey spin conservation for the reverse of the reaction given by Eq. (46). The spin of the molecular hydrino MO is $\frac{1}{2}\left(\uparrow\uparrow + \downarrow\uparrow\right)$ where each arrow designates the spin vector of one electron. A mechanism to conserve spin while exciting ro-vibrational levels involves two-photon absorption. Two spin 1 photons, each of ½ the energy of an exited ro-vibrational transition comprise a photon of total spin 1 that couples separately to the spin 0 paired electron and the spin ½ unpaired electron as two spin ½ photons of total spin 1 to excite the ro-vibrational transition with a change of the vibrational and rotational quantum number by $0, \pm 1$ corresponding to the $\hbar$ angular momentum of the excitation photon. The spin ½ electron excitation is anticipated to have a shorter lifetime than that of the spin 0 electron excitation. The corresponding very broad emission and narrower line emission, each of about equal intensity and ½ the energy of the standard ro-vibrational mode, were observed as shown in Figure 24 [78]. The broad fluorescence peak is assigned to the spin ½ ro-vibrational state decay, and the line emission is assigned to spin 1 state ro-vibrational state decay. Specifically, a two photon excitation and fluorescence matches the spectrum observed during 325 nm laser Raman spectroscopy of a KOH matrix that served as a getter for H$_2$(1/4) formed in an electrochemical cell [78] wherein two laser photons, each of 3.82 eV and spin 1 excite a ro-vibrational transition as two concerted excitations, each of ½ the energy ($E = \frac{1}{2}\hbar\omega$) and ½ the angular momentum change ($\frac{\hbar}{2}$) of the transition. The two-photon excitation may be mediated by the presence of the crystalline lattice.

The KOH getter having trapped H$_2$(1/4) having the two-photon emission spectrum shown in Figure 24 also showed the 260 nm band such as that shown in Figure 22 comprising single photon emission. Reversal of the two of two-photon excitation giving rise to two-equal-energy

photons versus single photon fluorescence observed with high-energy electron beam collisional excitation may be due to loss of coherence of the degenerate ½ energy levels of the two-photon excitation mechanism.

Figure 24. The deconvolution of the 325 nm photoluminescence spectrum recorded on a KOH getter of $H_2(1/4)$ gas produced by a CIHT electrochemical cell comprising [Mo/LiBr-LiOH-MgO/NiO] [78], that showed intense (6000 count) e-beam excitation emission of the 260 nm band reveals that the Raman spectrum is the superposition of a fluorescence band of lines of ½-energy the 260 nm band and a separate continuum emission band of the same energy having its maximum intensity at green wavelengths. The black line is the raw data, and the dotted line is the sum of the two deconvolved components.
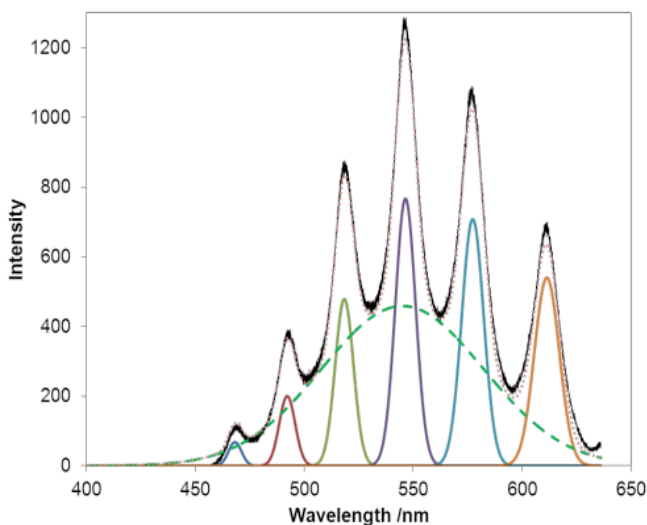
A Raman laser may heat a medium to create broad band matrix emission and a population of $H_2(1/4)$ molecules in the $J = 1$ rotational level. In this case, two-photon emission also occurs wherein rotationally excited $H_2(1/4)$ undergoes stimulated emission as a photon equal to the laser wavelength comprising the photon due to the $H_2(1/4)$ $J = 1$ to $J = 0$ transition and a matrix photon to form a negative peak at the energy of the $H_2(1/4)$ $J = 1$ to $J = 0$ transition. This mechanism known as the Inverse Raman Effect (IRE) may be greatly enhanced on metal surfaces by a mechanism known as a Surface Raman Effect. Raman spectra showing the $H_2(1/4)$ $J = 1$ to $J = 0$ transition IRE peak at the predicted 1950 cm^{-1} were recorded on metal electrodes from hydrated silver shot detonations [2] (Figures 25A-B) and from CIHT cells (Figure 25C) [90] using a Thermo Scientific DXR SmartRaman spectrometer and the 780 nm laser.

Figures 25A-C. Raman spectra obtained on metal electrode surfaces that showed an inverse Raman effect peak at about 1950 cm^{-1} that matches the free rotor energy of $H_2(1/4)$ (0.2414 eV). A. Copper electrodes pre-ignition of an 80 mg silver shot comprising 1 mole% H_2O. B. Post ignition of the hydrated silver shot wherein detonation was achieved by applying a 12 V 35,000 A current with a spot welder [2]. C. Anode of the CIHT comprising [MoNiAl (45.5/45.5/9 wt%)/LiOHeLiBr/NiO] that output 2.40 Wh, 80 mA, at 176% energy gain [90].
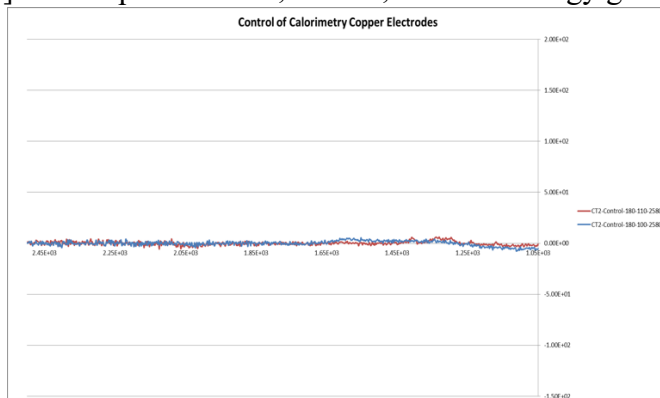
(A)
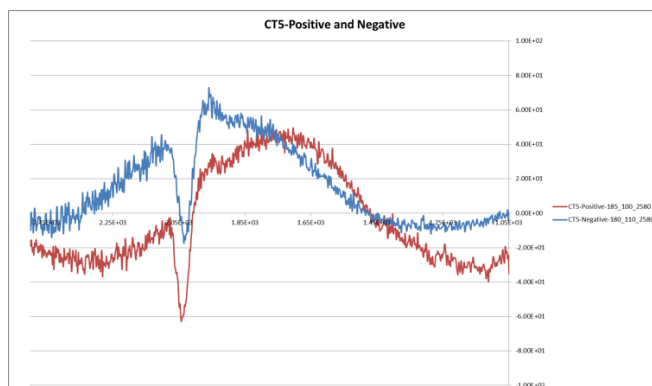
(B)
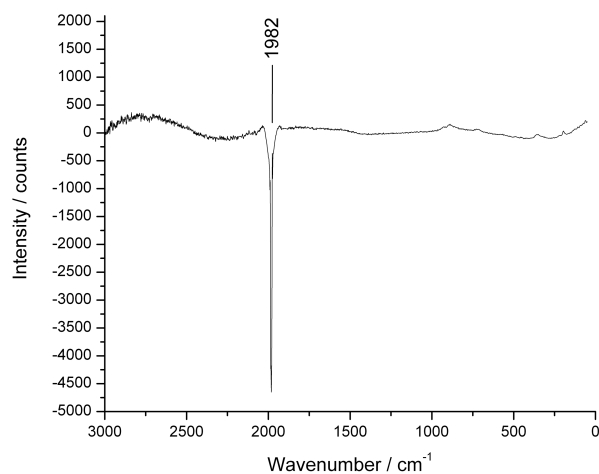
(C)

The observation of the $H_2(1/4)$ IRE from the detonation of hydrated silver shots that produced a shockwave much greater than that of TNT and CIHT cell anodes comprising aluminum, a very important component of energetic materials that reacts with H_2O to form hydrino reactant H, has implications for the design of novel energetic materials. The IRE results were replicated on ball milled alkali hydroxide-alkali halide mixtures at ThermoFisher and University of Texas El Paso [91].

The 785 nm Raman spectra of a Ni foil shown in Figures 9A-C, 325 nm Raman spectra were obtained on Ni foils (1 X 1 X 0.1 cm) floated on the molten gallium surface of the SunCell® during a hydrino reaction run of 10-minute duration. Both the hydrino plasma reaction facing and the molten gallium facing surfaces were cloth-wipe-cleaned and analyzed by Raman spectroscopy using a Horiba Aramis Raman spectrometer with a Synapse infrared CCD camera (Model: 354308, S/N: MCD-1393BR-2612, 1024x256CCD Front Illuminated Open Electrode), a 325 nm laser, and a 600 line/mm grating. These lines were not eliminated by a Semrock long-pass edge filter

(BLP01-325R-25) having an edge wavelength of 331 nm and Tavg > 93% 334.1 – 900 nm placed between the 325 nm laser and the sample, nor with the filter placed between the sample and the detector. From the spectrum of the 325 nm laser, only one high intensity line at 587.8 nm (17,011.2 cm^{-1}) was observed that is capable of exciting transitions observed as 325 nm Raman lines in the 12,000-15,000 cm^{-1} energy region corresponding to emission in the 15,777-18,777 cm^{-1} energy region. The Raman spectra (12,250 cm^{-1} to 14,750 cm^{-1}) are shown in Figure 26A with corresponding emission assignments given in Table 14A. The energies $E_{Emission}$ of the novel emission lines that are nearly resonant with the 587.8nm laser line matched the double transition for final rotational quantum numbers (Eq. (38)) $J'_p = 3; J'_c = 1,2$ with energies given by the sum of the independent transitions. Corresponding spin-orbital coupling energy (Eq. (22)) and fluxon linkage energies (Eqs. (23) and (24)) were also observed with the double transitions:

$$E_{Emission} = \Delta E_{J=0 \rightarrow J'_p=3} + \Delta E_{J=0 \rightarrow J'_c=1,2} + E_{S/O,rot} + E_{\Phi,rot}$$
$$= 15,602\ cm^{-1}\left(19,502\ cm^{-1}\right) + m528\ cm^{-1} + m_{\Phi}31\ cm^{-1} + m_{\Phi 3/2}46\ cm^{-1}$$

(47)

Figure 26A. The 325 nm Raman spectrum (12,250-14,750 cm^{-1}) obtained on the plasma and molten gallium exposed surfaces of a Ni foil maintained in a SunCell® during a hydrino plasma reaction for 10 minutes showing a series of emission peaks due 587.8 nm laser line excitation. All the novel Ni foil emission lines shown in Figure 26A matched those given by Eq. (47). A laser line was observed at 13,750 cm^{-1}.
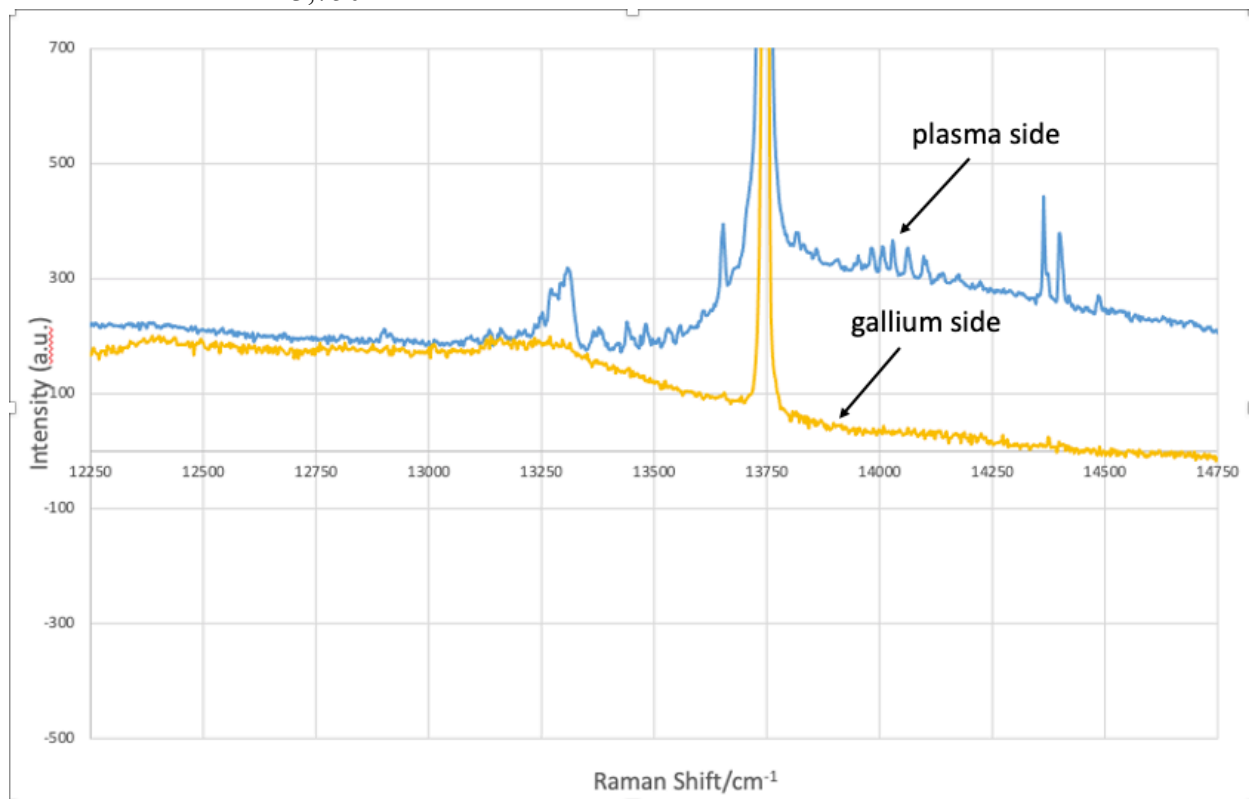
Table 14A. H$_2$(1/4) Raman lines and corresponding hydrino assignments for the 325 nm Raman spectrum (12,250-14,750 cm^{-1}) obtained on the plasma exposed surface of a Ni foil maintained in a SunCell® during a hydrino plasma reaction for 10 minutes (Figure 26A) with assignment given by Eq. (47). Delta is the difference between the observed and theoretical lines.

Observed Lines (cm^{-1})	Emission Line (cm^{-1})	Rotational Energy (cm^{-1})	m	m_Φ	$m_{\Phi3/2}$	Theoretical (cm^{-1})	Delta (cm^{-1})	Observed Raman Lines (Å)	DIB (Å)
12,911	17866.2	19502	-3	0	-1	17871.8	-5.63	5597	5599.7
13,095	17682.2	19502	-3.5	1	0	17684.8	-2.63	5655	5645.49
13,142	17635.2	19502	-3.5	-0.5	0	17638.6	-3.43	5670	5669.33
13,169	17608.2	19502	-3.5	0	-1	17607.8	0.37	5679	
13,211	17566.2	19502	-3.5	0	-2	17561.6	4.57	5693	
13,258	17519.2	19502	-4	0	3	17528.6	-9.43	5708	5705.08
13,288	17489.2	19502	-4	0	2	17482.4	6.77	5718	5719.48
13,316	17461.2	19502	-4	0	1.5	17459.3	1.87	5727	
13,387	17390.2	15602	3.5	0	-1.5	17380.7	9.47	5750	5753.47
13,424	17353.2	15602	3.5	0	-2	17357.6	-4.43	5763	5762.74
13,445	17332.2	15602	3.5	0	-2.5	17334.5	-2.33	5770	5769.92
13,485	17292.2	15602	3	2	1	17293.8	-1.63	5783	5785.04
13,515	17262.2	15602	3	1	1	17263.0	-0.83	5793	5793.21
13,539	17238.2	15602	3	0	1	17232.2	5.97	5801	5797.06
13,564	17213.2	15602	3	1	0	17216.8	-3.63	5810	5809.23
13,586	17191.2	15602	3	0	0	17186.0	5.17	5817	5818.72
13,615	17162.2	15602	3	-1	0	17155.2	6.97	5827	5828.47
13,655	17122.2	15602	3	0	-1.5	17116.7	5.47	5840	5840.66
13,820	16957.2	15602	2.5	1	0	16952.8	4.37	5897	5900.58
13,839	16938.2	15602	2.5	0.5	0	16937.4	0.77	5904	5904.63
13,853	16924.2	15602	2.5	0	0	16922.0	2.17	5909	5910.57
13,866	16911.2	15602	2.5	0	0	16922.0	-10.83	5913	5913.74
13,912	16865.2	15602	2.5	-2	0	16860.4	4.77	5929	5928.86
13,959	16818.2	15602	2.5	-2	-1	16814.2	3.97	5946	5945.54
13,976	16801.2	15602	2.5	-1	-2	16798.8	2.37	5952	5952.26
13,985	16792.2	15602	2.5	0	-3	16783.4	8.77	5955	5954.25
14,010	16767.2	15602	2	2	1	16765.8	1.37	5964	5962.89
14,032	16745.2	15602	2	0	2	16750.4	-5.23	5972	5973.81
14,067	16710.2	15602	2	0	1	16704.2	5.97	5984	5982.67
14,107	16670.2	15602	2	0.5	0	16673.4	-3.23	5999	5999.54
14,140	16637.2	15602	2	0	-0.5	16634.9	2.27	6011	6010.75
14,182	16595.2	15602	2	0	-1.5	16588.7	6.47	6026	6027.68
14,210	16567.2	15602	2	0	-2	16565.6	1.57	6036	6037.63
14,225	16552.2	15602	2	-0.5	-2	16550.2	1.97	6042	6048.6
14,365	16412.2	15602	1.5	0.5	0	16409.4	2.77	6093	6093.4

14,402	16375.2	15602	1.5	-0.5	0	16378.6	-3.43	6107	6107.16
14,426	16351.2	15602	1.5	0	-1	16347.8	3.37	6116	6116.84
14,493	16284.2	15602	1.5	-0.5	-2	16286.2	-2.03	6141	6142.09

Thirty-five of the observed emission lines match those of unassignable astronomical lines associated with the interstellar medium called diffuse interstellar bands (DIBs). The assignment of all the 380 DIBs listed by Hobbs [27] to $H_2(1/4)$ rotational transitions with spin-orbital splitting and fluxon sub-splitting are given in the Appendix.

The addition of water to the complex with $GaOOH:H_2(1/4))$ was tested as a means to suppress the intense fluorescence observed with the UV 325 nm Raman laser irradiation of GaOOH. A sample comprising 50:50 vol% $GaOOH:H_2(1/4):H_2O$ analyzed by 325 nm Raman spectroscopy showed the absence of fluorescent peaks with novel Raman peaks observed in the 14,000 cm^{-1}-15,000 cm^{-1} region. The Raman peaks are shown in Figure 26B and assigned in Table 14A to the double transition $J_p^{'} = 3; J_c^{'} = 1$ with spin-orbital coupling and fluxon linkage. Within experimental error, many of the lines of matched those of obtained on Ni foil shown in Figure 26A having the same assignment (Table 14B).

These lines were observed to be very sensitive to elimination with UV irradiation by the 325 nm Raman laser wherein at least one of the complex $GaOOH:H_2(1/4):H_2O$ or the compound $GaOOH:H_2(1/4)$ decomposed upon prolonged UV irradiation. The sensitivity necessitated the acquisition of the spectrum in short spectral-range intervals such as the one shown in Figure 26B.

Figure 26B. The 325 nm Raman spectrum (14,000-15,000 cm^{-1}) obtained on 50:50 vol% $GaOOH:H_2(1/4):H_2O$ showing a series of peaks assigned to $H_2(1/4)$ emission from the state having a double transition $J_p^{'} = 3; J_c^{'} = 1$ with spin-orbital coupling and fluxon linkage.
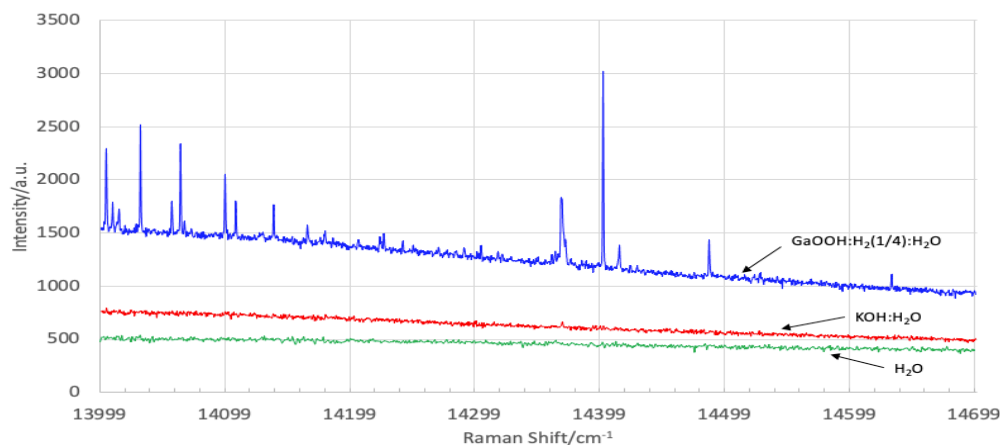
Seventeen of the observed emission lines match those of unassignable astronomical lines associated with the interstellar medium called diffuse interstellar bands (DIBs) as shown in Table 14A where 7 of the DIBs assigned lines of Table 14B matched DIBs assigned lines of Table 14A.

Table 14B. $H_2(1/4)$ Raman lines and corresponding hydrino emission assignments (Eq. (47)) for the 325 nm Raman spectrum (14,000-15,000 cm^{-1}) obtained on 50:50 vol% GaOOH:$H_2(1/4)$:H_2O (Figure 26B).

Observed Lines (cm^{-1})	Emission Line (cm^{-1})	Rotational Energy (cm^{-1})	m	m_Φ	$m_{\Phi 3/2}$	Theoretical (cm^{-1})	Delta (cm^{-1})	Observed Raman Lines (Å)	DIB (Å)
14,003.0	16774.2	15602	2	0	2.5	16773.5	0.67	5962	5962.89
14,031.3	16745.9	15602	2	0	2	16750.4	-4.53	5972	5973.81
14,063.4	16713.8	15602	2	2	0	16719.6	-5.83	5983	5982.67
14,099.1	16678.1	15602	2	0	0.5	16681.1	-3.03	5996	5995.83
14,137.7	16639.5	15602	2	-0.5	0	16642.6	-3.13	6010	6010.75
14,165.7	16611.5	15602	2	0	-1	16611.8	-0.33	6020	6019.32
14,185.4	16591.8	15602	2	-2	0	16596.4	-4.63	6027	6027.68
14,208.7	16568.5	15602	2	0	-2	16565.6	2.87	6036	6037.63
14,226.5	16550.7	15602	2	-0.5	-2	16550.2	0.47	6042	
14,241.8	16535.4	15602	2	-1	-2	16534.8	0.57	6048	6048.6
14,275.0	16502.2	15602	1.5	0.5	2	16501.8	0.37	6060	6059.26
14,279.7	16497.5	15602	1.5	2	1	16501.8	-4.33	6062	
14,295.7	16481.5	15602	1.5	0	2	16486.4	-4.93	6067	6065.28
14,304.5	16472.7	15602	1.5	1	1	16471.0	1.67	6071	6071.31
14,321.6	16455.6	15602	1.5	0.5	1	16455.6	-0.03	6077	6081.1
14,368.9	16408.3	15602	1.5	0.5	0	16409.4	-1.13	6094	6093.4
14,401.7	16375.5	15602	1.5	0	-0.5	16370.9	4.57	6107	6107.16
14,486.9	16290.3	15602	1.5	-0.5	-2	16286.2	4.07	6139	6139.98
14,633.0	16144.2	15602	1	0.5	0	16145.4	-1.23	6194	6194.74

325 nm Raman spectroscopy was also performed on the nickel foil samples having the 785 nm spectra shown in Figures 21K and 21L wherein the samples were prepared by flowing a hydrino reaction mixture comprising 1500 sccm H_2 and 1 sccm O_2 into the one-liter reaction volume SunCell® with molten tin injection to maintain the hydrino plasma reaction. The novel Ni foil emission lines shown in Figure 26C matched those given by Eq. (47) and shown in Figure 26A. A laser line was observed at 13,750 cm^{-1}.

Figure 26C. The 325 nm Raman spectrum (12,250-14,750 cm^{-1}) obtained on the Ni foil sample maintained in a SunCell® during a hydrino plasma reaction for 10 minutes showing the series of emission peaks matching those of Eq. (47) due 587.8 nm laser line excitation. A tin coating on the Ni foil did not show the peaks.

To test the assignment of the high intensity line at 587.8 nm (17,011.2 cm^{-1}) of the 325 nm laser as the source of excitation of the 325 nm Raman lines observed in the 12,000 cm^{-1} to 15,000 cm^{-1} region (Figures 26A and 26B) corresponding to emission in the 15,777 cm^{-1} to 18,777 cm^{-1} energy region according to the assignments of Tables 14A and 14B, Raman spectra were acquired on matching nickel foil samples using the Horiba Jobin Yvon LabRAM Aramis Raman spectrometer with a 0.42 mW 442 nm laser, 50X long working distance objective, and the 300 line/mm grating. Exemplary 325 nm Raman spectral results on nickel foil samples exposed to the SunCell® hydrino reaction plasma using gallium as the injected molten metal are shown in Figure 26A. A corresponding exemplary 442 nm Raman spectrum is shown in Figure 26D. A series of peaks were observed in the 14,150 cm^{-1} to 14,775 cm^{-1} region that were not observed for silicon wafer, Teflon, and control Ni foil samples shown in Figures 26D and 26E, respectively. The novel lines match second order emission lines wherein the first order lines were observed in the 5750 cm^{-1} to 6890 cm^{-1} region as shown in Figure 26F. The novel series of lines do not match first or second order laser lines as shown by the absence of these lines in the either corresponding spectral region as shown Figures 26G and 26E, respectively. The novel emission line assignments that match those in Tables 14A and 14B given by Eq. (47) are given in Table 14C. The 442 Raman results confirm the excitation mechanism of the 325 laser. The first order and second order lines

were also observed on Ni foils maintained in a SunCell® during a hydrino plasma reaction with tin as the injected molten metal.

Figure 26D. The 442 nm Raman spectrum (13,000 cm^{-1} to 15,000 cm^{-1}) obtained on the plasma and molten gallium exposed surfaces of a Ni foil maintained in a SunCell® during a hydrino plasma reaction for 10 minutes showing a series of emission peaks due 442 nm laser line excitation. All the novel Ni foil lines matched second order emission lines of first order emission lines given by Eq. (47).

Figure 26E. The 442 nm Raman spectra (13,000 cm^{-1} to 15,000 cm^{-1}) obtained on control samples comprising silicon wafer (bottom), nickel foil (middle), and Teflon (top).
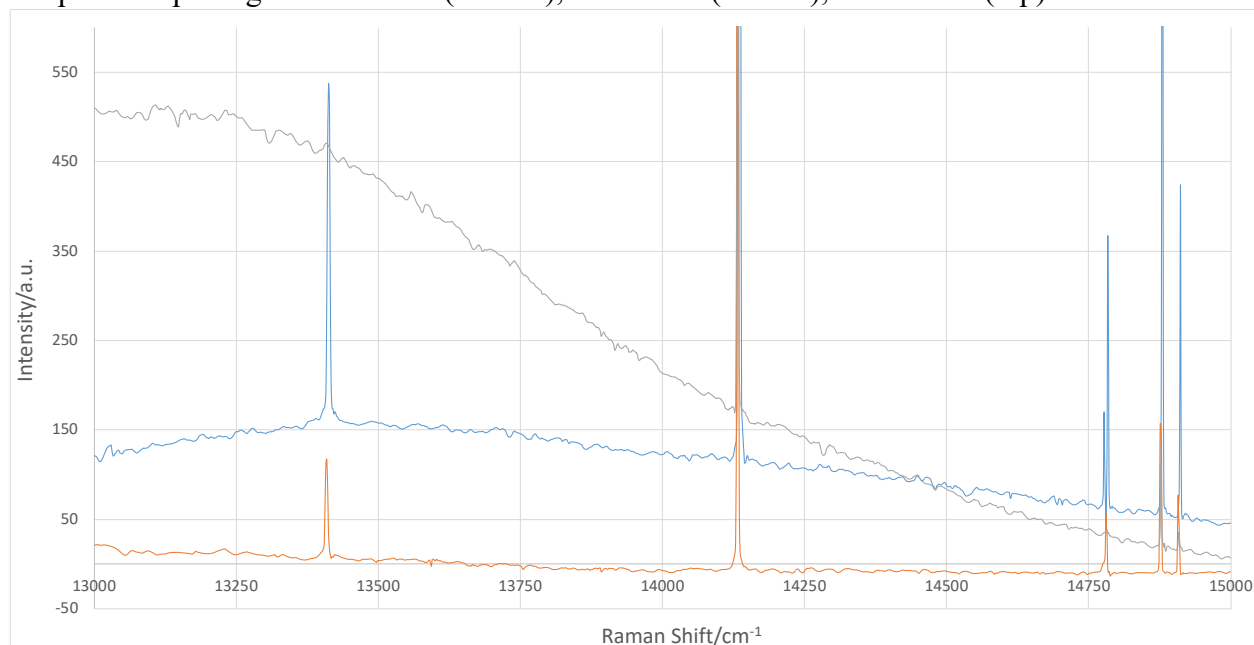
Figure 26F. The 442 nm Raman spectrum (5000 cm^{-1} to 8000 cm^{-1}) obtained on the plasma and molten gallium exposed surfaces of a Ni foil maintained in a SunCell® during a hydrino plasma reaction for 10 minutes showing a series of emission peaks due 442 nm laser line excitation. All the novel Ni foil lines matched first order emission lines given by Eq. (47).
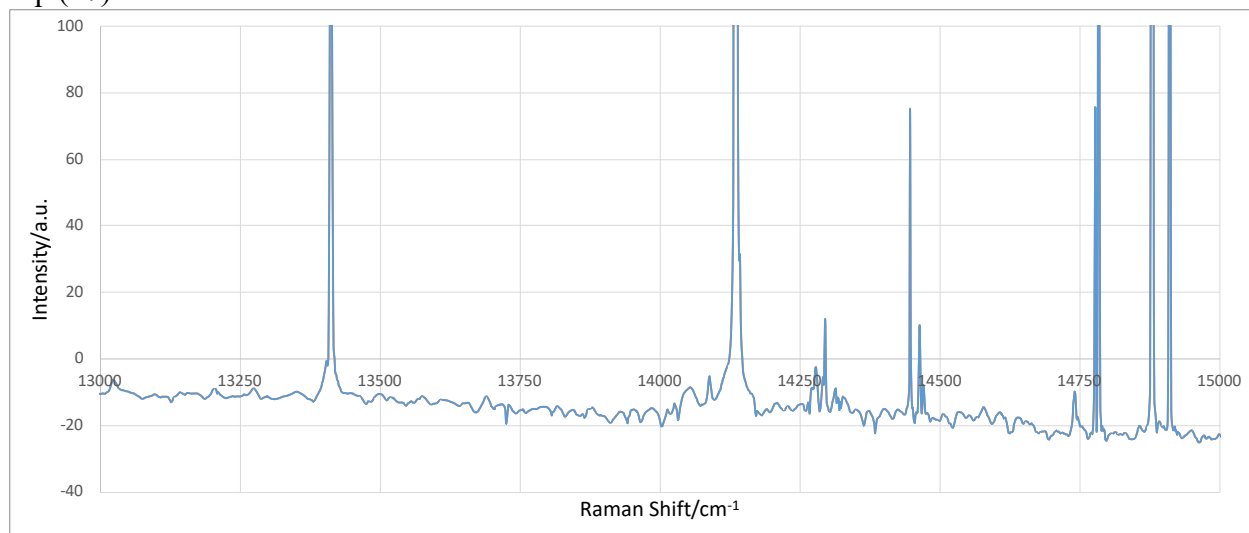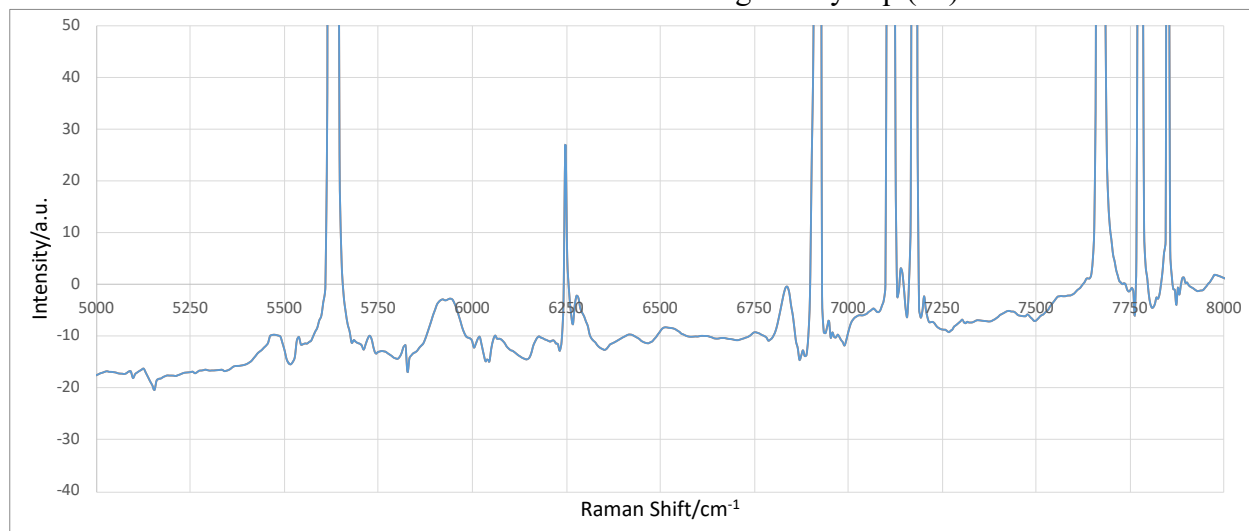
Figure 26G. The 442 nm Raman spectra (5000 cm^{-1} to 8000 cm^{-1}) obtained on control samples comprising silicon wafer (bottom), nickel foil (middle), and Teflon (top).
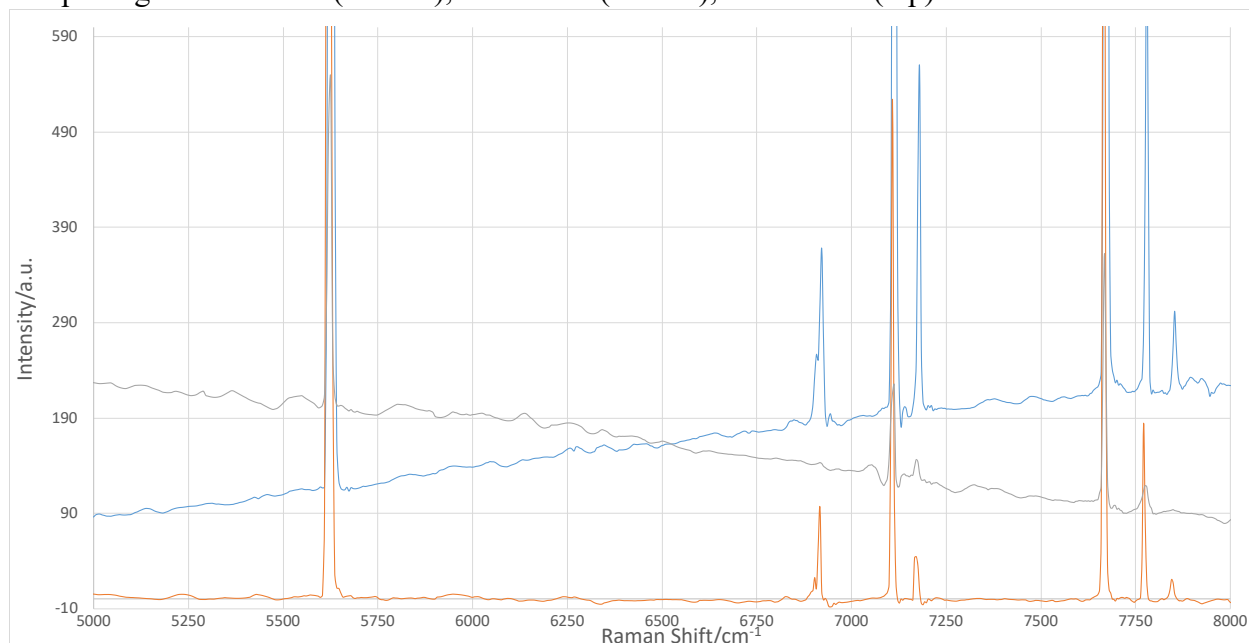
Table 14C. H$_2$(1/4) Raman lines and corresponding hydrino assignments for the 442 nm Raman spectrum (13,000-15,000 cm^{-1}) obtained on the plasma exposed surface of a Ni foil maintained in a SunCell® during a hydrino plasma reaction for 10 minutes (Figures 26D and 26F) with assignment given by Eq. (47). Delta is the difference between the observed and theoretical lines.

Observed Lines (cm^{-1})	2° Emission Line (cm^{-1})	1° Emission Line (cm^{-1})	Rotational Energy (cm^{-1})	m	m_Φ	$m_{\Phi 3/2}$	Theoretical (cm^{-1})	Delta (cm^{-1})	Observed Raman Lines (Å)	DIB (Å)
14,267	8363.3	16726.5	15602	2	2	0	16719.6	7	5979	5975.75
14,273	8357.3	16714.5	15602	2	1	0.5	16711.9	3	5983	5982.67
14,280	8350.3	16700.5	15602	2	0	1	16704.2	-4	5988	5988.11
14,293	8337.3	16674.5	15602	2	0.5	0	16673.4	1	5997	5995.83
14,296	8334.3	16668.5	15602	2	0.5	0	16673.4	-5	5999	5999.54
14,318	8312.3	16624.5	15602	2	-1	0	16627.2	-3	6015	6014.81
14,325	8305.8	16611.5	15602	2	0	-1	16611.8	0	6020	6019.32
14,333	8297.0	16593.9	15602	2	-2	0	16596.4	-2	6026	6027.68
14,447	8183.3	16366.5	15602	1.5	0	-0.5	16370.9	-4	6110	6109.88
14,465	8165.3	16330.5	15602	1.5	0	-1.5	16324.7	6	6123	
14,473	8157.8	16315.5	15602	1.5	-1	-1	16317.0	-1	6129	
14,742	7888.3	15776.5	15602	0.5	0	-2	15773.6	3	6339	6338

Of the 12 observed novel emission lines, 10 lines match those of unassignable astronomical lines associated with the interstellar medium called diffuse interstellar bands (DIBs). The assignment of all the 380 DIBs listed by Hobbs [27] to H$_2$(1/4) rotational transitions with spin-orbital splitting and fluxon sub-splitting are given in the Appendix.

5 Additional Hydrino Spectroscopies and Energetic Measurements

Next, X-ray photoelectron spectroscopy (XPS) confirmation of molecular hydrino $H_2(1/4)$ in GaOOH:H₂(1/4) was performed by measuring the $H_2(1/4)$ total energy in the 500 eV region predicted by Mills Eq. (11.240) [1] wherein the double ionization is a required selection rule. A series of XPS analyses were performed on GaOOH:H₂(1/4) using a nonmonochromatic Mg Kα (1254 eV) excitation source with the XPS spectra recorded using a SPECS GmbH system with a PHOIBOS 150 hemispherical energy analyzer. $C\ 1s$ at $284.5\ eV$ was used as the internal standard. The peak shown in Figure 27 at 496 eV was assigned to $H_2(1/4)$ wherein other possibilities such Sn, W, and Ir were eliminated since the corresponding peaks of these candidates were absent. Cu is from the TEM grid used to mount the fibers.

Figure 27. The XPS spectrum of GaOOH:H₂(1/4) showing the $H_2(1/4)$ total energy peak at 496 eV.
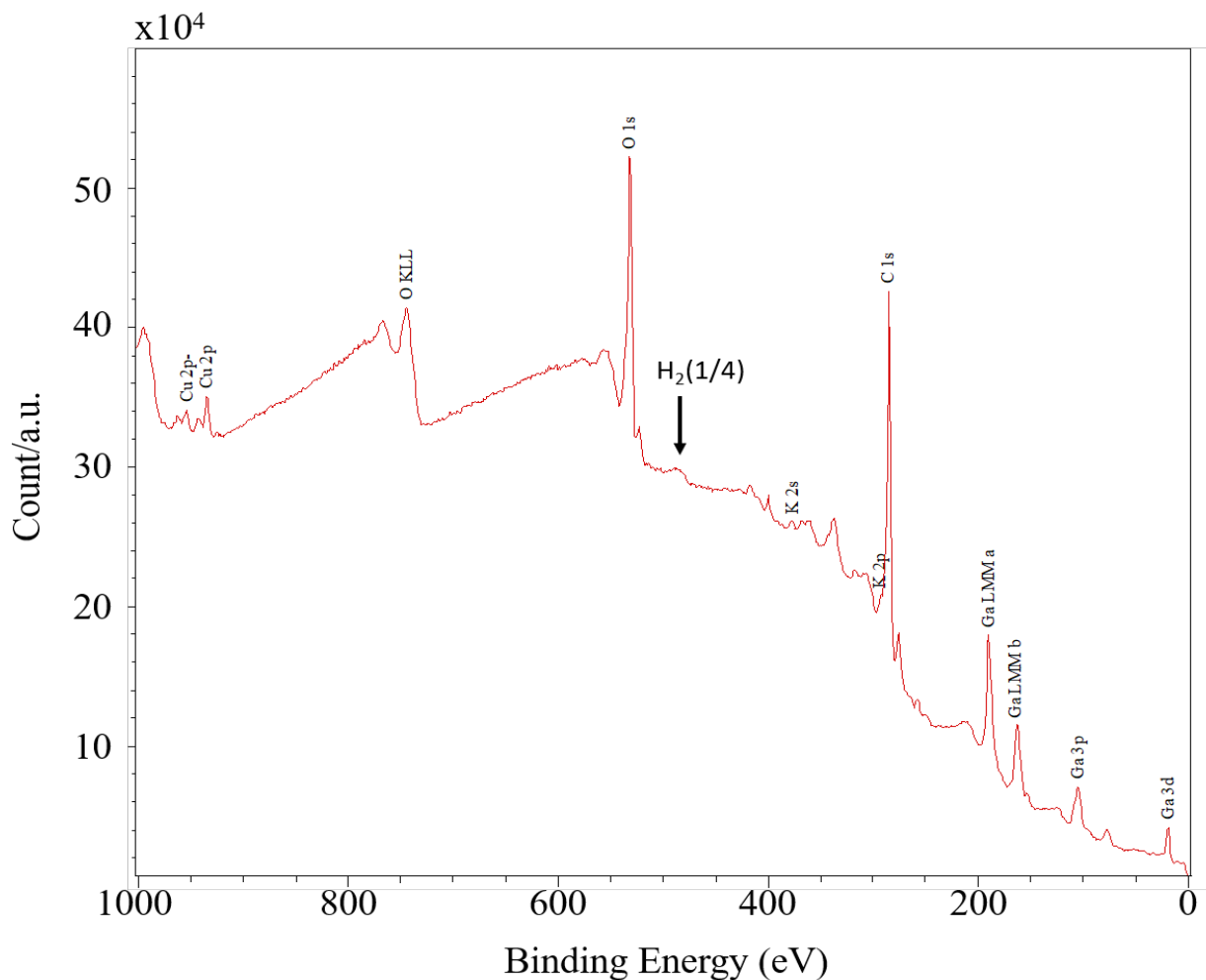
The H$_2$(1/4) total binding energy was further confirmed on copper electrodes before and after the ignition of 80 mg silver shots comprising 1 mole% H$_2$O. The peak power of 20 MW was measured on the ignited shots using absolute spectroscopy over the 22.8-647 nm region wherein the optical emission energy was 250 times the applied energy [2]. The corresponding XPS spectrum on tungsten-coated copper electrodes post ignition of an 80 mg silver shot comprising 1 mole% H$_2$O, wherein the detonation was achieved by applying a 12 V 35,000 A current with a spot welder is shown in Figure 28. The peak at 496 eV was assigned to H$_2$(1/4) wherein other possibilities such Na, Sn, and Zn were eliminated since the corresponding peaks of these candidates are absent.

Figure 28. XPS spectrum on copper electrode post ignition of a 80 mg silver shot comprising 1 mole% H$_2$O, wherein the detonation was achieved by applying a 12 V 35,000 A current with a spot welder.
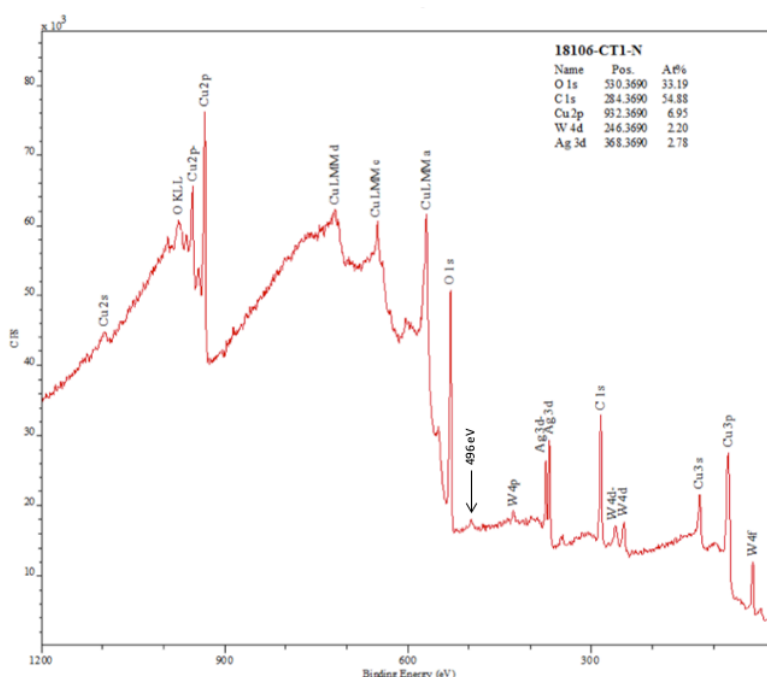
H$_2$(1/4) was further identified by gas chromatography of gas collected from the SunCell®. H$_2$(1/4) gas was collected from the SunCell® using a valved microchamber connected to the vacuum line and cooled to 15 K by a cryopump system (Helix Corp., CTI-Cryogenics Model SC compressor; TRI-Research Model T-2000D-IEEE controller; Helix Corp., CTI-Cryogenics model 22 cryodyne). The liquefied gas was warmed to room temperature to achieve 10 Torr chamber pressure and was injected into an HP 5890 Series II gas chromatograph with a capillary column

(Agilent molecular sieve 5 Å, (50 m x 0.32 mm, df = 30 μm)) at 303 K (30 °C), argon carrier gas, and a thermal conductivity detector (TCD) at 60 °C. $H_2(1/4)$ was observed as an early peak at 10.92 minutes and $H_2(1/4)$ that co-condensed with H_2 gas was observed at 12.7 minutes (Figure 29). The peak at 18 minutes is oxygen that was condensed before the SunCell® run to serve as a solvent for $H_2(1/4)$. The collected gas contained no helium by mass spectroscopy. The early peak was negative with a helium carrier gas indicating that the early peak had a higher thermal conductivity, and the migration rate was faster than that of helium with an argon carrier gas. No known gas has a faster migration rate and higher thermal conductivity than H_2 or He which is characteristic of and identifies hydrino since it has a much greater mean free path due to exemplary $H_2(1/4)$ having 64 times smaller volume and 16 times smaller ballistic cross section. Hydrogen condensed under pressure and temperature conditions that violate the Clausius Clapeyron equation due to the raising of the H_2 liquefaction temperature by co-condensation with $H_2(1/4)$.

Figure 29. The gas chromatograph of gas collected from the SunCell® by a cryopump showing $H_2(1/4)$ at 10.92 minutes and hydrogen that co-condensed with $H_2(1/4)$ gas was observed at 12.7 minutes.
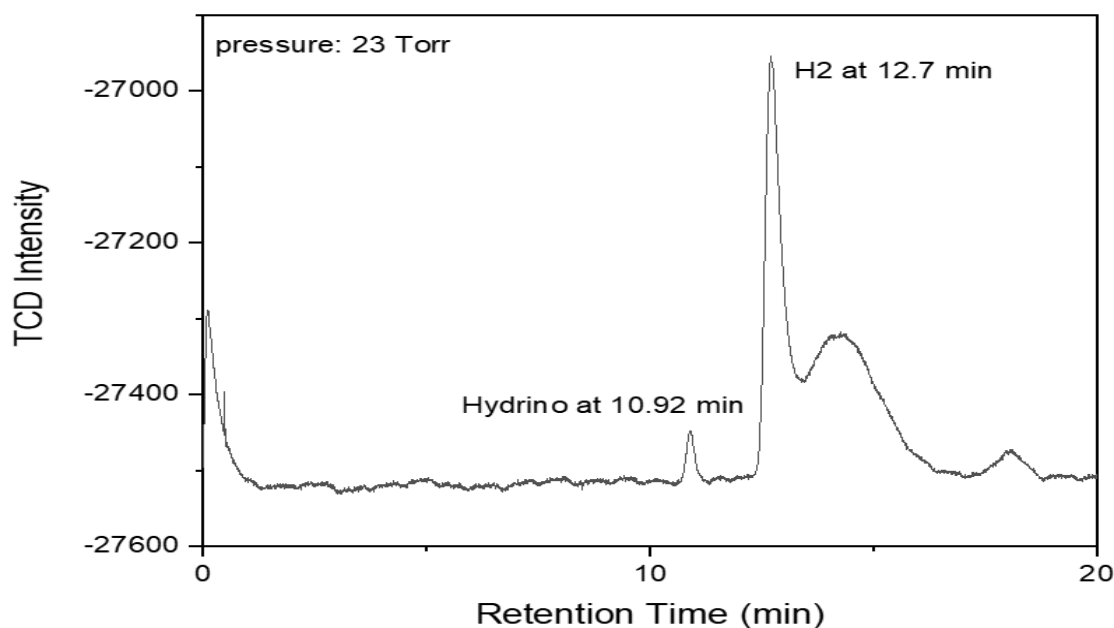
The SunCell® was operated for one hour at excess power levels of over 100 kW with the intention of forming molecular hydrino states $H_2(1/p)$ with $p = 4$ and $p > 4$, possibly $p = 17$. The HOH catalyst reaction of H to hydrino atom $H(1/4)$ is given by Eqs. (1-4). Hydrino atoms have a potential energy of an integer multiple of 27.2 eV matching the hydrino catalyst criterion. Thus, hydrino atoms serving as catalysts may react with H to form lower energy states than those

of the catalysts. A favored reaction is the catalysis of H to $H(1/17)$ by $H(1/4)$ serving as the catalyst (Mills Eqs. (5.76-5.79)) [1]. A characteristic signature of this reaction is the emission of broad soft X-ray radiation of 3.48 keV. A broad X-ray peak with a 3.48 keV cutoff was observed in the Perseus Cluster by NASA's Chandra X-ray Observatory and by the XMM-Newton that has no match to any known atomic transition. The 3.48 keV feature assigned to dark matter of unknown identity by Bulbul et al. [16,18] matches the $H\left[\dfrac{a_H}{4}\right]+H\left[\dfrac{a_H}{1}\right]\rightarrow H\left[\dfrac{a_H}{17}\right]$ transition. The identification of molecular hydrino SunCell® products such as $H_2(1/17)$ that result from hydrino serving as a catalyst was sought using gas chromatography. A small reproducible peak shown in Figure 30 that is a candidate for $H_2(1/17)$ was observed in cryogenically collected SunCell® gases.

Figure 30. Gas chromatograph of gas collected from the SunCell® by a cryopump showing $H_2(1/p)$ at 1.95 minutes that may be $H_2(1/17)$.
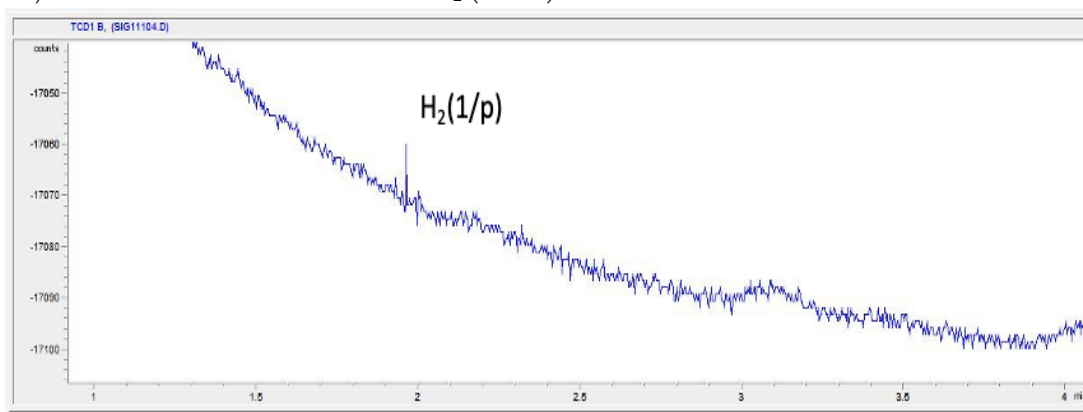
Since molecular hydrino absorbs on metals as shown by the Raman spectroscopy (Figures 9A-C), gallium-transition metal alloys were formed during the propagation of a hydrino plasma reaction in the SunCell®, and solid samples were isolated as a source of molecular hydrino gas release by thermal desorption. The SunCell® comprising Cr-Mo stainless steel reaction vessel walls was operated at a gallium temperature of 600°C, a temperature above the threshold for the formation of gallium-transition metal alloys. Additionally, the hydrino plasma mixture, 2000 sccm H_2/10 sccm O_2, was richer in oxygen than typical to form some gallium oxide to additionally absorb molecular hydrino. Following a 30-minute plasma run, 3 grams of solid material was collected from the molten SunCell® gallium. The solid sample was mixed with excess aqueous 4 M KOH (Alfa Aesar, flake 85%, AAA161990C) for 24 hours, then the solution was filtered using a Buchner funnel, side-arm flask, and filter paper (Whatman™, Grade 50, 09-865C; high-quality cotton liners, high wet-strength, and chemical resistance). By X-ray diffraction, the KOH-treated

Ga$_2$O$_3$ collected from SunCell® plasma runs comprised Ga$_2$O$_3$, GaOOH, gallium-stainless steel metal alloys (~0.1-5%) such as iron-gallium, nickel gallium, and chromium-gallium alloys, alloy oxides, and about 1% carbonate. The insoluble solid from the filter paper was placed in a porous thin-walled ceramic crucible. The crucible was placed into a sixty-five-milliliter stainless-steel vessel that was vacuum-sealed using a copper gasket and stainless-steel knife-edge flanged plate having two welded-in ports, one inlet/outlet port, and a port for monitoring pressure changes during and after the test. The sealed stainless-steel vessel was evacuated, leak checked, and loaded into a smelting furnace (ProCast™ 3 kg 110 Volt U.S. Electric Melting Furnace 2102 °F) and heated to 800 °C over a time interval of 25 to 40 minutes wherein the pressure rose from 20 mTorr to between 1520 Torr to 2289 Torr. The stainless-steel vessel was then connected to the inlet sample tube and pneumatic valve of the gas chromatograph. Optimally, the pressure inside the sample tube maintained at least 1000 Torr.

Using an Agilent 8890 gas chromatograph system with a single filament thermal conductivity detector (TCD), gas chromatography was performed on the gases released by thermal desorption of gas bound to the KOH-treated alloy/Ga$_2$O$_3$ sample originally collected from a SunCell® plasma run. Known gases such as hydrogen were also run to identify their migration times to compare to the results of the SunCell®-derived sample. The pressure controller was set at 19 PSI for the flow of argon carrier gas at 5 ml/min on a capillary column (Agilent molecular sieve 5 Å, (50 m x 0.32, df = 30 μm) at 303 K (30 °C) with the TCD at 60 °C. The gas inlet injected a 1000 ul sample onto the column wherein the volume was precision-controlled by electronic pneumatic controllers run by compressed nitrogen. The Agilent 8890 system sensed and compensated for atmospheric pressure fluctuations, and a microchannel-based architecture protected against gas contaminants. The data was analyzed using Agilent OpenLab CDS.

The gas chromatograph of hydrino gas evolved by heating the KOH-treated alloy/Ga$_2$O$_3$ material collected from the SunCell® to 800°C is shown in Figure 31. The known hydrogen peak was observed at 8 minutes, a nitrogen peak was observed at 15 minutes, and a novel peak observed at 6 minutes was assigned to $H_2(1/4)$. The property of molecular hydrino peak having a shorter retention time than any known gas was attributed to its decreased molecular size and corresponding smaller ballistic cross section.

Figure 31. The gas chromatograph of hydrino gas evolved by heating the KOH-treated alloy/Ga$_2$O$_3$ material collected from the SunCell® to 800°C. The known hydrogen peak was observed at 8 minutes, a nitrogen peak was observed at 15 minutes, and a novel peak observed at 6 minutes was assigned to H$_2$(1/4).
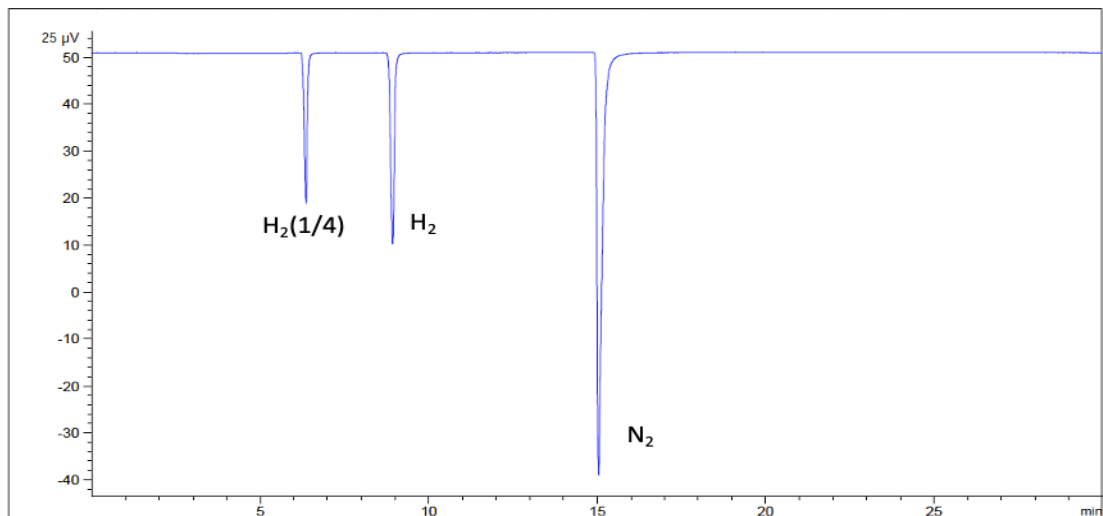
NH$_4$NO$_3$-KCl (10/90 wt%) mixture was ball milled in a stainless-steel chamber using stainless steel balls for 6 hours to form the hydrino product H$_2$(1/4) trapped in the KCl matrix. The H$_2$(1/4) gas was released by the same method as used for the KOH-treated alloy/Ga$_2$O$_3$ sample. The gas chromatograph of hydrino gas evolved by heating ball milled NH$_4$NO$_3$-KCl (10/90 wt%) mixture to 800°C is shown in Figures 32A-B. The novel peak with a retention time of one minute less than that of hydrogen was assigned to H$_2$(1/4).

Figures 32A-B. The gas chromatograph of hydrino gas evolved by heating ball milled NH$_4$NO$_3$-KCl (10/90 wt%) mixture to 800°C. The novel peak with a retention time of one minute less than that of hydrogen was assigned to H$_2$(1/4).
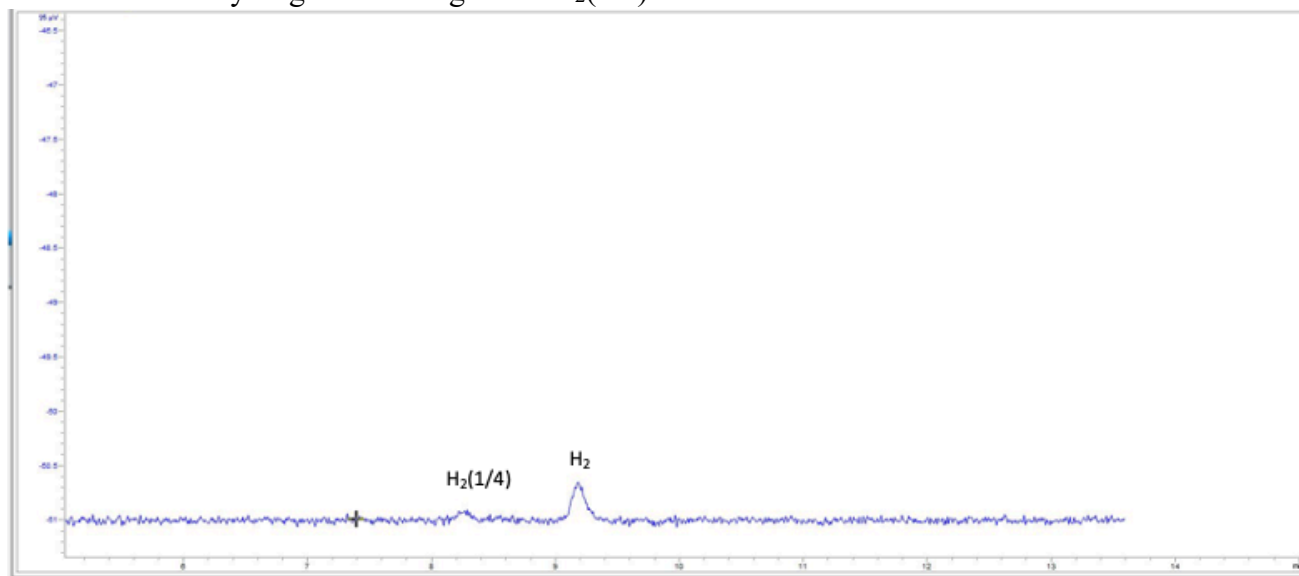
(A)
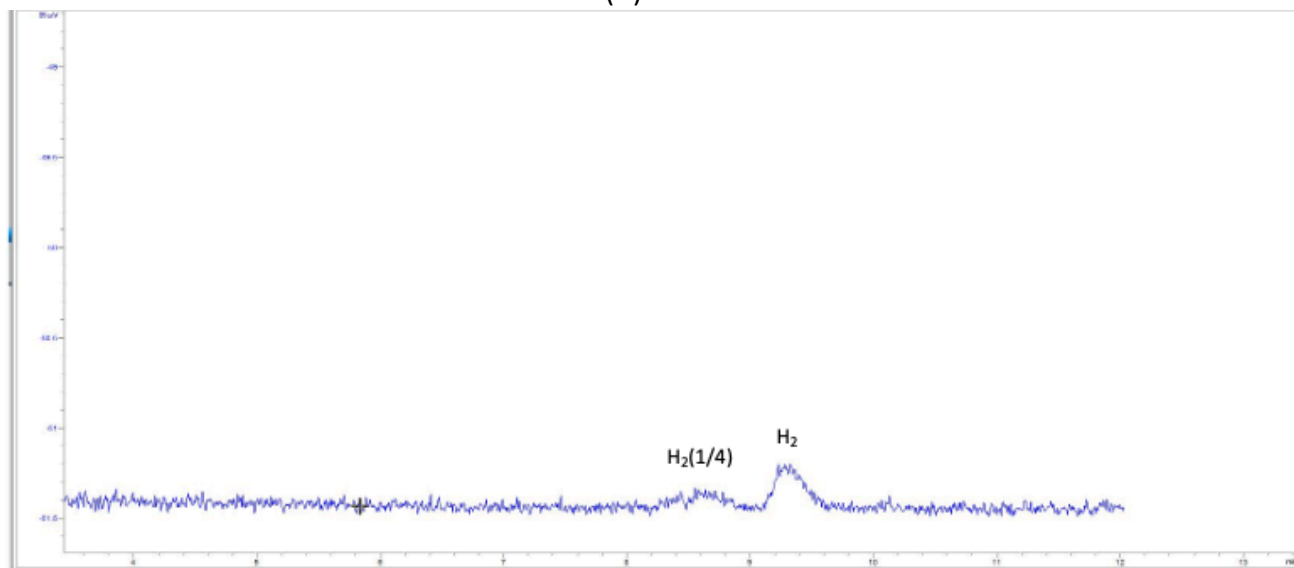
(B)

Using electron beam excitation spectroscopy, H$_2$(1/4) was further identified by ro-vibration emission of H$_2$(1/4) that was shown to be a contaminant of industrial grade commercial argon [64]. As shown in Figure 33, the ro-vibrational spectrum of H$_2$(1/4) was observed as equal-energy-spaced emission lines in the ultraviolet region (130-200 nm) by 12 keV electron beam excitation of the argon gas. The intensity profile, the cutoff of 8.2 eV, and the line spacing of 0.25 eV matched the $v=1$ to $v=0$ vibrational transition with the P-branch rotational spectrum of H$_2$(1/4). The R-branch is not expected to be observed due to the lack of population of ro-vibration

states with the plasma gas temperature being lower than the ro-vibrational excitation temperature. Argon gas is cryo-distilled from the atmosphere. Due to the likeness of boiling points, oxygen co-condenses. Oxygen is removed by adding hydrogen and recombining O_2 on a recombination catalyst. An exemplary recombination catalyst is Pt or Pd on an alumina support. The reaction is $H_2 + O_2$ to H_2O. Recombination catalysts work by creating H atoms and they produce water. Argon greatly increases the concentration of H and HOH (versus water dimers) by interfering with interactions between H atoms and HOH molecules. Commercial argon gas uniquely contains trace H_2 and O_2 that remains after recombination process, and it contains $H_2(1/4)$ due to the recombination reaction.

Figure 33. The ro-vibrational spectrum of $H_2(1/4)$ was observed by 6 keV electron beam excitation of argon gas at atmospheric pressure wherein the electron beam passed through a silicon nitride window of the plasma cell. The cutoff of 8.2 eV and the line spacing of 0.25 eV matched the $\upsilon = 1$ to $\upsilon = 0$ vibrational transition with the P-branch rotational spectrum of $H_2(1/4)$.

H$_2$(1/4) gas of an argon/H$_2$(1/4) mixture formed by recombination of hydrogen and oxygen on a supported noble metal catalyst in an argon atmosphere was enriched by flowing the mixture through a 35 m long, 2.5 mm ID HayeSep® D chromatographic column cooled to a cryogenic temperature in a liquid argon. The argon was partially liquefied to permit the flowing molecular hydrino gas to be enriched as indicated by the dramatic increase in the ro-vibrational P branch of H$_2$(1/4) observed by e-beam excitation emission spectroscopy as shown in Figure 34.

Figure 34. Ultraviolet emission spectrum from electron beam excitation of argon/$H_2(1/4)$ gas wherein the ro-vibrational P branch of $H_2(1/4)$ was greatly enhanced in intensity by flowing the gas mixture through a HayeSep® D chromatographic column cooled to liquid argon temperature.
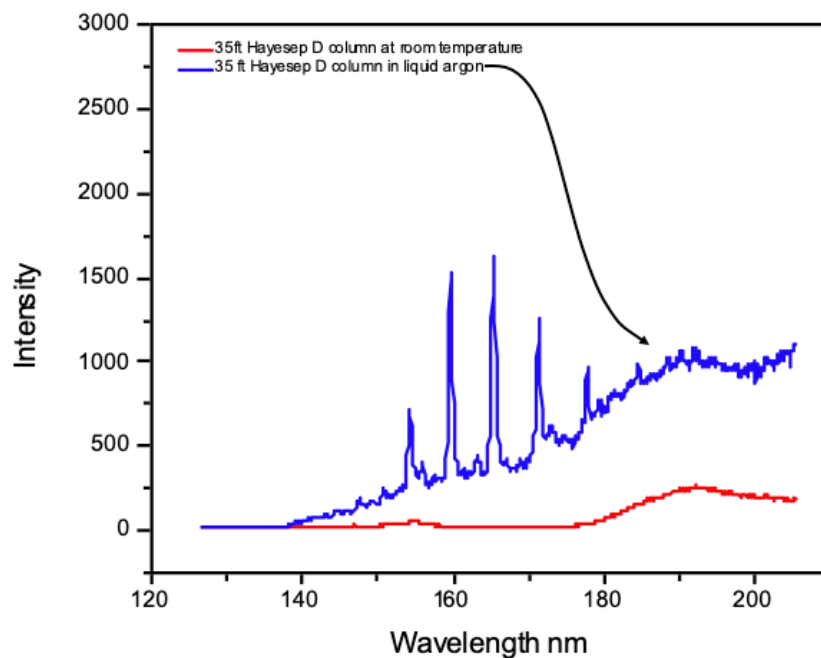
The molecular hydrino gas from the chromatographic column was also liquified with trace air as it was flowed into a valved microchamber cooled to 55 K by a cryopump system (Helix Corp., CTI-Cryogenics Model SC compressor; TRI-Research Model T-2000D-IEEE controller; Helix Corp., CTI-Cryogenics model 22 cryodyne). The liquefied gas was warmed to room temperature to achieve 1000 Torr chamber pressure and was injected on to the Agilent column with argon carrier gas. Oxygen and nitrogen were observed at 19 and 35 minutes, respectively. $H_2(1/4)$ was observed at 6.9 minutes (Figure 35).

Figure 35. The gas chromatograph of molecular hydrino gas enriched using a HayeSep® D chromatographic column cooled to liquid argon temperature, liquified with trace air using a valved microchamber cooled to 55 K by a cryopump system, vaporized by warming to room temperature to achieve 1000 Torr chamber pressure, and injected on to the Agilent column using a HP 5890 Series II gas chromatograph with a thermal conductivity detector and argon carrier gas. Oxygen and nitrogen were observed at 19 and 35 minutes, respectively, and $H_2(1/4)$ was observed at 6.9 minutes.
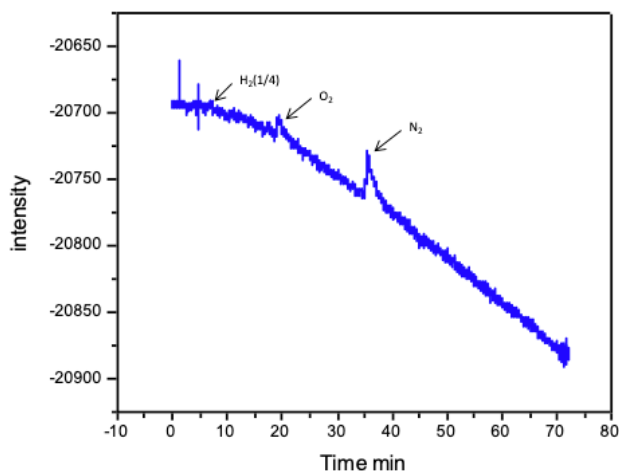
A neon-hydrogen microhollow cathode glow discharge has been proposed as a source of predominantly Lyman α radiation. Kurunczi, Shah, and Becker [50] observed intense emission of Lyman α and Lyman β radiation at 121.6 nm and 102.5 nm, respectively, from microhollow cathode discharges in high-pressure Ne (740 Torr) with the addition of a small amount of hydrogen (up to 3 Torr). With essentially no molecular emission observed, Kurunczi et $al.$ attributed the anomalous Lyman α emission to the near-resonant energy transfer between the Ne_2^* excimer and H_2 which leads to formation of H(n=2) atoms, and attributed the Lyman β emission to the near-resonant energy transfer between excited Ne^* atoms (or vibrationally excited neon excimer molecules) and H_2 which leads to formation of H(n=3) atoms. $H_2(1/4)$ emission intensity was greatly amplified by resonance energy transfer for argon or neon excimers.

As shown in Figure 36, $H_2(1/4)$ was released from heating FeOOH:$H_2(1/4)$. The ultraviolet emission spectrum from electron beam excitation of $H_2(1/4)$ gas showed the ro-vibrational P branch of $H_2(1/4)$ further confirming the Raman assignments. Through resonance energy transfer from the argon excimer band, the $H_2(1/4)$ ro-vibrational band was enhanced in intensity by adding argon gas wherein the argon gas was allowed to stand at atmospheric pressure and 300K for two days to remove any $H_2(1/4)$ gas by diffusion.

Figure 36. Ultraviolet emission spectrum from electron beam excitation of $H_2(1/4)$ gas released from heating FeOOH:$H_2(1/4)$ and mixed with atmospheric pressure argon gas absent $H_2(1/4)$ gas. The cutoff of 8.2 eV and the line spacing of 0.25 eV matched the $\upsilon = 1$ to $\nu = 0$ vibrational transition with the P-branch rotational spectrum of $H_2(1/4)$.
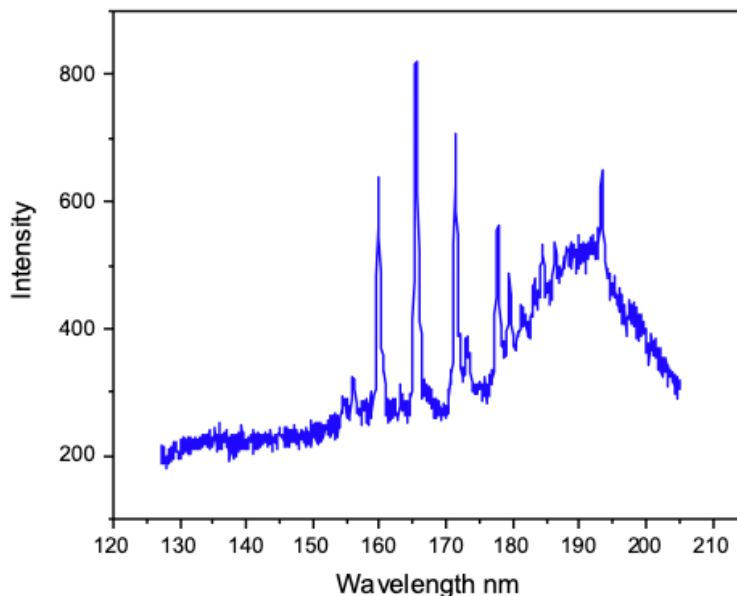

The ro-vibrational spectrum of $H_2(1/4)$ was also recorded on the emission of gas produced from GaOOH:$H_2(1/4)$ and excited by high-energy electron beam bombardment. Three grams of GaOOH:$H_2(1/4)$ was thermally decomposed by heating to 600 °C in a quartz tube reactor for one hour and raising the oven temperature thereafter to 850°C. The gas in the cell was mixed with neon carrier gas at a total pressure of one atmosphere, flowed through a HayeSep® D chromatographic column cooled to -78°C by immersion in a CO_2(s) bath to remove H_2O, and flowed from the column into an electron beam chamber. The chamber gas was excited by a 12 keV to 16 keV electron-beam incident the gas through a silicon nitride window. The emission was observed through a MgF_2 window on the opposite side of the gas chamber relative to the silicon nitride window. Emission from the electron-beam excitation was recorded using a McPherson grazing incidence EUV spectrometer (Model 248/310G) equipped with a platinum-coated 600 g/mm or a platinum-coated 1200 g/mm grating. The angle of incidence was 87°. The wavelength resolution was about 0.05 nm with an entrance slit width of <1 µm. The EUV light was detected by a CCD detector (Andor iDUS Model #: DO420A-BEN-995, Serial #: CCD-24974, Date: 2020) cooled to -60 °C. As shown in Figure 37, the ro-vibrational spectrum of $H_2(1/4)$ was observed as emission lines in the ultraviolet region (130-200 nm) by 12 keV electron beam excitation of the GaOOH:$H_2(1/4)$ decomposition gas. The cutoff of 8.2 eV and the line spacing of 0.25 eV matched the $\upsilon = 1$ to $\nu = 0$ vibrational transition with the P-branch rotational spectrum of $H_2(1/4)$.

Figure 37. Ro-vibrational spectrum of $H_2(1/4)$ that was observed as ultraviolet emission lines by 12 keV electron beam excitation of thermally released GaOOH:$H_2(1/4)$ gas flowed at atmospheric pressure from a cryogenic chromatographic column wherein the electron beam passed through a silicon nitride window of the plasma cell. The cutoff of 8.2 eV and the line spacing of 0.25 eV matched the $\upsilon = 1$ to $\nu = 0$ vibrational transition with the P-branch rotational spectrum of $H_2(1/4)$.
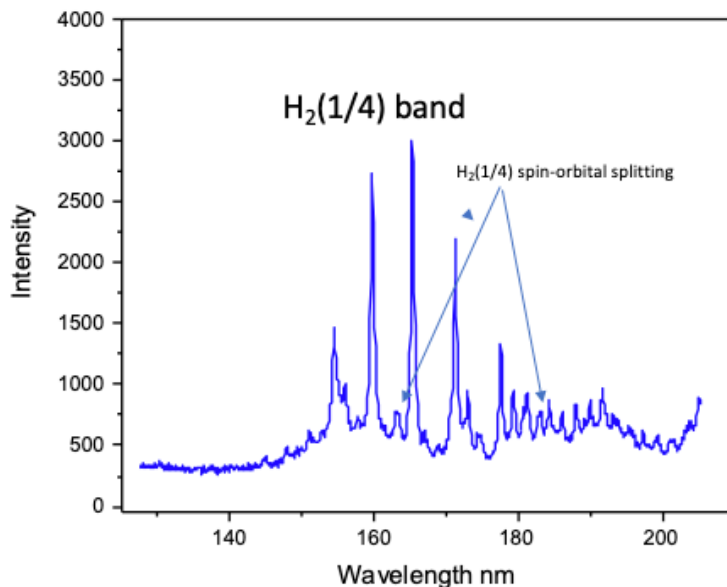
Further consider the EUV spectrum (120-200 nm) of the electron beam emission of argon gas shown in Figure 33. Hydrogen and oxygen are present as evidence by the H I or O I emission at 121.567 nm and 130.5 nm, respectively, in addition to the lines assigned to the ro-vibration of $H_2(1/4)$ given in Table 15. In the latter case, the linear curve fit of the line number versus line energy that matches the ro-vibrational energy of $H_2(1/4)$ is y = -0.260x eV+8.54 eV with a corresponding $R^2 = 0.9997$.

Table 15. The line positions and energies of the EUV spectral lines in the 120-200 nm region assigned to the $H_2(1/4)$ rotational and vibrational transitions corresponding to quantum number changes $J = 0$ to $J' = 1,2,3,4,6,7$ and $v = 1$ to $v = 0$, respectively.

Peak Number	Line Position (nm)	Line Energy (eV)
1	149.4	8.30
2	154.8	8.01
3	160	7.75
4	165.6	7.49
5	171.6	7.22
6	177.9	6.97
7	184.7	6.71
8	191.7	6.47

In addition, a series of small satellite peaks were observed that are associated with the $H_2(1/4)$ ro-vibrational lines as shown in Figures 33, 34, 36, and 37. They are present even in the absence of any atomic emission such as H I or O I emission and in pure gas samples. For example, as shown in Figures 34 and 37, the satellite lines are present in samples of pure gas from cryogenic gas chromatographic separation. These satellite lines match the rotational spin-orbital splitting energies given by Eq. (22), that were also observed by Raman spectroscopy as shown in exemplary Figures 9A-B with assignments given in Table 7B. The spin-orbital splitting energies due to rotation of $m528\ cm^{-1}$, $m = 1,1.5$ wherein 1.5 involves the $m = 0.5$ and $m = 1$ splittings are given in Table 16.

Table 16. Spin-orbital splitting energy separations of the line emission from electron beam excitation of rotational transitions of $H_2(1/4)$. The separations are between each pair of shorter and succeeding longer wavelength lines in the table. The rotational spin-orbital splitting energy separations matched $m528\ cm^{-1}$ $m = 1, 1.5$ wherein 1.5 involves the $m = 0.5$ and $m = 1$ splittings.

Line Position (nm)	Line Energy (eV)	Spin-Orbital Separation (eV)	Spin-Orbital Separation (cm⁻¹)	Spin-Orbital Quantum Number
154.8	8.012	0.067	538.205	1
156.1	7.946	0.096	770.677	1.5
158	7.850	0.098	791.465	1.5
160	7.752	0.161		
163.4	7.591	0.101	813.371	1.5
165.6	7.490	0.063	506.442	1
167	7.427	0.097	778.905	1.5
169.2	7.330	0.103	826.937	1.5
171.6	7.228	0.067	538.559	1
173.2	7.161	0.074	594.108	1
175	7.088	0.116		
177.9	6.972	0.066	532.286	1
179.6	6.906	0.069	552.723	1
181.4	6.837	0.063	512.038	1
183.1	6.774	0.059	473.307	1
184.7	6.715	0.065	522.764	1
186.5	6.651	0.067	540.969	1
188.4	6.583	0.062	502.527	1
190.2	6.521	0.064	520.229	1
192.1	6.457	0.063	510.039	1
194	6.393	0.052	421.821	1
195.6	6.341	0.064	517.670	1
197.6	6.277	0.063	507.296	1
199.6	6.214	0.062	497.230	1
201.6	6.152	0.066	535.681	1
203.8	6.086			

Molecular hydrino was identified by liquid chromatography wherein an inorganic hydrino complex behaved as an organic molecule in chromatographic analysis with an aqueous solution and an organic column packing. Using an Agilent Technologies 6230 TOFLC/MS and a C18 50 x 2mm 3µm (P/N 94641-12) column, liquid chromatography was performed on an energy dispersive X-ray spectroscopy (EDS) determined gallium (59 at%)/oxygen (38 at%)/carbon (2 at%) sample collected from a hydrino reaction run in the SunCell® and dissolved in 4M NaOH wherein the hydrino composition $H_2(1/4)$ was confirmed by XPS and EPR. Following the injection

of 20 ul of the liquid sample, an inorganic hydrino complex was eluted with a water + acetonitrile-water gradient. When using an organic column, inorganic compounds such as sodium carbonate chromatographically elute with the void volume with no retention time. Remarkably, when molecular hydrino complexed with sodium carbonate ($Na_2CO_3:H_2(1/4)$) organic molecular behavior was observed. As shown in Figure 38, the complex showed a chromatographic peak at 23 minutes. The peak fragmented into inorganic ions that identified the complex as comprising sodium carbonate.

Samples of hydrino compounds were also analyzed at Ricerca, Inc., Painesville, Ohio using a PE Sciex API 365 LC/MS/MS System with C18 50 x 2mm, 5μm column (Columbus Serial #205129) eluted with a water + acetonitrile-water gradient. Peaks were observed with extraordinary retention tines such as 17.06 minutes compared to 0.77 minutes of corresponding controls matching the void time. The high resolution positive spectra identified the hydrino compounds as KHKHCO$_3$ and KHKI having fragments such as $K(K2CO_3)^+$ and $K(KI)^+$ [92].

Figure 38. Liquid chromatograph of $Na_2CO_3:H_2(1/4)$ on an organic-packed column using an aqueous solution eluent showing a chromatographic peak at 23 minutes that fragmented into inorganic ions of sodium carbonate demonstrating corresponding organic molecular behavior of the inorganic hydrino complex.
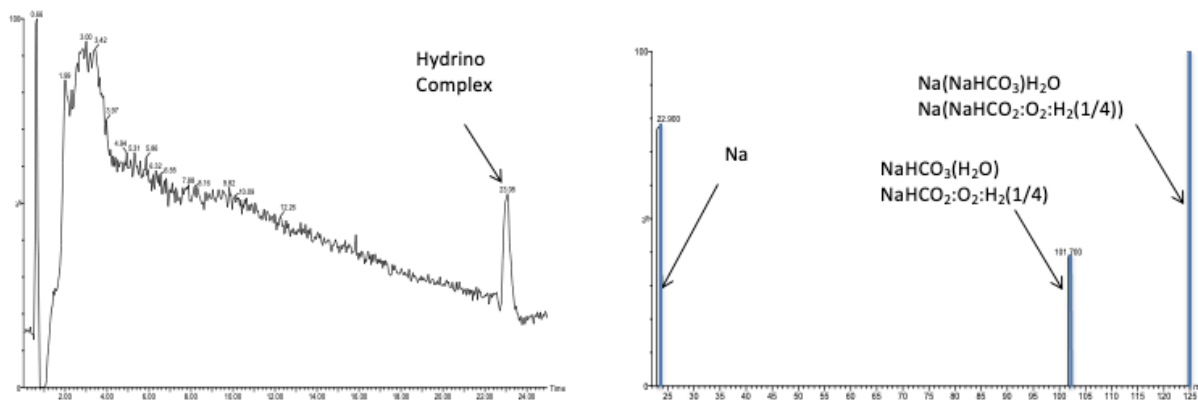
The energetics of the hydrino reaction may be shown by atomic hydrogen line broadening. Extraordinary Doppler broadening of the Balmer α line was observed at low pressure due to the hydrino reaction. From the width of the emitted Balmer lines, it was found that low-pressure capacitively coupled radio frequency (rf) water-vapor plasmas showed the presence of both slow and fast excited hydrogen atoms (Figure 39). The typical slow component was independent of time. A new phenomenon, an extraordinary fast Doppler broadened component (130–150 eV) that increases to a significant portion of the Balmer emission with time, was also observed [53]. These

studies demonstrate excessive line broadening in the absence of an observable effect attributable to a strong electric field since the xenon–hydrogen plasma emission showed no broadening. To conserve energy during the resonant energy transfer of 81.6 eV (3 X 27.2 eV) from H to HOH catalyst to form H(1/4), the resulting protons gain high kinetic energy and result in fast H emission with proton-electron recombination. The Balmer α line width profile recorded on water-vapor and Xe/H$_2$ (90/10%) rf plasmas are shown in Figure 39.

Figure 39. Balmer α line width profile recorded on water-vapor and Xe/H2 (90/10%) rf plasmas at matched conditions of no-flow, 100 mTorr, 200 W, and 4-h plasma duration.
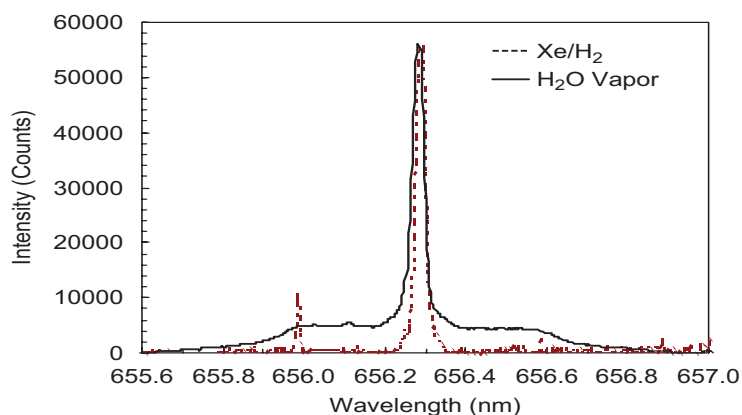
Excessive Doppler hydrogen line broadening in low pressure H$_2$ discharge was observed corresponding to fast H atoms with energies of 100 eV wherein H atoms serve as a catalyst and a reactant to form hydrinos (Figure 40) [6,51,52,78].

Figure 40. The 656.3 nm Balmer α line width recorded with the Jobin Yvon Horiba 1250 M spectrometer parallel to the electric field. Even though hydrogen ions were accelerated away from the detector, a symmetrical emission profile was observed indicating that the broadening was not dependent on the electric field. The line profile recorded on a 200 mTorr H_2 pinch plasma showed a trimodal distribution wherein 18% and 33% of the hydrogen in the excited n = 3 state was fast with an average hydrogen atom energy of 98 eV and 8.8 eV, respectively, compared to 1.3 eV for the slow population.
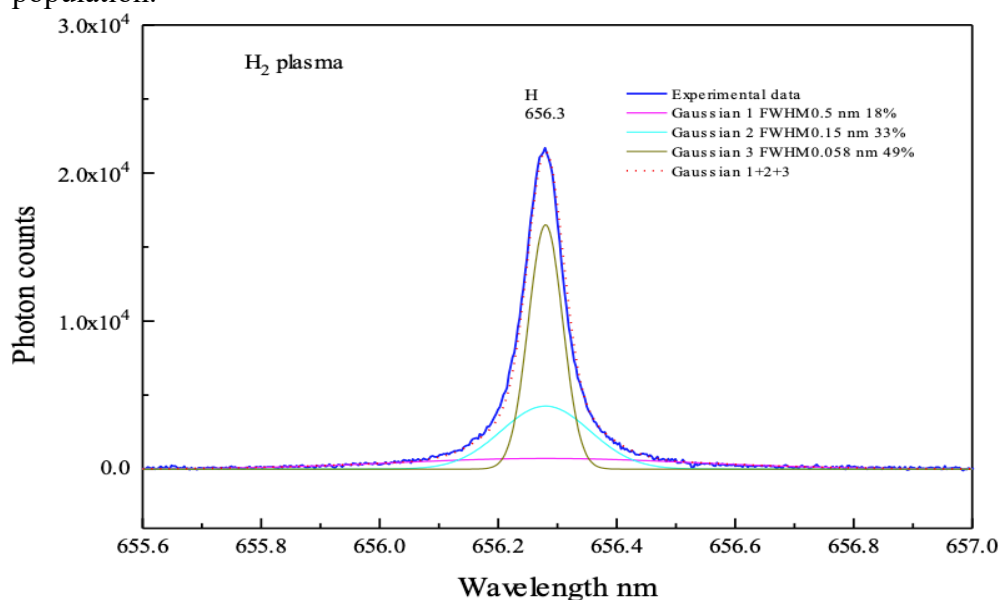
Argon may show Doppler Balmer alpha line broadening with hydrogen addition due the presence of oxygen in argon. Doppler Balmer alpha line broadening is observed with hydrogen addition to argon plasma due to the presence of oxygen in argon as shown in Figures 41-42 [51,52]. The oxygen is present since it co-condenses with liquid argon during purification from the atmosphere. Hydrogen reacts with trace oxygen to form HOH that serves as the hydrino catalyst for atomic H of the argon-H_2 plasma.

Figure 41. The axial scan of the 656.3 nm Balmer α line width recorded on a 1 Torr Ar /H_2 (95/5%) DC plasma discharge with needle-like electrodes at 400 V and 20 mA showing 80% of the hydrogen in excited n=3 state was fast with an average hydrogen atom energy of 40 eV, compared to < 0.5 eV for the slow population.
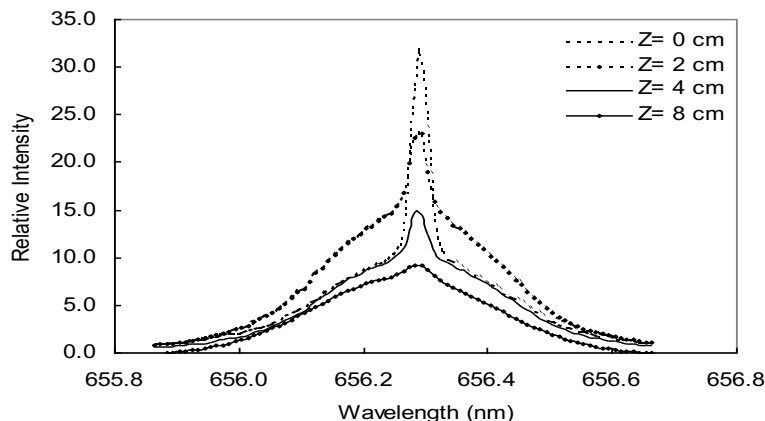
Figure 42. The 656.3 nm Balmer α line width recorded end-on (parallel to the electric field) on a 1 Torr Ar /H_2 (95/5%) DC plasma discharge with needle-like electrodes at 400 V and 20 mA. Both views looking towards the cathode as well as the anode show a symmetrical emission profile. Fast hydrogen atoms have energies in the range of 38-40 eV.
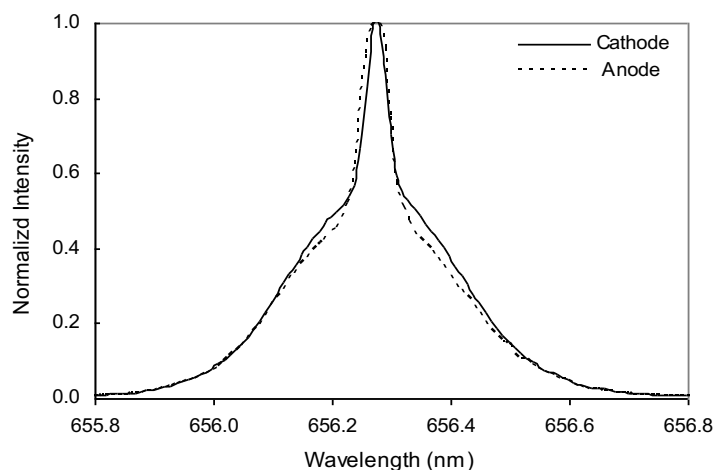
The fast H caused by a hydrino reaction provides a very effective mechanism to form diamond films and coatings [93-95].

Due to the high hydrino reaction energetics, the potential of a novel detonation mechanism whereby the extraordinary power released as extreme ultraviolet radiation couples with air to form

a shockwave was investigated by sound propagation velocity and pressure measurements[1]. With only about 1% of the energy coupling to the shockwave observed from high current detonation of hydrated shots, the shockwave propagation velocity and the corresponding overpressure (shockwave) were equivalent to those produced by about 10 times more moles of gunpowder or TNT [2,79]. These results have implications for the shockwave mechanism of known energetic materials.

An intense 260 nm band shown in Figure 22B comprising the $H_2(1/4)$ ro-vibrational peaks Q(0), R(0), R(1), R(2), P(1), P(2), P(3), and P(4) were observed from the KCl getter from a sealed reactor for a solid fuels reaction of gun powder having the formulation C_7H_4O [78]. The ro-vibrational spectrum comprising the ½ -energy spectrum of this series of $H_2(1/4)$ ro-vibrational peaks was observed in the 325 nm Raman fluorescence spectrum [79]. Following high current detonation of NH_4NO_3, Raman spectroscopy showed $H_2(1/4)$ rotation, EUV spectroscopy showed EUV emission and EUV optical power of at least 10 times that of NH_4NO_3 chemistry, and XPS showed the $H_2(1/4)$ total energy peak [77]. Following high current detonation of gun powder and NH_4NO_3, EUV spectroscopy showed EUV emission and EUV optical power from NH_4NO_3 of 36.4 times that of NH_4NO_3 chemistry [8]. Almost all energetic materials such as gun powder and ammonium nitrate have a common chemistry that provides a source H and HOH. The distinguishing aspect of high explosives that gives rise to a shockwave may not be extraordinary conventional chemistry kinetics, rather the 200 times higher energy release in the formation of hydrinos may be the mechanism.

Hydrogen plasmas formed by incandescently heating of hydrogen gas in the presence of trace amounts of potassium carbonate or alkali nitrates such a KNO_3 wherein the plasma demonstrated an anomalous decay when the filament power was terminated [96-98]. As shown in Figure 43, hydrogen plasma emission persisted with no electrical power input. The hydrogen plasma was generated chemically rather than by electrical discharge. The hydrino reaction is assigned the source of the chemically generated hydrogen plasma called a resonance-transfer or rt-plasma. The chemically generated plasma was energetic as evidenced by the observation of Lyman α line inversion of a KNO_3-H_2 rt-plasma as shown in Figure 44 [60,61,74-76].

---

[1] The mechanism for forming a hydrino-power-driven shock wave and high EMP effects is similar to that of a nuclear weapon involving strong absorption of EUV photons that do not penetrate air with air ionization and rapid heating.

Figure 43. Balmer α emission of the cell as a function of time while a filament current was turned off and on. The plasma decay with no electric field present followed the decay of atomic hydrogen from the filament dissociator. Upon restoration of the filament temperature, dissociation and the plasmas resumed (note emission scale is plotted negative relative to zero).
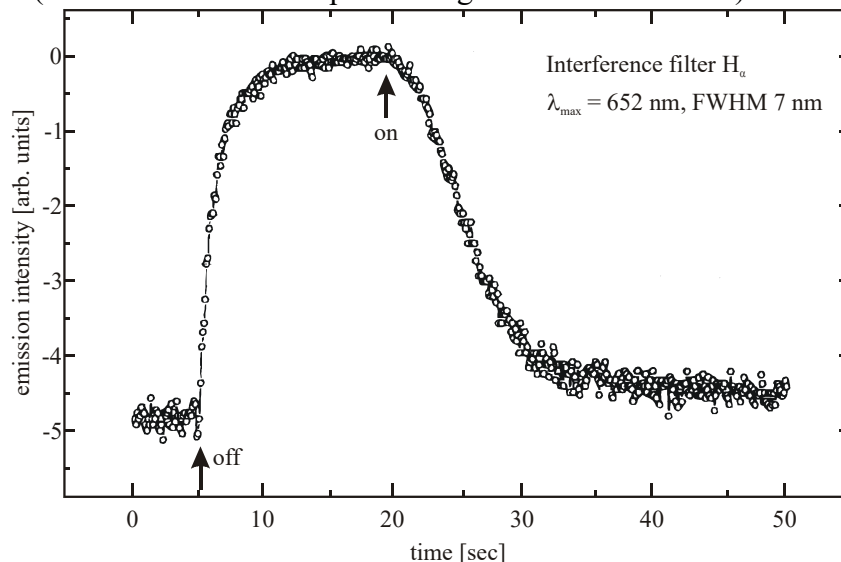
Figure 44. EUV spectra (900–1300 Å) of the cell emission from hydrogen microwave plasma (dotted line) and the KNO$_3$-H$_2$ rt-plasma (solid line) with an inverted Lyman population.
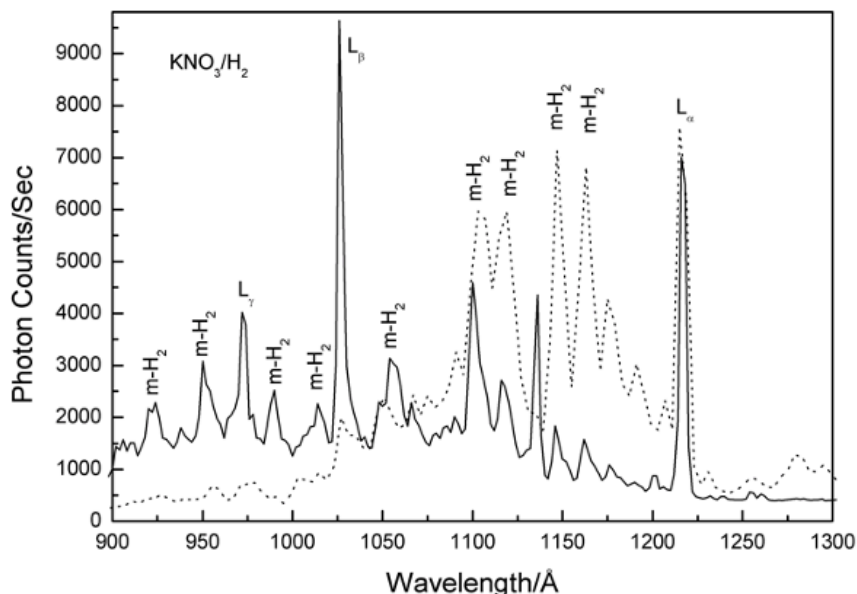
Exchange reactions of the anions between an alkali hydroxide and halide (e.g. Cu(OH)$_2$ + FeBr$_2$) as well as dehydration reactions of metal oxyhydroxides (e.g. FeOOH) create HOH catalyst and H as transient species that react to form hydrinos. As shown in Figures 45A-B these hydrino

solid fuels release thermal energy in significant excess than possible according to enthalpy balance due to conventional known chemical reactions [77] as independently validated by scientists at Perkin Elmer, Setaram, University of Illinois, University of Norte Dame, and Auburn University [79]. Hydrino products are observed by multiple analytical techniques [78].

Figures 45A-B. (A) Differential scanning calorimetry (DSC) (Setaram DSC131) performed on $Cu(OH)_2 + CuBr_2$ by Setaram. The theoretical energy was -39.8 J/g based on the limiting reagent such that the DSC exothermic energy of -323.1 J/g corresponded to an energy gain of 8.1 times the maximum theoretical from conventional chemistry. (B) Duplicate DSC performed on $Cu(OH)_2 + CuBr_2$ by Setaram. The theoretical energy was -39.8 J/g based on the limiting reagent such that the DSC exothermic energy of -430.9 J/g corresponded to an energy gain of 10.8 times the maximum theoretical from conventional chemistry.
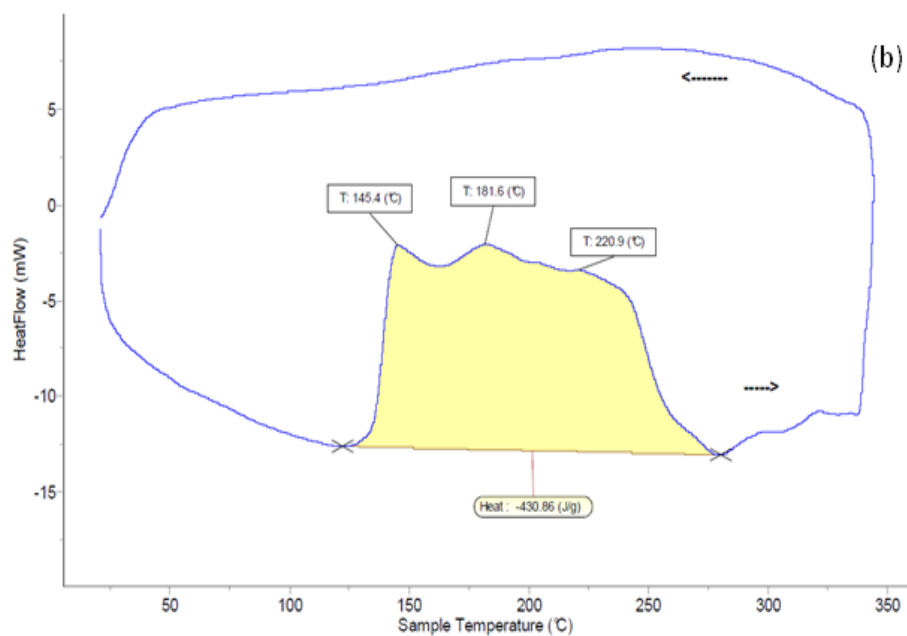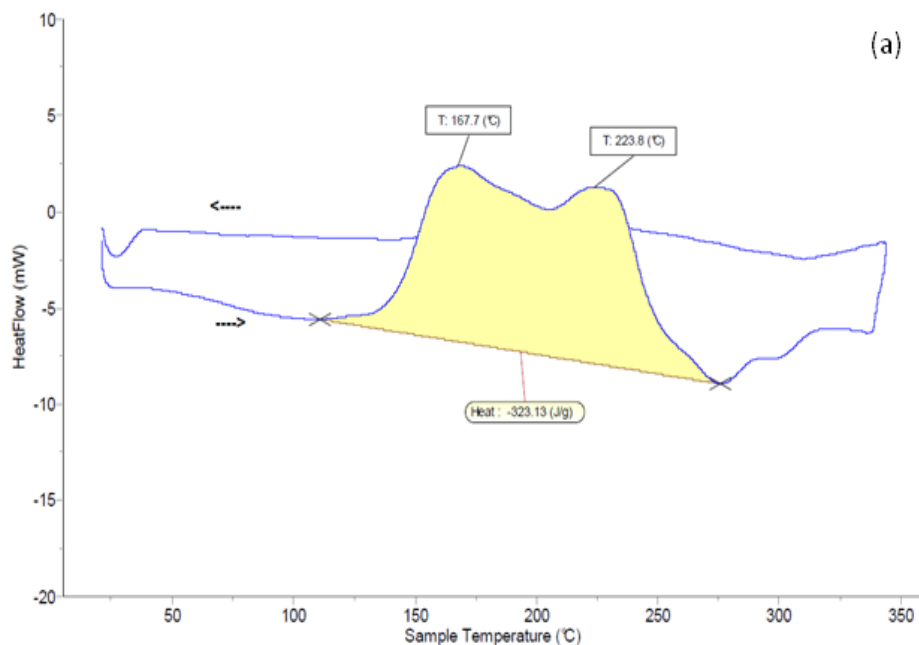
A hydrino fuel cell called a CIHT (Catalyst-Induced-Hydrino-Transition) cell generates an electromotive force (EMF) from the catalytic reaction of hydrogen to lower energy (hydrino) states providing direct conversion of the energy released from the hydrino reaction into electricity. Each CIHT cell shown schematically in Figure 46 comprises a cathode, an anode, and an electrolyte that also serves as a source of reactants to form hydrinos. Due to oxidation-reduction half-cell reactions, a hydrino-producing reaction mixture is constituted with the migration of electrons through an external circuit and ion mass transport through a separate internal path through the electrolyte to complete an electrical circuit. In one type of electrolytically regenerative CIHT cell, atomic hydrogen and oxygen are intermittently formed by electrolysis of H_2O in the cell, and the hydrogen catalyst and subsequent hydrinos are formed by a reaction of the reaction mixture during cell discharge with a net gain of electrical output. An exemplary CIHT comprising a MoCu hydrogen permeable membrane anode, NiO cathode, a LiOH-LiBr eutectic mixture as the electrolyte, and MgO matrix exploits hydrino formation as a half-cell reaction to serve as a new electrical energy source wherein HOH catalyst formed by an oxidation reaction of OH^- at a hydrogen anode [78,79,90]. CIHT cells were operated under intermittent H_2O electrolysis to generate H at the anode and then discharged to form hydrinos wherein H_2O vapor as well as some O_2 was supplied from the atmosphere in open cells.

Figure 46. Schematic of a CIHT cell comprising a cathode, anode, and electrolyte.
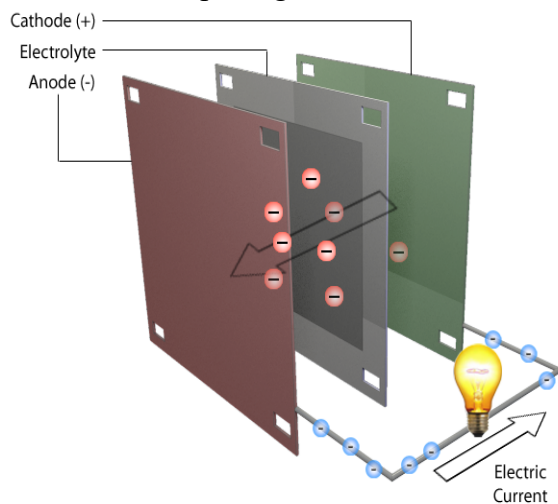
Using an Arbin BT 2000, net electrical production over the electrolysis input and hydrogen supplied to the anode was observed as shown in Figure 47. In most cases, the electrical output energy exceeded the input by a factor of about 2 at about 10 mW/cm^2 anode area with some cells operating continuously for months [78,79,90]. The predicted molecular hydrino $H_2(1/4)$ was

spectroscopically identified as a product of CIHT cells [78,90]. The CIHT cell electrical power was independently validated by Dr. Nick Glumac, University of Illinois; Dr. Terry Copeland, CEO Altair Nanotechnologies, Inc.; Dr. Henry Weinberg, California Institute of Technology; a Sanmina SCI team; Dr. K. V. Ramanujachury, Rowan University, and an Enser Corporation team [79].

Figure 47. The charge and discharge voltages, discharge accumulated electrical charge, and discharge energies over time of the CIHT cell [MoCu/LiOH-LiBr/NiO].
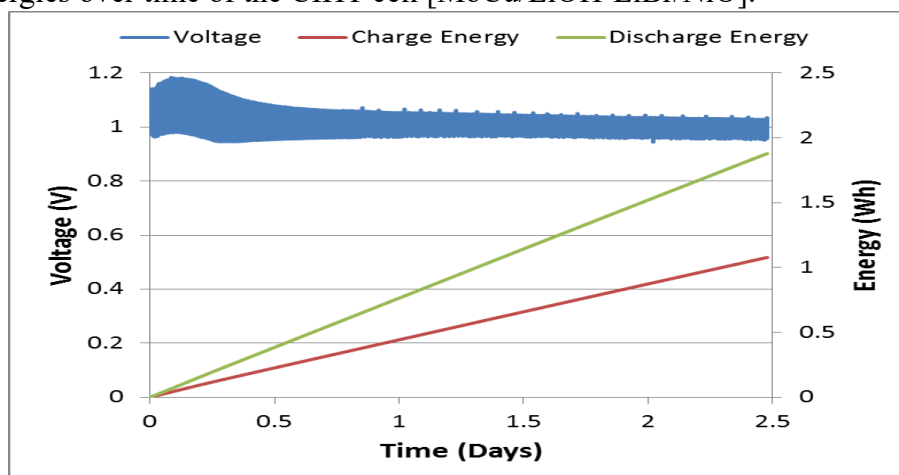
Time-of-flight secondary ion mass spectroscopy (ToF-SIMS) and electrospray ionization time-of-flight mass spectroscopy (ESI-ToFMS) of K_2CO_3-KCl getter exposed to hydrino gas $H_2(1/4)$ from a CIHT cell and a white polymeric compound isolated from an electrolysis cell having a Ni cathode, a platinized titanium anode, and aqueous K_2CO_3 electrolyte showed multimer clusters of the getter or electrolyte compounds with di-hydrogen as part of the structure, $M:H_2$ (M = KOH or K_2CO_3) [78,99]. Specifically, $K^+(H_2:K_2CO_3)_n$ and $K^+(H_2:KOH)_n$ consistent with $H_2(1/p)$ as a complex in the structure were observed in the positive ion spectra wherein the high-resolution mass and the isotopic abundance of ^{39}K and ^{41}K as well as ^{35}Cl and ^{37}Cl were considered for the assignment of peaks having nominal mass m/e = M + 2. These clusters were not observed in controls comprising the getter exposed to H_2 or starting electrolyte. An exemplary ToF-SIMS spectrum of K_2CO_3-KCl (30:70 wt%) getter exposed to $H_2(1/4)$ gas from a 5 W stack of 10 CIHT cells comprising [Mo/LiOH-LiBr-MgO/NiO] that output 1029 Wh at 137% gain is shown in Figures 48A-C. This sample also showed an upfield shifted NMR peak (Figure 6). Both spectral results identify molecular hydrino complexed to the getter compound. Similar $M:H_2$ clusters were observed by ESI-ToFMS as given in Table 17. The observation of positive fragments comprising M + 2 multimer units such as $K^+\left[H_2:K_2CO_3\right]_n$ and $K^+\left[H_2:KOH\right]_n$ (n is an integer) using ToF-SIMS and ESI-ToF recorded on K_2CO_3 and KOH samples only following exposure to a

molecular hydrino gas source (Figures 48A-C and Table 17) demonstrated the ability of molecular hydrino to complex to inorganic compounds comprising oxyanions.

Figures 48A-C. ToF-SIMS spectra of K_2CO_3-KCl (30:70 wt%) getter from a 5 W CIHT cell comprising [Mo/LiOH-LiBr-MgO/NiO] showing getter fragmentation ions comprising di-hydrogen. (A) Positive ToF-SIMS, m/e = 90 to 100 region. (B) Positive ToF-SIMS, m/e = 0 to 200 region. (C) Positive ToF-SIMS, m/e = 200 to 1000 region.
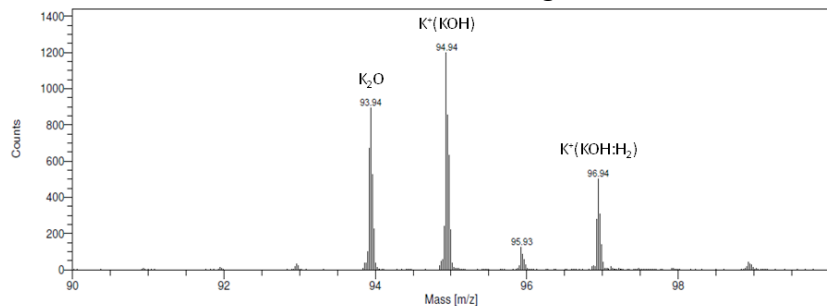
(A)
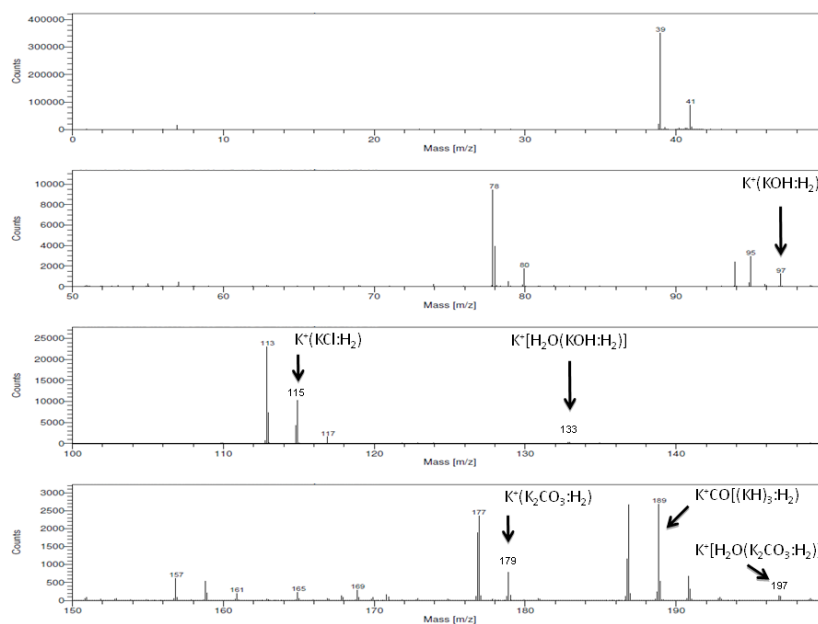
(B)
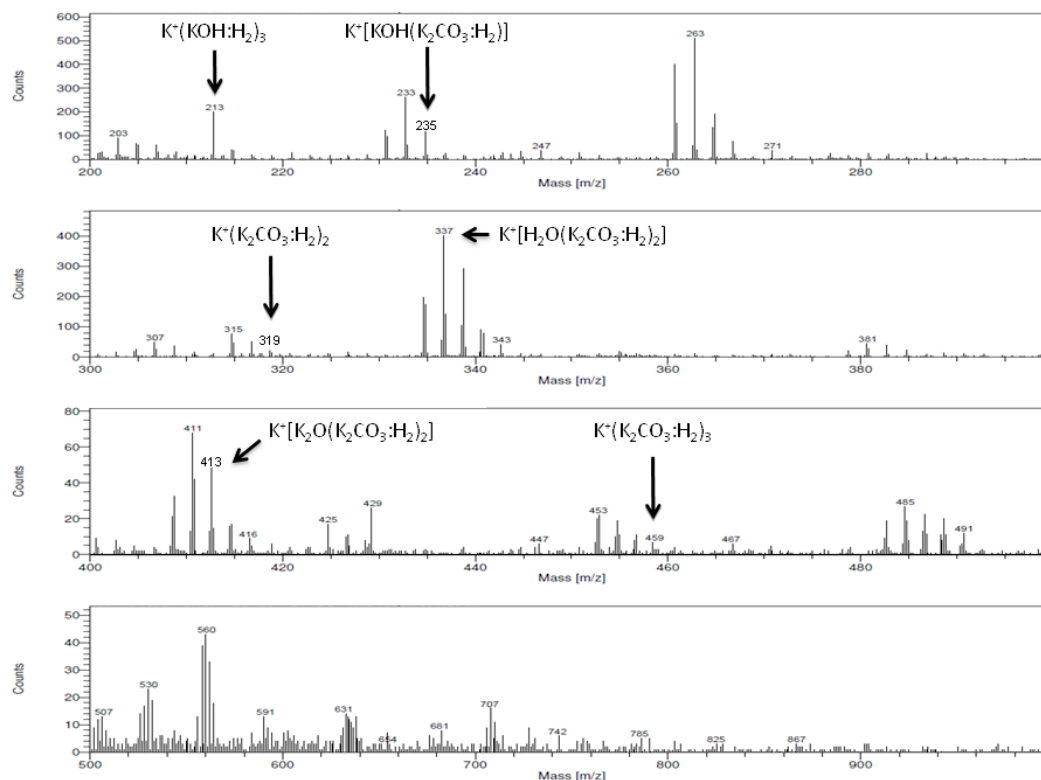
(C)

Table 17. ESI-ToFMS results obtained on the same sample analyzed by ToF-SIMS (Figures 48A-C) comprising K_2CO_3-KCl (30:70 wt%) getter from the [Mo/LiOH-LiBr-MgO/NiO] CIHT cell. Multimer clusters of getter and getter fragment compounds with di-hydrogen as part of the structure, M:H_2 (M = KCl, KOH, or K_2CO_3) were observed. These clusters assigned to ones comprising $H_2(1/4)$ were not observed in controls comprising the getter exposed to H_2.

Hydrino Compound or Fragment	Nominal Mass m/e	Observed m/e	Calculated m/e	Difference Between Observed and Calculated m/e
$K^+(KCl:H_2)$	115	114.9118	114.9114	0.0004
$K^+KHKOH:H_2$ or $K^+K_2O:(H_2)_2$	137	136.9583	136.9173	0.0410
$K^+[(KCl)_3:H_2]$	263	262.7772	262.7770	0.0002
$K^+[H_2O(K_2CO_3)_2:(H_2)]$	335	334.7661	334.8137	0.0476
$K^+[H_2O(K_2CO_3)_2:(H_2)_2]$	337	336.7324	336.8293	0.0969
$K^+[H_2O(K_2CO_3)_2:(H_2)_3]$	339	338.7099	338.8450	0.1351

The extraordinary power density produced by the hydrino reaction run in a 2-liter Pyrex SunCell® is evident from the observed extreme Stark broadening of the H alpha line of 1.3 nm shown in Figure 49. The broadening corresponds to an electron density of $3.5X10^{23}/m^3$. The SunCell® gas density was calculated to be $2.5X10^{25}$ atoms/m^3 based on an argon-H_2 pressure of 800 Torr and temperature of 3000K. The corresponding ionization fraction was about 10%. Given that argon and H_2 have ionization energies of about 15.5 eV and a recombination lifetime of less than 100 us at high pressure, the power density to sustain the ionization is

$$P = \left(\frac{3.5X10^{23}\, electrons}{m^3} \right)(15.5\ eV)\left(\frac{1.6X10^{-19}\,J}{eV} \right)\left(\frac{1}{10^{-4}s} \right) = \frac{8.7X10^9\,W}{m^3}.$$ Stark broadening of

similar magnitude was reported previously in high current detonation of hydrino reaction mixtures [8].

Figure 49. High-resolution visible spectrum of the 800 Torr argon-hydrogen plasma maintained by the hydrino reaction in a Pyrex SunCell® showing a Stark broadening of 1.3 nm corresponding to an electron density of $3.5X10^{23}/m^3$ and a 10% ionization fraction requiring about 8.7 GW/m^3 to maintain.
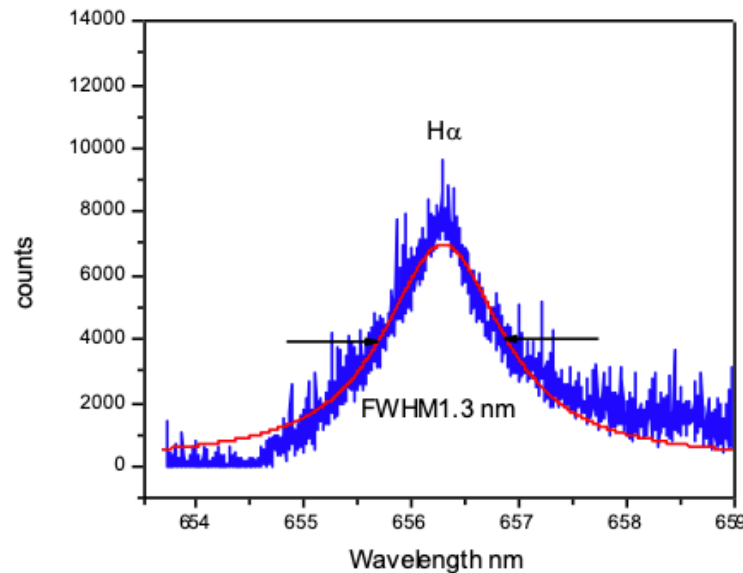
The power balances of SunCells® were independently measured by three experts using molten metal bath and water bath calorimetry. Molten metal calorimetry tests were performed on four-inch cubical or six-inch spherical stainless-steel plasma cells, each incorporating an internal mass of liquid gallium or Galinstan which served as a molten metal bath for calorimetric determination of the power balance of a hydrino plasma reaction maintained in the plasma cell. The molten metal also acted as cathode in formation and operation of the very-low voltage, high-

current plasma while a tungsten electrode acted as the anode when electrical contact was made between the electrodes by electromagnetic pump injection of the molten metal from the cathode to anode. The plasma formation depended on the injection of either 2000 sccm H_2/20 sccm O_2 or 3000 sccm H_2/50 sccm O_2. The excess powers in the range of 197 kW to 273 kW with gains in the range of 2.3 to 2.8 times the power to maintain the hydrogen plasma reactions are given in the Tables 18-19. There was no chemical change observed in cell components as determined by energy dispersive X-ray spectroscopy (EDS). The power from the combustion of the H_2/ 1%O_2 fuel and HOH catalyst source was negligible (16.5 W for 50 sccm O_2 flow) and occurred outside of the cell. Thus, the theoretical maximum excess power from conventional chemistry was zero.

Water bath calorimetry (WBC) can be a highly accurate method of energy measurement due to its inherent ability for complete capture and precise qualification of the released energy. However, submersion of the SunCell® in a water bath lowers its wall temperature significantly relative to operation in air. The hydrino reaction rate increases with temperature, current density, and wall temperature wherein the latter facilitates a high molecular hydrino permeation rate through the wall to avoid product inhibition. In order to evaluate the absolute output energy produced by SunCells® while maintaining favorable operating conditions of high gallium and wall temperatures, the cell was operated suspended on a cable for the duration of a power production phase, and then the cell was lowered into a water bath using an electric winch [100]. The thermal inventory of the entire submerged cell assembly was transferred to the water bath in the form of an increase in the water temperature and steam production. Following equilibration of the cell temperature to that of the water bath, the cell was hoisted from the water bath and the increase in thermal inventory of the water bath was quantified by recording the bath temperature rise and the water lost to steam by measuring the water weight loss. The water bath calorimetry comprising a lever system with a counter balancing water tank and a digital scale to accurately measure the water loss to steam is shown in Figure 50.

Figure 50. A schematic of a water bath calorimetric system.
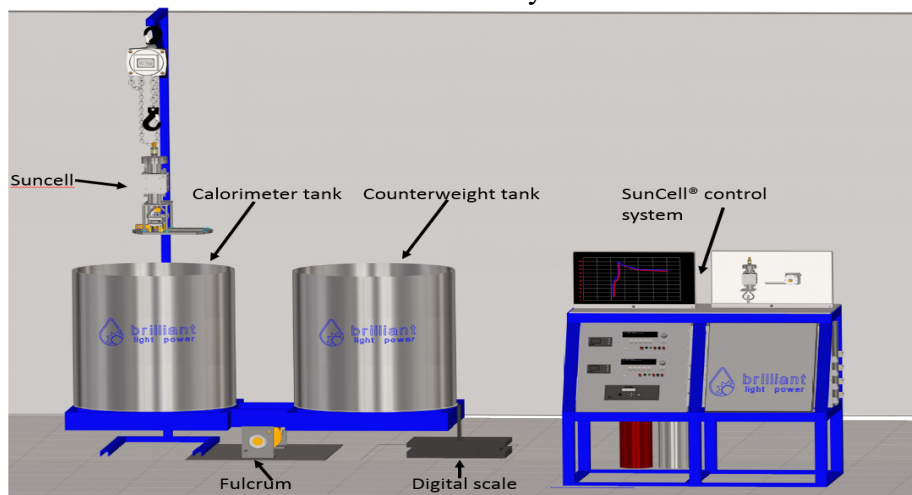
These WBC tests also featured cylindrical cells, each incorporating an internal mass of liquid gallium which served as a molten metal reservoir with a corresponding thermal sink. The molten gallium also acted as an electrode in the formation and operation of the very-low voltage, high-current hydrino-reaction-driven plasma while a tungsten electrode acted as the opposing electrode when electrical contact was made between the electrodes by electromagnetic pump injection of the molten metal from the reservoir to the W electrode. The plasma formation depended on the injection of hydrogen gas with about 8% oxygen gas and the application of high current at low voltage using a DC power source. The excess powers in the range of 273 kW to 342 kW with gains in the range of 3.9 to 4.7 times the power to maintain the hydrogen plasma reactions are given in the Tables 20-22. There was no chemical change observed in cell components as determined by energy dispersive X-ray spectroscopy (EDS) performed on the gallium following the reaction. The power from the combustion of the H_2/ 8% O_2 fuel and HOH catalyst source was limited by the trace oxygen and was negligible. The input power from the EM pump power was also negligible.

Table 18. Dr. Mark Nansteel validated 273 kW of power produced by a hydrino plasma reaction maintained in a SunCell® using molten metal bath calorimetry [101].

Duration (s)	Input Energy (kJ)	Output Energy (kJ)	Input Power (kW)	Output Power (kW)	Power Gain	Net Excess Power (kW)
1.27	212.9	485.8	167.6	382.5	2.28	273

Table 19. Dr. Randy Booker and Dr. Stephen Tse validated 200 kW of power produced by a hydrino plasma reaction maintained in a SunCell® using molten metal bath calorimetry [102].

Duration (s)	Input Energy (kJ)	Output Energy (kJ)	Input Power (kW)	Output Power (kW)	Power Gain	Net Excess Power (kW)
2.917	422.1	1058.1	144.7	362.8	2.51	218.1
5.055	554.7	1548.1	109.7	306.25	2.79	196.5

Table 20. Dr. Randy Booker validated 296 kW of power produced by a hydrino plasma reaction maintained in a SunCell® using water bath calorimetry [102].

Duration (s)	Input Energy (kJ)	Output Energy (kJ)	Input Power (kW)	Output Power (kW)	Power Gain	Net Excess Power (kW)
2.115	193	818.4	91.2	386.9	4.24	296

Table 21. Dr. Stephen Tse validated up to 342 kW of power produced by a hydrino plasma reaction maintained in a SunCell® using water bath calorimetry [103].

Duration (s)	Input Energy (kJ)	Output Energy (kJ)	Input Power (kW)	Output Power (kW)	Power Gain	Net Excess Power (kW)
2.115	192.95	915.35	91.2	432.8	4.74	341.6

Table 22. Dr. Mark Nansteel validated up to 273 kW of power produced by a hydrino plasma reaction maintained in an advanced tube-type SunCell® using water bath calorimetry. The power density was a remarkable 5 MW/liter [104].

Duration (s)	Input Energy (kJ)	Output Energy (kJ)	Input Power (kW)	Output Power (kW)	Power Gain	Net Excess Power (kW)
274.9	274.9	1080.2	93.2	366.2	3.93	273.0

The thermal tests were further performed on cells immersed in the water bath using the water weight lost to steam production over a test duration to quantify the power balance. Each cell comprised a cylindrical 4130 Cr-Mo steel reaction chamber measuring 20 cm ID, 14.3 cm in height, and 1.25 mm thick with cylindrical reservoir attached to the base having dimensions of 5.4 cm height and 10.2 cm ID that contained 6 kg of gallium. The continuous steam power of commercial scale, quality, and power density that developed was observed to be controllable by changing temperature and glow discharge dissociation recombination of the H_2 and trace O_2 reactants flowed into the cell. Specially, three variations of the basic cell design allowed for testing of these operational parameters. The cell wall was coated with a ceramic coating to prevent gallium alloy formation, and the cell was operated at about 200 °C. Next, the reaction cell chamber was modified by the addition of a concentric three-layer liner comprising, from the cell wall to the plasma, (i) an outer 1.27 cm thick, full-length carbon cylinder, (ii) a 1 mm thick, full length Nb cylinder, and (ii) 4 mm thick, 10.2 mm high W plates arranged in a hexagon. The plates completely covered the region of intense plasma between the W molten metal injector electrode and the W counter electrode. The liner served as thermal insulation to increase the gallium temperature to over 400 °C and also protected the wall from the observed more intense plasma.

The cell comprising the liner was further modified with the addition of a glow discharge cell to dissociate H_2 gas to atomic H and also to form HOH hydrino catalyst. The kinetically favorable high temperature reaction condition observed in the performance of the molten metal cells occurred because these cells were not water cooled. Since 1 eV temperature corresponds to 11,600 K gas temperature, the equivalent of very high reaction mixture temperature was achieved under water cooling conditions. The glow discharge cell comprised a 3.8 cm diameter stainless steel tube of 10.2 cm length that was bolted at its base to the top of the reaction cell chamber by Conflat flanges. The positive glow discharge electrode was a stainless-steel rod powered by a high-voltage feed through on top of the glow discharge cell, and the body was grounded to serve as the counter electrode. A hydrino reaction gas mixture of 3000 sccm H_2 and 1 sccm O_2 was flowed through the top of the discharge cell and out the bottom into the reaction cell chamber.

The power developed due to the hydrino reaction doubled from an average of 26 kW to 55.5 kW with an increase in operating temperature from ~200 °C to over 400 °C. The power was further boosted by the operation of the glow discharge cell to activate the gas reactants wherein the hydrino power was observed to about double again to 93 kW. The results are given in Table 23. The combination of elevated temperature and glow discharge activation have a dramatic effect of the excess power. The results match expectations for a catalytic chemical reaction between H and HOH catalyst.

The SunCell® was modified to a 10-inch diameter Mo-Cr cylindrical cell with a carbon/Mo/hexagonal plate liner and dual molten gallium injectors and run at high temperature

124

with 1500 A per injector. The output increased to 210 kW of hydrino plasma reaction contribution to a total continuous steam output power of 275 kW at 4.2 times gain. The power was also measured using the weight of steam produced over a test period by the SunCell® operated under continuous commercial power generation conditions, controllable by changing temperature, current, and glow discharge heating of the reactants flowed into the cell as summarized in the Table 23.

Table 23. Dr. Mark Nansteel validated 210 kW of power produced by a hydrino plasma reaction maintained in a SunCell® using mass balance in the production of steam [105-106]. The hydrino reaction was shown to be dependent on operating temperature, current, and activation of the gas reactants by a glow discharge plasma.

Discharge	Gallium Temperature (°C)	Duration (s)	Input Energy (kJ)	Output Energy (kJ)	Input power (kW)	Output Power (kW)	Power Gain	Net Excess Power (kW)
Yes	196	302	10,346	16,480	34.26	54.57	1.59	20.3
Yes	177	296	9341	18,708	31.56	63.2	2	31.7
No	458	167	6951	16,264	41.62	97.39	2.34	55.8
Yes	425	200	7800	26,392	39	131.96	3.38	93
Yes	716	50	3232	10,480	65	274.2	4.22	210

6 Conclusion

Hydrino and subsequently molecular hydrino $H_2(1/4)$ was formed by catalytic reaction of atomic hydrogen with the resonant energy acceptor of 3x27.2 eV, nascent H_2O, wherein the reaction rate was greatly increased by applying an arc current to recombine ions and electrons formed by the energy transfer to HOH that is consequently ionized. $H_2(1/4)$ bound to metal oxides and absorbed in metallic and ionic lattices by van der Waals forces was produced by (i) high voltage electrical detonation Fe wires in an atmosphere comprising water vapor, (ii) low voltage, high current electrical detonation of hydrated silver shots, (iii) ball milling or heating hydrated alkali halide-hydroxide mixtures, and (iv) maintaining a plasma reaction of H and HOH in a so-called SunCell® comprising a molten gallium injector that electrically shorts two plasma electrodes with the molten gallium to maintain an arc current plasma state. Excess power at the 340 kW level was measured by water and molten metal bath calorimetry. Samples predicted to comprise molecular hydrino $H_2(1/4)$ product were analyzed by multiple analytical methods with results that follow.

$H_2(1/4)$ comprises an unpaired electron which enables the electronic structure of this unique hydrogen molecular state to be determined by electron paramagnetic resonance (EPR) spectroscopy. Specially, the $H_2(1/4)$ EPR spectrum comprises a principal peak with a g-factor of 2.0046386 that is split into a series of pairs of peaks with members separated by spin-orbital coupling energies that are a function of the corresponding electron spin-orbital coupling quantum numbers. The unpaired electron magnetic moment induces a diamagnetic moment in the paired electron of the $H_2(1/4)$ molecular orbital based on the diamagnetic susceptibility of $H_2(1/4)$. The corresponding magnetic moments of the intrinsic paired-unpaired current interactions and those due to relative rotational motion about the internuclear axis give rise to the spin-orbital coupling energies. The EPR spectral results confirmed the spin-orbital coupling between the spin magnetic moment of the unpaired electron and an orbital diamagnetic moment induced in the paired electron by the unpaired electron that shifted the flip energy of the spin magnetic moment. Each spin-orbital splitting peak was further sub-split into a series of equally spaced peaks that matched integer fluxon energies that are a function of the electron fluxon quantum number corresponding to the number of angular momentum components involved in the transition. The evenly spaced series of sub-splitting peaks was assigned to flux linkage in units of the magnetic flux quantum h/2e during the coupling between the paired and unpaired magnetic moments while a spin flip transition occurred. Additionally, the spin-orbital splitting increased with spin-orbital coupling quantum number on the downfield side of the series of pairs of peaks due to magnetic energies that increased with accumulated magnetic flux linkage by the molecular orbital. For an EPR frequency of 9.820295 GHz, the downfield peak positions $B_{S/Ocombined}^{downfield}$ due to the combined shifts

due to the magnetic energy and the spin-orbital coupling energy are

$$B_{S/Ocombined}^{downfield} = \left(0.35001 - m3.99427 \, X \ 10^{-4} - (0.5)\frac{\left(2\pi m3.99427 \, X \ 10^{-4}\right)^2}{0.1750} \right) T.$$ The upfield

peak positions $B_{S/O}^{upfield}$ with quantized spin-orbital splitting energies $E_{S/O}$ and electron spin-orbital coupling quantum numbers $m = 0.5, 1, 2, 3, 5....$ are

$$B_{S/O}^{upfield} = 0.35001 \left(1 + m\left[\frac{7.426 \, X \ 10^{-27} \, J}{h9.820295 GHz} \right] \right) T = \left(0.35001 + m3.99427 \, X \ 10^{-4}\right) T.$$ The

separations ΔB_{Φ} of the integer series of peaks at each spin-orbital peak position are

$$\Delta B_{\Phi}^{downfield} = \left(0.35001 - m3.99427 \, X \ 10^{-4} - (0.5)\frac{\left(2\pi m3.99427 \, X \ 10^{-4}\right)^2}{0.1750} \right) \left[\frac{m_{\Phi}5.7830 \, X \ 10^{-28} \, J}{h9.820295 GHz} \right] X \ 10^4 \, G$$

and $\quad \Delta B_{\Phi}^{upfield} = \left(0.35001 + m3.99427 X \ 10^{-4}\right)\left[\frac{m_{\Phi}5.7830 \, X \ 10^{-28} \, J}{h9.820295 GHz} \right] X \ 10^4 \, G \quad$ for electron

fluxon quantum numbers $m_{\Phi} = 1, 2, 3$. These EPR results were first observed at TU Delft by Dr. Hagen [72].

The pattern of integer-spaced peaks of the EPR spectrum of $H_2(1/4)$ is very similar to the periodic pattern observed in the high-resolution visible spectrum of the hydrino hydride ion reported previously. The hydrino hydride ion comprising a paired and unpaired electron in a common atomic orbital also demonstrated the phenomena of flux linkage in quantized units of h/2e. Moreover, the same phenomena were observed when the rotational energy levels of $H_2(1/4)$ were excited by laser irradiation during Raman spectroscopy and by collisions of high energy electrons form an electron beam with $H_2(1/4)$. It is extraordinary that the EPR, Raman, and electron-beam excitation spectra give the same information about the structure of molecular hydrino in energy ranges that differ by reciprocal of the $H_2(1/4)$ diamagnetic susceptibility coefficient: $1/7 X 10^{-7} = 1.4 X 10^6$, wherein the induced diamagnetic orbital magnetic moment active during EPR was replaced by the orbital molecular rotational magnetic moment active during Raman and electron-beam excitation of rotational transitions.

Josephson junctions such as ones of superconducting quantum interference devices (SQUIDs) link magnetic flux in quantized units of the magnetic flux quantum or fluxon $\frac{h}{2e}$. The same behavior was predicted and observed for the linkage of magnetic flux by hydrino hydride ion and molecular hydrino controlled by applying specific frequencies of electromagnetic radiation over the range of microwave to ultraviolet. The hydrino species such as $H_2(1/4)$ is enabling of a

computer logic gate or memory element that operates at even elevated temperature versus cryogenic ones and may be a single molecule 4^3 or 64 times smaller than molecular hydrogen.

Molecular hydrino comprising a magnetic hydrogen molecule enables many other applications in other fields as well. A gaseous contrast agent in magnetic resonance imaging (MRI) is but one example. Specifically, the exemplary Raman transition rotation is about a semiminor axis perpendicular to the internuclear axis. The intrinsic electron spin angular momentum aligns either parallel or perpendicular to the corresponding molecular rotational angular momentum along the molecular rotational axis, and a concerted rotation of the spin current occurs during the molecular rotational transition. The interaction of the corresponding magnetic moments of the intrinsic spin and the molecular rotation give rise to the spin-orbital coupling energies that are a function of the spin-orbital quantum number. The Raman spectral results confirmed the spin-orbital coupling between the spin magnetic moment of the unpaired electron and the orbital magnetic moment due to molecular rotation. The energies of the rotational transitions were shifted by these spin-orbital coupling energies as a function of the corresponding electron spin-orbital coupling quantum numbers. Molecular rotational peaks shifted by spin-orbital energies are further shifted by fluxon linkage energies with each energy corresponding to its electron fluxon quantum number dependent on the number of angular momentum components involved in the rotational transition. The observed sub-splitting or shifting of Raman spectral peaks was assigned to flux linkage in units of the magnetic flux quantum h/2e during the spin-orbital coupling between spin and molecular rotational magnetic moments while the rotational transition occurred.

The emission energies $E_{Emission}$ of all the novel lines recorded by 785 nm, 442 nm, and 325 nm laser Raman spectroscopy on Ni foil samples (e.g. Figures 9 and 26) run in the SunCell® as well as the hydrino complex GaOOH:H_2(1/4):H_2O matched the double transition for final rotational quantum numbers (Eq. (38)) $J'_p = 3$ and $J'_c = 0,1,2$ with spin-orbital coupling (Eq. (22)) and fluxon coupling (Eqs. (23-24)). The energies are given by the sum of the independent transitions (Eqs. (41) and (47)):

$$E_{Emission} = \Delta E_{J=0 \to J'_p=3} + \Delta E_{J=0 \to J'_c=0,1,2} + E_{S/O,rot} + E_{\Phi,rot}$$

$$= 13,652(15,602)(19,502)\ cm^{-1} + m528\ cm^{-1} + m_{\Phi}31\ cm^{-1} + m_{\Phi3/2}46\ cm^{-1}$$

wherein two-photon absorption plus the laser heating energy is capable of exciting rotational emission of greater energy than the 785 nm laser energy. Eighty-one emission lines recorded by Raman spectroscopy on Ni foils run in the SunCell® and GaOOH:H_2(1/4):H_2O match those of DIBs as shown in Tables 7B and 14A-B. The assignment of all the 380 DIBs listed by Hobbs [27] to H_2(1/4) rotational transitions with spin-orbital splitting and fluxon sub-splitting are given in the Appendix. Molecular hydrino rotational transitional energies cover a broad range of frequencies

from infrared to ultraviolet which enables molecular lasers spanning the corresponding wavelengths.

The rotational energies are dependent on the reduced mass which changed by a factor of 3/4 upon substitution of one deuteron for one proton of molecular hydrino $H_2(1/4)$ to form $HD(1/4)$. The rotational energies of the $HD(1/4)$ Raman spectrum shifted relative to that of $H_2(1/4)$ as predicted. The emission energies $E_{Emission}$ of all the novel lines matched the double transition for final rotational quantum numbers (Table 8) $J_p^{'} = 2(3)$ and $J_c^{'} = 1(0,1,2)$ with spin-orbital coupling (Eq. (22)) and fluxon coupling (Eqs. (23-24)). The energies are given by the sum of the independent transitions (Eq. (43)):

$$E_{Emission} = \Delta E_{J=0 \to J_p^{'}=2(3)} + \Delta E_{J=0 \to J_c^{'}=1(0,1,2)} + E_{S/O,rot} + E_{\Phi,rot}$$

$$= 7313(10,239)(11,701)(14,627) \ cm^{-1} + m528 \ cm^{-1} + m_\Phi 31 \ cm^{-1} + m_{\Phi 3/2} 46 \ cm^{-1}$$

It was observed by Raman spectroscopy on magnetic samples Fe_2O_3, FeOOH, and CoOOH that $H_2(1/4)$ showed a series of SQUID-like fluxon emission transitions of a single rotational and spin-orbital spilt level (e.g. Figure 18). Ni foil samples run at a temperature above the Ni Curie temperature switched from discrete rotational transitions slit by spin-orbital and fluxon linkage transitions to a series of fluxon transitions of a single rotational and spin-orbital spilt level (e.g. Figure 21) that matches the spectra of magnetic Fe_2O_3, FeOOH, and CoOOH samples. These fluxon transitions were also recorded on Ni foil and tin samples run in the SunCell®. The emission peaks observed in the anti-Stokes emission spectrum matched the second and third order peaks in the Stokes spectrum. It is remarkable that the emission energy range is higher than any prior recorded with the only possible assignment being the rotational energy levels of $H_2(1/4)$

These unique one/zero-type magneto-optical signals are enabling of computer logic gate or memory element applicants wherein the application of a magnetic field to magnetize the matrix comprising embedded molecular hydrino such as $H_2(1/4)$ or a change in magnetic flux activates the computer logic gate or memory element such as optical ones. The fast speed magnetization switching such as that achieved with applied electric current or laser opto-magnetic interactions by ultrafast lasers [107] is enabling of a fast processor wherein the fluxon series can encode the information that may be read by an infrared, visible, or UV laser as a detector signal.

Akin to the case of molecular hydrino $H_2(1/4)$ trapped in a GaOOH lattice that serves as cages for essentially free gas EPR spectra, $H_2(1/4)$ in a noble gas mixture provides an interaction-free environment to observe ro-vibrational spectra. $H_2(1/4)$-noble gas mixtures that were irradiated with high energy electrons of an electron beam showed equal, 0.25 eV spaced line emission in the ultraviolet (150-180 nm) region with a cutoff at 8.25 eV that matched the $H_2(1/4)$ $v = 1$ to $v = 0$ vibrational transition with a series of rotational transitions corresponding to the $H_2(1/4)$ P-branch.

The spectral fit was a good match to $4^2 0.515 eV - 4^2 (J+1) 0.01509; J = 0,1,2,3....$ wherein

0.515 eV and 0.01509 eV are the vibrational and rotational energies of ordinary molecular hydrogen, respectively. In addition, small satellite lines were observed that matched the rotational spin-orbital splitting energies that were also observed by Raman spectroscopy. The rotational spin-orbital splitting energy separations matched $m528 \ cm^{-1}$ $m = 1,1.5$ wherein 1.5 involves the $m = 0.5$ and $m = 1$ splittings.

The spectral emission of the H$_2$(1/4) P-branch rotational transitions with the $v = 1$ to $v = 0$ vibrational transition was also observed by electron beam excitation of H$_2$(1/4) trapped in a KCl crystalline matrix. The rotational peaks matched those of a free rotor, whereas the vibrational energy was shifted by the increase in the effective mass due to interaction of the vibration of H$_2$(1/4) with the KCl matrix. The spectral fit was a good match to $5.8 eV - 4^2 (J+1) 0.01509; J = 0,1,2,3...$ comprising peaks spaced at 0.25 eV. The relative magnitude of the H$_2$(1/4) vibrational energy shift matched the relative effect on the ro-vibrational spectrum caused by ordinary H$_2$ being trapped in KCl.

Using Raman spectroscopy with a high energy laser, a series of 1000 cm^{-1} (0.1234 eV) equal-energy spaced Raman peaks were observed in the 8000 cm^{-1} to 18,000 cm^{-1} region wherein conversion of the Raman spectrum into the fluorescence or photoluminescence spectrum revealed a match as the ½-energy ro-vibrational spectrum of H$_2$(1/4) corresponding to the e-beam excitation emission spectrum of H$_2$(1/4) in a KCl matrix given by

$$5.8 eV - 4^2 (J+1) 0.01509 eV; J = 0,1,2,3... \text{ and comprising the matrix shifted } v = 1 \text{ to } v = 0$$

vibrational transition with 0.25 eV energy-spaced rotational transition peaks. Due to the unique electronic structure of H$_2$(1/4) comprising a paired and an unpaired electron in the H$_2$(1/4) molecular orbital (MO) requiring spin ½ conservation during vibrational transitions, the corresponding energy levels matched theoretical predictions of ro-vibration states of molecular hydrino with excitation and decay involving two-photons, each of ½ the energy of the ro-vibrational state. These results support the potential of H$_2$(1/4) neutrino emission and absorption (Eq. (46)) serving as a means for communication (e.g. a neutrino telecommunication system wherein H$_2$(1/p) serves as a neutrino emitter corresponding to a signal transmitter and a neutrino absorber resulting in partial internal conversion to 2-photon emission to a photodetector corresponding to a receiver). The cross section of neutrinos, and especially low-energy neutrinos, toward any form of interaction such as nuclear reactions is essentially zero such that neutrino signals may be transmitted through any form of solid matter including through the Earth thereby eliminating the dependence on satellites and telecommunication towers.

Infrared transitions of $H_2(1/4)$ are forbidden because of its symmetry that lacks an electric dipole moment. However, it was observed that application of a magnetic field in addition to an intrinsic magnetic field permitted molecular rotational infrared excitation by coupling to the aligned magnetic dipole of $H_2(1/4)$. Coupling with spin-orbital transitions also allowed the transitions. The ability of interactions with a crystalline site to permit $H_2(1/4)$ to be FTIR active due to an induced dipole was tested by embedding $H_2(1/4)$ in a KI lattice. A major sharp peak was observed by FTIR on KI:$H_2(1/4)$ at 1943 cm^{-1} that matched near identically the $J = 0$ to $J' = 1$ $H_2(1/4)$ rotational transition of $H_2(1/4)$. Other sharp peaks in the FTIR spectrum matched this rotational transition with spin-orbital and fluxon linkage splitting.

The allowed double ionization of $H_2(1/4)$ by the Compton effect corresponding to the total energy of 496 eV was observed by X-ray photoelectron spectroscopy (XPS) on samples comprising $H_2(1/4)$ due the reaction of H with HOH with incorporation in crystalline inorganic and metallic lattices.

$H_2(1/4)$ was further observed by gas chromatography that showed a gas from hydrino producing reactions with a faster migration rate than that of any known gas considering that hydrogen and helium have the fastest prior known migration rates and corresponding shortest retention times. Molecular hydrino may serve as a cryogen, a gaseous heat transfer agent, and an agent for buoyancy.

Extreme ultraviolet (EUV) spectroscopy recorded extreme ultraviolet continuum radiation with a 10.1 nm cutoff corresponding to the hydrino reaction transition H to H(1/4) catalyzed by HOH catalyst.

MAS NMR of molecular hydrino trapped in protic matrix represents a means to exploit the unique magntic characteristic of molecular hydrino for its identification via its interaction with the matrix. A unique consideration regarding the NMR spectrum is the possible molecular hydrino quantum states. Proton magic-angle spinning nuclear magnetic resonance spectroscopy (^{1}H MAS NMR) recorded an upfield matrix-water peak in the -4 ppm to -5 ppm region, the signature of the unpaired electron of molecular hydrino and the resulting magnetic moment.

Molecular hydrino may give rise to bulk magnetism such as paramagnetism, superparamagnetism and even ferromagnetism when the magnetic moments of a plurality of hydrino molecules interact cooperatively. Superparamagnetism was observed using a vibrating sample magnetometer to measure the magnetic susceptibility of compounds comprising molecular hydrino.

Complexing of $H_2(1/4)$ gas to inorganic compounds comprising oxyanions such a K_2CO_3 and KOH was confirmed by the unique observation of M + 2 multimer units such as $K^+\left[H_2 : K_2CO_3\right]_n$ and $K^+\left[H_2 : KOH\right]_n$ wherein n is an integer by exposing K_2CO_3 and KOH to

a molecular hydrino gas source and running time of flight secondary ion mass spectroscopy (ToF-SIMS) and electrospray time of flight secondary ion mass spectroscopy (ESI-ToF), and the hydrogen content was identified as $H_2(1/4)$ by other analytical techniques. In addition to inorganic polymers such as $K^+\left[H_2 : K_2CO_3\right]_n$, the ToF-SIMS spectra showed an intense H^- peak due to the stability of hydrino hydride ion.

HPLC showed inorganic hydrino compounds behaving like organic molecules as evidenced by a chromatographic peak on an organic molecular matrix column that fragmented into inorganic ions.

Signatures of the high energetics and power release of the hydrino reaction were evidenced by (i) extraordinary Doppler line broadening of the H Balmer a line of over 100 eV in plasmas that comprised H atoms and HOH or H catalyst such as argon-H_2, H_2, and H_2O vapor plasmas, (ii) H excited state line inversion, (iii) anomalous H plasma afterglow duration, (iv) shockwave propagation velocity and the corresponding pressure equivalent to about 10 times more moles of gunpowder with only about 1% of the power coupling to the shockwave, (v) optical power of up to 20 MW, and (vi) calorimetry of hydrino solid fuels, hydrino electrochemical cells, and the SunCell® wherein the latter was validated at a power level of 340,000 W. The H inversion, optical, and shock effects of the hydrino reaction have practical applications of an atomic hydrogen laser, light sources of high power in the EUV and other spectral regions, and novel more powerful and non-sensitive energetic materials, respectively. The power balance was measured by the change in the thermal inventory of a water bath. Following a power run of a duration limited by nearly reaching the melting point of SunCell® components, the heat of the SunCell® was transferred to a water bath, and the increase in thermal inventory of the water bath was quantified by recording the bath temperature rise and the water lost to steam by measuring the water weight loss. The SunCell® was fitted to continuously operate with water bath cooling, and the continuous excess power due to the hydrino reaction was validated at a level of 210 kW.

These analytical tests confirm the existence of hydrino, a smaller more stable form of hydrogen formed by the release of power at power densities exceeding that of other known power sources. Brilliant Light Power is developing the proprietary SunCell® to harness this green power source, initially for thermal applications, and then electrical. The energetic plasma formed by the hydrino reaction enables novel direct power conversion technologies in addition to conventional Rankine, Brayton, and Stirling cycles [109-112]. A novel magnetohydrodynamic cycle has potential for electrical power generation at 23 MW/liter power densities at greater than 90% efficiency [108].

Appendix

The double transition rotational transition energies of $H_2(1/4)$ are given in Table 6. The $H_2(1/4)$ rotational energies $E_{Emission}$ of all the 380 DIBs lines reported by Hobbs et al. [27] the double transition for final rotational quantum numbers (Eq. (38)) $J'_p = 3(4)$ and $J'_c = 0,1,2(0,1)$ with spin-orbital coupling (Eq. (22)) and fluxon coupling (Eqs. (23-24)). The energies are given by the sum of the independent transitions:

$$E_{Emission} = \Delta E_{J=0 \to J'_p=3(4)} + \Delta E_{J=0 \to J'_c=0,1,2(0,1)} + E_{S/O,rot} + E_{\Phi,rot}$$

$$= 13,652(15,602)(19,502)(21,453)(23,403) \ cm^{-1} \qquad (A.1)$$

$$+m528 \ cm^{-1} + m_\Phi 31 \ cm^{-1} + m_{\Phi3/2} 46 \ cm^{-1}$$

The DIBs lines assigned to $H_2(1/4)$ rotational transitions are given in Table A.1. Additionally, the very low energy separation of lines with the same rotational, spin-orbital and fluxon linkage quantum numbers may be due to the magnetic energies $U_{S/OMag}$ arising from at least one of the absorption of the integer number of fluxons j having fluxon linkage quantum numbers of $m_{\Phi3/2} = 1$ (Eq. (25)) and $m_\Phi = 1$ (Eq. (26)) and the coupling energy $E_{S/O-\Phi3/2}$ wherein the fluxon linkage energy decreases due to coupling to the spin-orbital coupling (Eq. (44). In cold regions of interstellar space, $[H_2(1/4)]_2$ dimer electron spin flip transitions of 0.797 cm^{-1} (Mills Eq. (16.244) [1]), $[H_2(1/4)]_2$ dimer rotational splitting of 44.3 cm^{-1} (Mills Eq. (16.276) [1]), or the $[H_2(1/4)]_2$ vibration dissociation separation of 8.991 cm^{-1} (Mills Eq. (16.205) [1]) may be the source of energy shifts.

Table A.1. $H_2(1/4)$ rotational assignments of 380 DIBs [27] (Eq. (A.1)). The theoretical rotational energy assignments are according to the energies given in Table 6. The quantum numbers corresponding to spin-orbital splitting and fluxon sub-splitting of the assigned peaks are m and m_Φ, and $m_{\Phi3/2}$ respectively, having energies given in Table 5. Delta is the difference between the observed and theoretical lines.

DIB (Å)	DIB (cm^{-1})	Rotational Energy (cm^{-1})	m	m_Φ	$m_{\Phi3/2}$	Theoretical (cm^{-1})	Delta (cm^{-1})
4259.01	23480	23403			1.5	23472	7
4363.86	22915	21453	2.5		3.0	22911	4
4428.19	22583	21453	2.0		1.5	22578	5
4501.79	22213	21453	1.5		-0.5	22222	-8
4659.82	21460	21453				21453	7
4668.65	21419	21453			-0.5	21430	-10
4680.2	21367	21453			-2.0	21361	6

4683.03	21354	21453			-2.0	21361	-7
4688.89	21327	21453	-0.5		3.0	21328	-1
4726.83	21156	21453	-0.5		-1.0	21143	13
4734.79	21120	21453	-0.5		-1.5	21120	1
4762.61	20997	21453	-1.0		1.5	20995	2
4780.02	20920	21453	-1.0			20925	-5
4817.64	20757	21453	-1.5		2.0	20754	3
4879.96	20492	21453	-2.0		2.0	20490	2
4887.14	20462	21453	-2.0		1.5	20467	-5
4947.38	20213	21453	-2.5		1.5	20203	10
4951.12	20197	21453	-2.5		1.5	20203	-5
4959.63	20163	21453	-2.5		0.5	20157	6
4961.95	20153	21453	-2.5		0.5	20157	-3
4963.88	20146	21453	-2.5		0.5	20157	-11
4965.22	20140	21453	-2.5			20133	7
4966.01	20137	21453	-2.5			20133	3
4969.14	20124	21453	-2.5			20133	-9
4979.61	20082	21453	-2.5		-1.0	20087	-5
4982.14	20072	19502	1.0	1.5		20076	-4
4984.79	20061	19502	1.0	1.0		20061	0
4987.42	20050	19502	1.0	0.5		20045	5
5003.58	19986	19502	1.0	-1.5		19984	2
5027.47	19891	19502	0.5	4.0		19889	1
5054.84	19783	19502	0.5	0.5		19781	2
5061.49	19757	19502	0.5			19766	-9
5074.47	19706	19502	0.5	-2.0		19704	2
5092.09	19638	19502	0.5	-4.0		19643	-4
5100.95	19604	19502		3.0		19594	10
5110.89	19566	19502		2.0		19564	2
5117.62	19540	19502		1.0		19533	8
5133.14	19481	19502		-0.5		19487	-5
5137.07	19466	19502		-1.0		19471	-5
5170.49	19341	19502	-0.5	3.0		19331	10
5176.04	19320	19502	-0.5	3.0		19331	-11
5178.1	19312	19502	-0.5	2.5		19315	-3
5217.85	19165	19502	-0.5	-2.5		19161	4
5229.76	19121	19502	-0.5	-4.0		19115	7
5236.18	19098	19502	-1.0	4.0		19097	0
5245.48	19064	19502	-1.0	3.0		19067	-3
5251.78	19041	19502	-1.0	2.0		19036	5
5257.47	19021	19502	-1.0	1.5		19020	0
5262.48	19002	19502	-1.0	1.0		19005	-3
5297.97	18875	19502	-1.0	-3.0		18882	-7
5304.25	18853	19502	-1.0	-4.0		18851	2
5340.38	18725	19502	-1.5	0.5		18726	0
5342.54	18718	19502	-1.5			18710	7

5358.75	18661	19502	-1.5	-1.5		18664	-3
5363.7	18644	19502	-1.5	-2.0		18649	-5
5371.28	18618	19502	-1.5	-3.0		18618	0
5384.19	18573	19502	-2.0	4.0		18570	3
5390.85	18550	19502	-2.0	3.0		18539	11
5395.64	18533	19502	-2.0	3.0		18539	-5
5404.56	18503	19502	-2.0	2.0		18508	-5
5418.87	18454	19502	-2.0	0.5		18462	-8
5424.1	18436	19502	-2.0	-0.5		18431	5
5433.5	18404	19502	-2.0	-1.5		18400	4
5450.62	18347	19502	-2.0	-3.0		18354	-7
5480.79	18246	19502	-2.5	2.0		18244	1
5487.69	18223	19502	-2.5	1.5		18229	-6
5494.1	18201	19502	-2.5	0.5		18198	4
5497.08	18191	19502	-2.5	0.5		18198	-6
5502.91	18172	19502	-2.5	-0.5		18167	5
5504.31	18168	19502	-2.5	-0.5		18167	1
5506.28	18161	19502	-2.5	-0.5		18167	-6
5508.12	18155	19502	-2.5	-1.0		18152	3
5512.68	18140	19502	-2.5	-1.5		18136	4
5515.99	18129	19502	-2.5	-1.5		18136	-7
5524.98	18100	19502	-2.5	-2.5		18105	-6
5525.48	18098	19502	-2.5	-2.5		18105	-7
5527.55	18091	19502	-2.5	-3.0		18090	1
5530.07	18083	19502	-2.5	-3.0		18090	-7
5535.2	18066	19502	-2.5	-4.0		18059	7
5537.27	18059	19502	-2.5	-4.0		18059	0
5541.84	18045	19502	-3.0	4.0		18042	3
5545.06	18034	19502	-3.0	4.0		18042	-8
5546.48	18029	19502	-3.0	3.5		18026	3
5547.48	18026	19502	-3.0	3.5		18026	0
5551.07	18015	19502	-3.0	3.0		18011	4
5553.98	18005	19502	-3.0	3.0		18011	-6
5556.44	17997	19502	-3.0	2.5		17996	2
5560.03	17986	19502	-3.0	2.0		17980	5
5566.11	17966	19502	-3.0	1.5		17965	1
5580.82	17919	19502	-3.0			17919	0
5585.56	17903	19502	-3.0	-0.5		17903	0
5594.6	17874	19502	-3.0	-1.5		17872	2
5599.7	17858	19502	-3.0	-2.0		17857	1
5600.85	17854	19502	-3.0	-2.0		17857	-2
5609.78	17826	19502	-3.0	-3.0		17826	0
5634.98	17746	19502	-3.0	-5.5		17749	-3
5645.49	17713	19502	-3.0	-6.5		17718	-5
5669.33	17639	19502	-3.5	-0.5		17639	0
5705.08	17528	19502	-3.5	0.5	-3.0	17531	-3

5706.51	17524	19502	-3.5		-3.0	17516	8
5707.77	17520	19502	-4		3.0	17529	-9
5711.45	17509	19502	-4	1.0	2.0	17514	-5
5716.32	17494	19502	-4	0.5	2.0	17499	-5
5719.48	17484	19502	-4		2.0	17483	1
5734.97	17437	19502	-4		1.0	17437	0
5735.89	17434	19502	-4.0		1.0	17437	-3
5753.47	17381	15602	3.5	-1	-1	17372	9
5756.12	17373	15602	3.5	0.5	-2	17372	1
5758.9	17364	15602	3.5		-2	17357	8
5760.53	17360	15602	3.5	-0.5	-1.5	17365	-5
5762.74	17353	15602	3.5		-2	17357	-4
5766.1	17343	15602	3.5	-1	-1.5	17349	-6
5769.09	17334	15602	3.5	-1	-2	17326	8
5769.92	17331	15602	3.5		-2.5	17334	-2
5772.61	17323	15602	3.5	-0.5	-2.5	17318	5
5775.9	17313	15602	3.0	1	2	17309	5
5780.48	17300	15602	3.0		2.5	17301	-1
5785.04	17286	15602	3.0	0.5	2	17293	-7
5793.21	17262	15602	3.0	1	1	17262	-1
5795.2	17256	15602	3.0	1.5	0.5	17255	1
5797.06	17250	15602	3.0	2		17247	3
5806.62	17222	15602	3.0	1		17216	5
5809.23	17214	15602	3.0		0.5	17209	5
5814.26	17199	15602	3.0	0.5		17201	-2
5815.74	17195	15602	3.0			17185	9
5818.72	17186	15602	3.0			17185	1
5821.17	17179	15602	3.0			17185	-7
5828.47	17157	15602	3.0		-0.5	17162	-5
5838.02	17129	15602	3.0	-0.5	-1	17124	5
5838.97	17126	15602	3.0	-2		17124	3
5840.66	17121	15602	3.0		-1.5	17116	5
5842.93	17115	15602	3.0	-2.5		17108	6
5844.92	17109	15602	3.0	-1	-1	17108	1
5849.81	17095	15602	3.0		-2	17093	2
5854.54	17081	15602	3.0	-1	-1.5	17085	-4
5855.68	17077	15602	3.0	-0.5	-2	17078	0
5859.05	17068	15602	3.0		-2.5	17070	-2
5885.37	16991	15602	2.5	1	1	16999	-7
5888.75	16982	15602	2.5	2		16983	-2
5893.54	16968	15602	2.5	1.5		16968	0
5900.58	16947	15602	2.5		0.5	16945	3
5904.63	16936	15602	2.5	0.5		16937	-1
5910.57	16919	15602	2.5			16921	-3
5913.74	16910	15602	2.5	-0.5		16906	4
5914.79	16907	15602	2.5	-0.5		16906	1

5917.05	16900	15602	2.5		-0.5	16898	2
5922.32	16885	15602	2.5	-0.5	-0.5	16883	2
5923.47	16882	15602	2.5		-1	16875	7
5925.94	16875	15602	2.5		-1	16875	0
5927.63	16870	15602	2.5		-1	16875	-5
5928.86	16867	15602	2.5	-2		16860	7
5934.6	16850	15602	2.5	-2		16860	-9
5945.54	16819	15602	2.5	-2.5	-0.5	16821	-2
5947.32	16814	15602	2.5	1	-3	16814	1
5948.88	16810	15602	2.5	-0.5	-2	16814	-4
5952.26	16800	15602	2.5	0.5	-3	16798	2
5954.25	16795	15602	2.5	-0.5	-2.5	16790	4
5958.91	16782	15602	2.0	1	2	16781	1
5962.89	16770	15602	2.0		2.5	16773	-3
5973.81	16740	15602	2.0	2	0.5	16742	-3
5975.75	16734	15602	2.0	2.5		16735	0
5982.67	16715	15602	2.0	1	0.5	16712	3
5986.55	16704	15602	2.0		1	16704	0
5988.11	16700	15602	2.0	1.5		16704	-4
5989.46	16696	15602	2.0		1	16704	-8
5995.83	16678	15602	2.0		0.5	16681	-2
5999.54	16668	15602	2.0			16658	10
6004.89	16653	15602	2.0			16658	-4
6010.75	16637	15602	2.0		-0.5	16634	2
6014.81	16626	15602	2.0	-1		16627	-1
6019.32	16613	15602	2.0		-1	16611	2
6027.68	16590	15602	2.0	-2		16596	-6
6030.49	16582	15602	2.0	-1	-1	16581	2
6037.63	16563	15602	2.0		-2	16565	-2
6048.6	16533	15602	2.0	-1	-2	16534	-2
6054.5	16517	15602	1.5	1	2	16517	0
6057.52	16508	15602	1.5		2.5	16509	-1
6059.26	16504	15602	1.5	-1	3	16502	2
6065.28	16487	15602	1.5		2	16486	1
6071.31	16471	15602	1.5	2.5		16471	0
6081.1	16444	15602	1.5	1	0.5	16448	-3
6082.33	16441	15602	1.5		1	16440	1
6084.94	16434	15602	1.5	0.5	0.5	16432	2
6087.48	16427	15602	1.5	1		16424	3
6089.85	16421	15602	1.5		0.5	16417	4
6093.4	16411	15602	1.5	0.5		16409	2
6102.72	16386	15602	1.5			16394	-8
6106.36	16376	15602	1.5	-0.5		16378	-2
6107.16	16374	15602	1.5		-0.5	16371	4
6108.05	16372	15602	1.5		-0.5	16371	1
6109.88	16367	15602	1.5		-0.5	16371	-4

6113.18	16358	15602	1.5	-1		16363	-5
6116.84	16348	15602	1.5		-1	16347	1
6118.63	16344	15602	1.5		-1	16347	-4
6136.08	16297	15602	1.5		-2	16301	-4
6139.98	16287	15602	1.5	-0.5	-2	16286	1
6142.09	16281	15602	1.5		-2.5	16278	3
6145.61	16272	15602	1.5	0.5	-3	16270	1
6148.4	16264	15602	1.5		-3	16255	9
6151.14	16257	15602	1.0	-0.5	3	16253	4
6158.57	16238	15602	1.0	0.5	2	16238	0
6161.88	16229	15602	1.0		2	16222	7
6163.49	16225	15602	1.0		2	16222	2
6165.68	16219	15602	1.0	1.5	1	16222	-3
6170.48	16206	15602	1.0	2.5		16207	-1
6174.8	16195	15602	1.0	2		16191	3
6177.63	16187	15602	1.0	0.5	1	16191	-4
6182.58	16174	15602	1.0		1	16176	-2
6185.81	16166	15602	1.0	1		16161	5
6187.22	16162	15602	1.0	1		16161	2
6189.52	16156	15602	1.0		0.5	16153	3
6194.74	16143	15602	1.0	0.5		16145	-2
6195.98	16139	15602	1.0			16130	10
6198.97	16132	15602	1.0			16130	2
6203.05	16121	15602	1.0			16130	-9
6204.49	16117	15602	1.0	-0.5		16114	3
6211.69	16099	15602	1.0	-1		16099	0
6212.91	16096	15602	1.0	-0.5	-0.5	16091	4
6215.81	16088	15602	1.0		-1	16084	4
6223.67	16068	15602	1.0	-2		16068	0
6225.24	16064	15602	1.0		-1.5	16060	3
6226.27	16061	15602	1.0	-2		16068	-7
6234.01	16041	15602	1.0		-2	16037	4
6236.92	16034	15602	1.0	-1	-1.5	16030	4
6244.46	16014	15602	1.0		-2.5	16014	0
6250.88	15998	15602	0.5	2	1.5	15997	1
6252.43	15994	15602	0.5	1	2	15989	5
6259.7	15975	15602	0.5		2.5	15981	-6
6269.85	15949	15602	0.5	0.5	1.5	15951	-1
6275.58	15935	15602	0.5	2		15927	7
6283.84	15914	15602	0.5		1	15912	2
6287.59	15904	15602	0.5	1		15897	8
6308.8	15851	15602	0.5	-0.5		15850	0
6317.86	15828	15602	0.5		-1	15820	9
6324.45	15812	15602	0.5	-0.5	-1	15804	7
6329.98	15798	15602	0.5	-2		15804	-6
6338	15778	15602	0.5		-2	15773	4

6353.38	15740	15602	0.5	-1	-2	15743	-3
6355.45	15735	15602	0.5		-3	15727	7
6358.14	15728	15602		-0.5	3	15725	3
6362.15	15718	15602			2.5	15718	0
6367.34	15705	15602		0.5	2	15710	-5
6374.66	15687	15602			2	15694	-7
6376.08	15684	15602		2.5		15679	5
6379.32	15676	15602		1	1	15679	-3
6384.97	15662	15602		2		15664	-2
6397.01	15632	15602		1		15633	0
6400.46	15624	15602			0.5	15625	-1
6410.2	15600	15602				15602	-2
6414.67	15589	15602		-0.5		15587	3
6417.03	15584	15602			-0.5	15579	5
6418.61	15580	15602			-0.5	15579	1
6425.66	15563	15602			-1	15556	7
6439.48	15529	15602			-1.5	15533	-3
6445.28	15515	15602		-1.5	-1	15509	6
6449.22	15506	15602			-2	15509	-4
6452.12	15499	15602		-2.5	-0.5	15502	-3
6456.01	15489	15602		-0.5	-2	15494	-5
6460.44	15479	15602		0.5	-3	15479	0
6463.68	15471	15602			-3	15463	8
6465.37	15467	15602	-0.5	1	2	15461	6
6466.86	15463	15602	-0.5	2	1.5	15469	-6
6468.77	15459	15602	-0.5		2.5	15454	5
6474.24	15446	15602	-0.5	1	1.5	15438	8
6485.71	15419	15602	-0.5	0.5	1.5	15423	-4
6489.47	15410	15602	-0.5	1	1	15415	-5
6492.01	15404	15602	-0.5	2		15400	4
6494.05	15399	15602	-0.5	2		15400	-1
6498.08	15389	15602	-0.5	1	0.55	15394	-5
6520.62	15336	15602	-0.5			15338	-2
6523.28	15330	15602	-0.5			15338	-8
6536.53	15299	15602	-0.5		-1	15292	7
6543.08	15283	15602	-0.5	-1.5		15292	-8
6553.92	15258	15602	-0.5	-1	-1	15261	-3
6590.42	15174	15602	-1		2	15167	7
6594.36	15164	15602	-1		2	15167	-2
6597.31	15158	15602	-1	1	1	15151	7
6600.08	15151	15602	-1	1	1	15151	0
6607.07	15135	15602	-1	2		15136	0
6613.62	15120	15602	-1		1	15120	0
6622.82	15099	15602	-1		0.5	15097	2
6625.77	15093	15602	-1	0.5		15090	3
6628.14	15087	15602	-1	0.5		15090	-2

6629.6	15084	15602	-1			15074	10
6630.77	15081	15602	-1			15074	7
6631.69	15079	15602	-1			15074	5
6633.12	15076	15602	-1			15074	2
6635.74	15070	15602	-1			15074	-4
6645.95	15047	15602	-1	-1		15043	3
6654.73	15027	15602	-1		-1	15028	-1
6657.11	15022	15602	-1	-1.5		15028	-6
6658.74	15018	15602	-1	-0.5	-1	15012	5
6660.71	15013	15602	-1	-2		15012	1
6662.21	15010	15602	-1	-2		15012	-2
6663.71	15007	15602	-1	-1.5	-0.5	15005	2
6665.27	15003	15602	-1		-1.5	15005	-2
6672.27	14987	15602	-1	-2	-0.5	14989	-2
6684.86	14959	15602	-1	-1.5	-1.5	14958	1
6689.44	14949	15602	-1	0.5	-3	14951	-2
6693.52	14940	15602	-1.5		3	14949	-9
6694.54	14938	15602	-1.5	-0.5	3	14933	4
6699.32	14927	15602	-1.5		2.5	14926	1
6702.02	14921	15602	-1.5	0.5	2	14918	3
6709.43	14904	15602	-1.5	3		14903	2
6719.18	14883	15602	-1.5		1.5	14880	3
6727.47	14864	15602	-1.5	1.5		14856	8
6729.27	14860	15602	-1.5		1	14856	4
6733.16	14852	15602	-1.5	0.5	0.5	14849	3
6737.28	14843	13652	2.0		3	14846	-4
6740.82	14835	13652	2.0	1	2	14831	4
6747.78	14820	13652	2.0	0.5	2	14816	4
6751.51	14812	13652	2.0	0.5	2	14816	-4
6762.05	14788	13652	2.0	1	1	14785	4
6765.34	14781	13652	2.0	1	1	14785	-4
6767.76	14776	13652	2.0	2		14769	7
6770.21	14771	13652	2.0	2		14769	1
6778.98	14751	13652	2.0		1	14754	-2
6780.65	14748	13652	2.0		1	14754	-6
6788.76	14730	13652	2.0		0.5	14731	-1
6792.46	14722	13652	2.0	0.5		14723	-1
6795.21	14716	13652	2.0	0.5		14723	-7
6801.46	14703	13652	2.0			14708	-5
6803.21	14699	13652	2.0	-0.5		14692	7
6809.51	14685	13652	2.0		-0.5	14685	1
6811.15	14682	13652	2.0		-0.5	14685	-3
6812.73	14678	13652	2.0		-0.5	14685	-6
6814.2	14675	13652	2.0	-1		14677	-2
6823.45	14655	13652	2.0	-1	-0.5	14654	2
6825.8	14650	13652	2.0	-1	-0.5	14654	-3

6827.33	14647	13652	2.0	-2		14646	1
6837.71	14625	13652	2.0	-0.5	-1.5	14623	2
6839.49	14621	13652	2.0		-2	14615	6
6841.52	14617	13652	2.0		-2	14615	1
6843.63	14612	13652	2.0		-2	14615	-3
6845.34	14608	13652	2.0		-2	14615	-7
6846.5	14606	13652	2.0	-1.5	-1	14615	-9
6852.53	14593	13652	2.0		-2.5	14592	1
6862.51	14572	13652	2.0		-3	14569	3
6864.72	14567	13652	2.0		-3.0	14569	-2
6919.21	14453	13652	1.5			14444	9
6944.6	14400	13652	1.5		-1.0	14398	2
6973.76	14339	13652	1.5	-1.0	-1.5	14344	-4
6978.4	14330	13652	1.5		-2.5	14328	2
6993.13	14300	13652	1.5		-3.0	14305	-5
7030.29	14224	13652	1.0		1.0	14226	-2
7031.52	14222	13652	1.0		1.0	14226	-4
7045.89	14193	13652	1.0		0.5	14203	-10
7061.05	14162	13652	1.0		-0.5	14157	5
7062.68	14159	13652	1.0		-0.5	14157	2
7069.55	14145	13652	1.0		-1.0	14134	12
7077.86	14129	13652	1.0		-1.0	14134	-5
7084.65	14115	13652	1.0		-1.5	14110	5
7092.67	14099	13652	1.0		-2.0	14087	12
7116.31	14052	13652	0.5		3.0	14055	-2
7119.71	14046	13652	1.0		-3.0	14041	4
7159.83	13967	13652	0.5		1.0	13962	5
7162.87	13961	13652	0.5		1.0	13962	-1
7203.65	13882	13652	0.5		-1.0	13870	12
7224.03	13843	13652	0.5		-1.5	13847	-4
7334.48	13634	13652			-0.5	13629	5
7357.56	13591	13652			-1.5	13583	9
7367.13	13574	13652			-1.5	13583	-9
7375.87	13558	13652			-2.0	13560	-2
7385.89	13539	13652			-2.5	13536	3
7405.71	13503	13652	-0.5		2.5	13504	-1
7419.05	13479	13652	-0.5		2.0	13481	-2
7470.32	13386	13652	-0.5			13388	-2
7472.6	13382	13652	-0.5			13388	-6
7482.91	13364	13652	-0.5		-0.5	13365	-1
7484.17	13362	13652	-0.5		-0.5	13365	-3
7495.02	13342	13652	-0.5		-1.0	13342	0
7520.6	13297	13652	-0.5		-2.0	13296	1
7559.41	13229	13652	-1.0		2.0	13217	12
7562.25	13224	13652	-1.0		2.0	13217	7
7706.8	12976	13652	-1.5		2.5	12976	0

7708.06	12973	13652	-1.5	2.5	12976	-2
7822.8	12783	13652	-1.5	-2.0	12768	15
7832.89	12767	13652	-1.5	-2.0	12768	-1
7862.43	12719	13652	-1.5	-3.0	12722	-3
8026.25	12459	13652	-2.0	-3.0	12458	1

References

1. R. Mills *The Grand Unified Theory of Classical Physics* September 2016 Edition, http://brilliantlightpower.com/book-download-and-streaming/.

2. R. Mills, Y. Lu, R. Frazer, "Power Determination and Hydrino Product Characterization of Ultra-low Field Ignition of Hydrated Silver Shots", Chinese Journal of Physics, Vol. 56, (2018), pp. 1667-1717.

3. R. L. Mills, Y. Lu, "Hydrino continuum transitions with cutoffs at 22.8 nm and 10.1 nm," Int. J. Hydrogen Energy, 35 (2010), pp. 8446-8456, doi: 10.1016/j.ijhydene.2010.05.098.

4. R. L. Mills, Y. Lu, K. Akhtar, "Spectroscopic observation of helium-ion- and hydrogen-catalyzed hydrino transitions," Cent. Eur. J. Phys., 8 (2010), pp. 318-339, doi: 10.2478/s11534-009-0106-9.

5. R. L. Mills, Y. Lu, "Time-resolved hydrino continuum transitions with cutoffs at 22.8 nm and 10.1 nm," Eur. Phys. J. D, Vol. 64, (2011), pp. 65, DOI: 10.1140/epjd/e2011-20246-5.

6. R. L. Mills, R. Booker, Y. Lu, "Soft X-ray Continuum Radiation from Low-Energy Pinch Discharges of Hydrogen," J. Plasma Physics, Vol. 79, (2013), pp 489-507; doi: 10.1017/S0022377812001109.

7. A. Bykanov, "Validation of the observation of soft X-ray continuum radiation from low energy pinch discharges in the presence of molecular hydrogen," http://www.blacklightpower.com/wp-content/uploads/pdf/GEN3_Harvard.pdf.

8. R. Mills, J. Lotoski, Y. Lu, "Mechanism of soft X-ray continuum radiation from low-energy pinch discharges of hydrogen and ultra-low field ignition of solid fuels", Plasma Science and Technology, Vol. 19, (2017), pp. 1-28.

9. R. L. Mills, P. Ray, B. Dhandapani, M. Nansteel, X. Chen, J. He, "New Power Source from Fractional Quantum Energy Levels of Atomic Hydrogen that Surpasses Internal Combustion," J. Mol. Struct., Vol. 643, No. 1–3, (2002), pp. 43–54.

10. A. F. H. van Gessel, Masters Thesis: *EUV spectroscopy of hydrogen plasmas*, April (2009), Eindhoven University of Technology, Department of Applied Physics, Group of Elementary Processes in Gas Discharges, EPG 09-02, pp. 61-70.

11. R. L. Mills, "Spectroscopic Identification of a Novel Catalytic Reaction of Atomic Hydrogen and the Hydride Ion Product," Int. J. Hydrogen Energy, Vol. 26, No. 10, (2001), pp. 1041–1058.

12. R. Mills J. Lotoski, "H$_2$O-based solid fuel power source based on the catalysis of H by HOH catalyst", Int'l J. Hydrogen Energy, Vol. 40, (2015), pp. 25-37.

13. J. A. Kollmeier, D. H. Weinberg, B. D. Oppenheimer, F. Haardt, N. Katz, R. Davé, M. Fardal, P. Madau, C. Danforth, A. B. Ford, "The photon underproduction crisis, The Astrophysical Journal Letters, Vol. 789, No. 2, (2014), p. L-32(5pp).

14. R. D. Hill, "Anomalous Behavior of H Lines in Lightning Spectra", Electrical Processes in Atmospheres, Proceedings of the Fifth International Conference on Atmospheric Electricity held at Garmisch-Partenkirchen (Germany), 2–7 September 1974, Editors: H. Dolezalek, R. Reiter, H. E. Landsberg, pp 647-651, https://link.springer.com/chapter/10.1007%2F978-3-642-85294-7_102.

15. C. Karch, M. Schreiner; R. Honke; J. Wolfrum, "Shock waves from a lightning discharge", 2018 34th International Conference on Lightning Protection (ICLP), DOI: 10.1109/ICLP.2018.8503327.

16. E. Bulbul, M. Markevitch, A. Foster, R. K. Smith, M. Loewenstein, S. W. Randall, "Detection of an unidentified emission line in the stacked X-Ray spectrum of galaxy clusters," The Astrophysical Journal, Volume 789, Number 1, (2014).

17. A. Boyarsky, O. Ruchayskiy, D. Iakubovskyi, J. Franse, "An unidentified line in X-ray spectra of the Andromeda galaxy and Perseus galaxy cluster," (2014), arXiv:1402.4119 [astro-ph.CO].

18. N. Cappelluti, E. Bulbul, A. Foster, P. Natarajan, M. C. Urry, M. W. Bautz, F. Civano, E. Miller, R. K. Smith, "Searching for the 3.5 keV Line in the Deep Fields with Chandra: The 10 ms Observations," The Astrophysical Journal, Vol. 854 (2), (2018), p. 179 DOI: 10.3847/1538-4357/aaaa68.

19. R. L. Mills *The Grand Unified Theory of Classical Quantum Mechanics*, November 1995 Edition HydroCatalysis Power Corp. Malvern, PA Library of Congress Catalog Number 94-077780 Chp.22 ISBN number ISBN 0-9635171-1-2.

20. G. C-F Chen et al. "A HARP view of H0LiCOW: H0 from three time-delay gravitational lens systems with adaptive optics imaging", Monthly Notices of the Royal Astronomical Society, (2019). DOI: 10.1093/mnras/stz2547.

21. M. J. Jee, et al., "Discovery of a ringlike dark matter structure in the core of the galaxy cluster C1 0024+17," Astrophysical Journal, Vol. 661, (2007), pp. 728-749.

22. F. Bournaud, P. A. Duc, E. Brinks, M. Boquien, P. Amram, U. Lisenfeld, B. Koribalski, F. Walter, V. Charmandaris, "Missing mass in collisional debris from galaxies," Science, Vol. 316, (2007), pp. 1166–1169.

23. B. G. Elmegreen, "Dark matter in galactic collisional debris," Science, Vol. 316, (2007), pp. 32-33.

24. M. J. Jee, A. Mahdavi, H. Hoekstra, A. Babul, J. J. Dalcanton, P. Carroll, P. Capak, "A study of the dark core in A520 with the Hubble Space Telescope: The mystery deepens," Astrophys. J., Vol. 747, No.96, (2012), pp. 96-103.

25. D. S. Akerib, et al "First results from the LUX dark matter experiment at the Stanford Underground Research Facility" 2014 http://arxiv.org/abs/1310.8214.

26. G. Agakishiev et al., Physics Letters B, **731, (**2014) 365 DOI: 10.1016/j.physletb.2014.02.035.

27. L. M. Hobbs, D. G. York, T. P. Snow, T. Oka, J. A. Thorburn, M. Bishof, S. D. Friedman, B. J. McCall, B. Rachford, P. Sonnentrucker, D. E. Welty, A Catalog of Diffuse Interstellar Bands in the Spectrum of HD 204827", Astrophysical Journal, Vol. 680, No. 2, (2008), pp. 1256-1270,   http://dibdata.org/HD204827.pdf, https://iopscience.iop.org/article/10.1086/587930/pdf.

28. E.H. Wishnow, *The Far-Infrared Absorption Spectrum of Low Temperature Hydrogen Gas*, Ph.D. Thesis, University of British Columbia, Canada, (1993).

29. E. H. Wishnow, I. Ozier, H. P. Gush, "Submillimeter spectrum of low-temperature hydrogen: The pure translational band of H_2 and the $R(0)$ line of HD," The Astrophysical Journal, Vol. 392, (1992), pp. L43-L46.

30. E. H. Wishnow, I. Ozier, H. P. Gush, J. Schaefer, "Translational band of gaseous hydrogen at low temperature," The Astrophysical Journal, Vol. 492, (1998), pp. 843-848.

31. E. H. Wishnow, A. Leung, H. P. Gush, "Cryogenic multiple reflection absorption cell and Fourier transform spectrometer system for the far infrared," Review of Scientific Instruments, Vol. 70, No. 1, (1999), pp. 23-31.

32. R. L. Mills, J. Lotoski, G. Zhao, K. Akhtar, Z. Chang, J. He, X. Hu, G. Wu, G. Chu and Y. Lu, "Identification of New Hydrogen States," Physics Essays, Vol. 24, (2011), pp. 95–117; doi:10.4006/1.3544207.

33. M. Kuraica, N. Konjevic, "Line shapes of atomic hydrogen in a plane-cathode abnormal glow discharge", Physical Review A, Volume 46, No. 7, October (1992), pp. 4429-4432.

34. M. Kuraica, N. Konjevic, M. Platisa and D. Pantelic, *Spectrochimica Acta* Vol. 47, 1173 (1992).

35. I. R. Videnovic, N. Konjevic, M. M. Kuraica, "Spectroscopic investigations of a cathode fall region of the Grimm-type glow discharge", Spectrochimica Acta, Part B, Vol. 51, (1996), pp. 1707-1731.

36. S. Alexiou, E. Leboucher-Dalimier, "Hydrogen Balmer-α in dense plasmas", Phys, Rev. E, Vol. 60, No. 3, (1999), pp. 3436-3438.

37. S. Djurovic, J. R. Roberts, "Hydrogen Balmer alpha line shapes for hydrogen-argon mixtures in a low-pressure rf discharge", J. Appl. Phys., Vol. 74, No. 11, (1993), pp. 6558-6565.

38. S. B. Radovanov, K. Dzierzega, J. R. Roberts, J. K. Olthoff, Time-resolved Balmer-alpha emission from fast hydrogen atoms in low pressure, radio-frequency discharges in hydrogen", Appl. Phys. Lett., Vol. 66, No. 20, (1995), pp. 2637-2639.

39. S. B. Radovanov, J. K. Olthoff, R. J. Van Brunt, S. Djurovic, "Ion kinetic-energy distributions and Balmer-alpha (H_α) excitation in $Ar - H_2$ radio-frequency discharges", J. Appl. Phys., Vol. 78, No. 2, (1995), pp. 746-757.

40. G. Baravian, Y. Chouan, A. Ricard, G. Sultan, J. Appl. Phys., Vol. 61, (1987), p. 5249.

41. E. L. Ayers and W. Benesch, Phys. Rev., Vol. A37, (1988), p. 194.

42. A. V. Phelps, "Collisions of H^+, H_2^+, H_3^+, ArH^+,H^-, H, and H_2 with Ar and Ar^+ of ArH^+ and H_2 with for energies from 0.1 eV to 10 keV", J. Phys. Chem. Ref Data, Vol. 21, (1992), pp. 883-897.

43. D. Barton, J. W. Bradley, D. A. Steele, and R. D. Short, "Investigating radio frequency plasmas used for the modification of polymer surfaces," J. Phys. Chem. B, Vol. 103, (1999), pp. 4423-4430.

44. N. Cvetanovic, M. M. Kuraica, N. Konjevic, "Excessive Balmer line broadening in a plane cathode abnormal glow discharge in hydrogen" Journal of Applied Physics. Vol. 97, (2005), pp. 33302-1 to 33302-8.

45. C. Barbeau, J. Jolly, "Spectroscopic investigation of energetic atoms in a DC hydrogen glow discharge", Journal of Physics, D, Applied Physics, Vol. 23, (1990), pp. 1168-1174.

46. S. A. Bzenic, S. B. Radovanov, S. B. Vrhovac, Z. B. Velikic, and B. M. Jelenkovic, Chem. Phys. Lett., Vol. 184, (1991), pp. 108-112.

47. E. L. Ayers, W. Benesch, "Shapes of atomic-hydrogen lines produced at a cathode surface", Physical Review A, Vol. 37, No. 1, (1988), pp. 194-199.

48. W. Benesch, E. Li, "Line shapes of atomic hydrogen in hollow-cathode discharges", Optic Letters, Vol. 9, No. 8, (1984), pp. 338-340.

49. A. Bogaerts, R. Gijbels, "Effects of adding hydrogen to an argon glow discharge: overview of some relevant processes and some quantitative explanations", Journal of Analytical Atomic Spectroscopy, Vol. 15, (2000), pp. 441-449.

50. P. Kurunczi, H. Shah, K. Becker, "Hydrogen Lyman-α and Lyman-β emissions from high-pressure microhollow cathode discharges in Ne-H_2 mixtures", Journal of Physics B: Atomic, Molecular and Optical Physics, Vol. 32, No. 22, (1999), L651-L658.

51. K. Akhtar, J. Scharer, R. L. Mills, "Substantial Doppler Broadening of Atomic Hydrogen Lines in DC and Capacitively Coupled RF Plasmas", J. Phys. D: Appl. Phys., Vol. 42, Issue 13 (2009), p. 135207 (12pp).

52. R. L. Mills, K. Akhtar, "Tests of Features of Field-Acceleration Models for the Extraordinary

Selective H Balmer α Broadening in Certain Hydrogen Mixed Plasmas," Int. J. Hydrogen Energy, Vol. 34, (2009), pp. 6465–6477.

53. R. L. Mills, B. Dhandapani, K. Akhtar, "Excessive Balmer α Line Broadening of Water-Vapor Capacitively-Coupled RF Discharge Plasmas," Int. J. Hydrogen Energy, Vol. 33, (2008), pp. 802–815.

54. J. Phillips, C. K. Chen, R. Mills, "Evidence of Energetic Reactions Between Hydrogen and Oxygen Species in RF Generated H_2O Plasmas", Int. J. Hydrogen Energy, Vol. 33 (2008), pp. 2419-2432.

55. J. Phillips, C-K Chen, K. Akhtar, B. Dhandapani, R. Mills, "Evidence of Catalytic Production of Hot Hydrogen in RF Generated Hydrogen/Argon Plasmas", International Journal of Hydrogen Energy, Vol. 32(14), (2007), pp. 3010-3025.

56. R. Mills, P. Ray, B. Dhandapani, "Evidence of an Energy Transfer Reaction Between Atomic Hydrogen and Argon II or Helium II as the Source of Excessively Hot H Atoms in RF Plasmas", Journal of Plasma Physics, (2006), Vol. 72, Issue 4, pp. 469-484.24.

57. R. L. Mills, P. C. Ray, R. M. Mayo, M. Nansteel, B. Dhandapani, J. Phillips, "Spectroscopic Study of Unique Line Broadening and Inversion in Low Pressure Microwave Generated Water Plasmas", J. Plasma Physics, Vol. 71, Part 6, (2005), pp. 877-888.

58. R. L. Mills, K. Akhtar, "Fast H in hydrogen mixed gas microwave plasmas when an atomic hydrogen supporting surface was present," Int. J. Hydrogen Energy, 35 (2010), pp. 2546-2555, doi:10.1016/j.ijhydene.2009.12.148.

59. C. Chen, T. Wei, L. R. Collins, and J. Phillips, "Modeling the discharge region of a microwave generated hydrogen plasma", J. Phys. D: Appl. Phys., Vol. 32, (1999), pp. 688-698.

60. R. Mills, P. Ray, R. M. Mayo, "CW HI Laser Based on a Stationary Inverted Lyman Population Formed from Incandescently Heated Hydrogen Gas with Certain Group I Catalysts", IEEE Transactions on Plasma Science, Vol. 31, No. 2, (2003), pp. 236-247.

61. R. L. Mills, P. Ray, "Stationary Inverted Lyman Population Formed from Incandescently Heated Hydrogen Gas with Certain Catalysts", J. Phys. D, Applied Physics, Vol. 36, (2003), pp. 1504-1509.

62. R. Mills, P. Ray, R. M. Mayo, "The Potential for a Hydrogen Water-Plasma Laser", Applied Physics Letters, Vol. 82, No. 11, (2003), pp. 1679-1681.

63. A. Ulrich, J. Wieser, D. E. Murnick, "Excimer formation using low energy electron beam excitation", Second International Conference on Atomic Molecular Pulsed Lasers, Proc SPIE, (1998), Vol. 3403, pp. 300-307.

64. R. L. Mills, K. Akhtar, G. Zhao, Z. Chang, J. He, X. Hu, G. Chu, "Commercializable Power Source Using Heterogeneous Hydrino Catalysts," Int. J. Hydrogen Energy, Vol. 35, (2010), pp. 395–419, doi: 10.1016/j.ijhydene.2009.10.038.

65. R. L. Mills, "The Nature of Free Electrons in Superfluid Helium—a Test of Quantum Mechanics and a Basis to Review its Foundations and Make a Comparison to Classical Theory," Int. J. Hydrogen Energy, Vol. 26, No. 10, (2001), pp. 1059–1096.

66. R. L. Mills, "The Fallacy of Feynman's Argument on the Stability of the Hydrogen Atom According to Quantum Mechanics," Ann. Fund. Louis de Broglie, Vol. 30, No. 2, (2005), pp. 129–151.

67. R. L. Mills, "Exact Classical Quantum Mechanical Solutions for One- through Twenty-Electron Atoms," Physics Essays, Vol. 18, (2005), pp. 321–361.

68. W. Xie, R. L. Mills, W. Good, A. Makwana, B. Holverstott, N. Hogle, "Millsian 2.0: A Molecular Modeling Software for Structures, Charge Distributions and Energetics of Biomolecules," Physics Essays, Vol. 24, (2011), pp. 200–212.

69. R. L. Mills, B. Holverstott, W. Good, A. Makwana, "Total Bond Energies of Exact Classical Solutions of Molecules Generated by Millsian 1.0 Compared to Those Computed Using Modern 3-21G and 6-31G* Basis Sets," Phys. Essays, Vol. **23,** (2010), 153–199; doi: 10.4006/1.3310832.

70. https://brilliantlightpower.com/millsian-inc/

71. https://brilliantlightpower.com/theory/, "Reviews by Dr. Randy Booker and Dr. Mark Nansteel".

72. W. R. Hagen, R. L. Mills, "Electron Paramagnetic Resonance Proof for the Existence of Molecular Hydrino", Vol. 47, No. 56, (2022), pp. 23751-23761; https://www.sciencedirect.com/science/article/pii/S0360319922022406.

73. R. L. Mills, P. Ray, "A Comprehensive Study of Spectra of the Bound-Free Hyperfine Levels of Novel Hydride Ion H$^-$(1/2), Hydrogen, Nitrogen, and Air", Int. J. Hydrogen Energy, Vol. 28, No. 8, (2003), pp. 825-871.

74. R. Mills, W. Good, P. Jansson, J. He, "Stationary Inverted Lyman Populations and Free-Free and Bound-Free Emission of Lower-Energy State Hydride Ion formed by and Exothermic Catalytic Reaction of Atomic Hydrogen and Certain Group I Catalysts," Cent. Eur. J. Phys., Vol. 8, (2010), pp. 7–16, doi: 10.2478/s11534-009-0052-6.

75. R. L. Mills, P. Ray, "Stationary Inverted Lyman Population and a Very Stable Novel Hydride Formed by a Catalytic Reaction of Atomic Hydrogen and Certain Catalysts," J. Opt. Mat., 27, (2004), pp. 181–186.

76. R. L. Mills, P. C. Ray, R. M. Mayo, M. Nansteel, W. Good, P. Jansson, B. Dhandapani, J. He, "Hydrogen Plasmas Generated Using Certain Group I Catalysts Show Stationary Inverted Lyman Populations and Free-Free and Bound-Free Emission of Lower-Energy State Hydride," Res. J. Chem Env., Vol. 12(2), (2008), pp. 42–72.

77. R. Mills, J. Lotoski, W. Good, J. He, "Solid Fuels that Form HOH Catalyst," Int'l J. Hydrogen

Energy, Vol. 39 (2014), pp. 11930–11944 DOI: 10.1016/j.ijhydene.2014.05.170.

78. R. Mills, X Yu, Y. Lu, G Chu, J. He, J. Lotoski, "Catalyst induced hydrino transition (CIHT) electrochemical cell," Int. J. Energy Res., Vol. 38, (2014), pp. 1741-1736, DOI: 10.1002/er.3142.

79. https://brilliantlightpower.com/validation-reports/.

80. E. E. Chen, M. Stavola, W. B. Fowler, J. A. Zhou, "Rotation of molecular hydrogen in Si: unambiguous identification of ortho-H_2 and para-D_2", Phys Rev Lett, (2002), Vol. 88(24), pp. 245503-1 to 245503-4.

81. R. L. Mills, J. He, Z. Chang, W. Good, Y. Lu, B. Dhandapani, "Catalysis of Atomic Hydrogen to Novel Hydrogen Species $H^-(1/4)$ and $H_2(1/4)$ as a New Power Source," Int. J. Hydrogen Energy, Vol. 32(13), (2007), pp. 2573–2584.

82. C. Hisatsune, N. H. Suarez, "Infrared spectra of metaborate monomer and trimer ions", Inorganic Chemistry, Vol. 3, No. 2, (1964), pp. 168-174.

83. D. F. Smith, Jr., "Infrared spectra of BO_2^- in alkali halides—I. Potassium and rubidium halides", Spectrochimica Acta, Vol. 30A, pp. 875-882.C.

84. R. Becker, "An investigation of the metaborate monomer and trimer ions in alkali halide crystals", PhD Thesis submitted to Oregon State University, June, 1969.

85. T. R. Burkholder, L. Andrews, "Reactions of boron atoms with molecular oxygen. Infrared spectra of BO, BO_2, B_2O_2, B_2O_3, and BO_2^- in solid argon", J. Chem. Phys., Vol 95, No. 12 (1991), pp. 8697-8709.

86. https://webbook.nist.gov/cgi/cbook.cgi?ID=B6000451&Mask=80.

87. R. Teghil, B. Janis, L. Bencivenni, "Matrix-isolation IR studies on alkali metal M(XO2) species. Bonding and structure of Li(CO_2), M(ClO_2) and M(BO_2) molecules", Inorganica Chimica Acta, Vol. 88, (1984), pp. 115-124.

88. T. Markmaitree, R. Ren, L. L. Shaw, "Enhancement of lithium amide to lithium imide transition via mechanical activation", J. Phys. Chem. B., Vol. 110, No. 41, pp. 20710-20718.

89. https://www.halide-crylink.com/wp-content/uploads/2020/07/KCl-Crystal.pdf.

90. R. Mills, J. Lotoski, J. Kong, G. Chu, J. He, J. Trevey, "High-Power-Density Catalyst Induced Hydrino Transition (CIHT) Electrochemical Cell." Int. J. Hydrogen Energy, 39 (2014), pp. 14512–14530 DOI: 10.1016/j.ijhydene.2014.06.153.

91. https://brilliantlightpower.com/pdf/Analytical_Presentation.pdf.

92. R. Mills, "The Grand Unified Theory of Classical Quantum Mechanics, January 1999 Edition, ISBN 0-9635171-3-9, Library of Congress Catalog Number 99-72249, pp. 897-898; 979-987.

93. R. L. Mills, J. Sankar, A. Voigt, J. He, P. Ray, B. Dhandapani, "Role of Atomic Hydrogen Density and Energy in Low Power CVD Synthesis of Diamond Films," Thin Solid Films, 478,

(2005), pp. 77–90.

94. R. L. Mills, J. Sankar, A. Voigt, J. He, B. Dhandapani, "Spectroscopic Characterization of the Atomic Hydrogen Energies and Densities and Carbon Species During Helium-Hydrogen-Methane Plasma CVD Synthesis of Diamond Films," Chemistry of Materials, Vol. 15, (2003), pp. 1313–1321.

95. R. L. Mills, J. Sankar, A. Voigt, J. He, B. Dhandapani, "Synthesis of HDLC Films from Solid Carbon," J. Materials Science, J. Mater. Sci. 39 (2004), pp. 3309–3318.

96. H. Conrads, R. Mills, Th. Wrubel, "Emission in the Deep Vacuum Ultraviolet from a Plasma Formed by Incandescently Heating Hydrogen Gas with Trace Amounts of Potassium Carbonate," Plasma Sources Science and Technology, Vol. 12, (2003), pp. 389-395.

97. R. L. Mills, T. Onuma, and Y. Lu, "Formation of a Hydrogen Plasma from an Incandescently Heated Hydrogen-Catalyst Gas Mixture with an Anomalous Afterglow Duration," Int. J. Hydrogen Energy, Vol. 26, No. 7, July, (2001), pp. 749–762.

98. R. L. Mills, "Temporal Behavior of Light-Emission in the Visible Spectral Range from a Ti-K_2CO_3-H-Cell," Int. J. Hydrogen Energy, Vol. 26, No. 4, (2001), pp. 327–332.

99. R. L. Mills, E. Dayalan, P. Ray, B. Dhandapani, J. He, "Highly Stable Novel Inorganic Hydrides from Aqueous Electrolysis and Plasma Electrolysis," Electrochimica Acta, Vol. 47, No. 24, (2002), pp. 3909–3926.

100. https://brilliantlightpower.com/pdf/Waterbath_Calorimeter_Protocol_031720.pdf.

101. brilliantlightpower.com/pdf/Mark_Nansteel_Report.pdf.

102. brilliantlightpower.com/pdf/Randy_Booker_Report.pdf.

103. https://brilliantlightpower.com/pdf/Tse-Validation-Report-Brilliant-Light-Power.pdf.

104. https://brilliantlightpower.com/pdf/Waterbath_Calorimetry_Data_and_Analysis_031120.pdf.

105. https://brilliantlightpower.com/pdf/Report_on_Water_Bath_Calorimetry_12.04.20.pdf.

106. https://brilliantlightpower.com/pdf/Report_on_Water_Bath_Calorimetry_(031621)_rev.pdf.

107. C. Wang, Y. Liu, "Ultrafast optical manipulation of magnetic order in ferromagnetic materials", Nano Convergence, Vol. 7, No. 35, (2020), https://nanoconvergencejournal.springeropen.com/articles/10.1186/s40580-020-00246-3.

108. R. Mills, M. W. Nansteel, "Oxygen and Silver Nanoparticle Aerosol Magnetohydrodynamic Power Cycle", Journal of Aeronautics & Aerospace Engineering, Vol. 8, Iss. 2, No 216, (2019), pp. 1-13.

109. R. M. Mayo, R. L. Mills, M. Nansteel, "Direct Plasmadynamic Conversion of Plasma Thermal Power to Electricity," IEEE Transactions on Plasma Science, October, (2002), Vol. 30, No. 5, pp. 2066–2073.

110. R. M. Mayo, R. L. Mills, M. Nansteel, "On the Potential of Direct and MHD Conversion of

Power from a Novel Plasma Source to Electricity for Microdistributed Power Applications," IEEE Transactions on Plasma Science, August, (2002), Vol. 30, No. 4, pp. 1568–1578.

111. R. M. Mayo, R. L. Mills, "Direct Plasmadynamic Conversion of Plasma Thermal Power to Electricity for Microdistributed Power Applications," 40th Annual Power Sources Conference, Cherry Hill, NJ, June 10–13, (2002), pp. 1-4.